

PSU-IRL-SCI-451

Classification Numbers 1.5.3



THE PENNSYLVANIA
STATE UNIVERSITY

IONOSPHERIC RESEARCH

Scientific Report 451

A COMPARISON BETWEEN THE CURRENT MODELS OF MID-LATITUDE SPREAD F AND DATA FROM THE ARECIBO OBSERVATORY

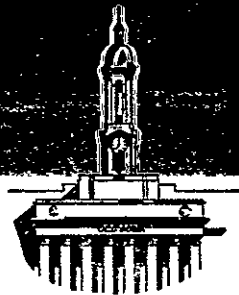
by

George Inel

January 20, 1977

*The research reported in this document has been supported
by The National Aeronautics and Space Administration under
Grant No. NGL-39-009-003.*

IONOSPHERE RESEARCH LABORATORY



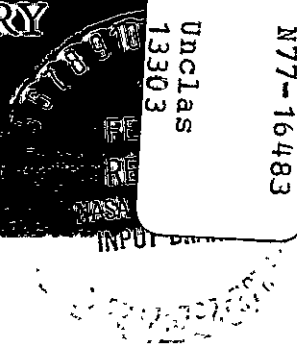
University Park, Pennsylvania

(NASA-CR-149467) A COMPARISON BETWEEN THE
CURRENT MODELS OF MID-LATITUDE SPREAD F AND
DATA FROM THE ARECIBO OBSERVATORY
(Pennsylvania State Univ.) 186 p
HC A09/WF A01

CSCI 04A G3/46

Unclas
13303

N77-16483



made. Two of four nights studied are nights with F_s .

The Perkins model is derived in a frame of reference moving with the velocity of the neutral wind; the model is transformed to the rest frame to facilitate comparison with data. Several data handling techniques are introduced. In particular, an integration interval that remains constant in length, but follows the vertical motion of the peak of the F layer is used to obtain the field integrated quantities of the Perkins model.

It was found that the Perkins model describes the general time behavior of the field integrated Pedersen conductivity if recombination is included, and the boundary flux is neglected. The numerical agreement is usually within a factor of two. It was found that the flux data is inconsistent with the rest of the data. Errors on the order of 30 m/s in the individual velocity measurements are believed to be present to account for the differences.

The Perkins model is able to predict reasonable growth rates of the development of F_s ; however, a direct comparison between the growth rates predicted by the model and actual onset times is not possible because of the lack of data on the eastward neutral wind.

The linear growth rate of the Perkins model is extended by including recombination, and a short wavelength damping term and coupling to the E region. It is found that, for wavelength perturbations several kilometers or longer, the E region can short circuit instabilities in the F region and reduce the growth rate.

NONE

PSU-IRL-SCI-451
Classification Numbers 1.5.3

Scientific Report 451

A Comparison Between the Current Models of
Mid-Latitude Spread F and Data from the Arecibo Observatory

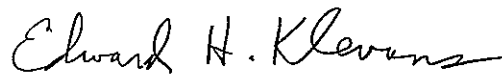
by

George Imel

January 20, 1977

The research reported in this document has been supported by The
National Aeronautics and Space Administration under Grant No.
NGL-39-009-003.

Submitted by:



E. H. Klevans, Professor
Nuclear Engineering

Approved by:



J. S. Nisbet, Director
Ionosphere Research Laboratory

Ionosphere Research Laboratory
The Pennsylvania State University
University Park, Pennsylvania 16802

ACKNOWLEDGEMENTS

I wish to express my appreciation to Dr. Edward Klevans for his guidance during this work and my graduate education and to Drs. A. Jacobs, G. Fleming and E. Kenney for serving on my doctoral committee.

Many helpful suggestions were obtained from the staff of the Ionosphere Research Laboratory, especially Drs. L. Carpenter, G. Zinchenko and J. Nisbet for which I am grateful. This work also benefited greatly from discussions with Dr. F. Perkins of Princeton University and Dr. S. Ossakow of the Naval Research Laboratory.

I also wish to acknowledge the invaluable computer programming help given by Mr. R. Divany and Ms. B. Beiswenger of the Ionosphere Research Laboratory.

The data was provided by Dr. Robert Harper of the Arecibo Observatory and his cooperation is greatly appreciated. Graphs presenting E region conductivities (Figures 66 and 67) were prepared by Dr. Gleb Zinchenko and appeared in IRL Report 445. His permission in using these graphs is gratefully acknowledged.

This work was supported by the National Aeronautics and Space Administration under grant No. NGL 39-009-003.

TABLE OF CONTENTS

	Page
ACKNOWLEDGEMENTS	ii
LIST OF TABLES	iv
LIST OF FIGURES	v
LIST OF SYMBOLS	x
ABSTRACT	xiii
CHAPTER I INTRODUCTION	1
CHAPTER II MODELS	6
2.1 The Perkins Model	6
2.2 Scannapieco Model	20
2.3 Reid Model	24
2.4 Statement of the Problem	30
CHAPTER III EQUILIBRIUM ANALYSIS	34
3.1 Derivation of the Equations in the Laboratory Frame	34
3.2 Introduction to the Data	41
3.3 Analysis of the Data - Fixed Limit Integration	46
3.4 Analysis of the Data - Peak-Centered Integration	83
3.5 Fluxes and Gradients	113
3.6 Equilibrium Behavior of F_s Nights vs. Non F_s Nights	126
CHAPTER IV GROWTH RATE ANALYSIS	134
4.1 Comparison With the Data	134
4.2 Extension of the Perkins Model	143
4.2.1 Short Wavelength Diffusion	144
4.2.2 E Region Coupling	150
CHAPTER V SUMMARY AND CONCLUSIONS	162
APPENDIX DESCRIPTION OF ARECIBO MODEL USED FOR CALCULATION OF COLLISION FREQUENCY	167
REFERENCES	170
VITA.	172

LIST OF TABLES

Table		Page
1	Neutral winds required to yield reasonable growth times predicted by the Perkins and Scannapieco models for September 17, 1974	137
2	Neutral winds required to yield reasonable growth times predicted by the Perkins and Scannapieco models for November 9, 1974	137
3	Neutral winds required to yield reasonable growth times predicted by the Perkins and Scannapieco models for May 18, 1975	138
4	Neutral wind required to yield reasonable growth times predicted by the Perkins and Scannapieco models for October 14, 1975.	138

LIST OF FIGURES

Figure		Page
1	Sample ionograms	2
2	Coordinate system.	8
3a	Orientation of the \underline{E} and \underline{k} vectors	16
3b	The production of the resultant electric field from the electric field and the neutral wind.	17
4	Physical model of the Perkins instability	19
5	Physical model of the Scannapieco instability	23
6	Physical model of the Reid instability	25
7	Density profiles.	45
8	Time variation of hm	50
9	Time variation of the eastward electric field	53
10	Time variation of the neutral wind at peak and the neutral wind weighted by the square root of the S/N ratio	56
11	Time variation of the resultant eastward electric field and hm for September 17, 1974.	57
12	Time variation of the resultant eastward electric field and hm for November 9, 1974	59
13	Time variation of the resultant eastward electric field and hm for May 18, 1975	60
14	Time variation of the resultant eastward electric field and hm for October 14, 1975.	61
15	Time variation of the F region integrated Pedersen conductivity and hm for September 17, 1974	63
16	Time variation of the F region integrated Pedersen conductivity and hm for November 9, 1974	64
17	Time variation of the F region integrated Pedersen conductivity and hm for May 18, 1975	65
18	Time variation of the F region integrated Pedersen conductivity and hm for October 14, 1975	66

Figure	Page
19	Time variation of F region integrated ion density. 68
20a	Time variation of the flux at 201.6 km. 70
20b	Time variation of the flux at 230.6 km. 71
20c	Time variation of the flux at 259.6 km. 72
20d	Time variation of the flux at 288.6 km. 73
20e	Time variation of the flux at 317.6 km. 74
20f	Time variation of the flux at 346.5 km. 75
20g	Time variation of the flux at 375.5 km. 76
20h	Time variation of the flux at 404.5 km. 77
20i	Time variation of the flux at 433.5 km. 78
20j	Time variation of the flux at 462.4 km. 79
20k	Time variation of the flux at 404.5 km and 433.5 km . . . 81
21	Time variation of the net flux (fixed boundaries) 82
22	Time variation of the net flux (peak centered boundaries). 84
23	Time variation of N_E obtained from the data, and the solution of Equation 3.8 including recombination only . . . 86
24	Time variation of N_E obtained from the data, and the solution of Equation 3.8 including recombination and the flux. 87
25	Time variation of the net flux (peak centered boundaries). 88
26	Time variation of N_E obtained from the data, and the solution of Equation 3.8 including recombination only . . . 89
27	Time variation of N_E obtained from the data, and the solution of Equation 3.8 including recombination and the flux. 90
28	Time variation of the net flux (peak centered boundaries). 91
29	Time variation of N_E obtained from the data, and the solution of Equation 3.8 including recombination only . . . 92

Figure	Page
30 Time variation of N_E obtained from the data, and the solution of Equation 3.8 including recombination and the flux	93
31 Time variation of the net flux (peak centered boundaries).	94
32 Time variation of N_E obtained from the data, and the solution of Equation 3.8 including recombination only . . .	95
33 Time variation of N_E obtained from the data, and the solution of Equation 3.8 including recombination and the flux	96
34 Time variation of Σ_E obtained from the data, and the solution of Equation 3.10 including E_{RESY} and gravity only	98
35 Time variation of Σ_E obtained from the data, and the solution of Equation 3.10 including E_{RESY} , gravity, and recombination	99
36 Time variation of Σ_E obtained from the data, and the solution of Equation 3.10 including E_{RES} , gravity, recombination and diffusion	100
37 Time variation of Σ_E obtained from the data, and the solution of Equation 3.10 including E_{RES} , gravity, recombination, diffusion and the flux	101
38 Time variation of Σ_E obtained from the data, and the solution of Equation 3.10 including E_{RES} , gravity, recombination and diffusion	102
39 Time variation of Σ_E obtained from the data, and the solution of Equation 3.10 including E_{RES} , gravity, recombination, diffusion and the flux	103
40 Time variation of Σ_E obtained from the data, and the solution of Equation 3.10 including E_{RES} , gravity, recombination and diffusion	104
41 Time variation of Σ_E obtained from the data, and the solution of Equation 3.10 including E_{RES} , gravity, recombination, diffusion and the flux	105
42 Time variation of Σ_E obtained from the data, and the solution of Equation 3.10 including E_{RES} , gravity, recombination and diffusion	106

Figure	Page
43	Time variation of Σ_F obtained from the data, and the solution of Equation 3.10 including E_{RES} , gravity, recombination, diffusion and the flux 107
44	Time variation of Σ_F obtained from the data, the solution of Equation 3.10 including E_{RES} and gravity, and the quasi-equilibrium solution of the Perkins model (Equation 2.12). 108
45	Time variation of Σ_F obtained from the data, the solution of Equation 3.10 including E_{RES} and gravity, and the quasi-equilibrium solution of the Perkins model (Equation 2.12). 109
46	Time variation of Σ_F obtained from the data, the solution of Equation 3.10 including E_{RES} and gravity, and the quasi-equilibrium solution of the Perkins model (Equation 2.12). 110
47	Time variation of Σ_F obtained from the data, the solution of Equation 3.10 including E_{RES} and gravity, and the quasi-equilibrium solution of the Perkins model (Equation 2.12). 111
48	Time variation of top flux, and flux required to satisfy Equations 3.8 and 3.10 115
49	Time variation of bottom flux, and flux required to satisfy Equations 3.8 and 3.10 116
50	Time variation of top flux, and flux required to satisfy Equations 3.8 and 3.10 117
51	Time variation of bottom flux, and flux required to satisfy Equations 3.8 and 3.10 118
52	Time variation of net flux, and flux required to satisfy Equations 3.8 and 3.10 119
53	Time variation of net flux, and flux required to satisfy Equations 3.8 and 3.10 120
54	Time variation of net flux, and flux required to satisfy Equations 3.8 and 3.10 121
55	Time variation of net flux, and flux required to satisfy Equations 3.8 and 3.10 122

Figure	Page
56	Time variation of northward electric field 127
57	Time variation of eastward electric field 128
58	Time variation of northward electric field 129
59	Time variation of eastward electric field 130
60	Time variation of northward electric field 131
61	Time variation of eastward electric field 132
62	Time variation of northward electric field 133
63	Time variation of neutral wind 139
64	Time variation of neutral wind 140
65	Time variation of neutral wind 141
66	Time variation of integrated F region Pedersen conductivity, and E region Pedersen and Hall conductivities (from Zinchenko, 1976) 152
67	Time variation of integrated F region Pedersen conductivity, and E region Pedersen and Hall conductivities (from Zinchenko, 1976) 153
68	E region coupling model 155

LIST OF SYMBOLS

T	ion temperature (ergs)
n	ion (electron) density (cm^{-3})
e	charge (stat-coulombs)
c	speed of light ($\text{cm} - \text{sec}^{-1}$)
\underline{v}	plasma velocity ($\text{cm} - \text{sec}^{-1}$)
ϕ	electrostatic potential (statvolt)
M	ion mass (grams)
g	force due to gravity ($\text{cm} - \text{sec}^{-2}$)
ν_{in}	ion-neutral collision frequency (sec^{-1})
ω_{ci}	ion-cyclotron frequency (sec^{-1})
\underline{j}_{\perp}	total electrical current perpendicular to \underline{B} (stat-coulombs - $\text{cm}^{-2} - \text{sec}^{-1}$)
N	field integrated density (cm^{-2})
Σ	field integrated Pedersen conductivity ($\text{cm} - \text{sec}^{-1}$)
D	magnetic field dip angle
H	neutral atmosphere scale height (cm)
\underline{E}_0	equilibrium electric field (statvolt - m^{-1})
M_n	mass of the neutrals (grams)
γ, ω	perturbation growth rate (sec^{-1})
τ	perturbation growth time (sec)
\underline{k}	perturbation wavenumber (cm^{-1})
λ	perturbation wavelength (cm)
q_s	charge of species "S" (stat-coulombs)
ν_{sn}	frequency of collisions between species "S" and the neutrals (sec^{-1})

LIST OF SYMBOLS (continued)

H_p	plasma scale height (cm)
\underline{E}_{RES}	resultant electric field
Φ_z	ion flux along the magnetic field ($\text{cm}^{-2} \text{ sec}^{-1}$)
β	recombination loss rate (sec^{-1})
σ_P	local Pedersen conductivity (sec^{-1})
σ_H	local Hall conductivity (sec^{-1})
\underline{V}_H	neutral wind velocity ($\text{cm} - \text{sec}^{-1}$)
ψ	field integrated Hall conductivity ($\text{cm} - \text{sec}^{-1}$)
$\langle \beta \rangle$	flux tube averaged recombination coefficient with density weighting (sec^{-1})
$\bar{\beta}$	flux tube averaged recombination coefficient with Pedersen conductivity weighting (sec^{-1})
hm	height of maximum plasma density (km),

ABSTRACT

The current models of mid-latitude F_s are studied. The assumptions and derivations of the Reid model, the Scannapieco model, and the Perkins model are presented in detail.

Incoherent-scatter data of the density profiles and velocity profiles were obtained from the Arecibo Observatory in order that the models could be evaluated on the basis of experimental data. Initial studies indicated that the Perkins model was most representative of the data from Arecibo, so a detailed comparison of the predictions of the Perkins model and the data was made. Two of four nights studied are nights with F_s .

The Perkins model is derived in a frame of reference moving with the velocity of the neutral wind; the model is transformed to the rest frame to facilitate comparison with data. Several data handling techniques are introduced. In particular, an integration interval that remains constant in length, but follows the vertical motion of the peak of the F layer is used to obtain the field integrated quantities of the Perkins model.

It was found that the Perkins model describes the general time behavior of the field integrated Pedersen conductivity if recombination is included, and the boundary flux is neglected. The numerical agreement is usually within a factor of two. It was found that the flux data is inconsistent with the rest of the data. Errors on the order of 30 m/s in the individual velocity measurements are believed to be present to account for the differences.

The Perkins model is able to predict reasonable growth rates of the development of F_g ; however, a direct comparison between the growth rates predicted by the model and actual onset times is not possible because of the lack of data on the eastward neutral wind.

The linear growth rate of the Perkins model is extended by including recombination, and a short wavelength damping term and coupling to the E region. It is found that, for wavelength perturbations several kilometers or longer, the E region can short circuit instabilities in the F region and reduce the growth rate.

CHAPTER I

INTRODUCTION

Spread (F_s) is caused by the presence of plasma density irregularities aligned along the earth's magnetic field (B) in the F region of the ionosphere. The term "spread F" is derived from the spreading of the returned signal on an ionogram. An ionogram, which is a measurement produced by reflecting radio waves from the ionosphere, normally would have two discrete traces of the returned signal from the F region indicating the reflection height vs. frequency. During F_s , the field aligned irregularities cause a smearing, or spreading of these traces. The smearing can either appear as "range spreading", when there are many reflection heights for the same frequency, or "frequency spreading", when waves of different frequencies are reflected at the same height. Two ionograms are shown in Figure 1; the ordinate is the virtual height of reflection of the signal, and the abscissa is the frequency of the signal. One shows normal traces from the undisturbed ionosphere, and the other shows the spreading of the signal representative of F_s .

The density irregularities that cause F_s can be grouped into two general classes: very large patches that extend horizontally for several hundred kilometers, and smaller individually aligned irregularities with sizes on the order of kilometers or less. It is likely that the large patches are composed of many of the smaller ones. The irregularities are seen from the bottom of the F layer to around 1000 km (Herman, 1966).

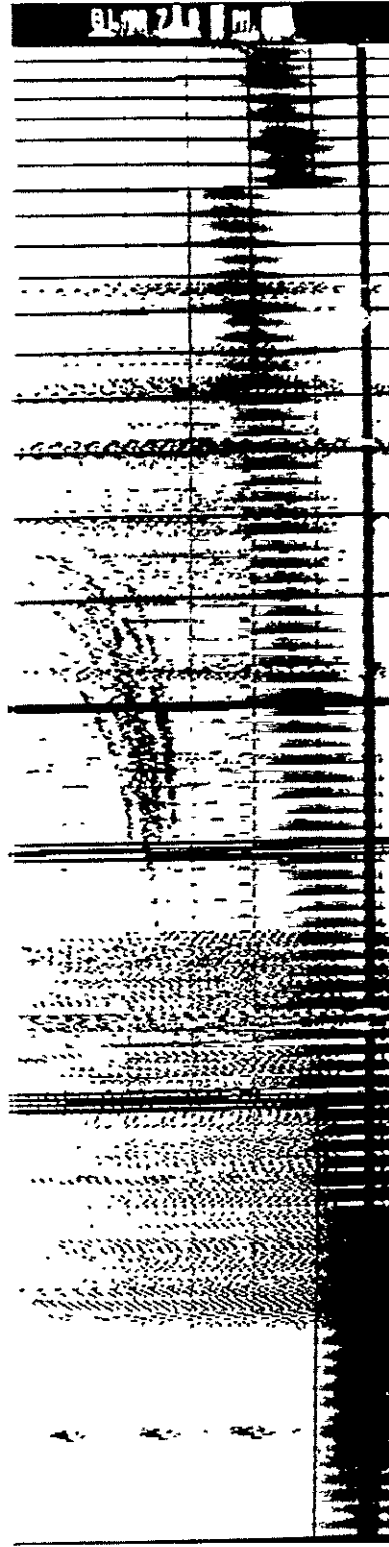
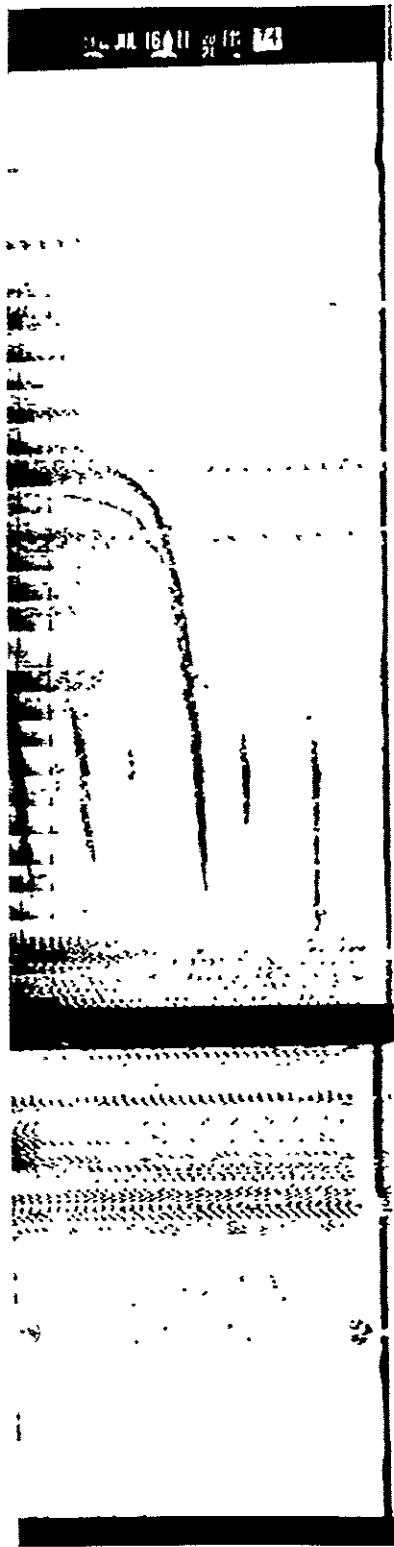


Figure 1: Sample ionograms.

ORIGINAL PAGE IS
OF POOR QUALITY

The occurrence of F_s is negatively correlated with magnetic activity at the equator and positively correlated at the poles. In general, F_s appears more during spring and fall than summer and winter, and is rarely observed between 20° and 40° latitude (Herman, 1966).

Recently, Zinchenko (1976) studied the probability of occurrence of F_s at Arecibo Observatory as a function of season, time of day, and solar activity. He has shown that the Arecibo Observatory is atypical of some of the general characteristics described above. In particular, Zinchenko (1976) found that Arecibo, which is at 30° latitude and is not expected to see F_s , observes F_s quite often, especially in the winter and summer months. In fact, during December and January, the probability of observing F_s on any given night approaches 90 per cent.

There is a great deal of data on F_s occurring at equatorial latitudes. (Farley, et al., 1970; McClure and Woodman, 1972; Balsley et al., 1972; Farley, 1974). Farley et al., (1970) list some of the important characteristics of the irregularities that produce equatorial F_s : 1) the irregularities usually appear when the F layer is high, and moving up. They may persist for an hour or more as the layer moves down, and then are quenched; 2) the irregularities are most often seen on the bottomside of the F layer; 3) they usually appear a few hours after sunset, but may be delayed if the upward motion of the layer is delayed; and 4) they are never seen during the day, even during a total solar eclipse.

The data base for mid-latitude F_s is not as extensive as that for equatorial F_s . The important works are those of Zinchenko (1976), describing probabilities of occurrence of F_s at Arecibo, and Kelley (1972) and Dyson et al., (1974) that show that F_s occurs simultaneously with electrostatic turbulence.

A number of theoretical models have been proposed to account for equatorial and mid-latitude F_s . Those of Hudson and Kennel (1975) and Williams and Weinstock (1970) are applicable only to equatorial latitudes. Reid (1968) and Cunnold (1969) proposed an $\underline{E} \times \underline{B}$ drift instability that is applicable at all latitudes, and Perkins (1973) and Scannapieco et al., (1975) propose detailed models that are applicable to mid-latitudes only. Each of these models make certain assumptions about ionospheric conditions. Each postulates a definite set of onset parameters that must be satisfied before F_s will occur. However, a comparison of the models and their assumptions with the available data has not been made. This thesis will partially fill that void, by comparing the current models of mid-latitude F_s with data from the Arecibo Observatory.

The derivations of the Perkins model, the Scannapieco model, and the Reid and Cunnold models are presented in Chapter II. The data that are available from the Arecibo Observatory are introduced in Chapter III. Several data handling techniques, as well as methods of obtaining ionospheric parameters from the raw data are also presented in Chapter III. Also, the Perkins model is extended, and the equilibrium conditions predicted by the extended model are compared with the data from Arecibo.

In Chapter IV it is shown that the data available from the Arecibo Observatory are insufficient to calculate growth rates predicted by the Perkins and the Scannapieco models. However, it is shown that the models do have the capability of predicting reasonable (i. e., physical) growth rates. The Perkins model of F_s is extended by including recombination, E region coupling, and short wavelength damping due to diffusion.

The summary and conclusions are presented in Chapter V.

CHAPTER II

MODELS

In this chapter, three mid-latitude models will be discussed. These include the Perkins (1973) model, the model of Scannapieco et al. (1975), and the Reid (1968) model. The Cunnold (1969) model is similar to the Reid (1968) model and will not be discussed separately. The three models chosen are the most current and complete models relevant to mid-latitude F_s .

The derivations of the models are discussed in fairly complete detail to enable the reader to better understand them. They also set the stage for the extensions that will be added in later chapters.

2.1 The Perkins Model.

The basic premise of the Perkins model is that the nighttime F region is supported against gravity by electrodynamic forces ($\underline{j} \times \underline{B}$) and the neutral wind (Perkins, 1973). The current \underline{j} is the Pedersen current, which is parallel to the electric field (\underline{E}) and perpendicular to the magnetic field (\underline{B}). The Hall current, which is perpendicular to \underline{E} and \underline{B} , is assumed negligible in the F region because it is of order $(\nu_{in}^2 / \omega_{ci}^2)$, where ν_{in} is the ion-neutral collision frequency and ω_{ci} is the ion cyclotron frequency. The ratio ν_{in} / ω_{ci} is much less than unity in the F region. The Perkins model also assumes that: (1) the ions and electrons are isothermal; (2) recombination and ion drag are negligible because the time scales for these processes at night is on the order of hours, which is much

longer than the time scale for the development of F_s ; (3) the magnetic field is uniform; (4) the neutral atmosphere consists of a single species distributed exponentially in altitude with a constant scale height, H ; and (5) E region contributions to the integrated conductivities are neglected.

Two of these assumptions, the neglect of recombination and the neglect of E region contributions, will be examined in later chapters. The neglect of recombination is not valid when the F layer is low; the time scales then approach 15-30 minutes, which is of the same order as the time scale for the development of F_s . Perkins (1973) neglected the E region contributions to the integrated conductivity because he assumed that the much greater extent of the F region would overcome the greater conductivity per particle in the E region when integrated quantities were calculated. Zinchenko (1976) found that this assumption is not generally valid.

The equations of motion are written in a drift frame moving with the neutral wind (\underline{V}_n), which is assumed constant. The coordinate system that will be used exclusively in this thesis is shown in Figure 2. The view is toward the east in the northern hemisphere. The vectors labelled \hat{h} and \hat{l} point towards the vertical and northward directions respectively, while those labelled \hat{z} and \hat{x} are parallel and perpendicular to the magnetic field respectively. The magnetic field is pointing downward, with a dip angle D from the northward direction. The equations of motion are the following:

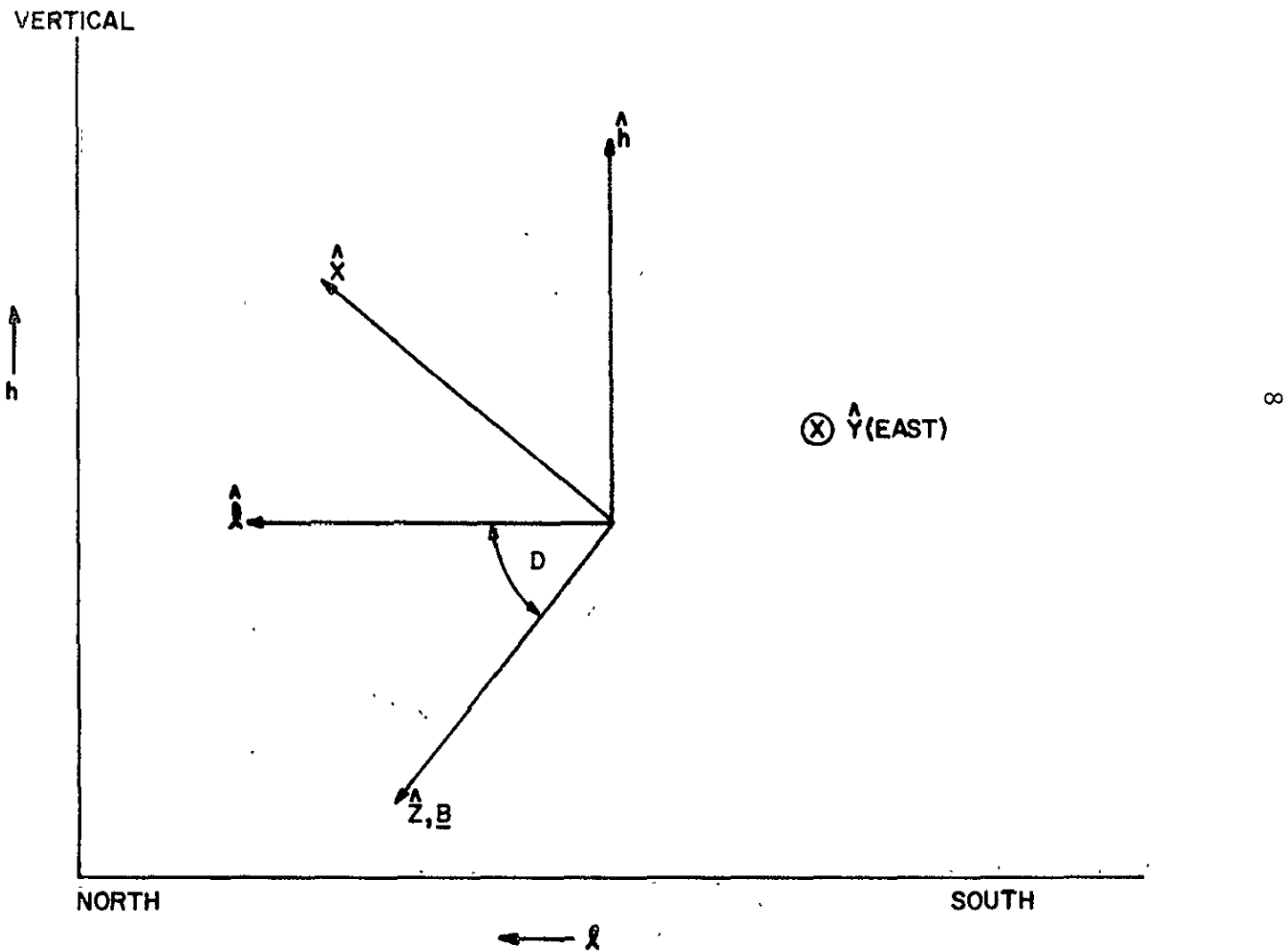


Figure 2: Coordinate system.

ions:

$$-T \underline{\nabla} n + ne \frac{\underline{v}_i \times \underline{B}}{c} - ne \underline{\nabla} \Phi + n M g$$

$$-Mn \underline{v}_i \cdot \underline{v}_{in} = 0$$

electrons:

$$-T \underline{\nabla} n - ne \frac{\underline{v}_e \times \underline{B}}{c} + ne \underline{\nabla} \Phi = 0$$

The view is toward the east in the northern hemisphere. The vectors labelled \hat{h} and \hat{l} point towards the vertical and northward directions respectively, while those labelled \hat{z} and \hat{x} are parallel and perpendicular to the magnetic field respectively. The magnetic field is pointing downward, with a dip angle D from the northward direction. The effect of collisions on electron motion has been neglected reflecting the fact that the electrons are tied quite strongly to the field lines in the F region. Gravity has been neglected because of the low mass of electrons.

By solving the electron equation of motion for $\underline{\nabla}_i \Phi$, the potential can be separated into two parts.

$$\Phi = \phi(x, y) + \frac{T}{e} \ln \frac{n}{n_0}$$

The quantity n_0 is a reference density. The equations of motion may now be written.

ions:

$$-2 \frac{T}{n} \nabla n + ne \frac{\underline{v}_i \times \underline{B}}{c} - ne \nabla \phi + n \cdot M \underline{g} - M n \underline{v}_i \cdot \underline{v}_{in} = 0 \quad (2.1)$$

electrons:

$$-\frac{\underline{v}_e \times \underline{B}}{c} + \nabla \phi \cong 0 \quad (2.2)$$

Because the Perkins model is developed in a frame of reference moving with the neutral wind, the electric field ($\nabla \phi$) as written in Equations 2.1 and 2.2 is actually a resultant electric field that implicitly contains the neutral wind. It is of the form shown below:

$$\underline{E}_{RES} = \underline{E} + \frac{\underline{V}_N \times \underline{B}}{c}$$

where \underline{E} is the electric field that would be measured from a stationary reference frame, and \underline{V}_N is the neutral wind velocity (assumed constant). This point is quite important when one desires to compare the Perkins model with data; electric field measurements are usually made from the ground, and thus are in the stationary frame. The parallel and perpendicular ion velocities and perpendicular electron velocity are obtained from Equations 2.1 and 2.2.

$$v_{zi} = \frac{g \sin D}{v_{in}} - \frac{2T}{Mv_{in}} \cdot \frac{1}{n} \frac{\partial n}{\partial z} \quad (2.3)$$

$$\begin{aligned}
\underline{v}_{\perp i} = & -\frac{c}{B} \underline{\nabla} \phi \times \hat{z} - \frac{2T}{e} \frac{c}{B} \frac{\underline{\nabla} n \times \hat{z}}{n} + \frac{\underline{g} \times \hat{z}}{\omega_{ci}} \\
& - \frac{v_{in}}{\omega_{ci}} \left(\frac{c}{B} \underline{\nabla}_{\perp} \phi + \frac{2T}{e} \frac{c}{B} \frac{\underline{\nabla}_{\perp} n}{n} - \frac{\underline{g}_{\perp}}{\omega_{ci}} \right) \\
& + \text{order } (v_{in}^2/\omega_{ci}^2)
\end{aligned} \tag{2.4}$$

$$\underline{v}_{\perp e} = -\frac{c}{B} \underline{\nabla} \phi \times \hat{z} \tag{2.5}$$

The ion continuity equation is

$$\begin{aligned}
& \frac{\partial n}{\partial t} + \underline{\nabla}_{\perp} n \cdot \left(\frac{\underline{g} \times \hat{z}}{\omega_{ci}} - \frac{c}{B} \underline{\nabla} \phi \right) \\
& + \frac{\partial}{\partial z} \left(\frac{ng \sin D}{v_{in}} - \frac{2T}{M v_{in}} \frac{\partial n}{\partial z} \right) = 0
\end{aligned} \tag{2.6}$$

Terms of first order in v_{in}/ω_{ci} have been neglected in Equation 2.6 because they are much smaller than the zero order terms. However, in the calculation of the transverse electrical current, the zero order terms cancel out, so the first order terms must be retained. This procedure of taking Equations 2.6 and 2.7 to two different orders in v_{in}/ω_{ci} leads to a slight inconsistency, which will be pointed out in Chapter III.

The electric current perpendicular to the magnetic field (\underline{j}_{\perp}) is obtained from Equations 2.4 and 2.5:

$$\begin{aligned}
 j_{\perp} = & -\frac{2Tc}{B} \nabla_{\perp} n \times \hat{z} + ne \frac{g_{\perp} \times \hat{z}}{\omega_{ci}} - \frac{ec}{B} \frac{v_{in}}{\omega_{ci}} n \nabla_{\perp} \phi \\
 & - \frac{2Tc}{B} \frac{v_{in}}{\omega_{ci}} \nabla_{\perp} n + \frac{e}{\omega_{ci}} \frac{v_{in}}{\omega_{ci}} n g_{\perp} \quad (2.7)
 \end{aligned}$$

Two moments of the ion density distribution are introduced:

$$\begin{aligned}
 N(x, y) &= \int n dz \\
 \Sigma(x, y) &= \frac{ec}{B} \int \frac{v_{in}}{\omega_{ci}} n dz
 \end{aligned}$$

It is assumed by Perkins (1973) that the limits of integration can be chosen so that the density and derivative of the density vanish at the limits. This is equivalent to assuming that the flux vanishes at the endpoints. This assumption does not represent the true F layer, as will be shown in the next chapter. The quantity N is the field integrated ion density, or the plasma content of a field tube, and Σ is the field integrated F region Pedersen conductivity.

In the absence of ionization and recombination no net current will enter or leave a flux tube. Consequently,

$$\nabla_{\perp} \cdot \int j_{\perp} dz = 0 \quad (2.8)$$

This is really a statement of plasma quasi-neutrality, as can be seen by subtracting the electron continuity equation from the ion continuity equation, and integrating. By substituting Equation 2.7 into 2.8, and using the moment definitions of Σ and N , one obtains:

$$\begin{aligned} \nabla_{\perp} \cdot \Sigma \nabla_{\perp} \phi - \frac{\partial N}{\partial y} \frac{g e \cos D}{\omega_{ci}} + \frac{2T}{e} \nabla_{\perp}^2 \Sigma \\ + \frac{\partial \Sigma}{\partial x} \cos D \left(\frac{2T}{eH} + \frac{Mg}{e} \right) = 0 \end{aligned} \quad (2.9)$$

It has been assumed that the ion-neutral collision frequency has the same height distribution as the neutral atmosphere.

$$v_{in} = v_{in 0} e^{-h/H}$$

The ion continuity equation, Equation 2.6, is integrated along a field line to obtain the equation describing the time evolution of the plasma content of a flux tube:

$$\frac{\partial N}{\partial t} + \frac{g}{\omega_{ci}} \cos D \frac{\partial N}{\partial y} - \nabla_{\perp} N \cdot \frac{c}{B} \nabla \phi \hat{x} \hat{z} = 0 \quad (2.10)$$

To complete the description, one also needs an equation for the time evolution of the integrated Pedersen conductivity. This equation is obtained by multiplying Equation 2.6 by $\frac{ec}{B} \frac{v_{in}}{\omega_{ci}}$, and integrating along z :

$$\begin{aligned} \frac{\partial}{\partial t} + \underline{\nabla} \cdot \underline{\Sigma} \cdot \left(\frac{\underline{g} \times \underline{z}}{\omega_{ci}} - \frac{c}{B} \underline{\nabla} \phi \times \underline{z} \right) \\ = \frac{ec \sin^2 D}{\omega_{ci} BH} gN + \underline{\Sigma} \frac{\partial \phi}{\partial y} \frac{c \cos D}{BH} \end{aligned} \quad (2.11)$$

Equations 2.9, 2.10 and 2.11 form a complete set of equations for the description of N , $\underline{\Sigma}$, and ϕ .

The equilibrium state, i. e., the state before F_s , is one in which there are no gradients in N and $\underline{\Sigma}$ transverse to \underline{B} , and a transverse electric field is present. The equilibrium solution of Equation 2.11 is a requirement that there be an eastward Pedersen current to support the F layer against gravity:

$$\underline{\Sigma}_0 \cdot \underline{E}_{oy} = \frac{N_0 e g \sin^2 D}{\omega_{ci} \cos D} \quad (2.12)$$

The F_s model is based on the fact that this equilibrium is unstable to small perturbations. This is shown by linearizing Equations 2.9, 2.10, and 2.11 about the equilibrium, and assuming a solution of the form $e^{\underline{ik} \cdot \underline{x} + \gamma t}$ for the perturbed quantities in a frame of reference moving with the velocity

$$\left(\frac{\underline{g} \times \underline{B}}{\omega_{ci}} - \frac{c}{B} \underline{\nabla} \phi_0 \times \underline{z} \right) .$$

No perturbations are allowed in N because there is no way to change the plasma content of a flux tube in the absence of recombination or ionization.

The complex growth rate γ obtained by the perturbation analysis is:

$$\begin{aligned} \gamma = & \frac{c}{B} E_o \frac{\cos D}{H} \left\{ \sin \alpha \sin (\theta - \alpha) \right. \\ & - \frac{\cos D \cos \theta \langle v_{in} \rangle}{(\sin^2 D) \omega_{ci}} \left[\sin \alpha \cos \alpha \cos D \left(\frac{2M_n}{M} + 1 \right) \right. \\ & \left. \left. + i (k_y H) \frac{2M_n}{M} \right] \right. \end{aligned} \quad (2.13)$$

The quantity M_n is the neutral mass, the angles α and θ are shown in Figure 3a, and

$$\langle v_{in} \rangle = \frac{\int n v_{in} dz}{\int n dz} = \frac{\sum_o \omega_{ci} B}{ec N_o} = \frac{g B \sin^2 D}{c E_{oy} \cos D}$$

It should be re-emphasized that the electric fields in Equations 2.12 and 2.13 are resultant electric fields as shown in Figure 3b. A positive value of real γ is required for growth; a negative value means the perturbation will be damped.

The first term in brackets in Equation 2.13 will dominate because $v_{in} \ll \omega_{ci}$. The maximum growth rate is obtained when $\alpha = \theta/2$.

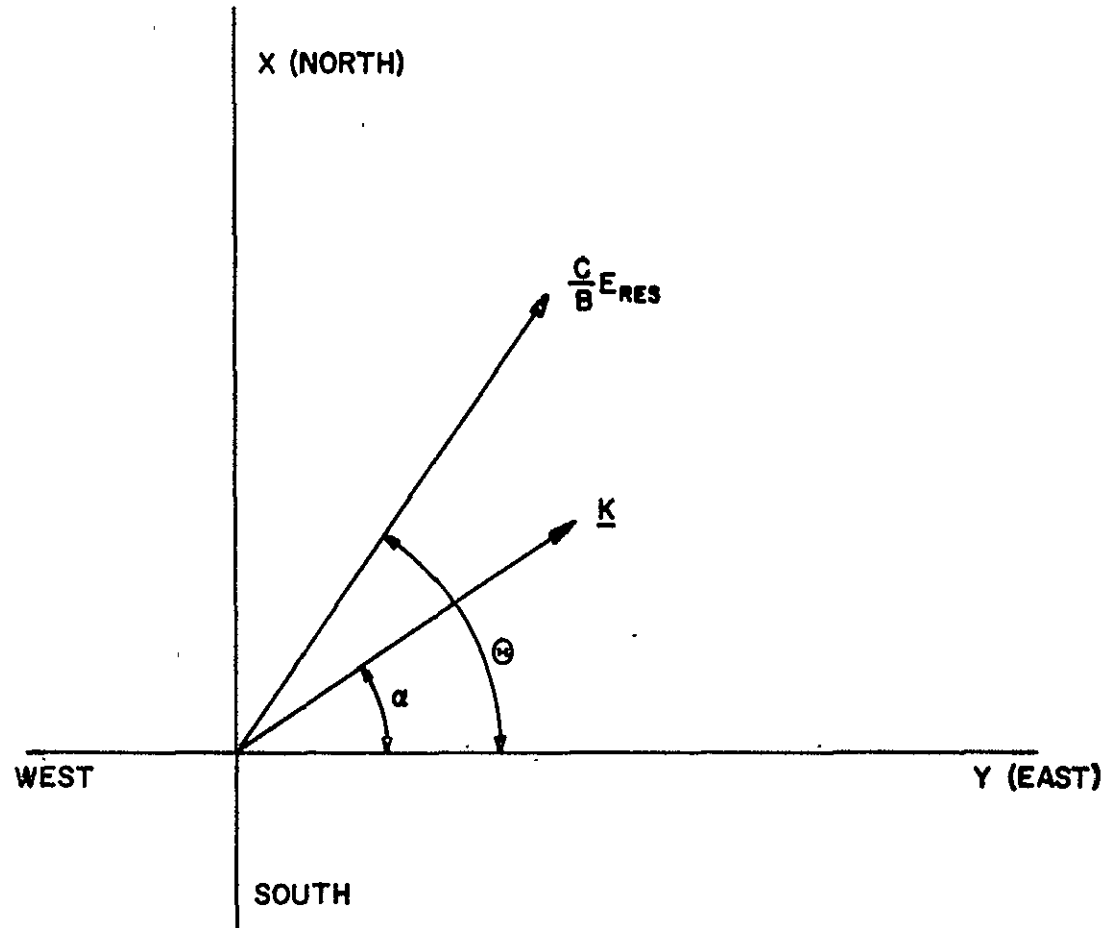


Figure 3a: Orientation of the \underline{E} and \underline{k} vectors.

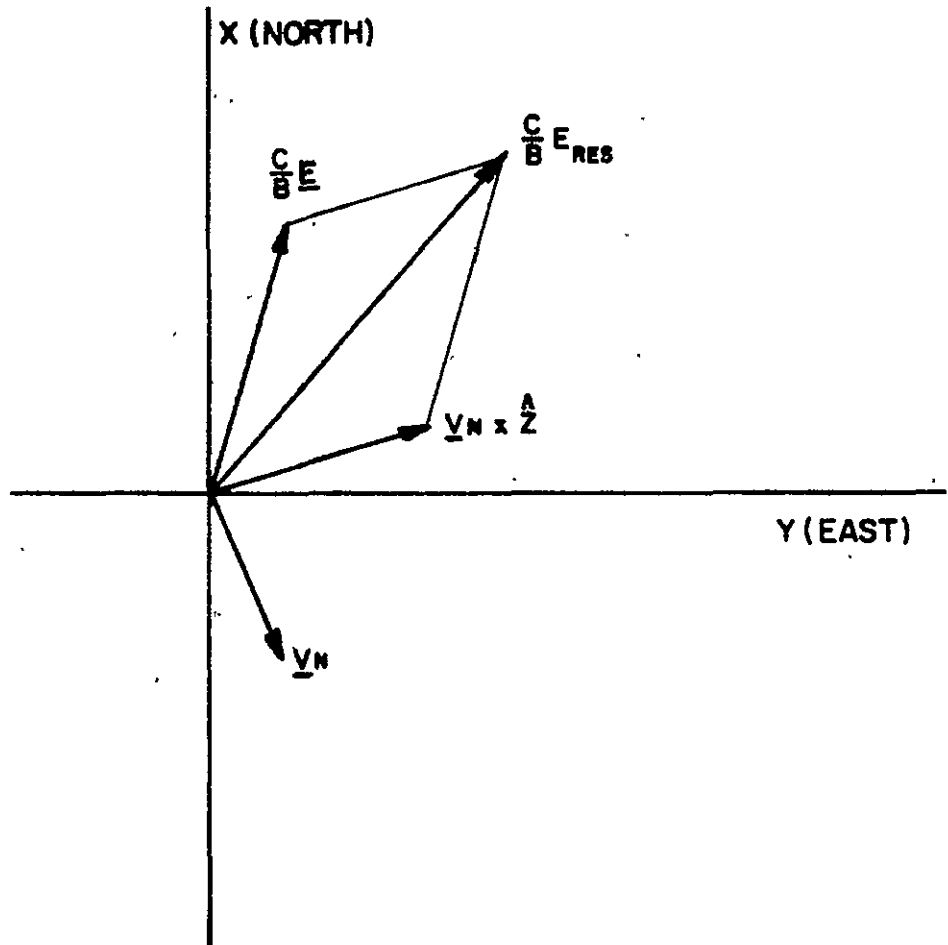


Figure 3b: The production of the resultant electric field from the electric field and the neutral wind.

$$\gamma_{\text{MAX}} = \frac{g}{H \langle v_{\text{in}} \rangle} \frac{\sin^2 D \sin^2 \theta/2}{\cos \theta} \quad (2.14)$$

Equation 2.14 predicts that F_g will be more likely to occur when the layer is high, because $1/\langle v_{\text{in}} \rangle$ increases with height. This is in agreement with observation (Herman, 1966). It also predicts a maximum growth when there is a large north-south component of the equilibrium resultant electric field; and the orientation of the striations, which is the direction perpendicular to \underline{k} , will be more north-south than east-west. It should be noted that there is no wavelength dependence in the Perkins growth rate. It will be shown in Chapter IV that the wavelength dependence is contained in the terms of order $v_{\text{in}}^2/\omega_{\text{ci}}^2$ that were neglected in the Perkins derivation.

This instability can be described physically with the help of Figure 4. The ionosphere has been perturbed in such a way that there are rising and falling sheets of ionization aligned along the field lines. In region 2 the F layer has fallen so that Σ_2 has increased over the equilibrium value Σ_1 , in region 1. Because $\underline{\nabla} \cdot \underline{J} = 0$ and $\underline{\nabla} \times \underline{E} = 0$, the normal component of the current, which is assumed to be a Pedersen current, must be continuous, and the tangential component of the electric field must be continuous. Since $\underline{J} = \Sigma \underline{E}$ and $\Sigma_2 > \Sigma_1$ then $J_{t2} > J_{t1}$ and $E_{n1} > E_{n2}$. Thus, the supporting eastward current has been decreased in region 2 as shown in Figure 4, and the F layer will fall even further, causing Σ_2 to become even larger. Because there is no damping mechanism, the process will continue and the system as shown is unstable.

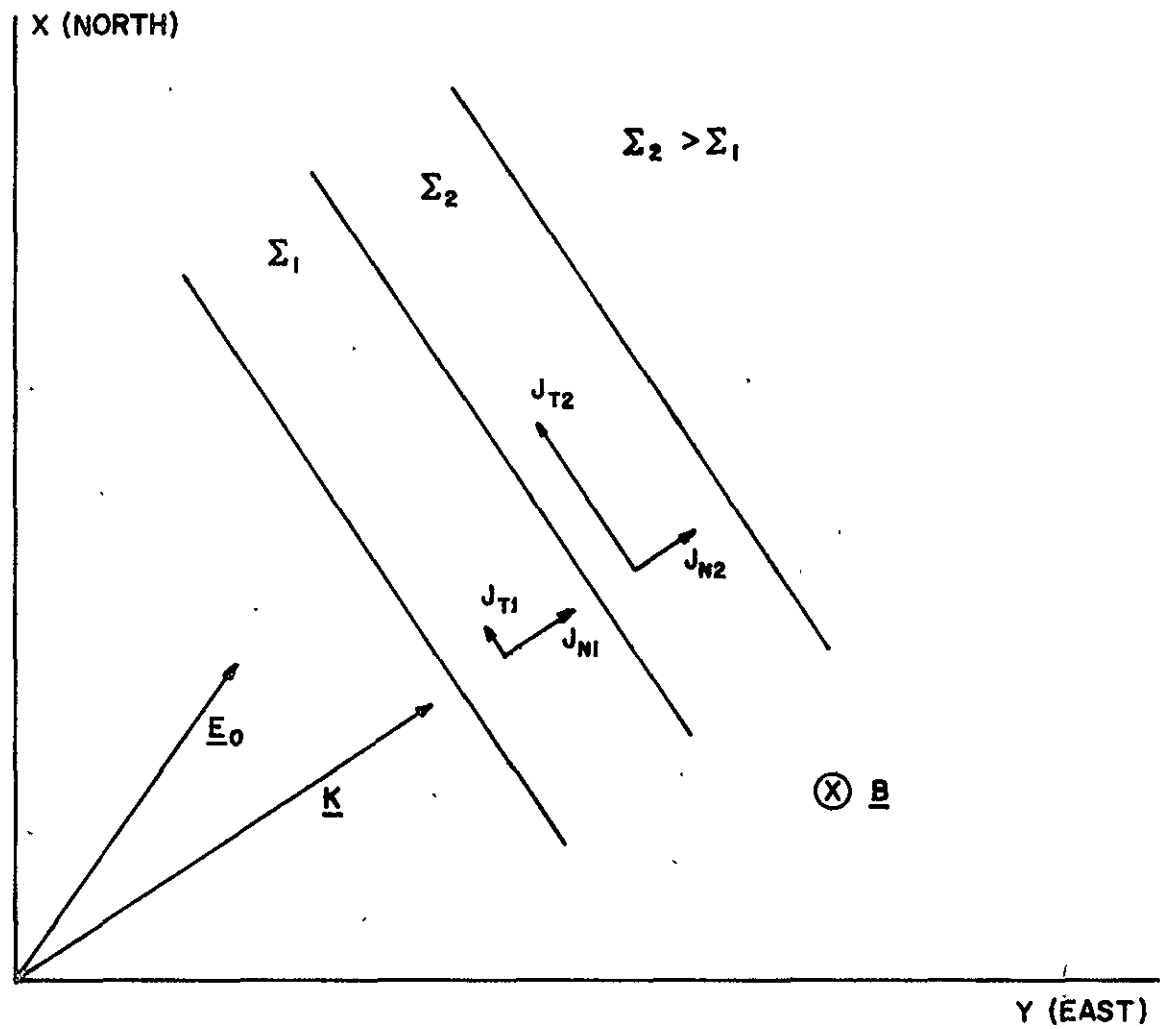


Figure 4: Physical model of the Perkins instability.

2.2 Scannapieco Model

The Scannapieco model, as described in two recent papers by McDonald et al., (1975), and Scannapieco et al., (1975), starts with the same flux tube equations as the Perkins model (Equations 2.9, 2.10 and 2.11). However, by the assumption of a different equilibrium state, a totally different model of F_s is obtained. It is of the $\underline{E} \times \underline{B}$ gradient instability type, as will be shown.

What makes this model different from the Perkins model is the assumption of an east-west gradient in the field integrated Pedersen conductivity. The equilibrium is studied in a reference frame moving eastward with the velocity:

$$V_y = \frac{g \cos D}{\omega_{ci}} - \frac{c}{B} E_{ox} + \frac{2T}{e} \frac{c \cos D}{BH}$$

The equilibrium condition on the Pedersen current is obtained from Equation 2.11:

$$\Sigma_o \frac{\partial \phi_o}{\partial y} = \frac{-2T}{e} \frac{\partial \Sigma_o}{\partial y} - \frac{eg \sin^2 D N_o}{\omega_{ci} \cos D} \quad (2.15)$$

This condition must also be consistent with Equations 2.9 and 2.10.

The following is obtained by integrating Equation 2.9 in y :

$$\Sigma_o \frac{\partial \phi_o}{\partial y} = \text{CONSTANT} + \frac{eg \cos D N_o}{\omega_{ci}} - \frac{2T}{e} \frac{\partial \Sigma_o}{\partial y} \quad (2.16)$$

By comparing Equations 2.15 and 2.16, one obtains:

$$\text{CONSTANT} = \frac{-N_0 e g}{\cos D \omega_{ci}}$$

It is not inconsistent with Equation 2.10 to have N_0 constant so there is internal consistency among the three equations. Actually, the assumption that N_0 is a constant can be justified by the data, at least for time scales on the order of an hour. This will be demonstrated in Chapter III.

The growth rate analysis begins with the assumption that all perturbed quantities have the form $e^{ik_x x + \gamma t}$. Propagation of the irregularities is only allowed in the x direction because of the gradient in Σ in the y direction. A perturbation propagating in the y direction can not be allowed in this normal mode analysis unless the wavelength of the perturbation is much less than the characteristic length of the equilibrium gradient.

By linearizing Equations 2.9, 2.10 and 2.11, and substituting the assumed solution for perturbed quantities, one obtains the following expression for the real part of γ , which is the growth rate:

$$\gamma_r = \frac{\partial \phi_0}{\partial y} \left[\frac{c \cos D}{BH} + \frac{1}{\Sigma_0} \frac{\partial \Sigma_0}{\partial y} \right] \left[\frac{c}{B} \cos D \left(\frac{2T}{eH} + \frac{Mg}{e} \right) + \frac{c}{B} \frac{\partial \phi_0}{\partial x} \right]$$

The final form is obtained by substituting Equation 2.15 for $\frac{\partial \phi_0}{\partial y}$:

$$\gamma_r = \frac{c}{B} \left(\frac{Bg \cos D}{\omega_{ci} c} - E_{ox} \right) \frac{1}{\Sigma_0} \frac{\partial \Sigma_0}{\partial y} - \frac{c}{BH} \frac{eg \sin^2 D N_0}{\omega_{ci} \Sigma_0} \quad (2.17)$$

If there is no Pedersen gradient, a pure damping solution is obtained, which is the same as the Perkins model result for propagation in the x direction (c.f. Equation 2.13).

This model of F_g is really of the $\underline{E} \times \underline{B}$ gradient instability class, as can be demonstrated with the help of Figure 5. The ionosphere has been perturbed such that alternating sheets of Pedersen conductivity exist, oriented purely in the east-west direction. In region 2, the F layer has risen, so $\Sigma_2 < \Sigma_1$. The x component of the electric field will cause $\underline{E} \times \underline{B}$ drifts towards the east, as shown in Figure 5.

Because the current normal to the striations must be continuous, $\Sigma_1 E_{n1} = \Sigma_2 E_{n2}$. Since $\Sigma_2 < \Sigma_1$, then $E_{n2} > E_{n1}$. Thus, the eastward drift velocity in region 2 will be greater than that in region 1. Region 2 is a region of depleted Pedersen conductivity moving rapidly into larger ambient conductivity because of the equilibrium gradient. This makes the value of $\delta \Sigma / \Sigma_0$ even greater as time goes on, and hence it is unstable. Region 1 remains stable.

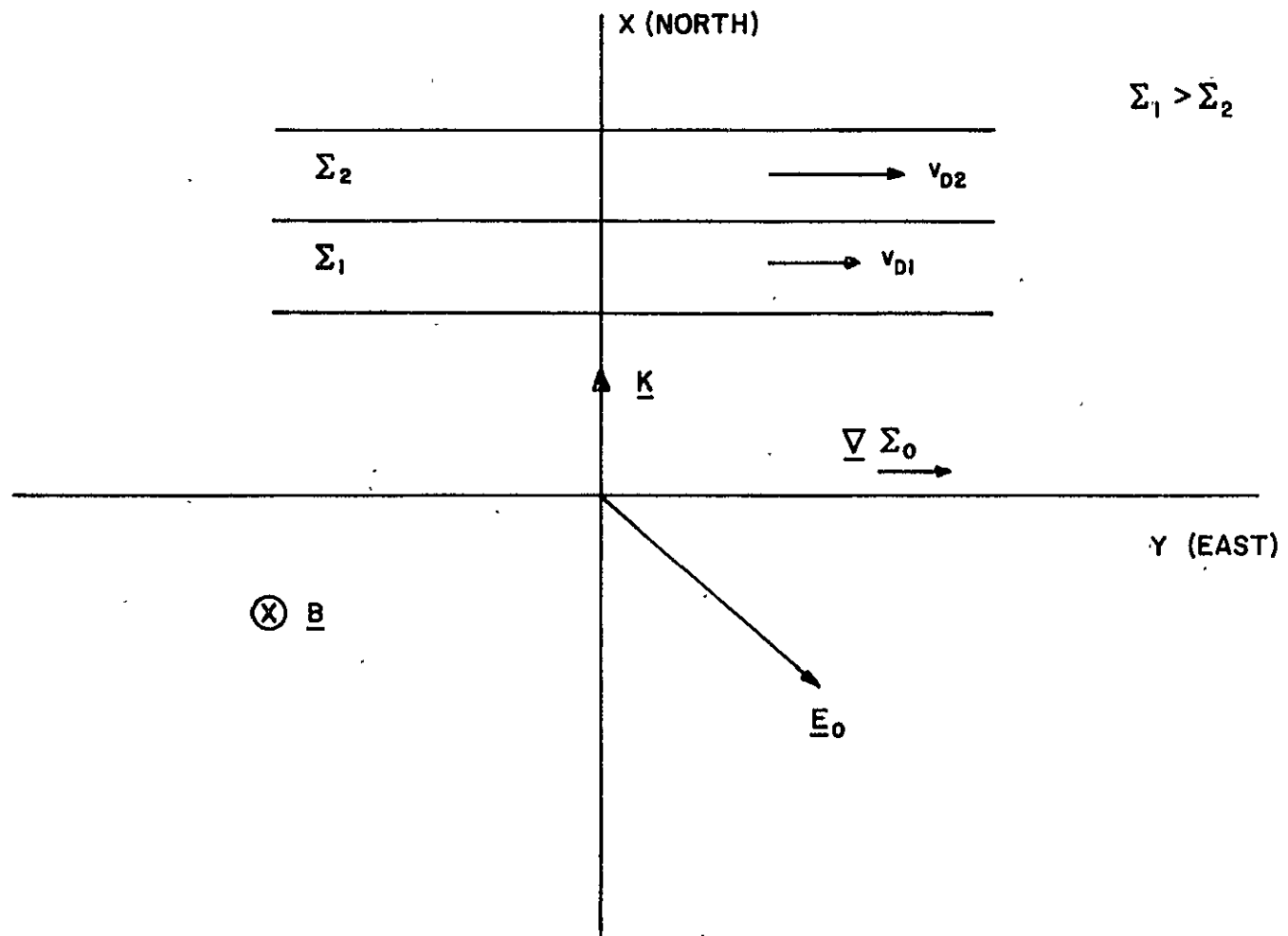


Figure 5: Physical model of the Scannapieco instability

The gravity term in Equation 2.17 would normally be expected to be small. However, it can contribute to the instability because the $\underline{g} \times \underline{B}$ drift would cause the whole layer to move eastward into the ambient gradient.

The constant damping term in Equation 2.17 represents the linear increase of Σ as the layer falls down the field lines. As the Pedersen conductivity in region 2 becomes smaller due to the rising of the F layer in that region, the tangential electric field must be continuous. This causes the tangential current, which is the supporting eastward current, to decrease. The layer falls and Σ increases, thus contributing a damping mechanism.

2.3 Reid Model

The Reid model, presented in a paper by Reid (1968) and extended later by Cunnold (1969), is totally different from the two previous models discussed in that it is not a flux tube model. No quantities are integrated along the field lines; it is thus a local model and its predictions are a function of altitude.

The Reid model is of the $\underline{E} \times \underline{B}$ instability type, and depends on the fact that the transverse mobilities are different for the electrons and ions. It can be described with the help of Figure 6. The solid horizontal line represents the unperturbed electron (and ion) density. If the density is now perturbed, as in the sinusoidal curve, the whole plasma will move to the left due to the $\underline{E} \times \underline{B}$ drift. The greater Hall mobility of the electrons will enable them to move further to the left than the ions. This is shown on the figure by using two sinusoidal

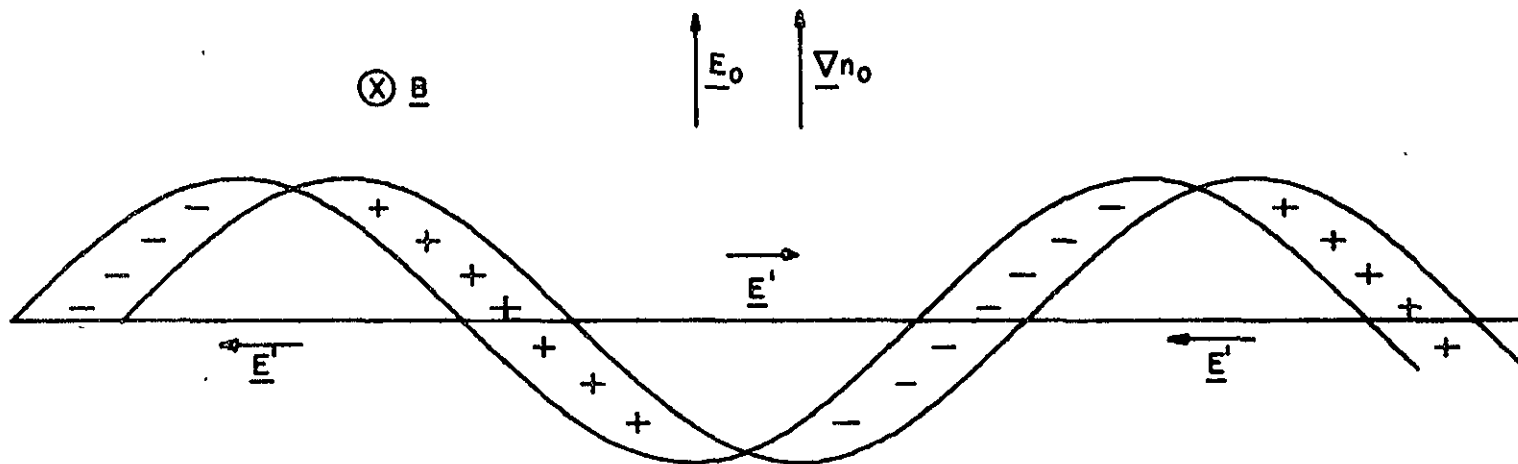


Figure 6: Physical model of the Reid instability.

curves slightly out of phase. As shown, space changes will develop causing perturbed electric fields (\underline{E}') which will in turn cause $\underline{E}' \times \underline{B}$ drifts. The region of excess ionization will move into a region of less ambient ionization, as shown by the direction of the ambient density gradient, while the region of depleted ionization will move into a region of greater ambient density. The process will continue in the absence of a damping mechanism causing $\delta n/n_0$ to further increase. The same effect could occur with an electric field directed to the right since the Pedersen mobilities are different for electrons and ions.

The equations used in the Reid model are the equation of motion

$$-\nabla n_s T + n_s \underline{E} + \underline{j}_s \times \underline{B} - \frac{m_s v_{sn}}{q_s} \underline{j}_s = 0$$

and the continuity equation:

$$\frac{\partial n_s}{\partial t} + \nabla \cdot n_s \underline{v}_s = 0$$

The subscript "s" represents the species, i.e. "e" for electrons and "i" for ions. Thus there are four equations.

The equation of motion is solved for the particle flux which is then substituted into the continuity equation. The two resulting equations are linearized, and a solution of the form

$$\exp \frac{-x \cos D}{H_p} e^{-i(\omega t - k_y y)}$$

is assumed for all perturbed quantities. The quantity H_p is the plasma scale height. The Reid model only allows propagation in the eastward direction.

The growth rate is found by assuming that the wavelength of the perturbation is less than a few kilometers, and H_p is greater than 5 km, i.e. $kH_p \gg 1$. By substituting the assumed solution in the continuity equations for electrons and ions, one obtains the growth rate:

$$\omega_i = \frac{-k_y^2}{k_y^2 K_1^2 + \cos^2 D L_1^2} \left[K_1 (K_2 k_y^2 + \cos D E_{ox} L_4 - \cos D E_{oy} L_2) + \cos D L_1 (\cos D L_3 + E_{ox} K_3) \right]$$

where

$$K_1 = \mu_p^+ + \mu_p^-$$

$$K_2 = \mu_p^+ D_p^- + \mu_p^- D_p^+$$

$$K_3 = \mu_p^+ \mu_H^- + \mu_p^- \mu_H^+$$

$$L_1 = \mu_H^- \gamma^- - \mu_H^+ \gamma^+$$

$$L_2 = \mu_p^+ \mu_H^- \gamma^- + \mu_p^- \mu_H^+ \gamma^+$$

$$L_4 = D_p^+ \mu_H^- \gamma^- - D_p^- \mu_H^+ \gamma^+$$

$$\gamma^{\pm} = H_p^{-1} + (\ell^{\pm})^{-1}$$

ℓ^{\pm} is the scale height of μ_H^{\pm} .

The quantities D_p , D_H , μ_p , and μ_H are the Pedersen and Hall components of the diffusion coefficients and mobilities, respectively, and are defined as

$$D_p^{\pm} = D_o^{\pm} \frac{(\nu^{\pm})^2}{(\nu^{\pm})^2 + (\omega_c^{\pm})^2}$$

$$D_H^{\pm} = D_o^{\pm} \frac{\omega_c^{\pm} \nu^{\pm}}{(\nu^{\pm})^2 + (\omega_c^{\pm})^2}$$

The mobilities have the same form, and

$$\mu_o^{\pm} = \frac{e}{m^{\pm} \nu^{\pm}}$$

$$D_o^{\pm} = \frac{T}{m^{\pm} \nu^{\pm}}$$

The requirement for the onset of the instability is that $\omega_i > 0$.

If $k_y^2 \neq 0$, then the onset condition is

$$E_{ox} (K_1 L_4 \cos D + K_1 K_3 \cos D) - E_{oy} (K_1 L_2 \cos D)$$

$$> - (K_1 K_2 k_y^2 + L_1 L_3 \cos^2 D)$$

with a minimum wavelength given by:

$$\lambda_{\text{MIN}} < 2\pi \left[E_{oy} \cos D - E_{ox} \left(\frac{L_4}{K_2} \cos D + \frac{L_1 K_3}{K_1 K_2} \cos D \right) - \frac{L_1 L_3}{K_1 K_2} \cos^2 D \right]^{-1/2}$$

If the equilibrium electric field (\underline{E}_0) is increased, the minimum wavelength and growth time are decreased. The growth times are also dependent on latitude, becoming infinite at the poles where $D = 90^\circ$.

Reid (1968) proposed that irregularities are produced by this instability in the E region, where the differences in the mobilities are the greatest, and are then transmitted to the F region via the field lines causing F_s . No analysis was performed to determine the conditions for such propagation. The instability is damped at high latitudes because of the dip angle D, but there are increased electric fields at high latitudes to compensate. At mid-latitudes, there are no large fields, and the instability is damped, thus explaining the absence of F_s between 20° and 40° latitude. The correlation with magnetic activity is explained also. During magnetically active times at high latitudes there is much uneven particle precipitation, causing increased density gradients, and stronger electric fields. These two conditions will enhance the instability, thereby explaining the positive correlation. At the equator, there is a strong return current during

magnetically active times that will oppose the normal post-sunset current. The electric field is decreased, explaining the negative correlation.

Cunnold (1969) extended the Reid model by including electron-ion collisions, losses due to recombination, and propagation in an arbitrary direction. The positive part of the growth rate obtained by Cunnold (1969) is

$$\frac{k_y K_{\perp} \cdot (V_{oi} - V_{oe})}{\mu_{\perp}^{\pm} K_{\perp}^2 H_p}$$

where

$$\mu_{\perp}^{\pm} = \frac{\omega_{ci} v_{in}}{\omega_{ci}^2 + v_{in}^2}$$

V_o = drift velocity due to the zero order electric field.

This term must overcome any damping effects (e.g. diffusion) to have a growing solution.

Perkins (1973) makes the following criticisms of the Reid model: 1) the growth rate changes sign as a function of altitude; 2) the question of whether there is a bona-fide equilibrium about which to perform stability calculations was never brought up; and 3) the vertical dependence of the perturbation amplitude was treated in an ad-hoc manner.

2.4 Statement of the Problem

Each of the three models discussed in the previous sections describe an instability that could produce F_s on an ionogram.

However, none of the models has been adequately tested by comparison with the data that are currently available on the nighttime ionosphere. The Perkins model is chosen for detailed comparison with the data for the reasons described below.

The Reid model is an E region model. The instability depends on the fact that the mobilities for motion perpendicular to the magnetic field are different for electrons and ions. Because the collision frequencies are so large in the E region, transport across field lines is easy, and the mechanism described by the Reid model could easily occur. In fact, Reid predicted growth times on the order of several minutes using typical ionospheric parameters for the E region. Ions and electrons in the F region, however, are much more tightly bound to the field lines because of their lower collision frequencies. Thus, the $\underline{E} \times \underline{B}$ instability proposed by Reid would not be effective in the F region. This has been checked by the data introduced in Chapter III and it was found that even on the bottomside of the F region, where the gradients and collision frequencies are largest, the growth times predicted by the Reid model are on the order of hours. This is not physically meaningful in the case of F_s , which can appear in a matter of one half hour.

Reid (1968) proposed that his model could produce irregularities in the E region, and these irregularities could then produce perturbations in the F region. However, recent work by Zinchenko and Nisbet (1976) shows that the perturbations of wavelengths shorter than 5-10 km will not be transmitted from the E to the F region. Consequently, the Reid model has been ruled out as a viable means of explaining F_s .

The Scannapieco model, which allows equilibrium gradients in the Pedersen conductivity is essentially an extension of the Perkins model. However, for the four nights studied in this work, the existence of the horizontal gradient is not found, except at sunset. Scannapieco et al., (1975) state that the gradient at sunset would remain into the night because it is an equilibrium solution. The data from Arecibo Observatory which is discussed in Chapter III does not support this contention. In fact, the east-west horizontal gradients seen are quite small. The growth times predicted by the Scannapieco model using the data available are even longer than those predicted by the Reid model. However, it should be pointed out that it is difficult to acquire data on the horizontal structure of the Pedersen conductivity, and the data that was used to obtain the growth times mentioned above may not be accurate enough to make a definitive statement about the existence of a gradient. Discussion of this point will be continued in Chapter IV.

The Perkins model was chosen for detailed study because it has the capability of predicting reasonable growth times (10-30 minutes) and the equilibrium state described by the model in which the nighttime F layer is supported by $\underline{E} \times \underline{B}$ forces and neutral winds is generally accepted as true (Behnke and Kohl, 1974; Harper, 1973; Behnke and Harper, 1973). The Perkins model is a flux tube model, reflecting both the field aligned nature of the striations associated with F_s and the fact that plasma particles in the F region are tightly bound to the field lines.

A major gap in the literature on F_s is a comparison between the models of F_s and the available data. This thesis will attempt to fill this gap by comparing the Perkins model of F_s with data from the Arecibo Observatory in Puerto Rico. The Perkins model is also extended based on the findings of the data analysis.

CHAPTER III

EQUILIBRIUM ANALYSIS

3.1 Derivation of the Equations in the Laboratory Frame

Certain changes must be made to the Perkins model before it can be compared with the data. The Perkins model, as well as the other models discussed in Chapter II, was derived in a frame of reference that is moving with the constant velocity of the neutral wind. However, the data is obtained in the laboratory frame. The transformation to this frame introduces an extra term, $\frac{B}{c} \underline{V}_N \times \hat{z}$, that is added to the electric field. As was indicated in Chapter II, a resultant electric field is produced, and is of the form shown below:

$$\frac{c}{B} \underline{E}_{RES} = - \frac{c}{B} \underline{\nabla} \phi + \underline{V}_N \times \hat{z}$$

The electric field terms that appear in the models are actually resultant electric fields of the form shown above. The authors of these models are not neglecting the effect of the neutral wind, but are implicitly including it in the electric field terms. It is also assumed in the Perkins model that the F layer is a slab of plasma in which the density and the derivative of the density go to zero at the endpoints. This is an oversimplification of the actual shape of the F layer, as will be shown later.

The Perkins model is rederived now in the laboratory frame of reference including the boundary conditions of the F layer "slab" and also recombination. The other assumptions of the model are detailed in Chapter II.

The equation of motion for the ions in the F region is:

$$\begin{aligned}
 -2T \nabla n + \frac{ne}{c} \underline{v} \times \underline{B} - ne \nabla \phi + nM\underline{g} \\
 - Mn v_{in} (\underline{v} - \underline{V}_N) = 0
 \end{aligned} \tag{3.1}$$

The ion velocities parallel and perpendicular to \underline{B} are obtained from Equation 3.1.

$$\begin{aligned}
 \underline{v}_{\perp i} &= \frac{-2T}{Mn\omega_{ci}} \nabla n \times \hat{z} - \frac{c}{B} \nabla \phi \times \hat{z} + \frac{\underline{g} \times \hat{z}}{\omega_{ci}} \\
 &+ \frac{v_{in}}{\omega_{ci}} \left[\frac{-2T}{Mn\omega_{ci}} \nabla n - \frac{c}{B} \nabla \phi + \underline{V}_N \times \hat{z} + \frac{\underline{g}_{\perp}}{\omega_{ci}} \right] \\
 &+ \text{order } (v_{in}^2 / \omega_{ci}^2)
 \end{aligned} \tag{3.2}$$

$$v_{zi} = V_{NZ} + \frac{g \sin D}{v_{in}} - \frac{2T}{Mn v_{in}} \frac{\partial n}{\partial z} \tag{3.3}$$

In these equations, $\nabla \phi$ is the electric field measured in the stationary frame of reference, and not the resultant electric field used by Perkins (1973).

The perpendicular electron velocity is obtained in a similar manner. Neglecting collisions and gravity, one obtains:

$$\underline{v}_{\perp e} = - \frac{c}{B} \underline{\nabla} \phi \times \hat{z} \quad (3.4)$$

The ion continuity equation is:

$$\frac{\partial n}{\partial t} + \underline{\nabla}_{\perp} \cdot n \underline{v}_{\perp i} + \frac{\partial}{\partial z} (n v_{zi}) = - \beta n \quad (3.5)$$

The quantity β is the loss rate due to recombination. Equation 3.5 is integrated along a field line, which goes down in the northern hemisphere.

$$\frac{\partial N_F}{\partial t} + \underline{\nabla}_{\perp} \cdot \int_{\text{TOP}}^{\text{BOT}} n \underline{v}_{\perp i} = \Phi_T - \Phi_B - \langle \beta \rangle N_F \quad (3.6)$$

where

$$N_F \equiv \int_{\text{TOP}}^{\text{BOT}} n \, dz$$

$$\Phi_T \equiv (n v_{zi})_{\text{TOP}}$$

$$\Phi_B \equiv (n v_{zi})_{\text{BOT}}$$

$$\langle \beta \rangle = \frac{\int_{\text{TOP}}^{\text{BOT}} \beta n \, dz}{\int_{\text{TOP}}^{\text{BOT}} n \, dz}$$

The assumption of plasma neutrality allows one to subtract the electron continuity equation from the ion continuity equation and integrate this result to obtain the following condition:

$$\nabla_{\perp} \cdot \int n \underline{v}_{\perp i} = \nabla_{\perp} \cdot \int n \underline{v}_{\perp e} \quad (3.7)$$

It has also been assumed in obtaining Equation 3.7 that the electron and ion velocities parallel to \underline{B} are equal. This is a good assumption because high electron mobility keeps the electrons with the ions, thereby preventing a space charge buildup along field lines in the F region.

Equations 3.7, 3.6 and 3.4 are combined to give the equation describing the time evolution of the field integrated density.

$$\frac{\partial N_F}{\partial t} - \nabla_{\perp} N_F \cdot \frac{\nabla \phi \times \hat{z} c}{B} = \Phi_T - \Phi_B - \langle \beta \rangle N_F \quad (3.8)$$

The quantity N_F in Equation 3.8 represents the total plasma content of a flux tube. It will change in time as a net flux of particles enters

or leaves a flux tube, as particles are lost by recombination, or as the $\underline{E} \times \underline{B}$ drift causes a gradient to move into or out of the observed location.

Equation 3.8 differs from that of the Perkins model (Equation 2.10) in a number of ways. First, there is the inclusion of boundary terms which represents particle fluxes into or out of the flux tubes. The Perkins model, by assuming $n = 0$ and $\frac{\partial n}{\partial t} = 0$ at the end points, assumes that there is no particle flux at the boundaries. Second, recombination is included. Third, the quantity $\underline{\nabla} \phi$ in the Perkins model is the electric field as seen in a moving frame of reference, and implicitly contains the neutral wind.

The fourth difference is the gravity term in Equation 2.10. This term was carried through in Perkins' derivation because he did not write the continuity and current equations to the same order in v_{in}/ω_{ci} . If he had done that, he could then substitute the $\underline{\nabla} \cdot \underline{J} = 0$ equation in the more complete continuity equation, and the gravity term would vanish. This result must be obtained to be consistent with Equation 3.7.

The Pedersen conductivity, which is the conductivity for currents parallel to \underline{E} and perpendicular to \underline{B} , is defined as:

$$\sigma_p = \frac{ne c}{B} \frac{v_{in} \omega_{ci}}{v_{in}^2 + \omega_{ci}^2} \quad (3.9)$$

In the F region, $v_{in} \ll \omega_{ci}$, so that σ_p can be approximated by:

$$\sigma_p \approx \frac{nec}{B} \frac{v_{in}}{\omega_{ci}}$$

To obtain an equation describing the time evolution of the F region Pedersen conductivity, Equations 3.2 and 3.3 are substituted into Equation 3.5 and the result is multiplied by $\frac{ec}{B} \frac{v_{in}}{\omega_{ci}}$ and integrated along a field line. Terms of order v_{in}^2/ω_{ci}^2 are neglected. One obtains:

$$\begin{aligned} \frac{\partial \Sigma_F}{\partial t} + \underline{\nabla} \Sigma_F \cdot \left(\frac{\underline{g} \times \hat{z}}{\omega_{ci}} - \frac{c}{B} \underline{\nabla} \phi \times \hat{z} \right) \\ = \frac{c}{B} \frac{\cos D}{H} \frac{\partial \phi}{\partial y} \Sigma_F + \frac{ec}{\omega_{ci} B} \frac{g \sin^2 D}{H} N_F \\ + \frac{\sin D}{H} V_{NZ} \Sigma_F + \frac{ec}{\omega_{ci} B} \left((v_{in} \Phi)_T - (v_{in} \Phi)_B \right) \\ + \frac{ec}{\omega_{ci} B} \cdot \frac{2\tilde{T}}{M} \frac{\sin D}{H} \left((n)_T - (n)_N \right) - \bar{\beta} \Sigma_F \end{aligned} \quad (3.10)$$

where:

$$\Sigma_F = \int_{\text{TOP}}^{\text{BOT}} \frac{ec}{B} \frac{v_{in}}{\omega_{ci}} n dz$$

$$\bar{\beta} = \frac{\int_{\text{TOP}}^{\text{BOT}} n v_{in} \beta dz}{\int_{\text{TOP}}^{\text{BOT}} n v_{in} dz}$$

Because Equation 3.10 was derived in the laboratory frame, it is different from Equation 2.11 of the Perkins model. The transformation of Equation 2.10 to the moving frame is accomplished by making the substitutions

$$\underline{v} = \underline{v}' + \underline{V}_N$$

$$-\frac{c}{B} \underline{\nabla} \phi = -\frac{c}{B} \underline{\nabla} \phi' - \underline{V}_N \times \hat{z}$$

$$\frac{\partial}{\partial t} = \frac{\partial}{\partial t'} + \underline{V}_N \cdot \underline{\nabla}$$

where \underline{v}' and $\underline{\nabla} \phi'$ are the velocities and electric fields in the moving frame. Also, the relation, $V_N \sin D = V_{NX} \cos D$ has been used.

Equation 3.10 describes the time evolution of the field integrated Pedersen conductivity in the nighttime F region. The gradient term on the LHS represents a convective change in Σ_F due to the $\underline{g} \times \underline{B}$ and $\underline{E} \times \underline{B}$ drifts of gradients in the Pedersen conductivity. The electric field and neutral wind terms express the change in the

integrated Pedersen conductivity as the F layer rises and falls due to changes in these forces. The term containing N_F represents the increase in Pedersen conductivity as the plasma falls down a field line due to gravity. The terms $(\nu \Phi)$ represent the change in conductivity as a net flux goes in or out of the flux tube. The physical significance of the boundary term containing $(n_T - n_B)$ is unclear. It has been labelled as a diffusion type term because it comes from the diffusion term in Equation 3.3. It probably represents the loss or gain of Pedersen conductivity as particles enter or leave the flux tube because of the vertical density gradient. The recombination term represents the decrease in Pedersen conductivity as plasma particles are lost by recombining.

3.2 Introduction to the Data

The data used in this thesis were taken at the Arecibo Observatory, Arecibo, Puerto Rico, using the incoherent-scatter technique (Evans, 1969; Behnke and Harper, 1973). Incoherent-scatter is a technique that measures the radar scattering from the ionospheric plasma. It is possible to obtain plasma drift velocities, ion temperatures, and density profiles using this technique.

The Arecibo data are ideal for studies of mid-latitude F_s for the following reasons. First, the Observatory provided high resolution data for this study. Second, the probability of observing F_s at Arecibo is high, so it was possible to study nights with F_s . Third, the dip angle at Arecibo is 50° , which makes it ideal for studying mid-latitude models. On the other hand, it has the

disadvantage that models of the neutral wind can not be used at Arecibo because anomalous pressure behavior prevents a calculation of the east-west component of the neutral wind. The significance of this will become apparent in Chapter IV.

This study concentrates on four nights: September 17, 1974; November 9, 1974; May 18, 1975; and October 15, 1975. Ionograms for these nights, also provided by Arecibo, were inspected. It was found that F_s occurred on the September and May nights, but not on the November and October nights. Zinchenko (1976) states that F_s first appeared at 2150 on September 17, 1974 and at 1945 on May 18, 1975. A personal inspection of these ionograms indicates that there is considerable uncertainty associated with trying to assign definite onset times. This uncertainty is as much as several hours past the onset times given by Zinchenko (1976), and is primarily due to the traces being too weak to read.

The data tape (provided by Dr. Robert Harper of the Arecibo Observatory) contains density profiles, with a density measurement every 1.2 km from 82 to 156 km, and every 6 km from 156 to 475 km. There are ion drift velocity profiles, with measurements every 29 km from 201 to 491 km, yielding 11 such values, and a signal to noise (S/N) ratio associated with each measurement. A S/N ratio of greater than 1.0 is required for the velocity measurements to be meaningful because the statistical error in these measurements when the S/N ratio is less than 1.0 increases rapidly with decreasing S/N ratios below 1.0 (Evans, 1969).

The plasma velocity measurements available at each of the 11 heights are v_{NS} (positive north), v_{EW} (positive east) and v_H (positive with height). Conversion to the coordinate system given in Figure 2 is accomplished by the following transformations:

$$v_x = v_H \cos D - v_{NS} \sin D$$

$$v_y = v_{EW}$$

$$v_z = -v_H \sin D - v_{NS} \cos D$$

The tape also contains ion temperature profiles from 137 to 492 km, with values every 29 km.

The above data are given approximately every 20 minutes through the night.

A computer program was also provided by the Arecibo Observatory which produces ion-neutral collision profiles using a neutral atmosphere model. Since these collision frequency profiles were used in this analysis, a brief description of the model is given in the Appendix.

In this chapter, the comparison of the equilibrium values of Σ_F and N_F predicted by the model equations (Equations 3.8 and 3.10) will be compared with the data described in the previous section. The model equations describe the behavior of N_F and Σ_F as changes in other ionospheric parameters occur. For example, Equation 3.8 states that the integrated density will change as more particles enter or leave a flux tube via the field lines, and as particles

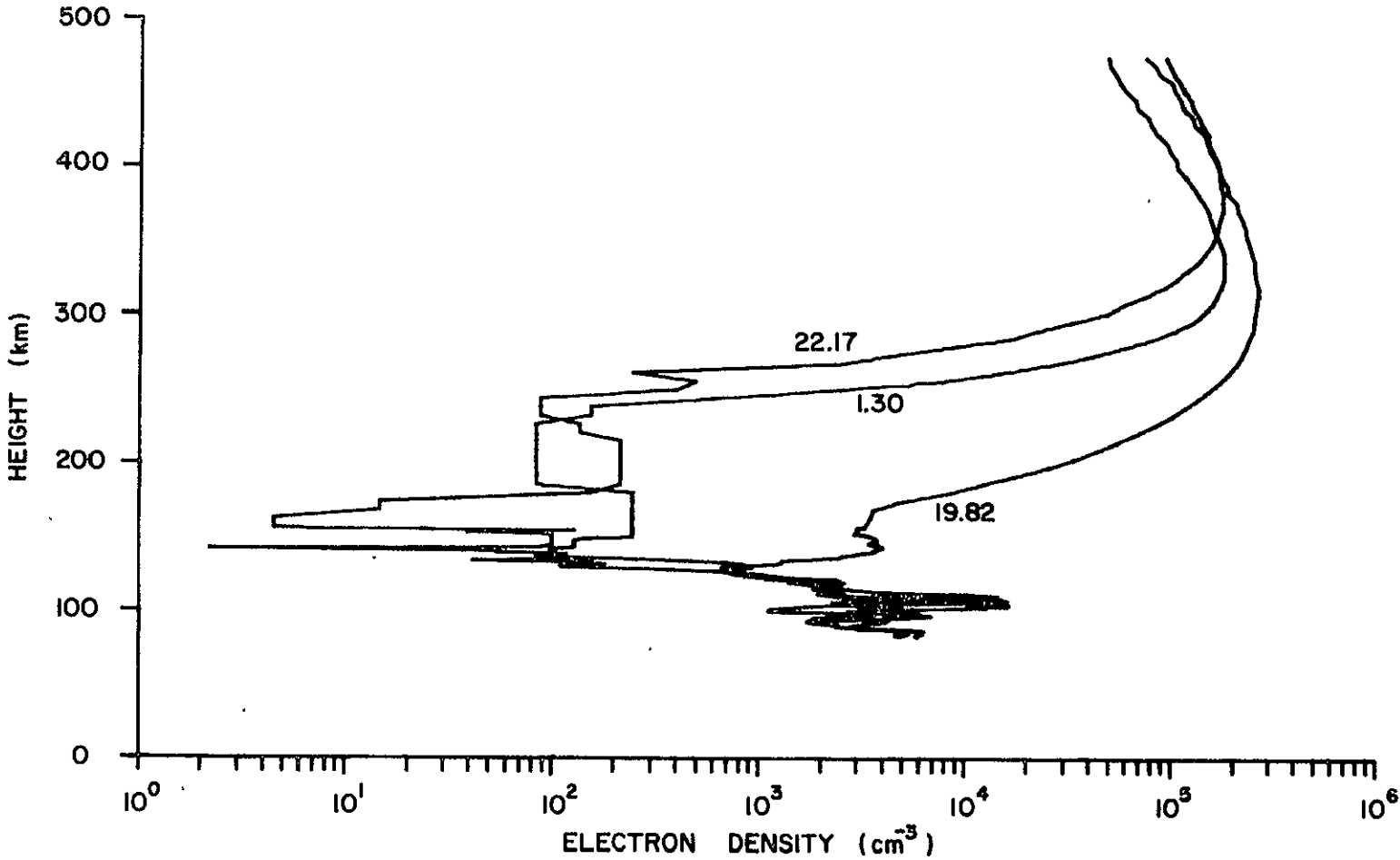
are lost through recombination. Equation 3.10 states that the integrated Pedersen conductivity will change as the F layer rises and falls due to gravitational, collisional and electrostatic forces. Changes in the integrated conductivity will also occur as particles enter or leave a flux tube along the field lines, or are lost due to recombination.

To completely analyze Equations 3.8 and 3.10, knowledge of the following quantities is needed: Φ_T , Φ_B , $\langle \beta \rangle$, N_F , H , E_{oy} , Σ_F , V_{NZ} , $(v_{in})_T$, $(v_{in})_B$, $(v_{zi})_T$, $(v_{zi})_B$, $\bar{\beta}$, $\nabla_{\perp} \Sigma_F$, and $\nabla_{\perp} N_F$. Most of these can be inferred from the data as will be shown in the next section.

Before starting the analysis, it is useful to look at the density profiles shown in Figure 7. The F layer is well defined, but it is immediately seen that the assumption of Perkins (1973) that the density goes to zero at the top and bottom of the layer, is an oversimplification. It is also seen that the shape of the layer does not change greatly during the night. The major shape changes occur at the bottomside of the layer, when the layer is low. This is attributed to recombination. Because the recombination rate depends on the neutral atmosphere density, the loss of particles due to recombination will be greatest at the lower altitudes, and particles will be removed from the bottom of the F layer at a faster rate than at the top of the F layer. This causes the increase in the density gradient from 19.82 to 22.17 at the bottom of the layer.

It is also noticed that the F layer moves up and down throughout the night. The motion of the layer is usually defined by the change

SEPTEMBER 17, 1974



45

Figure 7: Density profiles.

in time of the height at which the F region density is a maximum (h_m). According to density profiles shown in Figure 7, h_m is 320 km at 19.82, 380 km at 22.17, and moves back down to 336 km at 1.30. According to Behnke and Kohl (1974), the motion of the layer is governed by the east-west electric field and the north-south neutral wind. This will be examined in the next section.

It should also be noted that the density profiles shown in Figure 7 are for a night with F_s . The presence of the irregularities that cause F_s do not seem to have an effect on the density profiles.

3.3 Analysis of the Data.- Fixed Limit Integration

The initial step in the data analysis must be a selection of the boundaries of the F region. A method whereby the boundaries of the F region are fixed regardless of the motion of the layer is presented in this section. An alternate method is presented in the next section.

The choice of fixed boundaries is limited a great deal by the data. While there are density profiles and collision frequency profiles extending down to 82 km, the velocity data only extends down to 200 km. To make matters worse, the S/N ratio is dependent on the density of particles at the height of the measurement. When the layer rises, the density of particles at 200 km can be quite low as shown in Figure 7. The layer does rise to quite high altitudes, and can remain high for long periods of time. For this reason, the S/N ratio for measurements taken at the two lowest altitudes (201.6 and 230.6 km) fall below 1.0 a significant amount of time. Thus, the third height, which is 259.6 km, is chosen as the bottom of the F layer. The

tenth height, which is 462.4 km, is chosen as the top because the density data only goes to 475 km.

A recombination coefficient is calculated using the Stubbe model as referenced in Behnke and Kohl (1974).

$$\beta = 1.5 \times 10^{-11} n(\text{O}_2) + 5.0 \times 10^{-13} n(\text{N}_2)$$

The oxygen and nitrogen densities are calculated using the models described in the Appendix.

The integrals needed (N_F , Σ_F , $\langle \beta \rangle$, $\bar{\beta}$) are calculated using Simpson's Rule. The range of integration was from 255.0 to 463.6 km; there are 36 points in this interval.

Once the integrals are calculated, complete density and collision frequency profiles are no longer needed for the analysis of Equations 3.8 and 3.10. Because it takes a large amount of computer time to simply read the data tape without doing any calculations (around 60 seconds), it was decided to take only the data needed from the tape and punch it on a disk system. This is a very inexpensive storage system that is easily accessible, in contrast to the tape which must be hand loaded for each run.

The following data were stored on disks: 1) h_m , $\langle \beta \rangle$, $\bar{\beta}$, Σ_F , N_F , and T_{EX} for each time, and 2) S/N ratio, VHA, VNS, n_e , v_{in} , and $\frac{\partial n}{\partial z}$ for each time at each of the 10 heights. The quantity h_m is the height at which the density is a maximum, and T_{EX} is the exospheric temperature defined in the Appendix. The quantities S/N, VHA, VNS, n_e , v_{in} , and $\frac{\partial n}{\partial z}$ are the S/N ratio, vertical ion drift velocity, north-south ion drift velocity, electron density,

ion-neutral collision frequency, and electron density gradient along a field line, respectively, for each of the ten heights.

A slight problem arises because the density measurements are not given at the same heights as the velocity measurements. An example is shown below:

Density Heights	Velocity Heights
191.2	
197.0	201.6
202.8	
208.6	
214.4	
220.2	
226.0	230.6
231.8	
237.6	
243.4	

To interpolate the density measurements to the same heights as the velocity measurements, a linear least squares fit was performed on the natural logarithm of the density. This is justified because particles in diffusive equilibrium will distribute themselves exponentially with altitude. Five points centered around the altitude at which an interpolated density was required were used in the fit. Thus, to interpolate the density at 201.6 km, the fit was performed on the densities at 191.2, 197.0, 202.8, 208.6, and 214.4 km. The slope of line is the derivative of the logarithm of the density, so the density

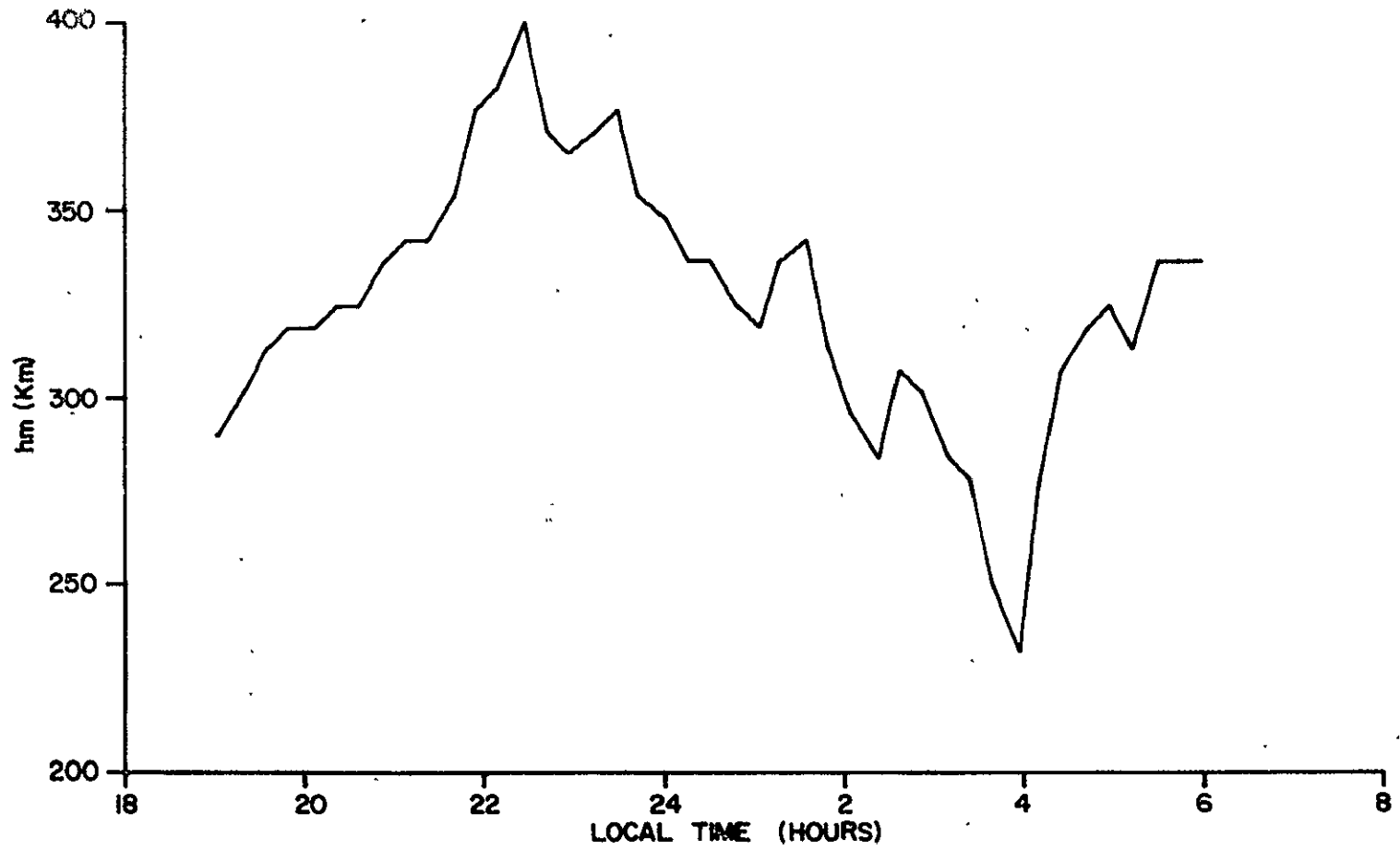
gradient is easily calculated. The same method of interpolation was used for the collision frequencies.

September 17, 1974, which was the first day on the tape, will now be analyzed in detail using the quantities calculated above.

The motion of the F layer peak during the night of September 17 is shown in Figure 8. It is seen that the peak moves up and down periodically, reaching a maximum of almost 400 km at 2230 and a minimum of 230 km at 0400. This behavior is typical of nights previously reported by Behnke and Kohl (1974). It becomes obvious at this early stage of the analysis that the choice of boundaries at 259.6 and 462.4 km is going to lead to trouble during those times when h_m is near its minimum and its maximum. At 2230, when the layer is high, the density of particles at 259.6 km will be so low that the S/N ratio will fall below 1.0. At 0400 when the peak has fallen to 230 km, the lower boundary is actually above the peak. This is not really in the spirit of the flux tube model as derived by Perkins (1973); one should at least include the maximum of the function that is being integrated if the assumption that $n \rightarrow 0$ at both limits of integration is to have any meaning at all. The alternate scheme presented in the next section represents a solution to this problem. However, the fact remains that Equations 3.8 and 3.10 should predict the behavior of N_F and Σ_F for any limits of integration if the boundary conditions are properly treated.

Behnke and Kohl (1974) state that the motion of the peak is determined by the electric field and neutral winds. The Perkins

SEPTEMBER 17, 1974



50

Figure 8: Time variation of h_m .

model also assumes that the nighttime F layer is supported by the eastward electric field and the neutral wind.

The electric fields are inferred from the ion drift velocity measurements. This can be explained with the help of Equation 3.2, and the following approximate values for F region parameters:

$$\begin{aligned} T &= 10^{-13} \text{ ergs} \\ M &= 2 \times 10^{-23} \text{ g} \\ \omega_{ci} &= 2 \times 10^2 \text{ sec}^{-1} \\ g &= 10^3 \text{ cm} \cdot \text{sec}^{-2} \\ \frac{v_{in}}{\omega_{ci}} &= 10^{-2} - 10^{-3} \end{aligned}$$

It is clear that terms of order v_{in}/ω_{ci} will not contribute much to the perpendicular ion drift velocity. The $\underline{g} \times \hat{z}$ term will only contribute a term on the order of .05 m/s to the velocity. The gradient term is of the order $\frac{5 \times 10^7}{H_p}$ cm/sec, where H_p is the characteristic length of the density gradient perpendicular to the field lines. This length would have to be on the order of 1 km for the density gradient term to even contribute 5 m/s to the perpendicular drift velocity. In fact, the characteristic length of the density gradient in the F region is in the range 50 to 100 km and the drift velocities are generally much larger than 5 m/s. One can conclude that the dominant cause of perpendicular ion drift is the electric field:

$$\begin{aligned} \underline{v}_{Di} &\approx \frac{c}{B} \underline{E} \times \hat{z} \\ v_{Dx} &= \frac{c}{B} E_{oy} \\ v_{Dy} &= - \frac{c}{B} E_{ox} \end{aligned}$$

It should be noted that electric fields in the F region are usually inferred by this method. It is both conventional and convenient to represent the magnitude of electric fields in terms of the drift velocity they would cause rather than the actual unit of statvolts/cm. Thus, electric fields are multiplied by c/B and are given in units of meters/sec.

It was stated that there are drift velocity measurements for 10 heights with a S/N ratio associated with each measurement. An average F region drift velocity is obtained by multiplying each of the 10 drift velocities by the square root of the S/N ratio associated with each measurement, summing the products, and dividing by the sum of the square roots of the S/N ratios:

$$\langle v_D \rangle = \frac{\sum_{i=1}^{10} \left[\sqrt{(S/N)_i} (v_D)_i \right]}{\sum_{i=1}^{10} \sqrt{(S/N)_i}}$$

A measurement is thrown out if the S/N ratio is less than 1.0. In this manner, average F region values are found for v_{Dx} and v_{Dy} , and the equilibrium electric fields inferred from the averages.

The eastward electric field during the night of September 17, 1974 is shown in Figure 9. There is some correlation between the direction and magnitude of the eastward electric field and the motion of the peak shown in Figure 8, but it is not good enough to say that the electric field is the dominant lifting force. This fact is especially

SEPTEMBER 17, 1974

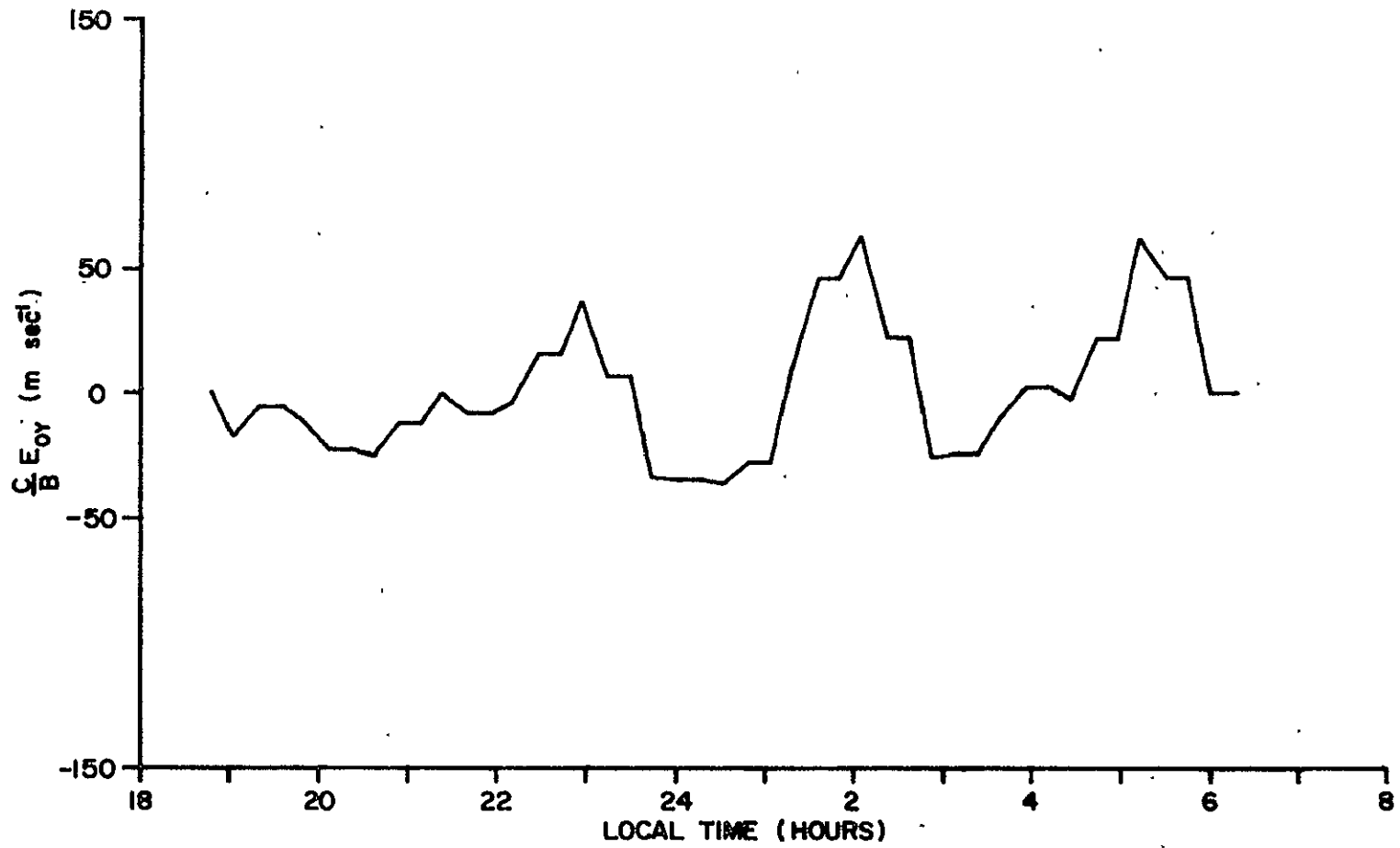


Figure 9: Time variation of the eastward electric field.

clear if one looks at the times before 2200 when the layer is rising rapidly. The electric field is in the westward direction, meaning it is causing ion motion downward.

The north-south neutral wind, which can literally blow ionization up the field lines, is the missing factor. It will now be shown that the neutral wind and the electric field are the dominant factors governing the motion of the F layer peak, further substantiating the work of Behnke and Kohl (1974).

The neutral wind must also be inferred from the drift velocity measurements. Equation 3.3 provides a direct solution of the neutral wind along the magnetic field (V_{NZ}) with v_{zi} being the parallel ion drift velocity given by the data.

$$V_{NZ} = v_{zi} - \frac{g \sin D}{v_{in}} + \frac{2T}{Mn v_{in}} \frac{\partial n}{\partial z}$$

The neutral wind is assumed to have no vertical component.

Using the available data, one can solve for a value of V_{NZ} at each of the 10 heights. Since an average F region value is desired, a logical first step would be to solve for a value of V_{NZ} at each height, and then find an average by weighting with the square root of the S/N ratio as described previously. This method does not yield good results, however, because small fluctuations in $\frac{\partial n}{\partial z}$ at high altitudes are greatly magnified by $1/v_{in}$.

An alternative method used by Behnke and Kohl (1974) is to evaluate V_{nz} at the peak, where $\partial n/\partial z$ is zero and the S/N ratio is large, and assume that this is the average velocity of the neutral wind.

A comparison of the results of the two methods is shown in Figure 10. The general behavior is the same, but the value of V_{NZ} obtained at the peak shows far less fluctuation. For this reason, the use of V_{NZ} at h_m will be adopted.

The neutral wind is added to the electric field to produce the resultant electric field. The value of the eastward component of the resultant electric field (E_{RESY}) is shown in Figure 11; h_m is plotted on the same graph to show the excellent correlation between h_m and E_{RESY} . There are only two periods in which the motion of peak can not be explained by the resultant eastward electric field. These are the time periods 1900 and 1930 and 0400 to 0430. In these two periods the layer is rising, although the field is westward. Even though the magnitude of the westward field is decreasing steadily until the field becomes eastward, a westward field of any magnitude should produce a downward motion of the peak, reinforcing the effect of gravity. The behavior of the peak in these two periods can be explained with the help of Figure 7. It is seen that recombination has removed more particles below the peak than above the peak between the times 19.82 and 22.17 shown in Figure 7. This will cause the peak to rise, even in the absence of bulk plasma motion upward. The same conclusion holds for the time period after 0400. The layer is quite low, so recombination would be expected to be important. One can thus conclude that the addition of recombination to the model is not a trivial extension, because it is required to explain the peak behavior during certain times of the night.

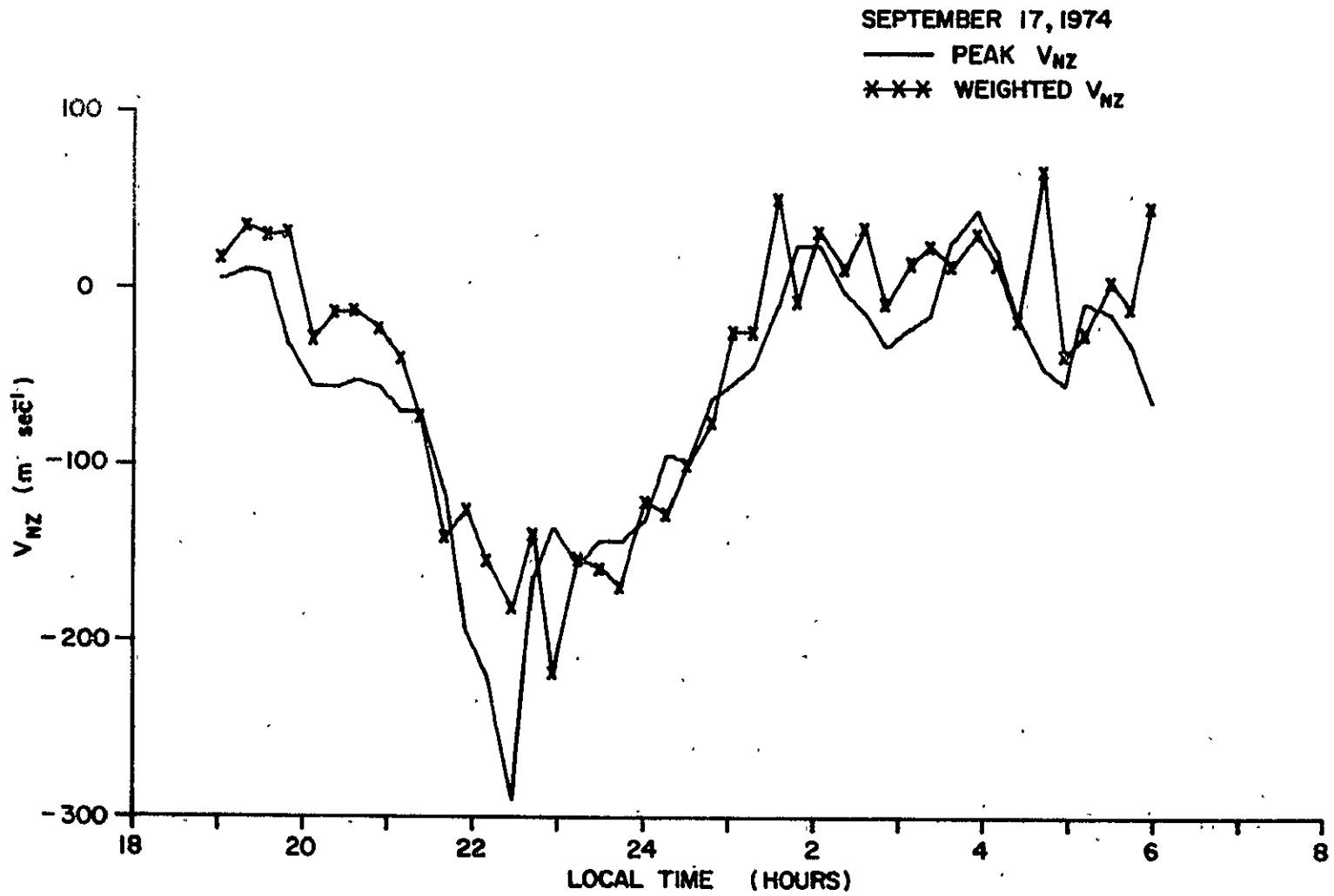


Figure 10: Time variation of the neutral wind at peak and the neutral wind weighted by the square root of the S/N ratio.

SEPTEMBER 17, 1974

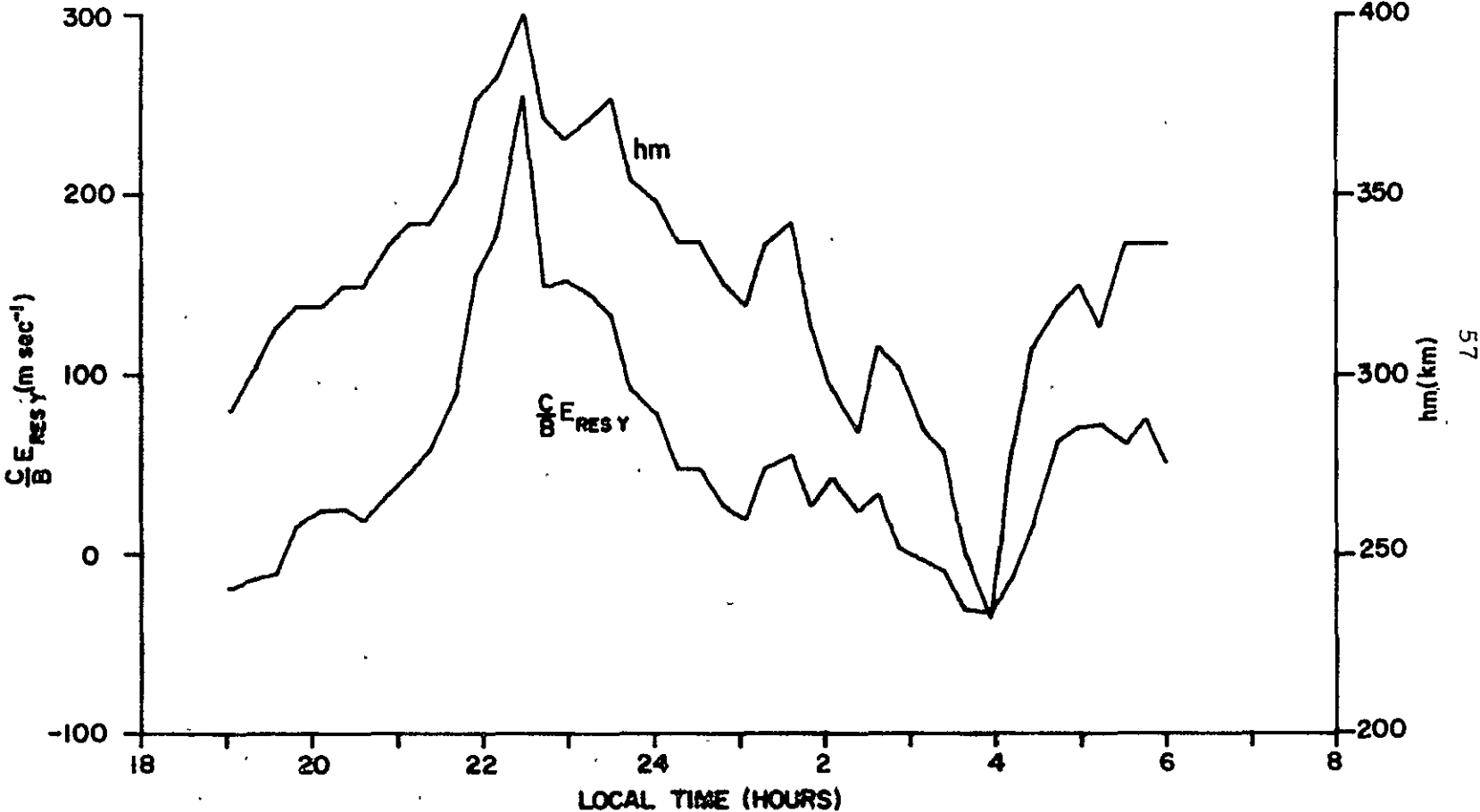


Figure 11: Time variation of the resultant eastward electric field and hm for September 17, 1974.

Before continuing with the analysis of the night of September 17, it is useful to show that the same correlation between E_{RESY} and h_m is found on the other nights (Figures 12, 13 and 14). It is seen that the resultant electric field on the November night, which is a night without F_s , is much smaller in magnitude than the field for the two nights with F_s (May 18 and September 17). It also shows far less time variation. The field during the October night, which is also a night without F_s , shows smoother time variations than the two nights with F_s , but its behavior is not as smooth as the November night. One can not draw any conclusions based on this. However, it should be noted that the resultant eastward electric field provides a stabilizing force for the Perkins model of F_s ; it is the northward field that causes the instability to develop. The northward electric fields for the four nights will be examined at a later time.

The analysis so far has shown that the correlation between the eastward resultant electric field and the motion of the F' layer peak is good, with the exception of times when the layer is low and recombination must be added. One could develop a model describing the motion of the peak by including only the eastward electric field, the neutral wind, and recombination, as essentially was done by Behnke and Kohl (1974). However, the Perkins model is a flux tube model, whereas a model describing the motion of the peak would be primarily local.

The Perkins model states that the field integrated Pedersen conductivity (Σ_F) will change in time as the layer is moved up and down by gravitational, electrostatic, and collisional (neutral wind)

NOVEMBER 9, 1974

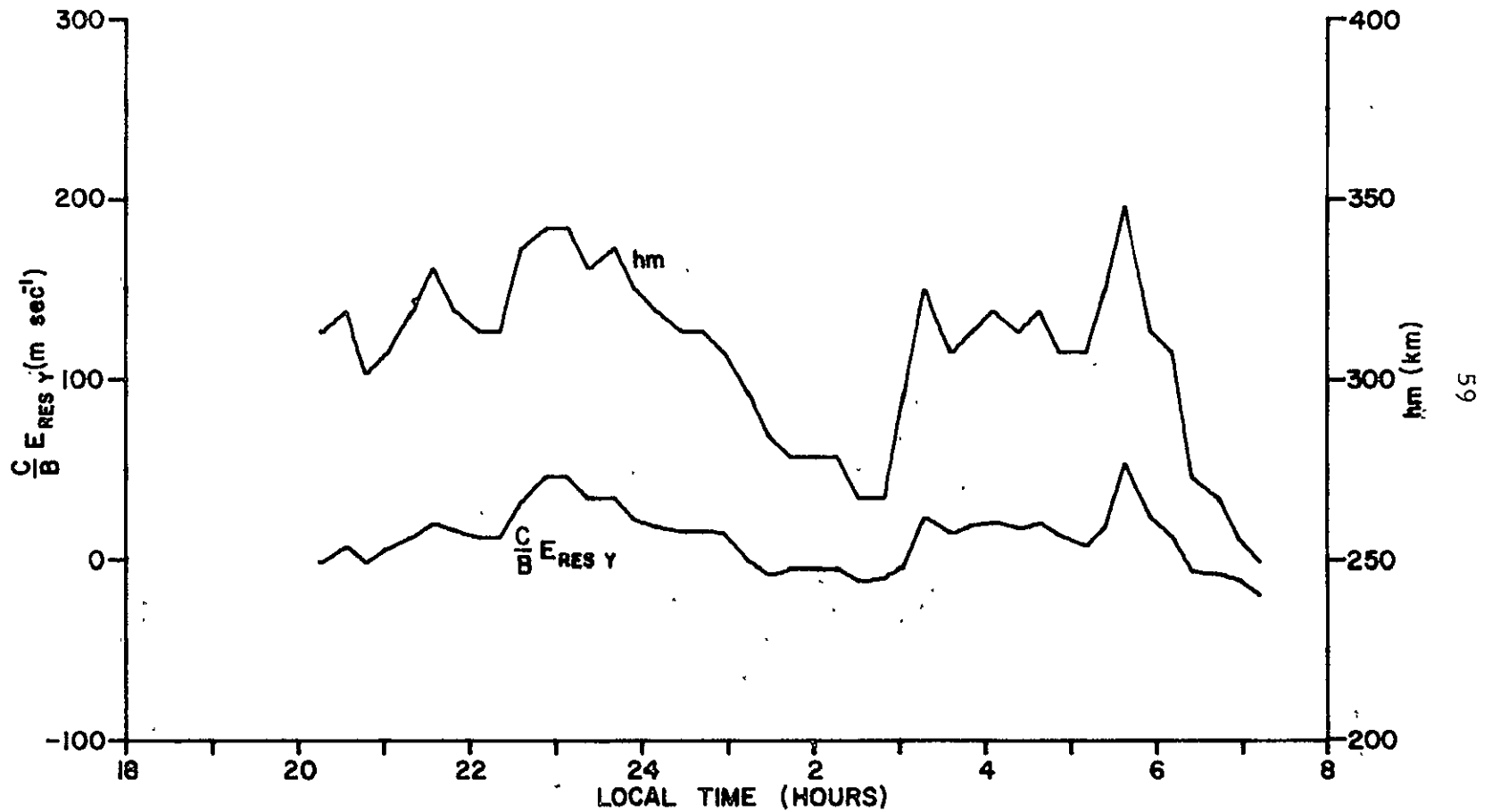


Figure 12: Time variation of the resultant eastward electric field and hm for November 9, 1974.

MAY 18, 1975

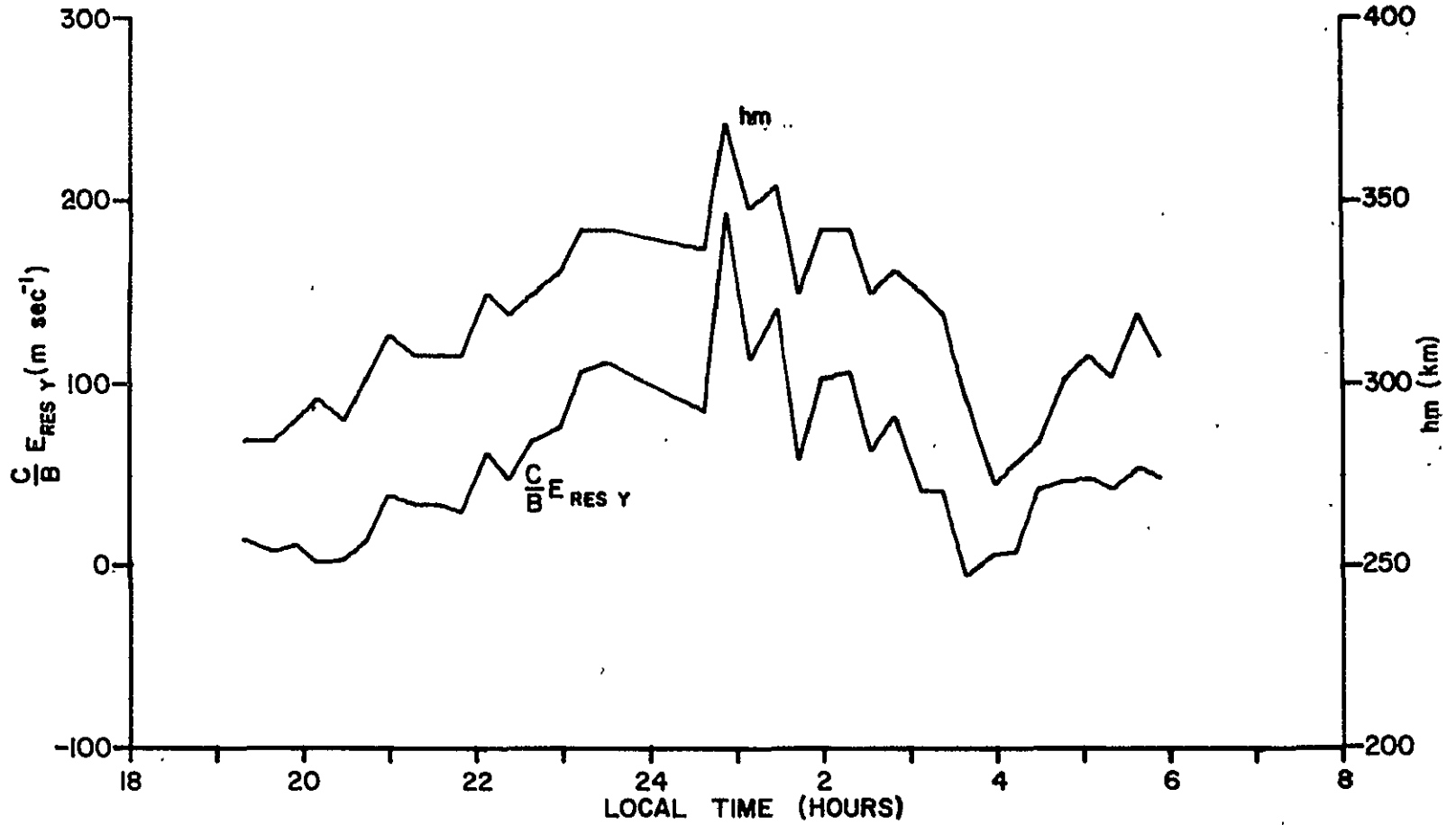


Figure 13: Time variation of the resultant eastward electric field and hm for May 18, 1975.

OCTOBER 14, 1975

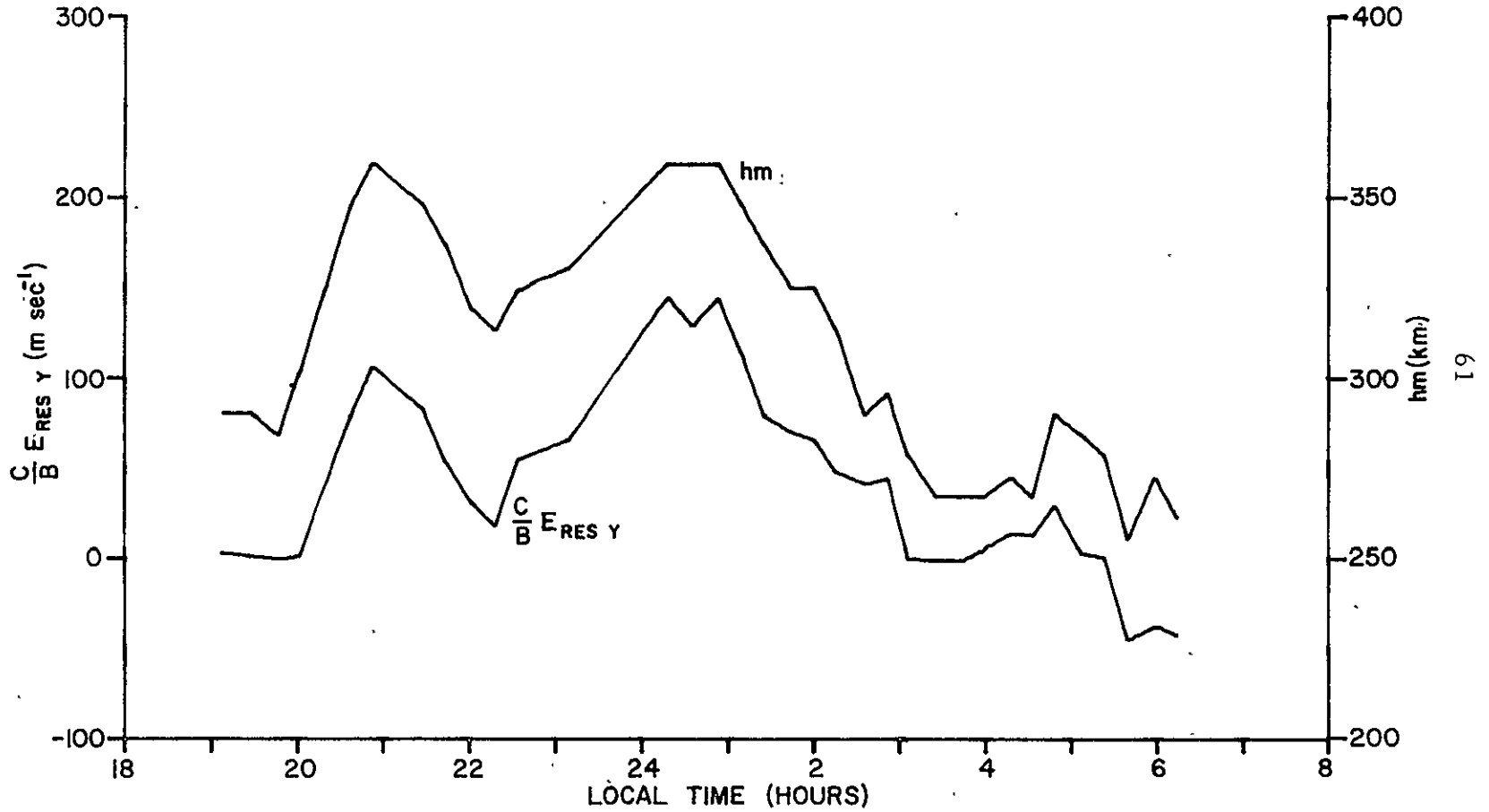


Figure 14: Time variation of the resultant eastward electric field and hm for October 14, 1975.

forces. If the layer shape remains reasonably constant, as it does (Figure 7), then the time behavior of Σ_F should be anti-correlated with the behavior of the peak, because v_{in}/ω_{ci} decreases with an increase in altitude. As the layer goes down, the integrated conductivity should increase because it depends on v_{in}/ω_{ci} .

It is seen by looking at Figure 15 that Σ_F and h_m are indeed anti-correlated. When the layer rises, Σ_F decreases, and when it falls Σ_F increases. The time period that represents an exception to the above statement is from 0230 to 0400, when the layer has fallen to 230 km but Σ_F has not increased. This is primarily due to choosing the lower limit of integration at 259.0 km. When the peak falls below this value, as it does at 0400, a sizable number of particles are not counted in the integration process. The value of Σ_F also depends on N_F , the total number of particles in the flux tube. Thus, if N_F decreases, Σ_F will also decrease even if the layer is not moving up. Failures in the anti-correlation between Σ_F and h_m can usually be attributed to changes in N_F . The alternate scheme to be presented of Σ_F and h_m for the other nights is shown in Figures 16, 17 and 18. The anti-correlation for the May night is the weakest.

It has now been shown that the resultant electric field is the dominant mechanism governing the height of the peak, and that the height of the peak is anti-correlated with the value of the integrated Pedersen conductivity. It can be concluded that the equilibrium solution of the Perkins model, in which the value of the field integrated conductivity depends on the resultant eastward electric field and the integrated density (Equation 2.11) is physically meaningful.

SEPTEMBER 17, 1974

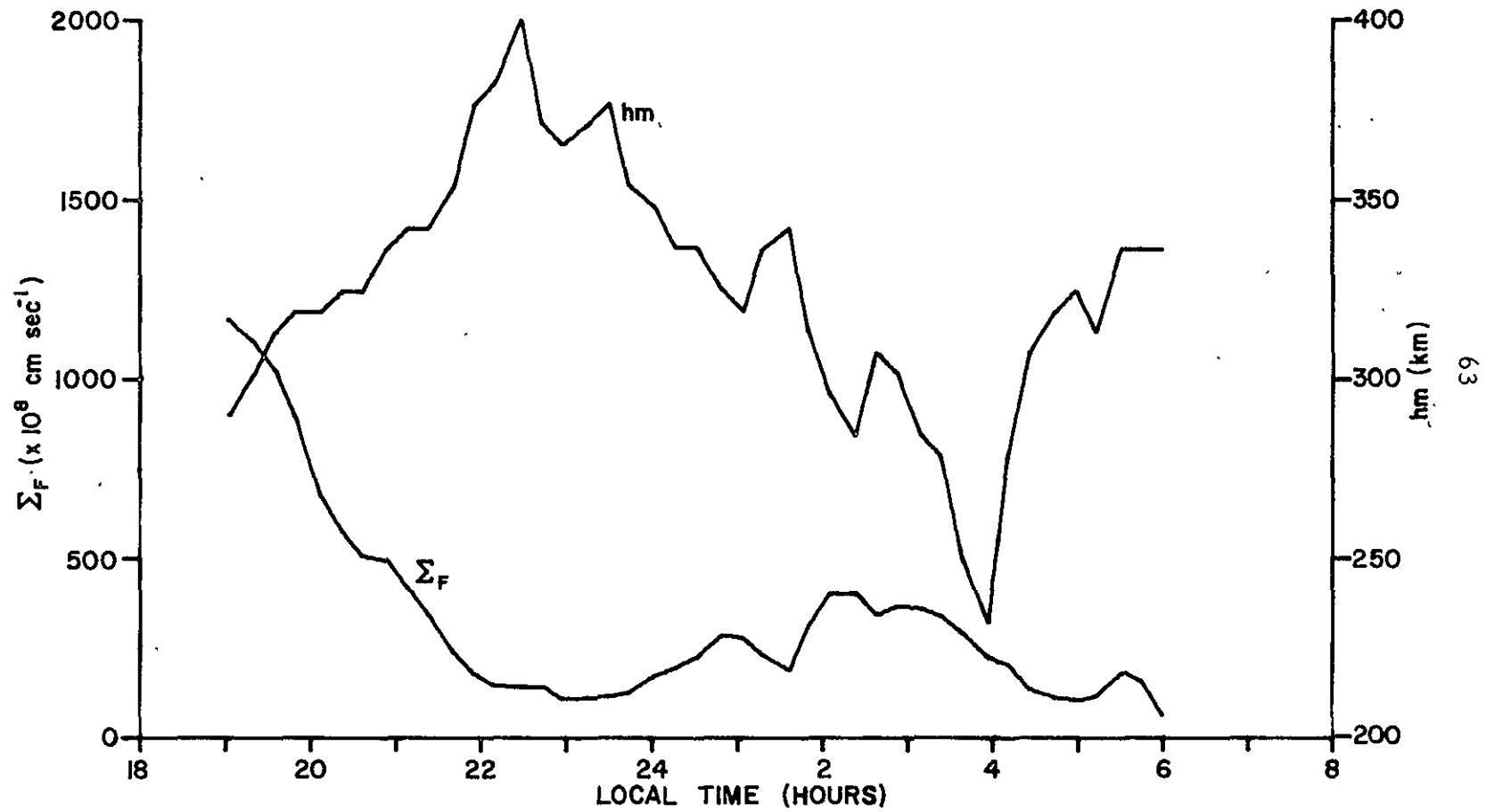


Figure 15: Time variation of the F region integrated Pedersen conductivity and hm for September 17, 1974.

NOVEMBER 9, 1974

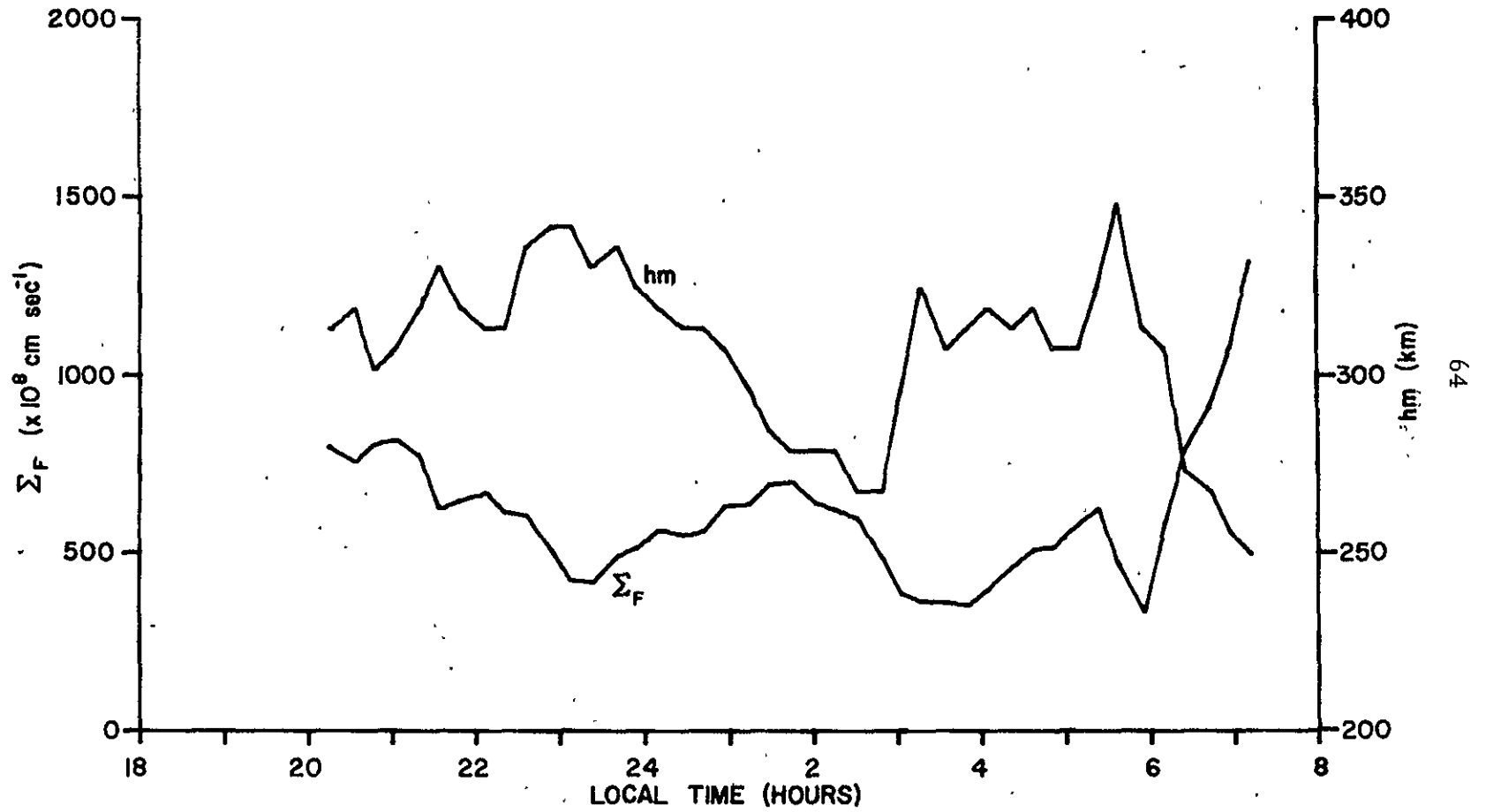


Figure 16: Time variation of the F region integrated Pedersen conductivity and hm for November 9, 1974.

MAY 18, 1975

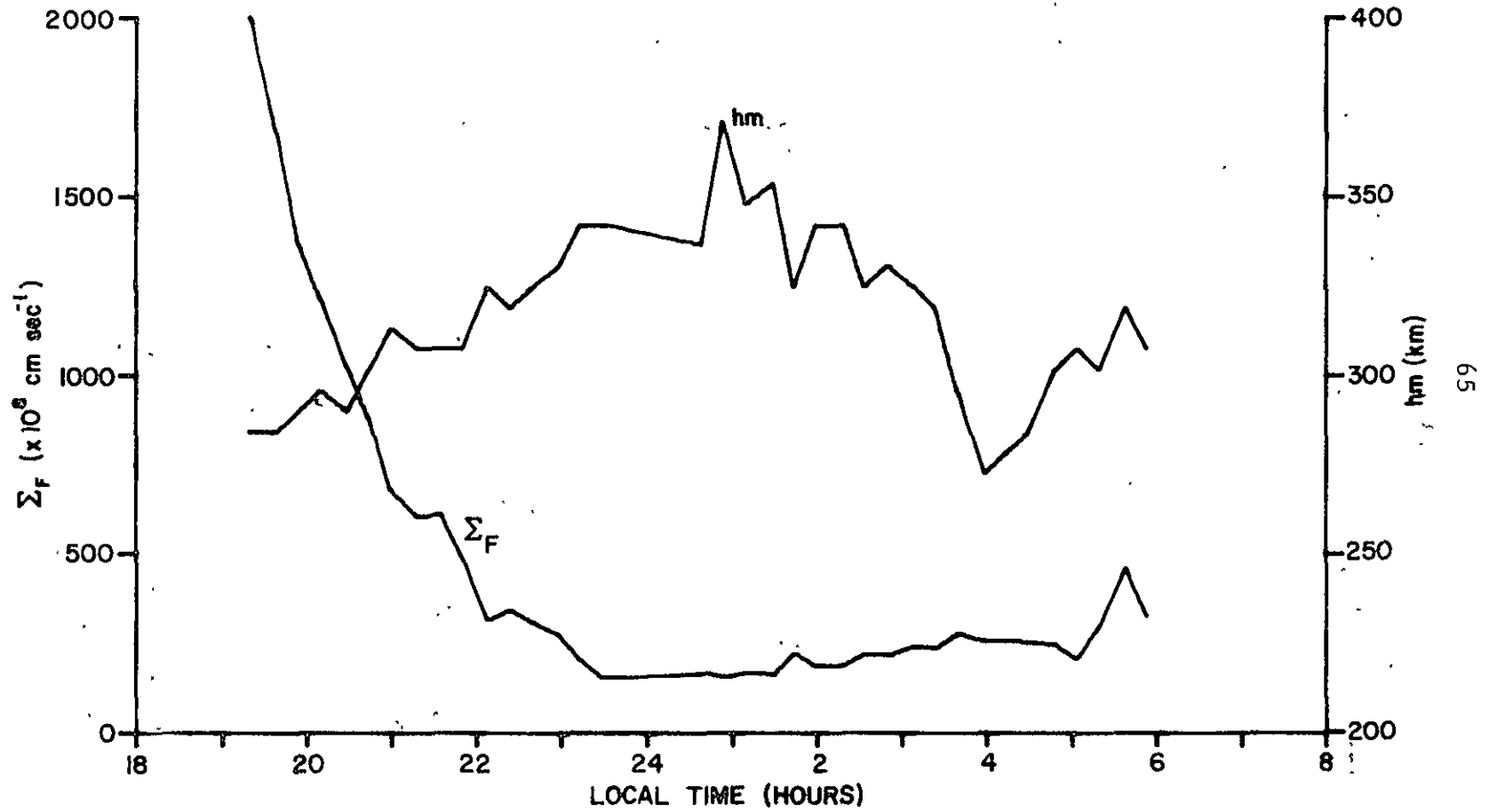


Figure 17: Time variation of the F region integrated Pedersen conductivity and h_m for May 18, 1975.

OCTOBER 14, 1975

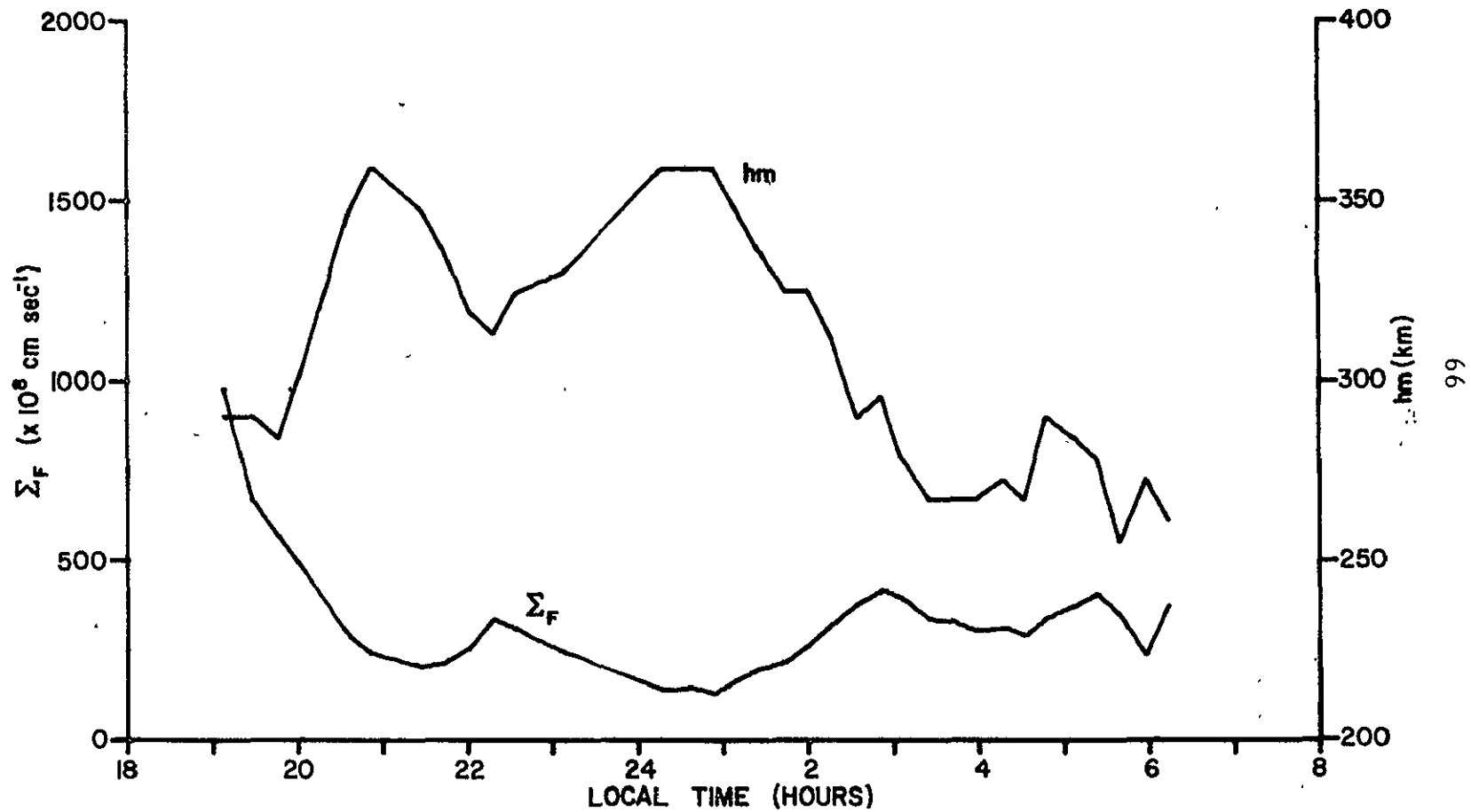


Figure 18: Time variation of the F region integrated Pedersen conductivity and hm for October 14, 1975.

Equation 3.10 has a lot of extra terms in it that would not be expected to be important based on the above conclusion, at least for most of the night. One exception is recombination, which has been found to be important when the layer is low. The effect of the extra terms will be discussed later in this chapter.

The behavior of the integrated plasma density (N_F), is shown in Figure 19. It is seen that the integrated density decreases steadily until around midnight, when it increases. It then holds constant for a few hours until it starts to decrease again after 0200. Since recombination will cause a steady depletion throughout the night, the increase in N_F must come either from a density gradient drifting into the region of observation, or from a flux of particles coming in at the boundaries of the flux tube. The decrease of N_F through most of the night can be explained by recombination, but the midnight increase can only be explained by more particles coming into a flux tube than are lost by recombination. It is the assumption at this stage that a net input of particles at the boundaries of order $3 \times 10^{11} \text{ cm}^{-2}$ over a period of 40 minutes is the dominant mechanism that accounts for the input of particles. This requires an input flux of roughly $2 \times 10^8 \text{ cm}^{-2} \text{ sec}^{-1}$. The question of the density gradient will be considered later.

The fluxes are determined at each of the 10 heights simply by multiplying the bulk ion drift velocity along the magnetic field by the density at the height in question. If the S/N ratio is less than 1.0 at any height, the flux is set equal to zero for the purposes of

SEPTEMBER 17, 1974

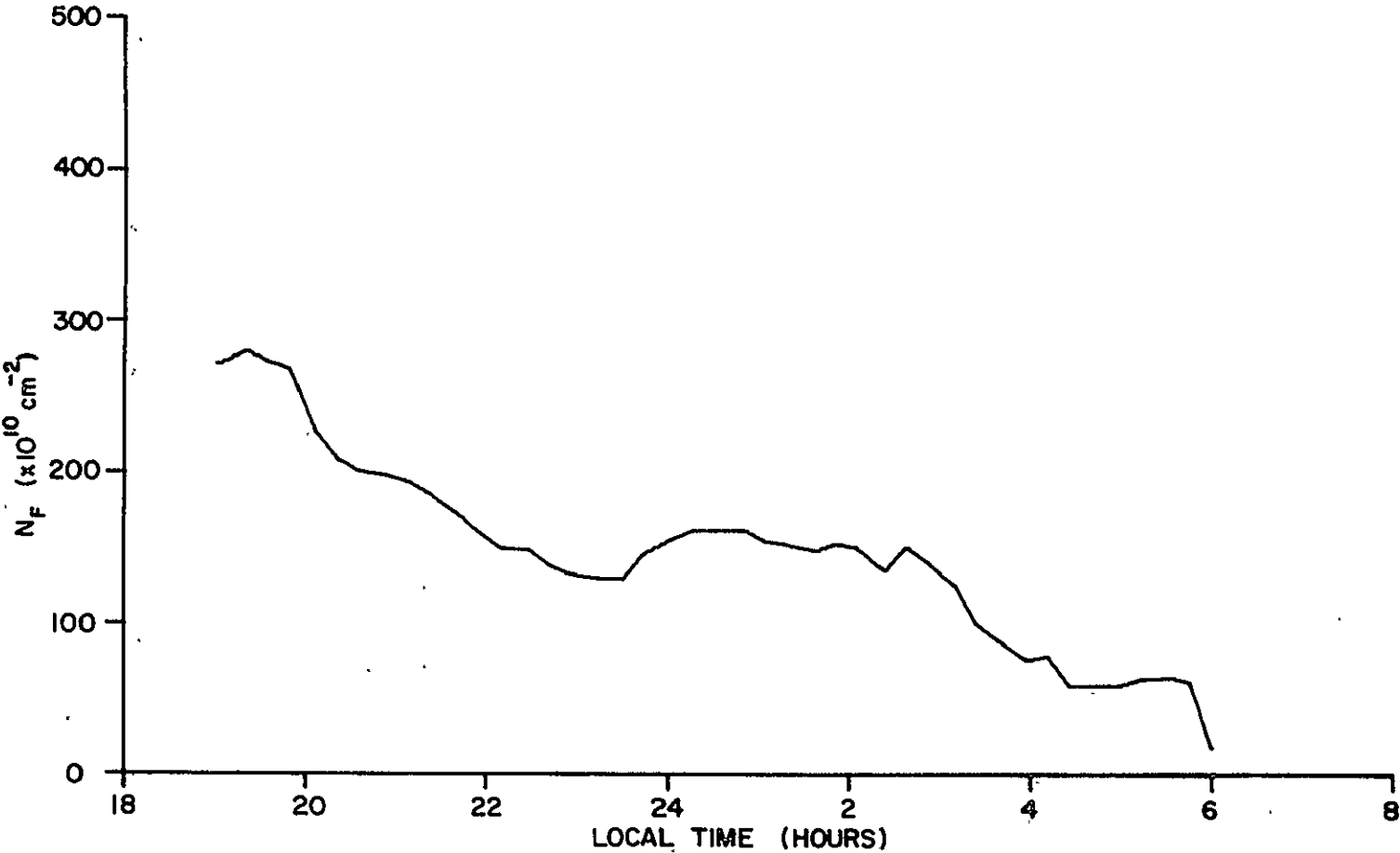


Figure 19: Time variation of F region integrated ion density.

plotting. The fluxes at each of the 10 heights for the night of September 17 are shown in Figures 20 a-j. A positive flux is downward along the magnetic field.

It is immediately seen that the fluxes at the lower heights are generally smaller than at the higher heights. The velocity that contributes to the flux is a combination of the diffusion velocity and the neutral wind velocity (cf. Equation 3.3). At the higher altitudes, $1/v_{in}$ is quite large so the diffusion velocity is expected to be large. On the other hand, n is decreasing with the result that the flux at the higher altitudes should not change significantly from one altitude to the next since recombination is negligible. In fact, the fluxes calculated by these data do change over adjacent heights. This is illustrated in Figure 20 k. Also, the fluxes vary a great deal in time. These two facts raise serious questions about the accuracy of the fluxes. Further indications of the inaccuracy of the fluxes will appear when the fluxes are used in Equations 3.8 and 3.10.

Because of the large amount of time and space variation of the fluxes, an attempt was made to calculate the fluxes directly from Equation 3.3. This method does not work, however, because of the $1/v_{in}$ dependence of the diffusion velocity. Even with a least squares smoothing of density data near the top, there are still small fluctuations in $\partial n/\partial z$ that are magnified by the $1/v_{in}$ factor. The resulting fluxes calculated directly by Equation 3.3 showed even larger variations in both time and space than those calculated with velocity data.

SEPTEMBER 17, 1974

201.6 km

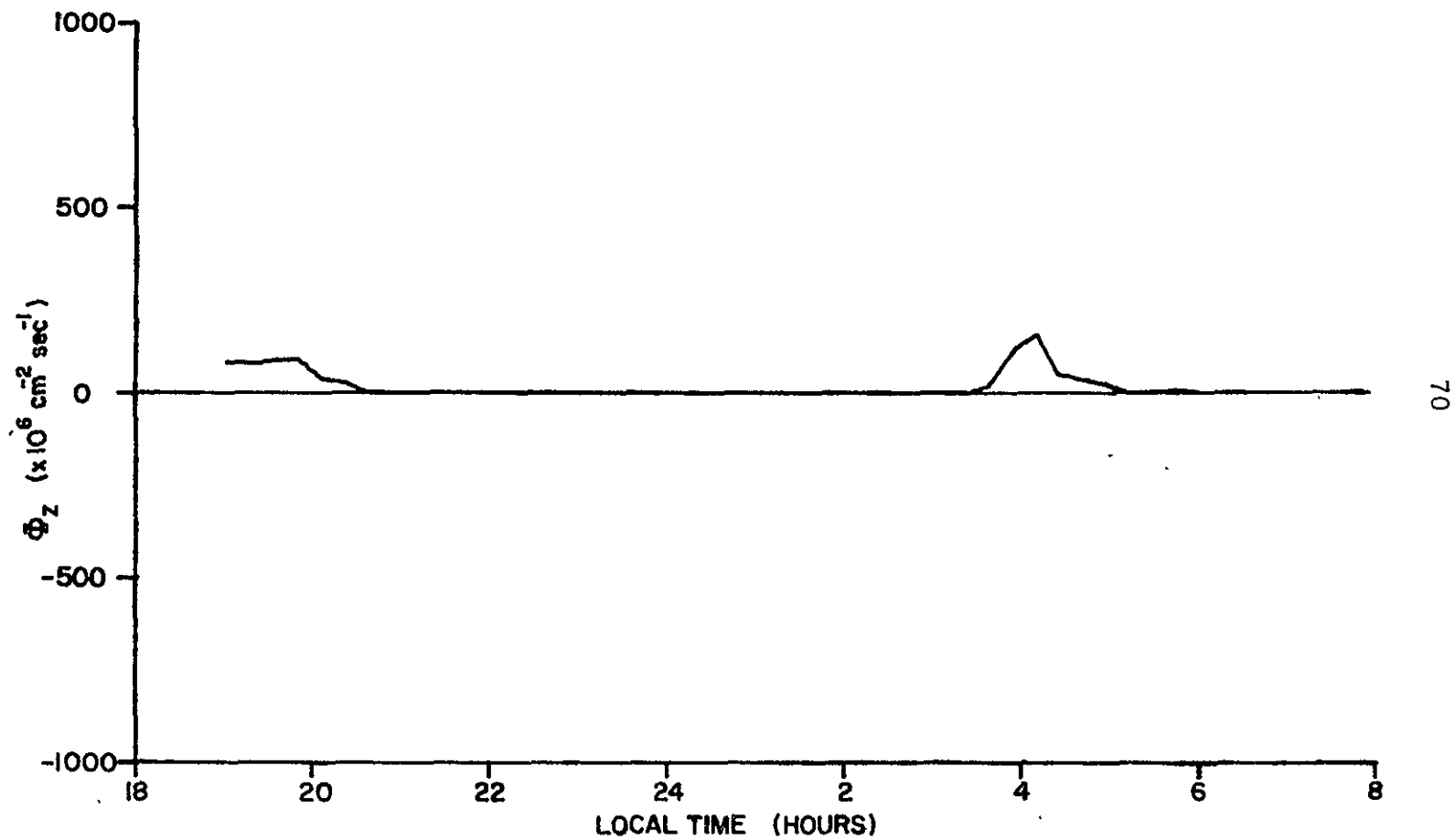
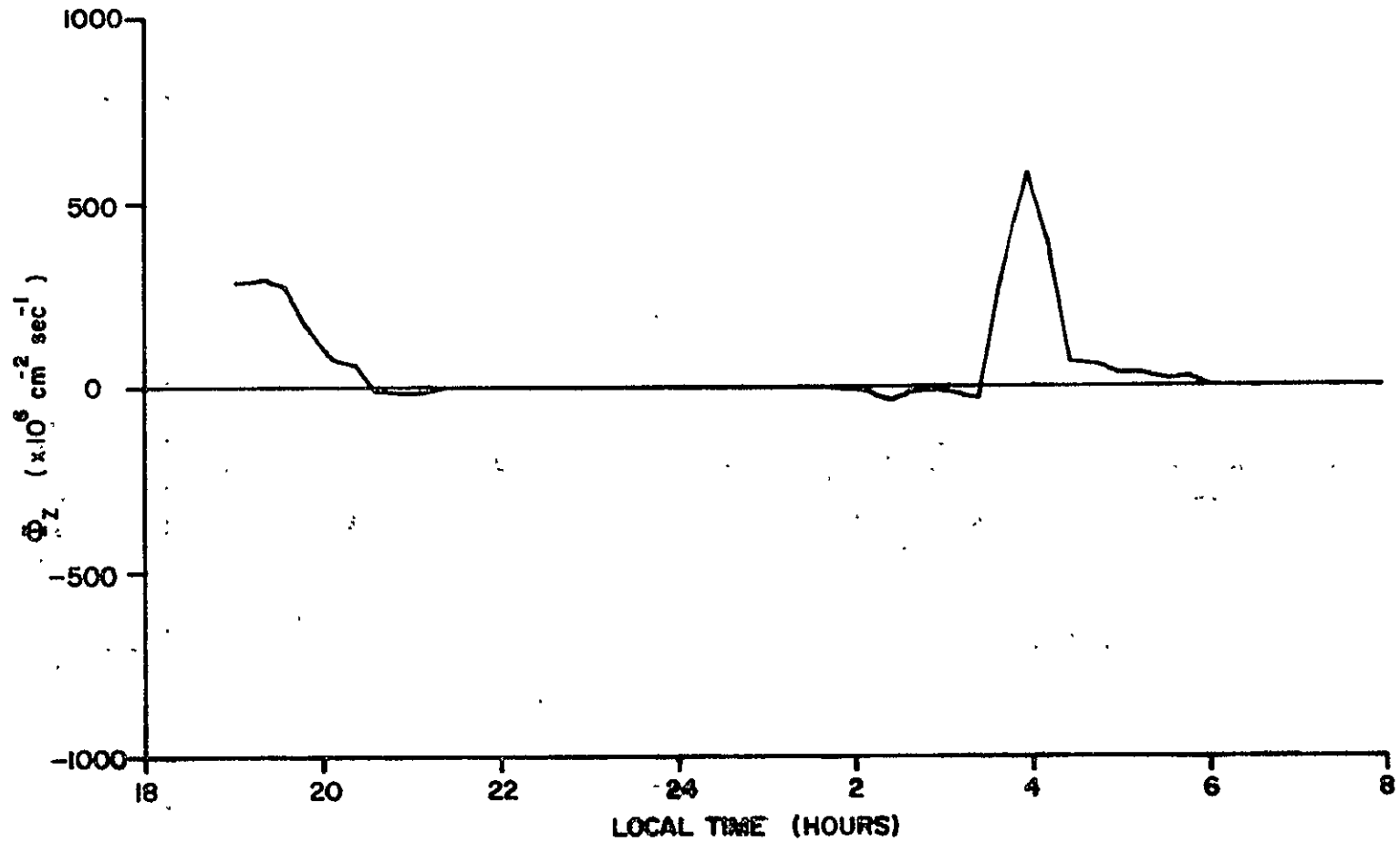


Figure 20a: Time variation of the flux at 201.6 km.

SEPTEMBER 17, 1974
230.6 km

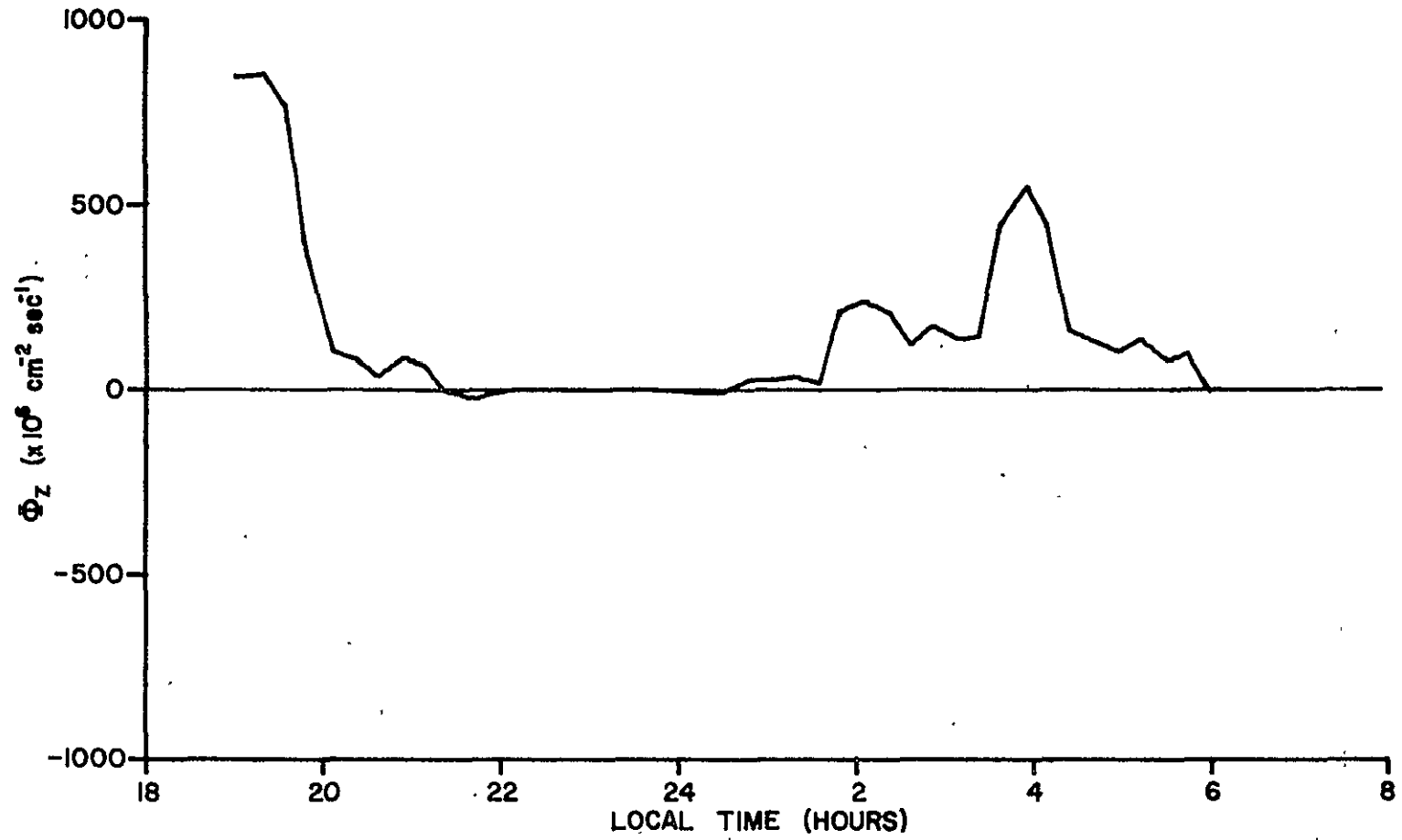


71

Figure 20b: Time variation of the flux at 230.6 km.

SEPTEMBER 17, 1974

259.6 km



72

Figure 20c: Time variation of the flux at 259.6 km.

SEPTEMBER 17, 1974
288.6 km

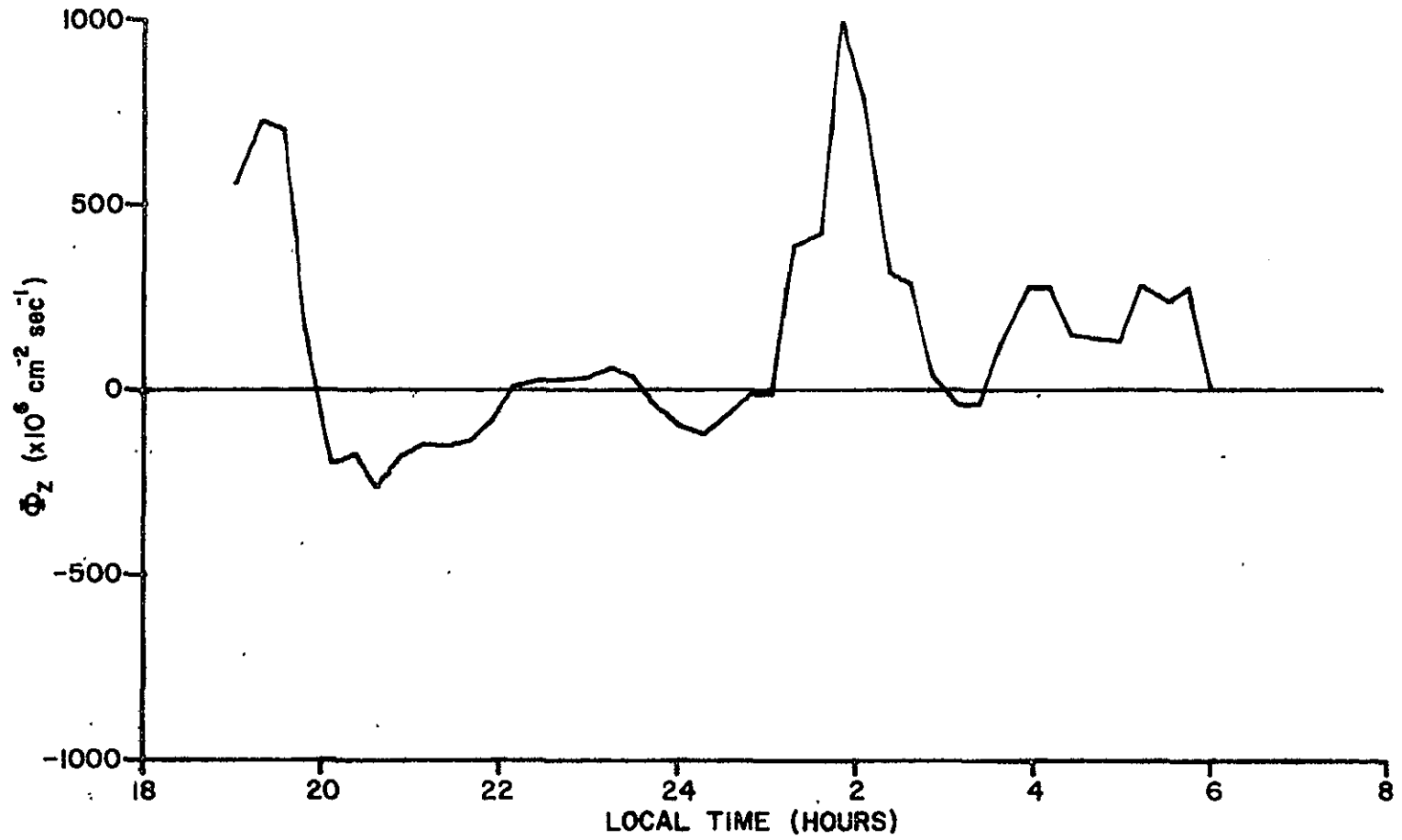


Figure 20d: Time variation of the flux at 288.6 km.

SEPTEMBER 17, 1974
317.6 km

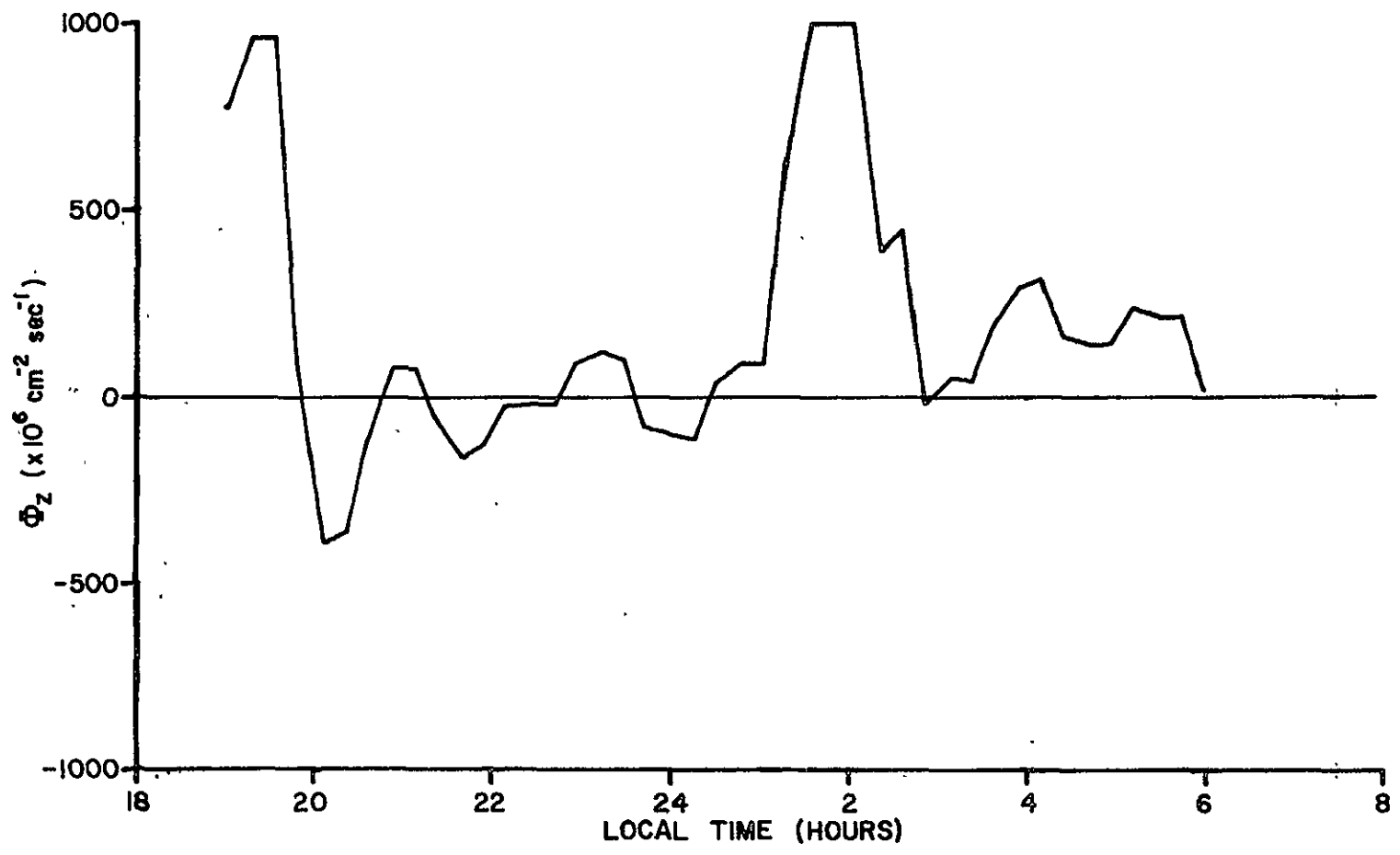


Figure 20e: Time variation of the flux at 317.6 km.

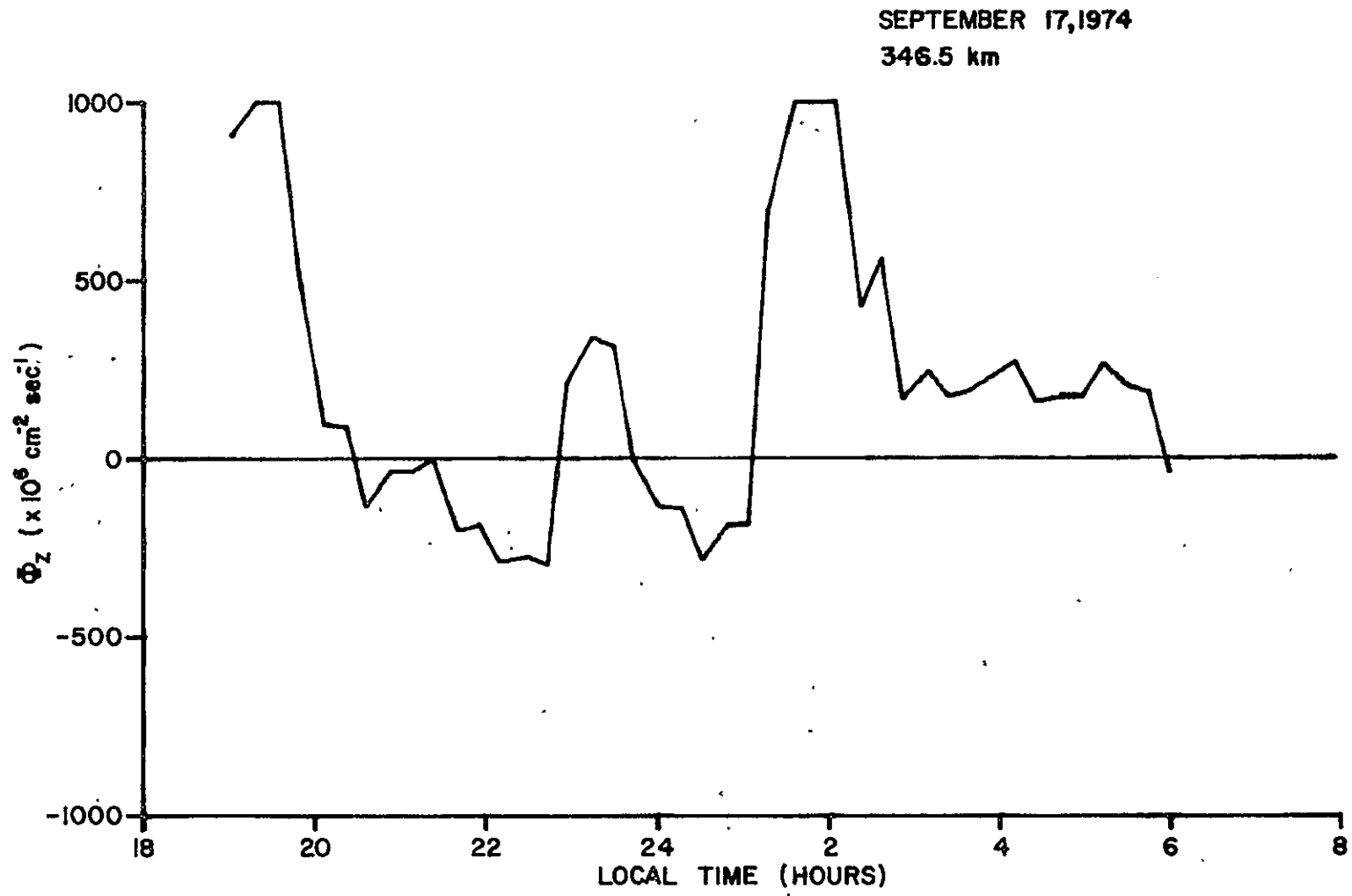


Figure 20f: Time variation of the flux at 346.5 km.

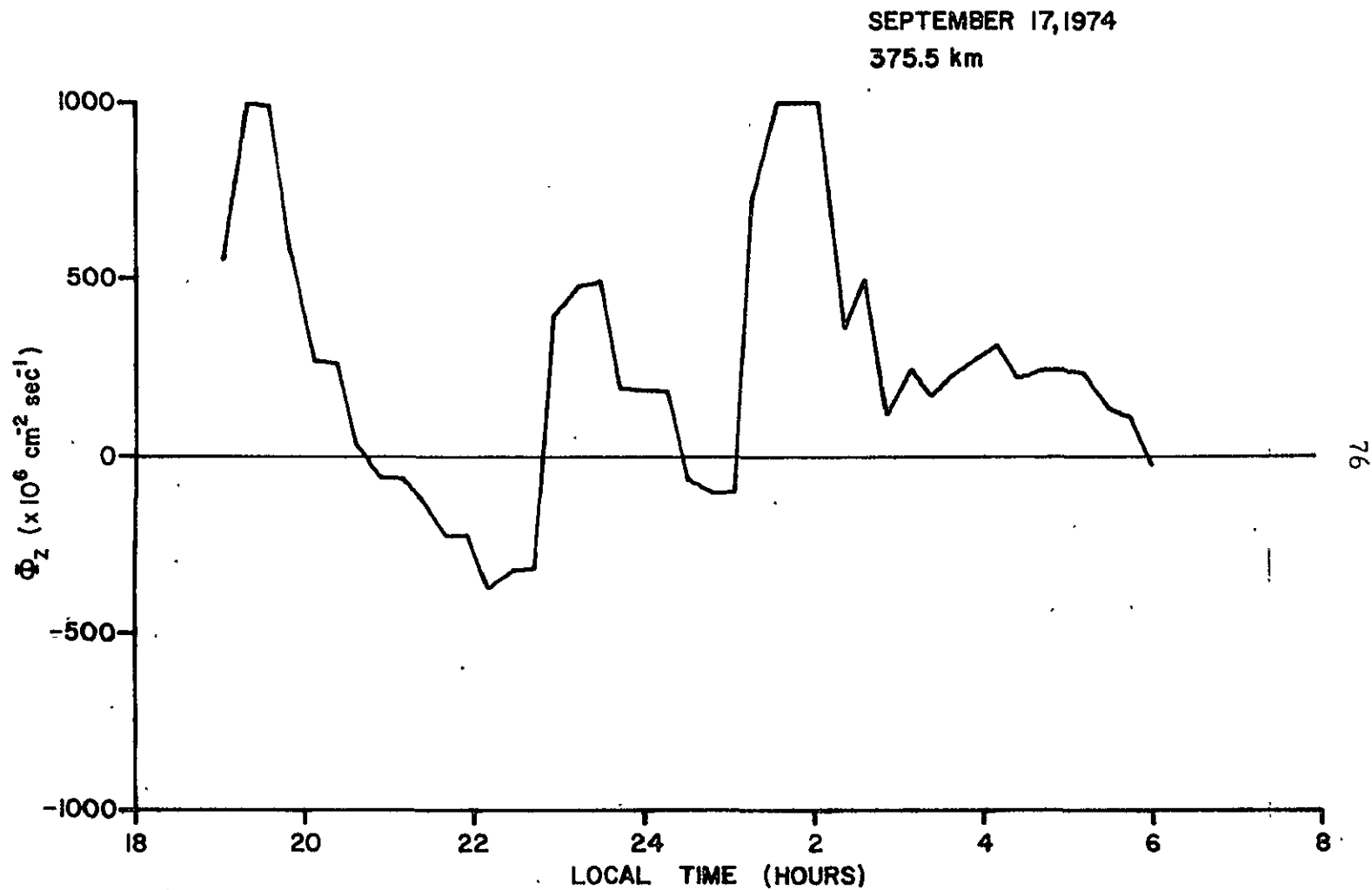


Figure 20g: Time variation of the flux at 375.5 km.

SEPTEMBER 17, 1974
404.5 km

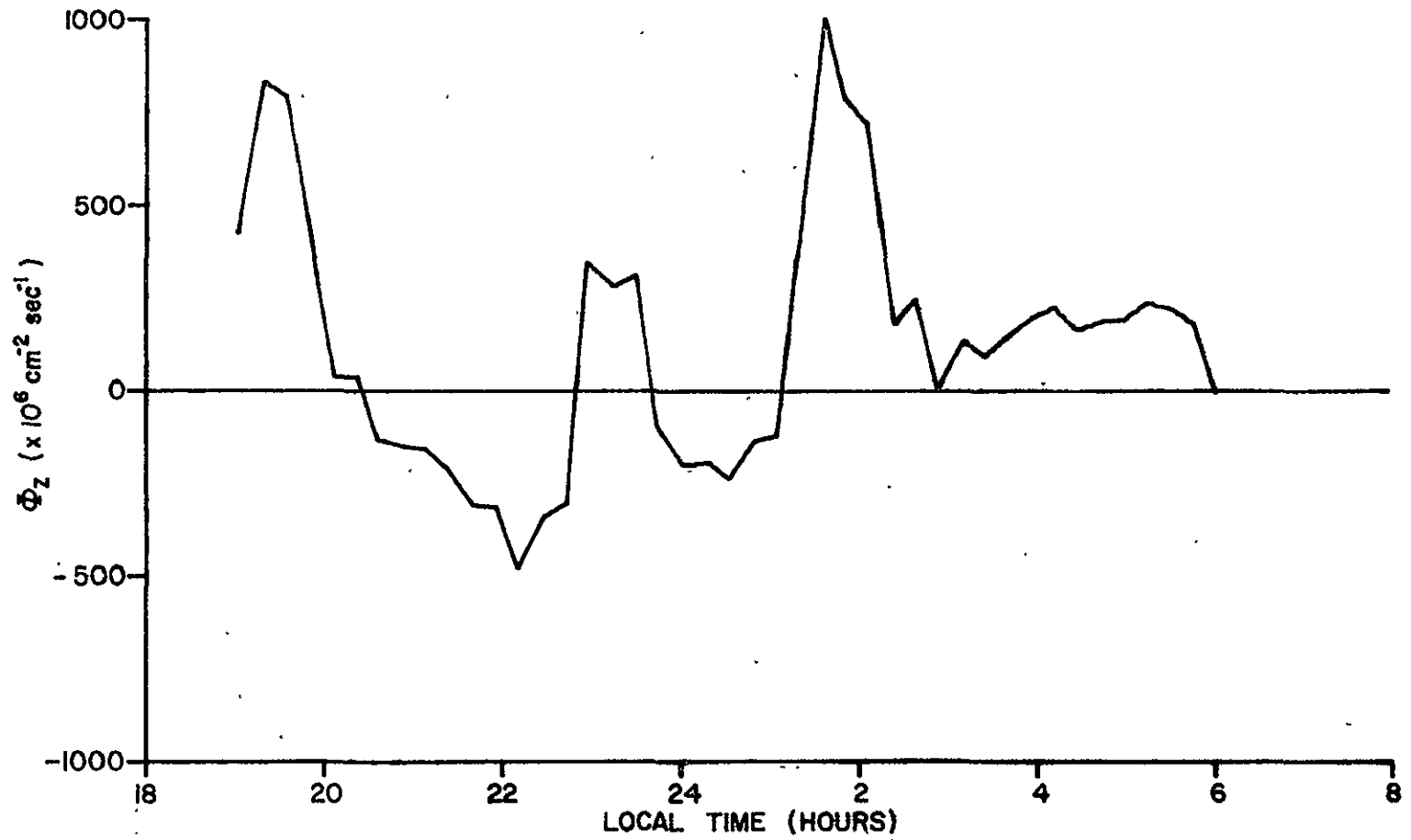


Figure 20h: Time variation of the flux at 404.5 km.

SEPTEMBER 17, 1974
433.5 km

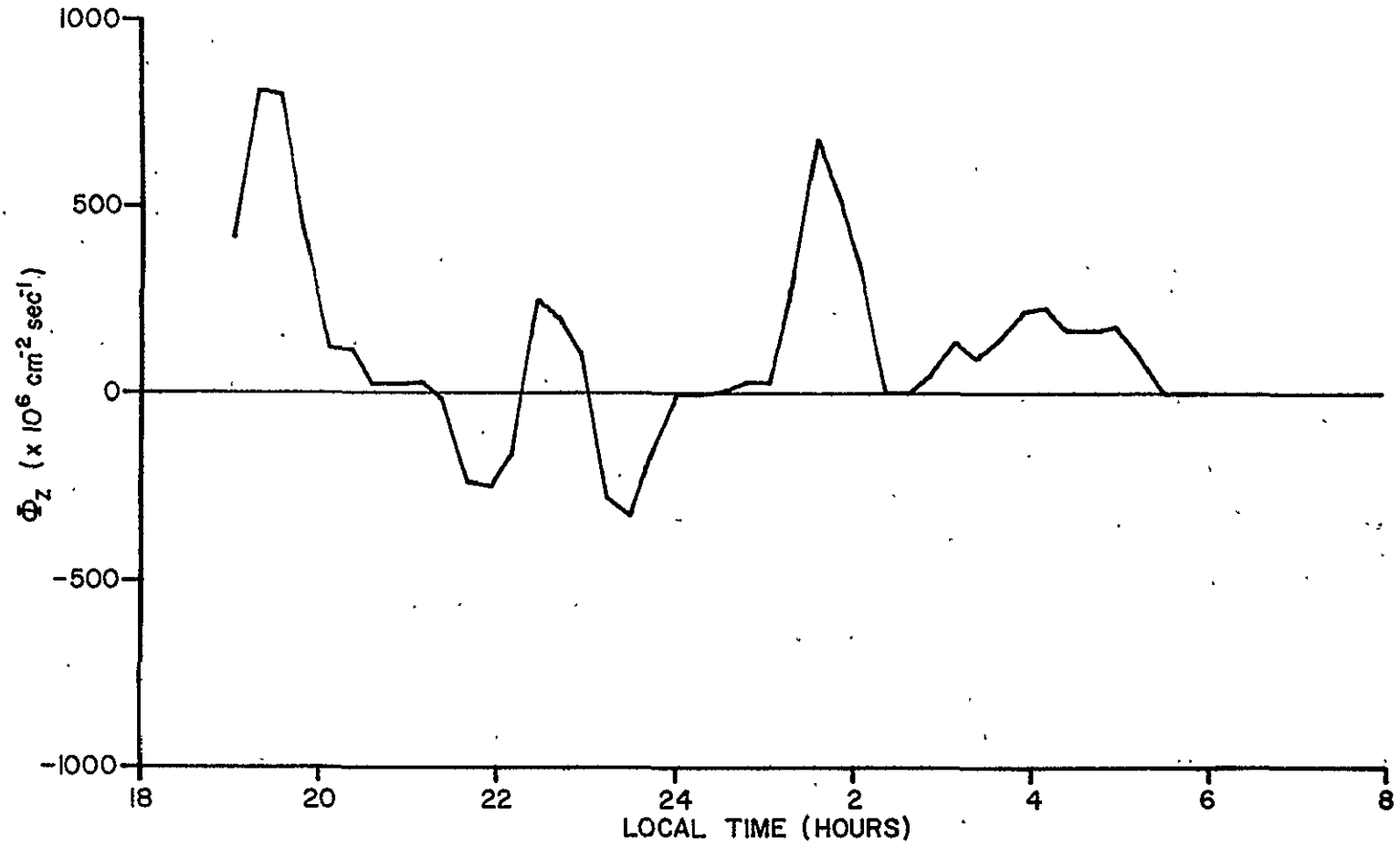


Figure 20i: Time variation of the flux at 433.5 km.

SEPTEMBER 17, 1974
462.4 km

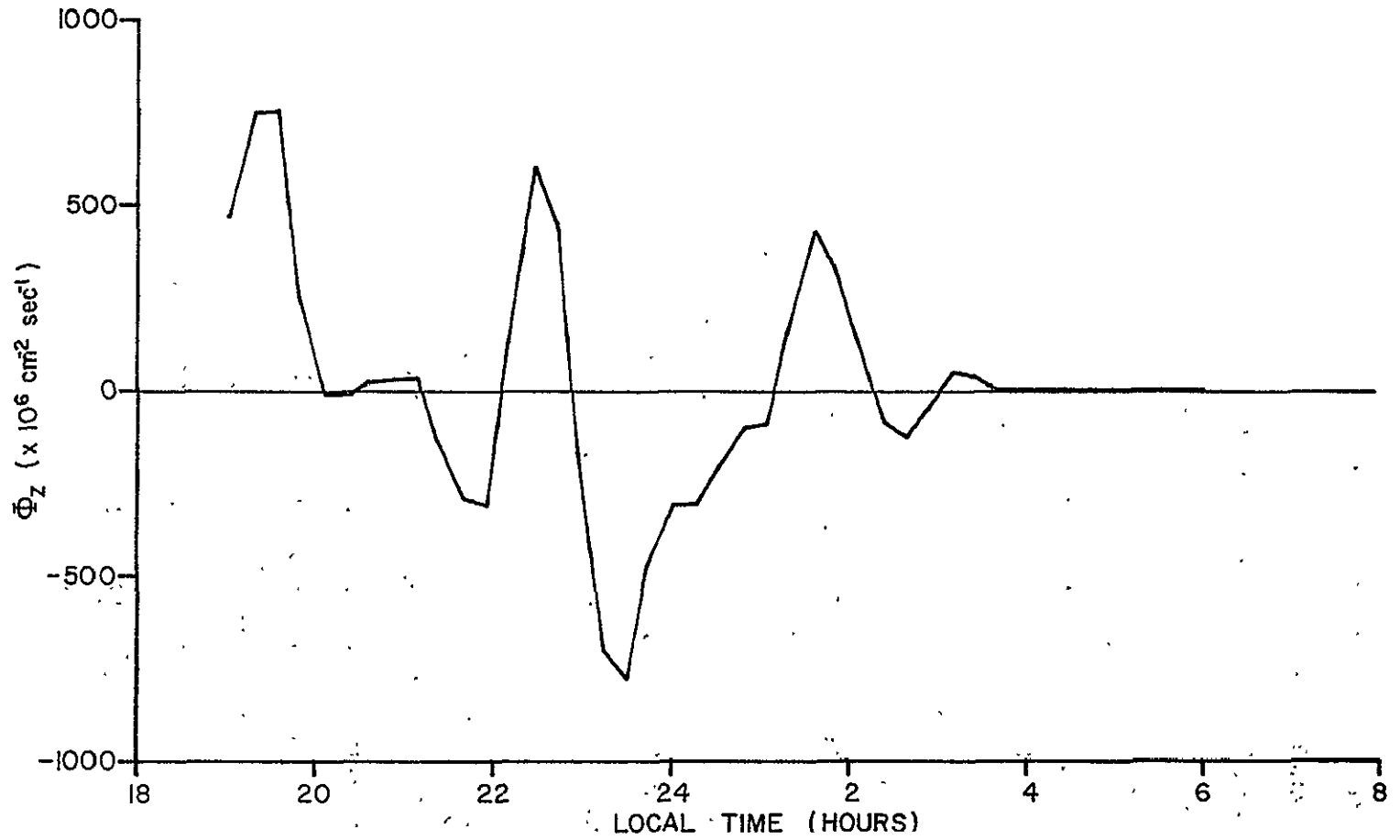


Figure 20j: Time variation of the flux at 462.4 km.

The quantity desired in Equations 3.8 and 3.10 is the net flux into a flux tube, i. e. $\Phi_T - \Phi_B$. When the S/N ratio is below 1.0 for measurements at 259.6 km, the velocity at the next higher height that has a S/N ratio of greater than 1.0 is used with the density at 259.6 km to calculate the flux. The net flux into a flux tube is shown in Figure 21.

It is obvious that the net flux shown in Figure 21 will not explain the behavior of the integrated density. The period just before midnight, when the density is increasing, is one when there is a large amount of particles leaving the flux tube via the field lines. A flux into the flux tube of $2 \times 10^8 \text{ cm}^{-2} \cdot \text{sec}^{-1}$ is required to explain the density increase; the data shows a flux of greater than 5×10^8 leaving the flux tube. The net out-flux of particles in the period from 2300 to 0100 represents a loss of around 2×10^{12} particles cm^{-2} . This would certainly be seen in Figure 19 if such an outflow did indeed exist.

Because the fluxes calculated at the boundaries (259.6 and 462.4 km) were so different, causing a much larger net flux than the integrated content data indicated, it was initially thought that narrowing the integration interval would alleviate the problem somewhat. The behavior of the fluxes at adjacent heights (Figure 20k) indicates that this procedure is not going to help much. There are other reasons for choosing different boundaries, however, and they will be discussed in the next section.

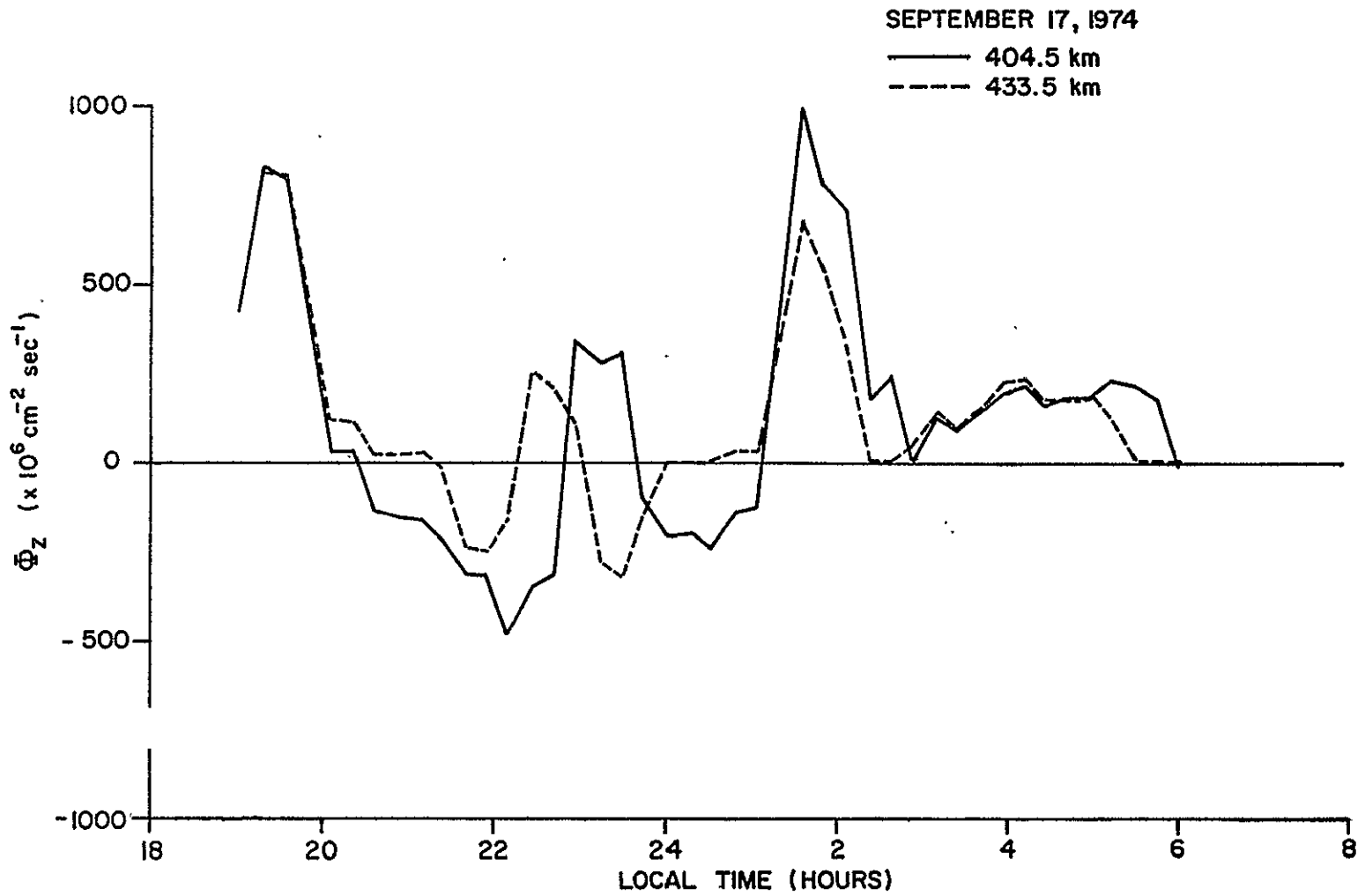


Figure 20k: Time variation of the flux at 404.5 km and 433.5 km.

C-2

SEPTEMBER 17, 1974

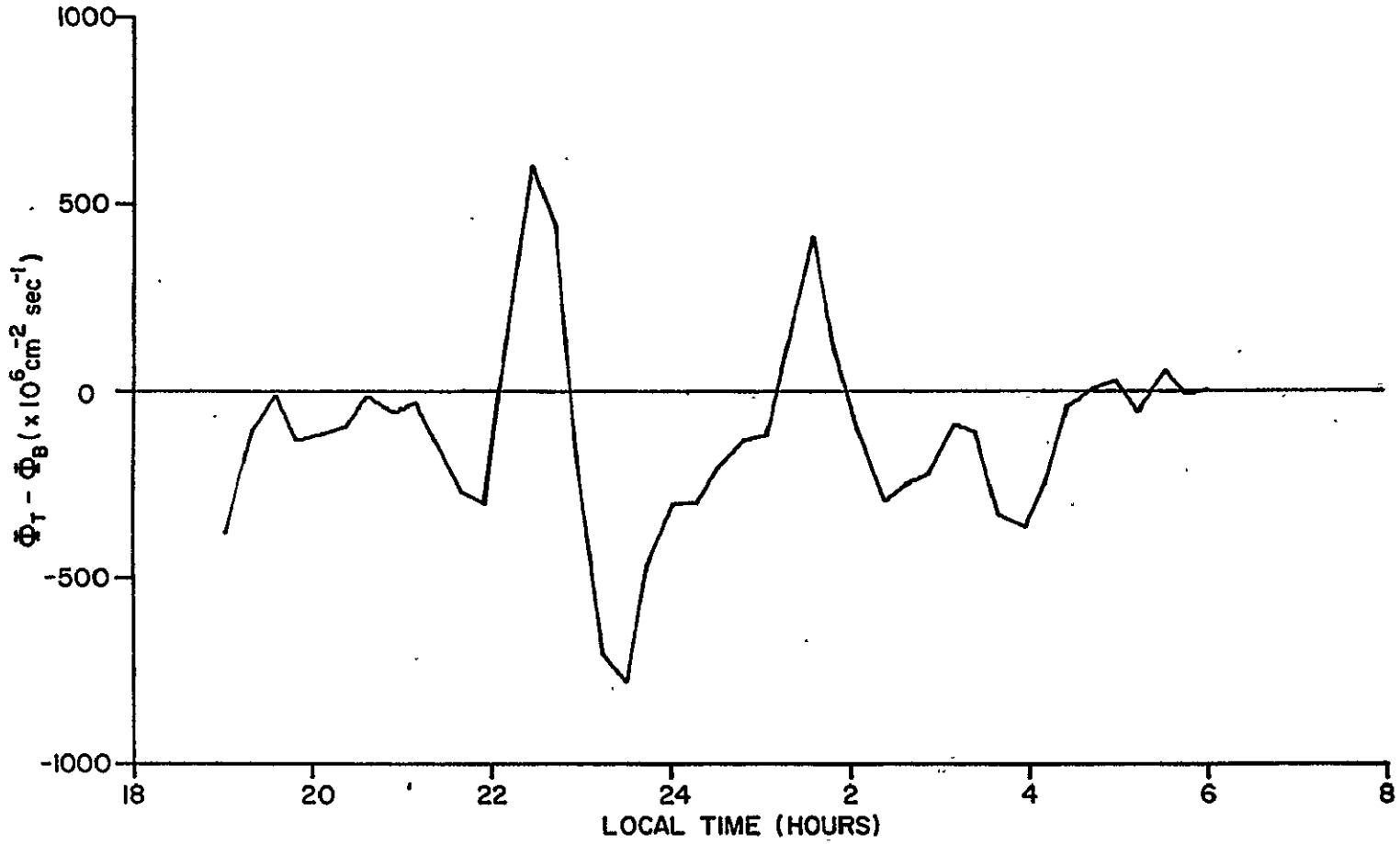


Figure 21: Time variation of the net flux (fixed boundaries).

3.4 Analysis of the Data -- Peak-Centered Integration

The problems associated with the fixed limit integration scheme are two-fold. The first is that when the peak is at a maximum or minimum height, the S/N ratio at one of the boundaries may be less than 1.0. The second is that the peak may actually fall below one of the boundaries and the integration will not include a sizable portion of the layer. The method of analysis presented in this section eliminates both of these problems by narrowing the interval of integration and requiring that the interval follow the peak up and down. By narrowing the interval (to 90 km) and centering it around the peak, it is insured that the S/N ratio will be high at the boundaries. In addition, it was hoped that perhaps the net flux would show better agreement with the data on N_F .

The net flux calculated by the peak-centered method is shown in Figure 22. As is seen, it still shows a great deal of time variation, and the net outward flux before midnight is still there. Consequently, this problem is still unresolved.

Now that a method of analysis has been chosen which is in the spirit of the Perkins flux tube model, Equations 3.8 and 3.10 can be compared to the data. Assuming no horizontal gradients in N or Σ , the two model equations are of the form:

$$\frac{dx}{dt} = -A(t)x + S(t)$$

where $A(t)$ and $S(t)$ are determined from the data. The solution to this equation is

SEPTEMBER 17, 1974

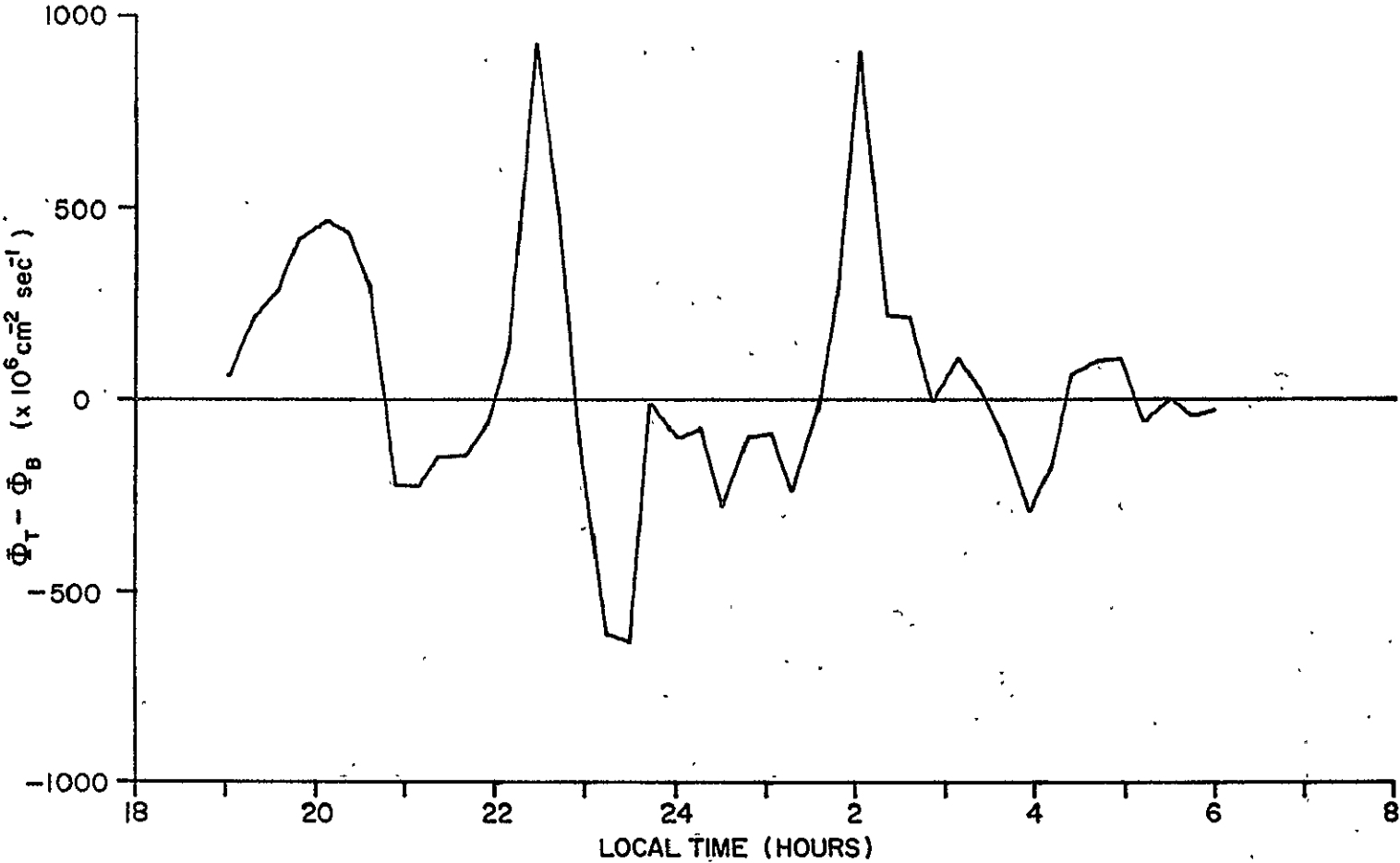


Figure 22: Time variation of the net flux (peak-centered boundaries).

$$X(t) = X(t_1) \left(\exp - \int_{t_1}^t A(t') dt' \right) \int_{t_1}^t s(t') \left(\exp \int_{t_1}^t A(t'') dt'' \right) dt' \quad (3.11)$$

The integrals in this equation are calculated using the trapazoidal rule.

The solution of Equation 3.8 is compared with the actual values of $N_F(t)$ calculated by the data in Figures 23 and 24. In Figure 23 the fluxes are not included, while in Figure 24 they are included. It is immediately seen that the model with only recombination added represents the data quite well. When the net flux is added, the model breaks down completely. The fluxes are just too large and turbulent compared to what the data for N_F predicts they should be. The fact that the model with only recombination added predicts the density behavior fairly accurately suggests that the measured fluxes are much too high. The same conclusion is reached when the other nights are analyzed (Figures 27, 30 and 33), although the agreement between the model with recombination added is not as good as it was during the September night (Figures 26, 29 and 32). This indicates that there is some flux entering or leaving, but it is not the flux given by the data.

The flux terms in the equation describing the behavior of Σ_F (Equation 3.10) also give trouble, as will now be demonstrated. Terms were successively added to the model by first including only

SEPTEMBER 17, 1974
RECOMBINATION ADDED

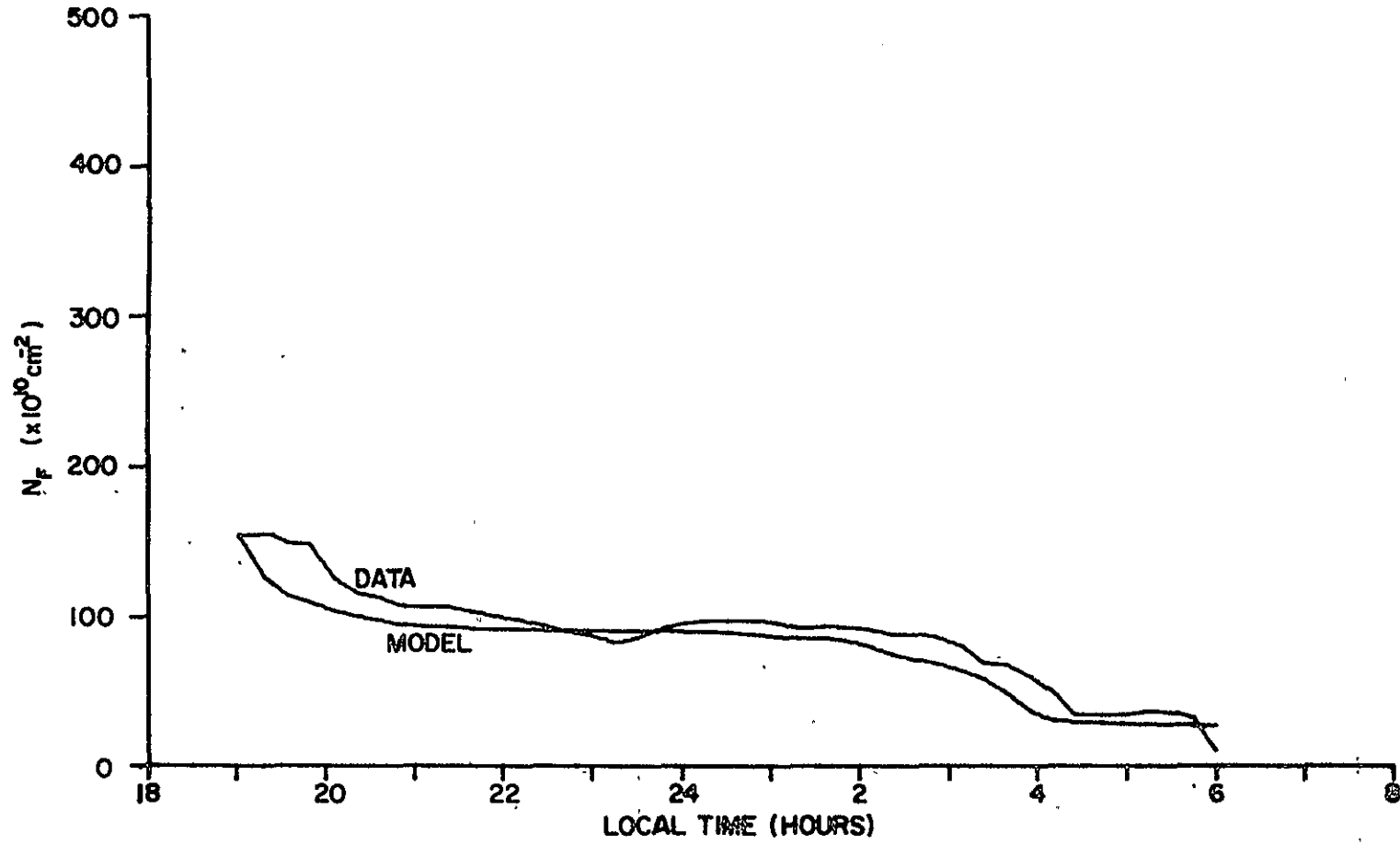


Figure 23: Time variation of N_F obtained from the data, and the solution of Equation 3.8 including recombination only.

SEPTEMBER 17, 1974
FLUXES ADDED

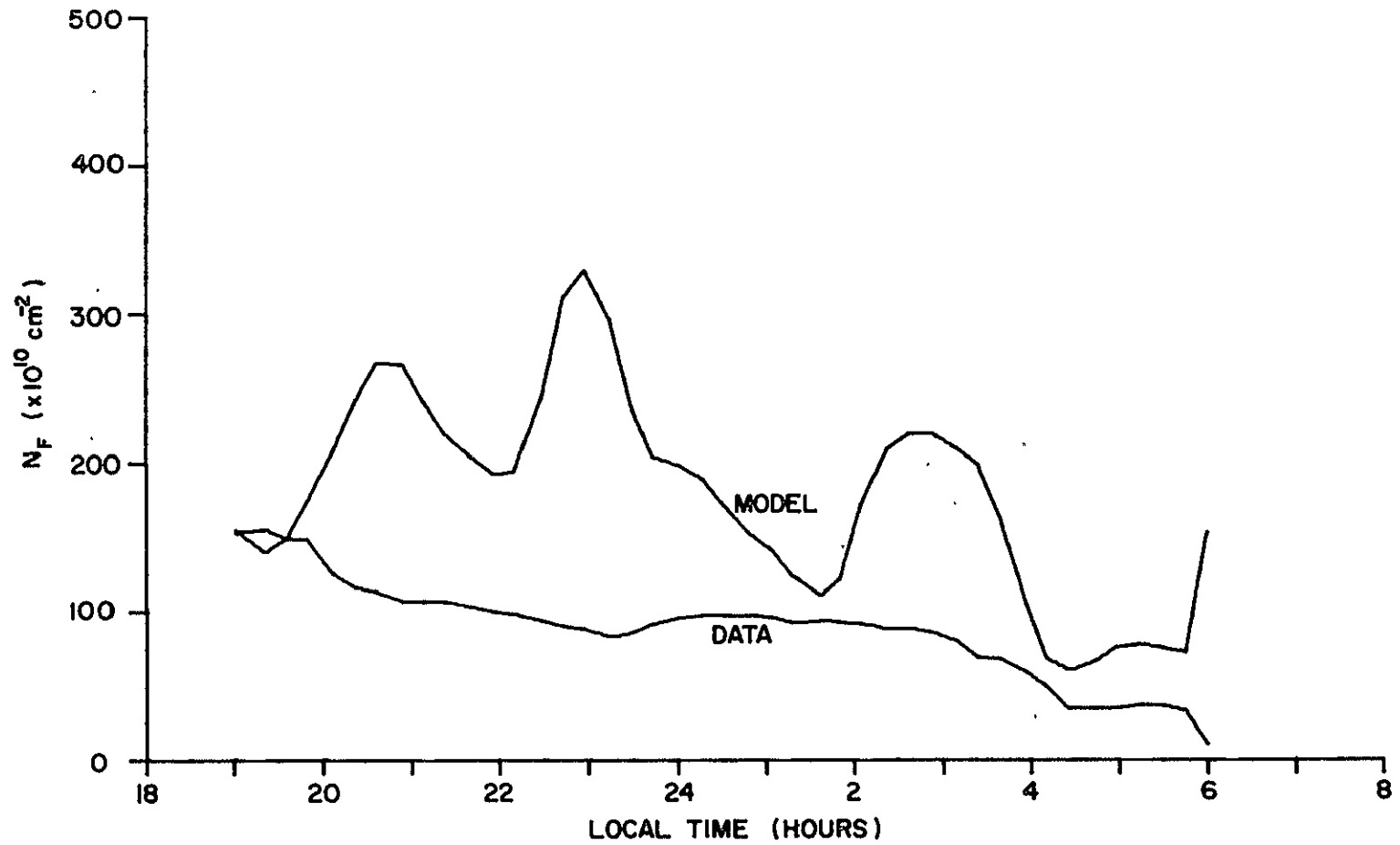


Figure 24: Time variation of N_F obtained from the data, and the solution of Equation 3.8 including recombination and the flux.

NOVEMBER 9, 1974

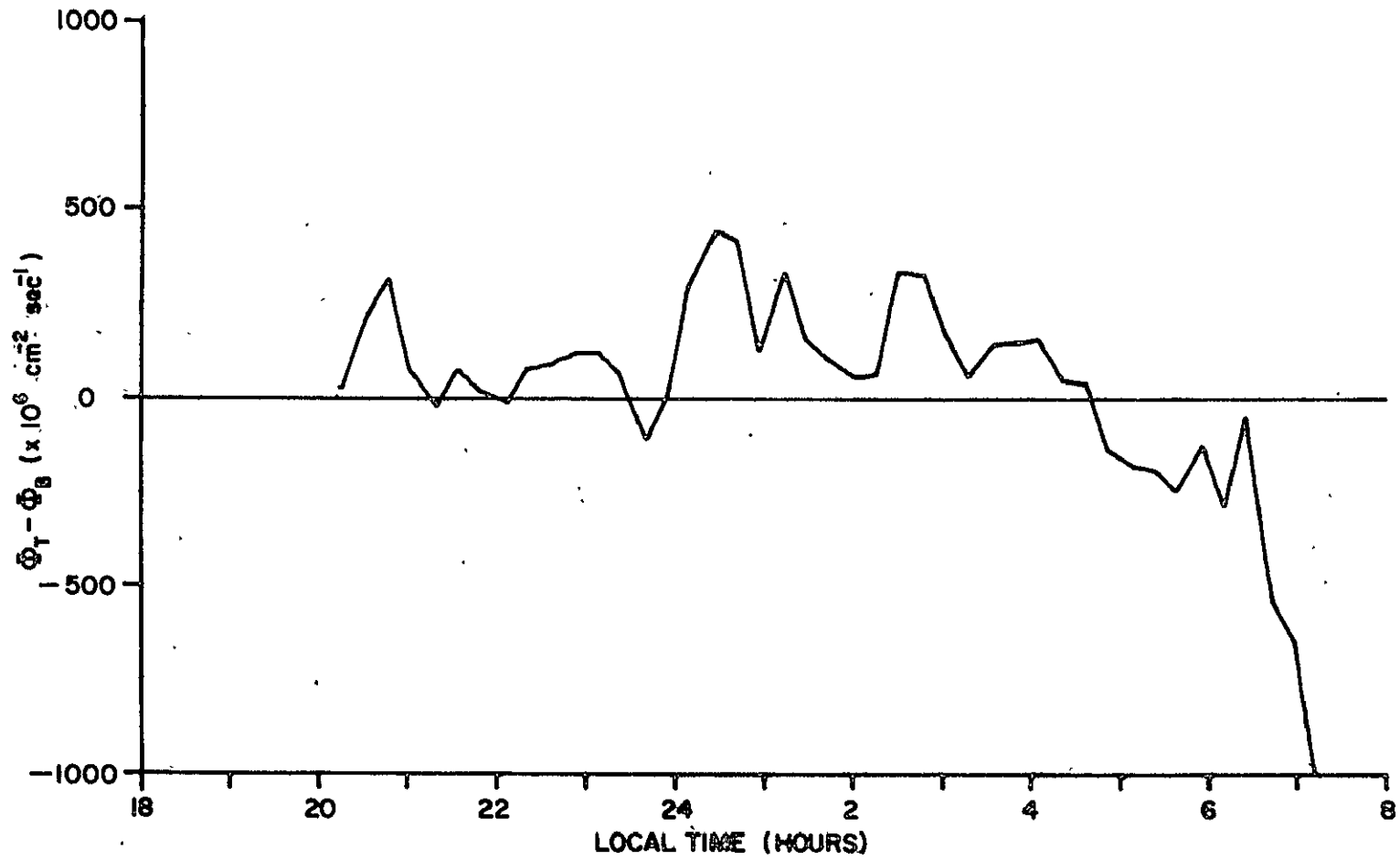


Figure 25: Time variation of the net flux (peak-centered boundaries).

NOVEMBER 9, 1974
RECOMBINATION ADDED

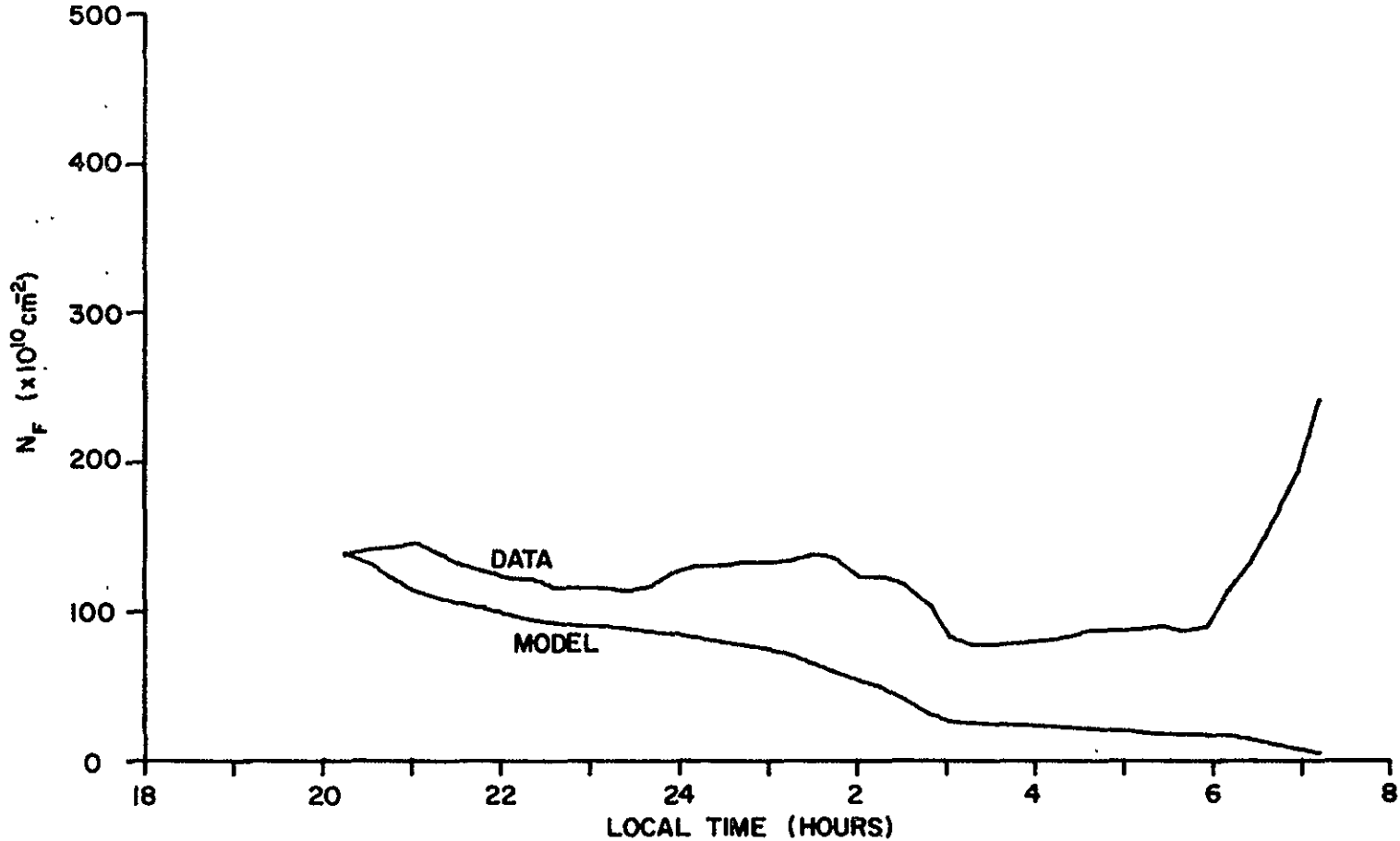


Figure 26: Time variation of N_F obtained from the data, and the solution of Equation 3.8 including recombination only.

NOVEMBER 9, 1974
FLUXES ADDED

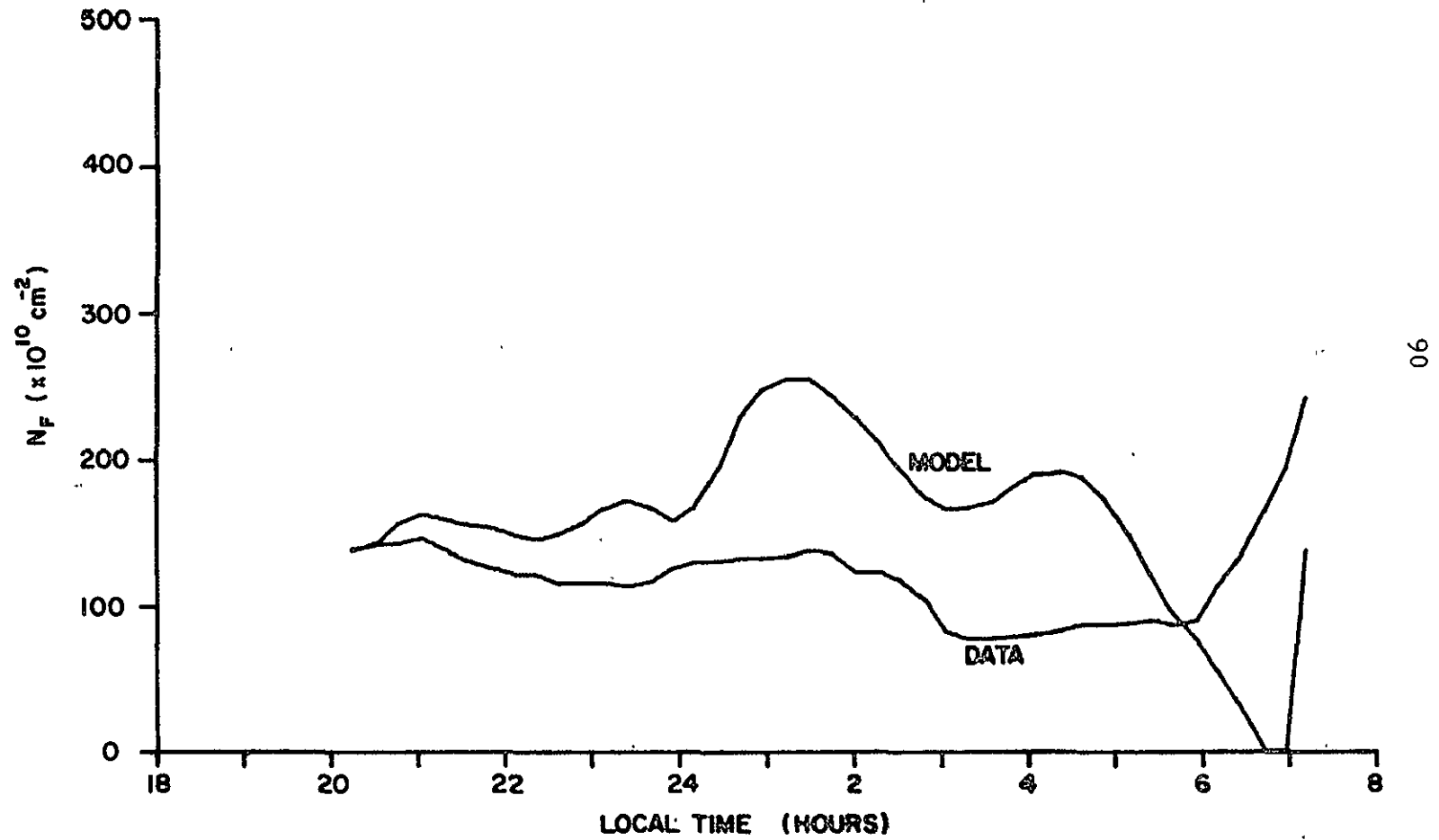


Figure 27: Time variation of N_F obtained from the data, and the solution of Equation 3.8 including recombination and the flux.

MAY 18, 1975

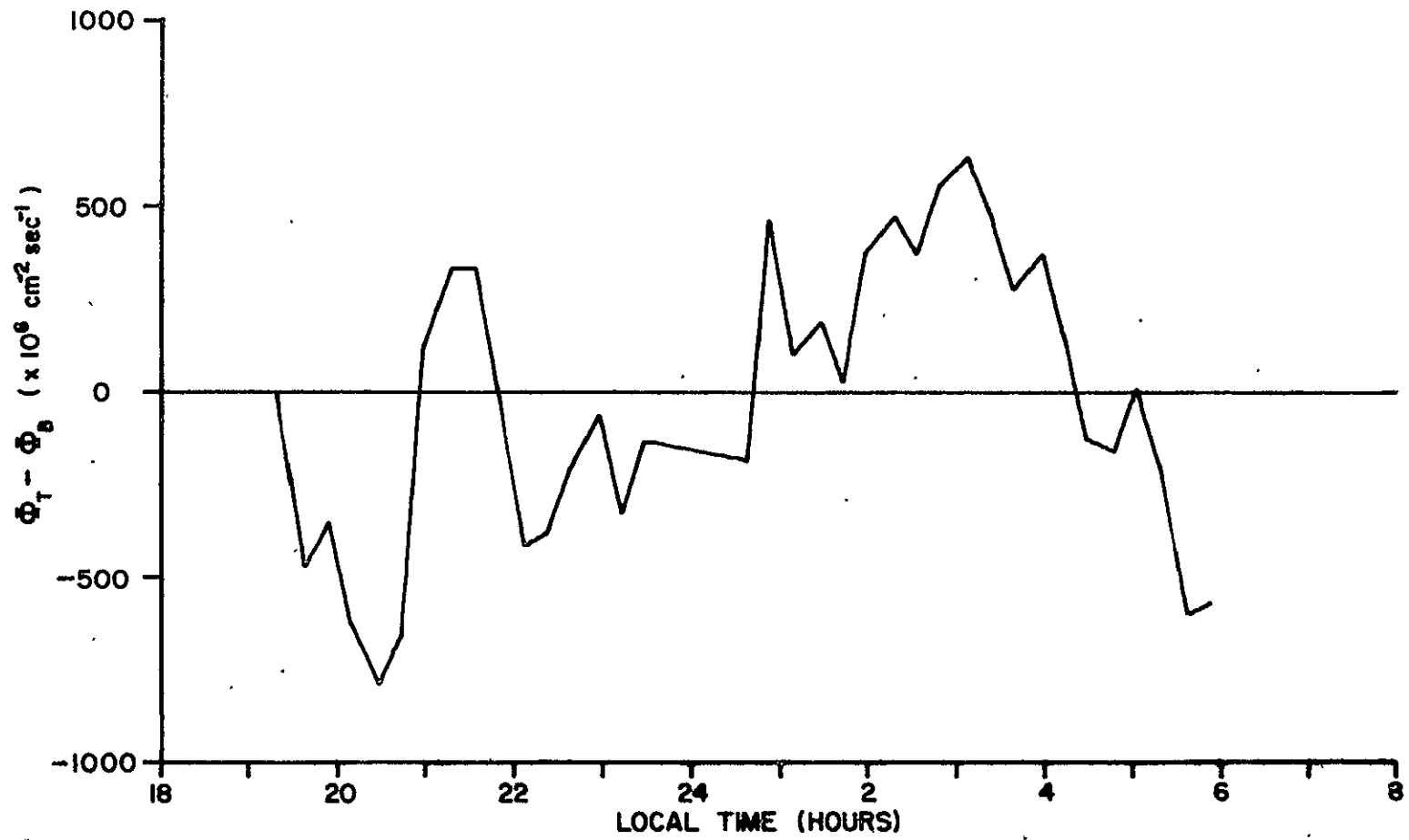


Figure 28: Time variation of the net flux (peak-centered boundaries).

MAY 18, 1975
RECOMBINATION ADDED

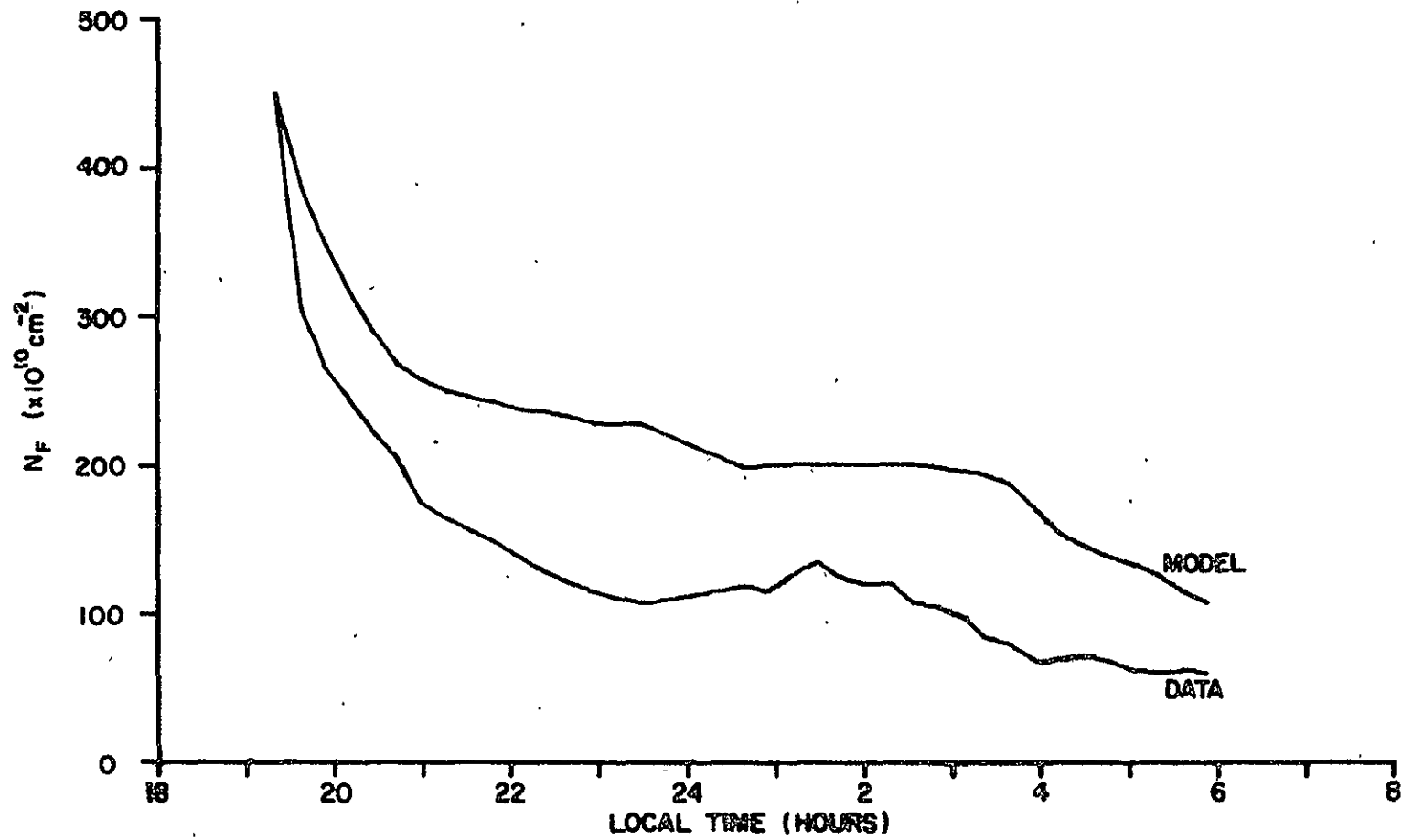


Figure 29: Time variation of N_F obtained from the data, and the solution of Equation 3.8 including recombination only.

MAY 18, 1975
FLUXES ADDED

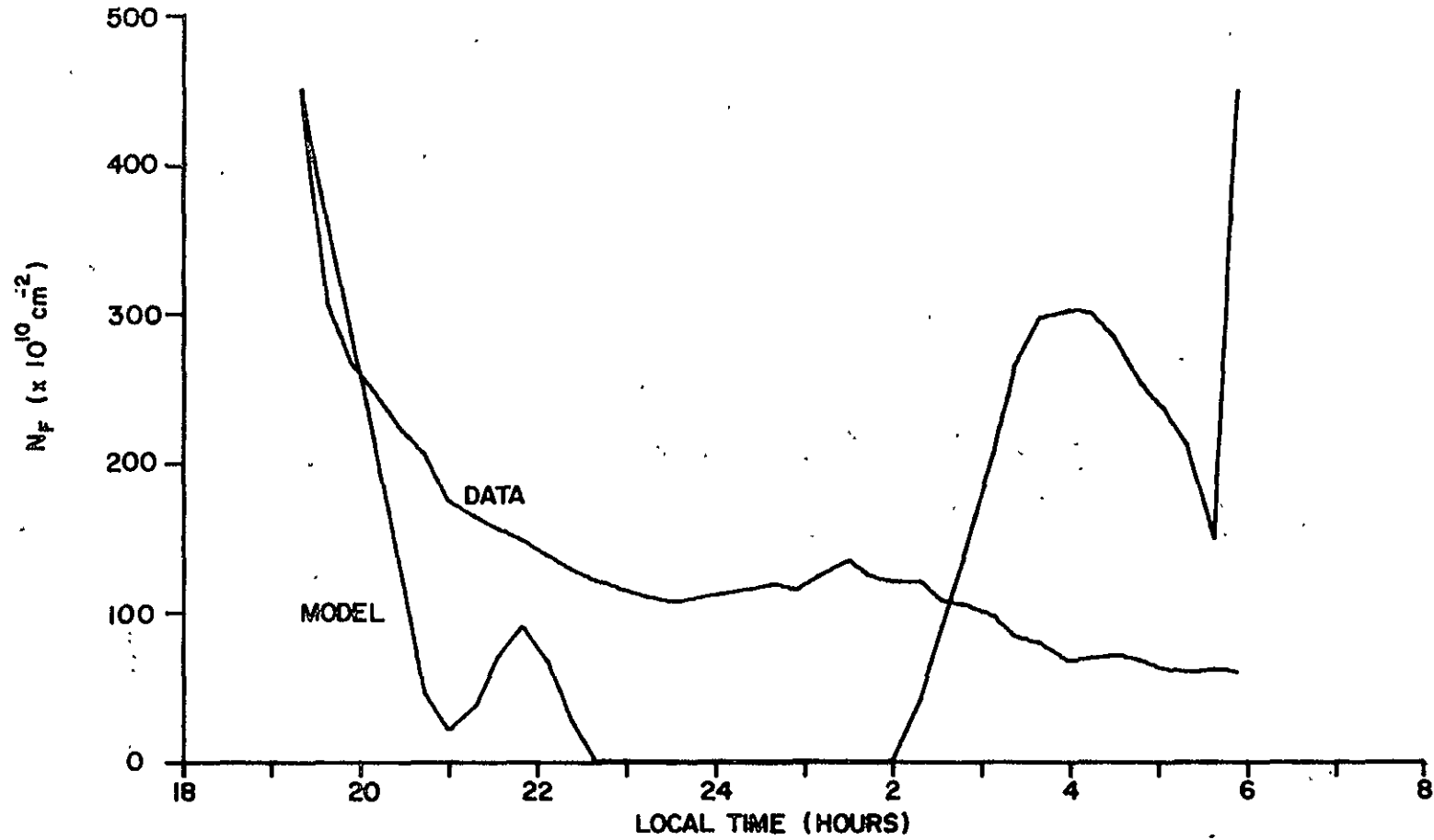
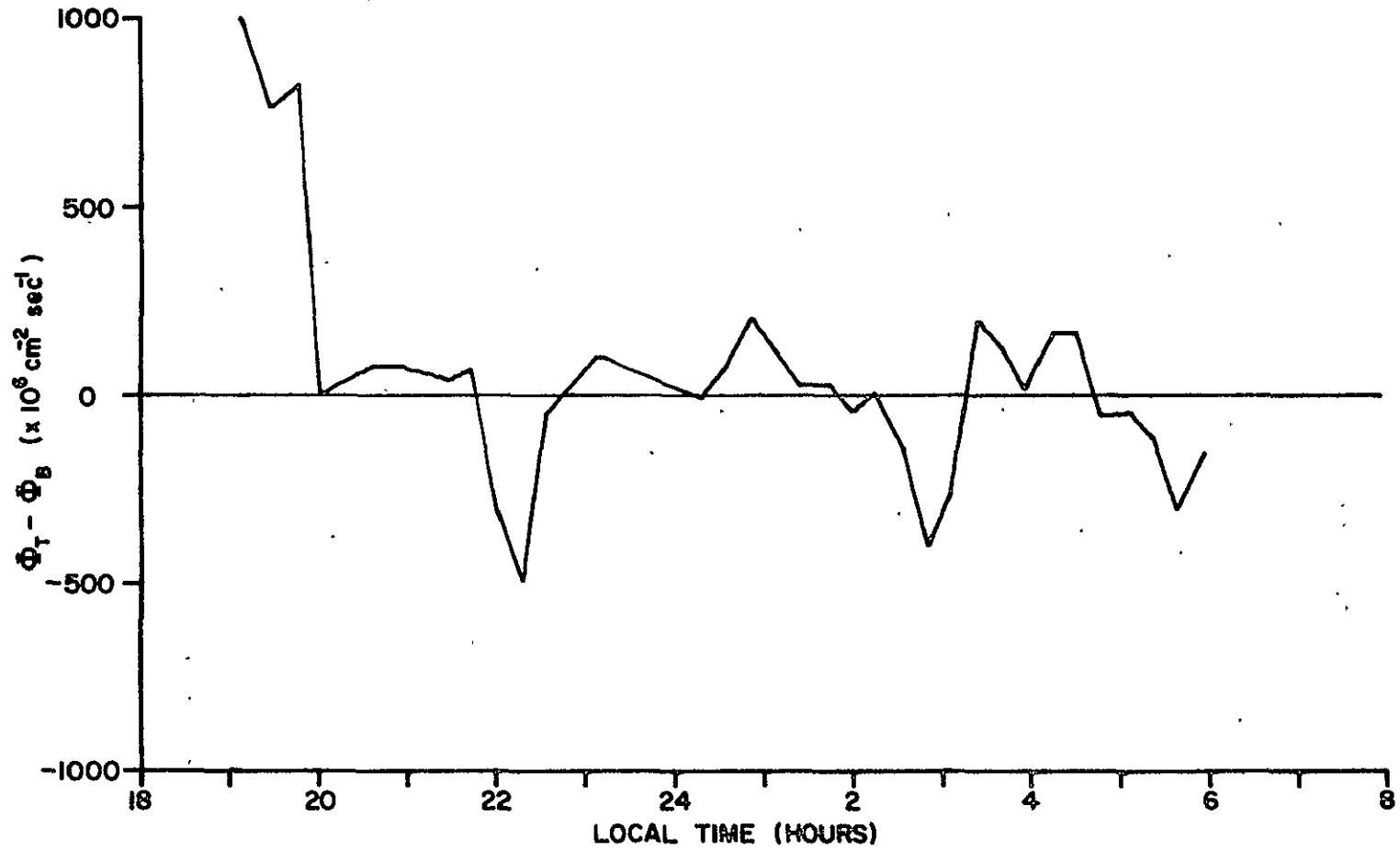


Figure 30: Time variation of N_F obtained from the data, and the solution of Equation 3.8 including recombination and the flux...

OCTOBER 14, 1975



94

Figure 31: Time variation of the net flux (peak-centered boundaries).

OCTOBER 14, 1975
RECOMBINATION ADDED

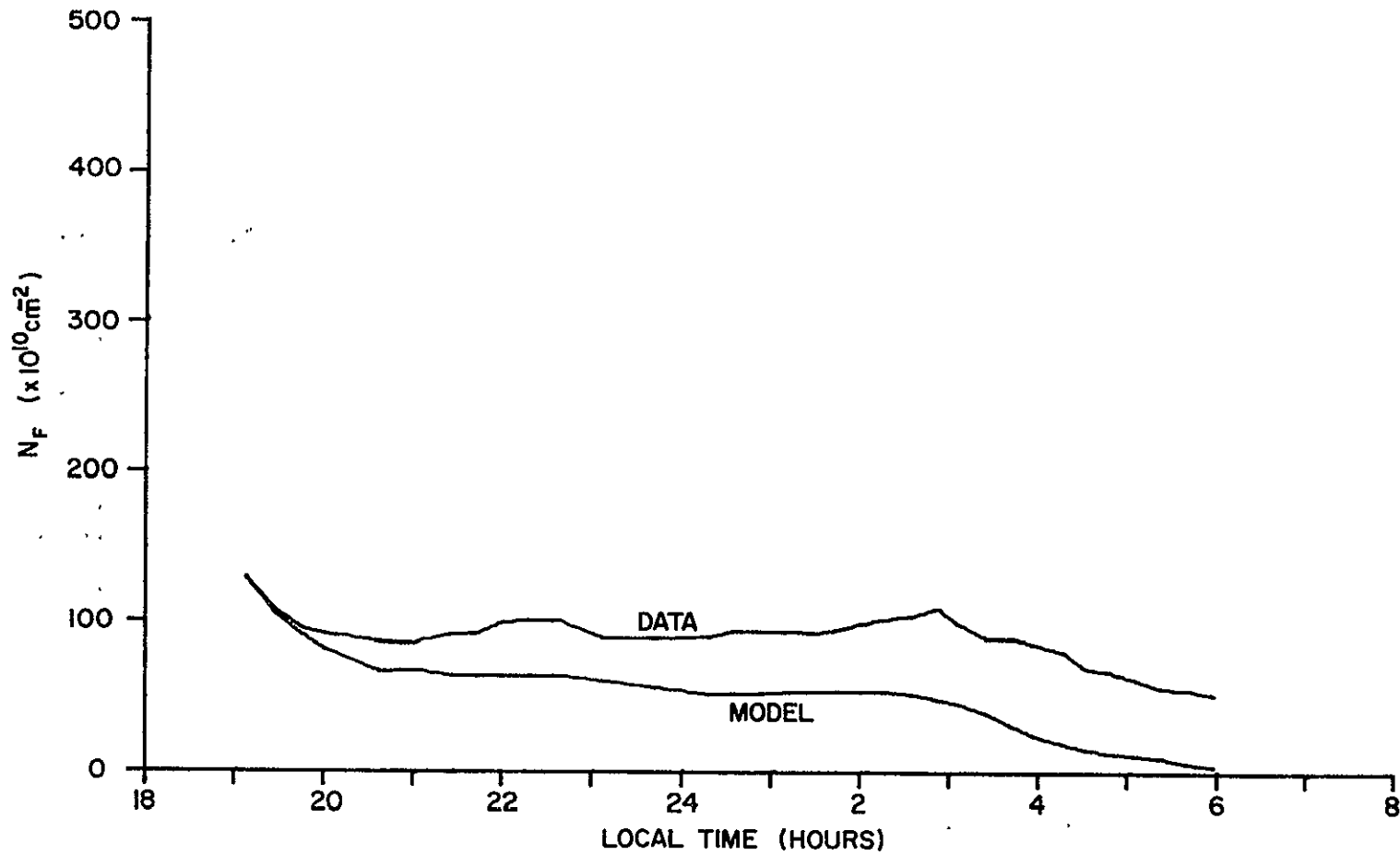


Figure 32: Time variation of N_F obtained from the data, and the solution of Equation 3.8 including recombination only.

OCTOBER 14, 1975
FLUXES ADDED

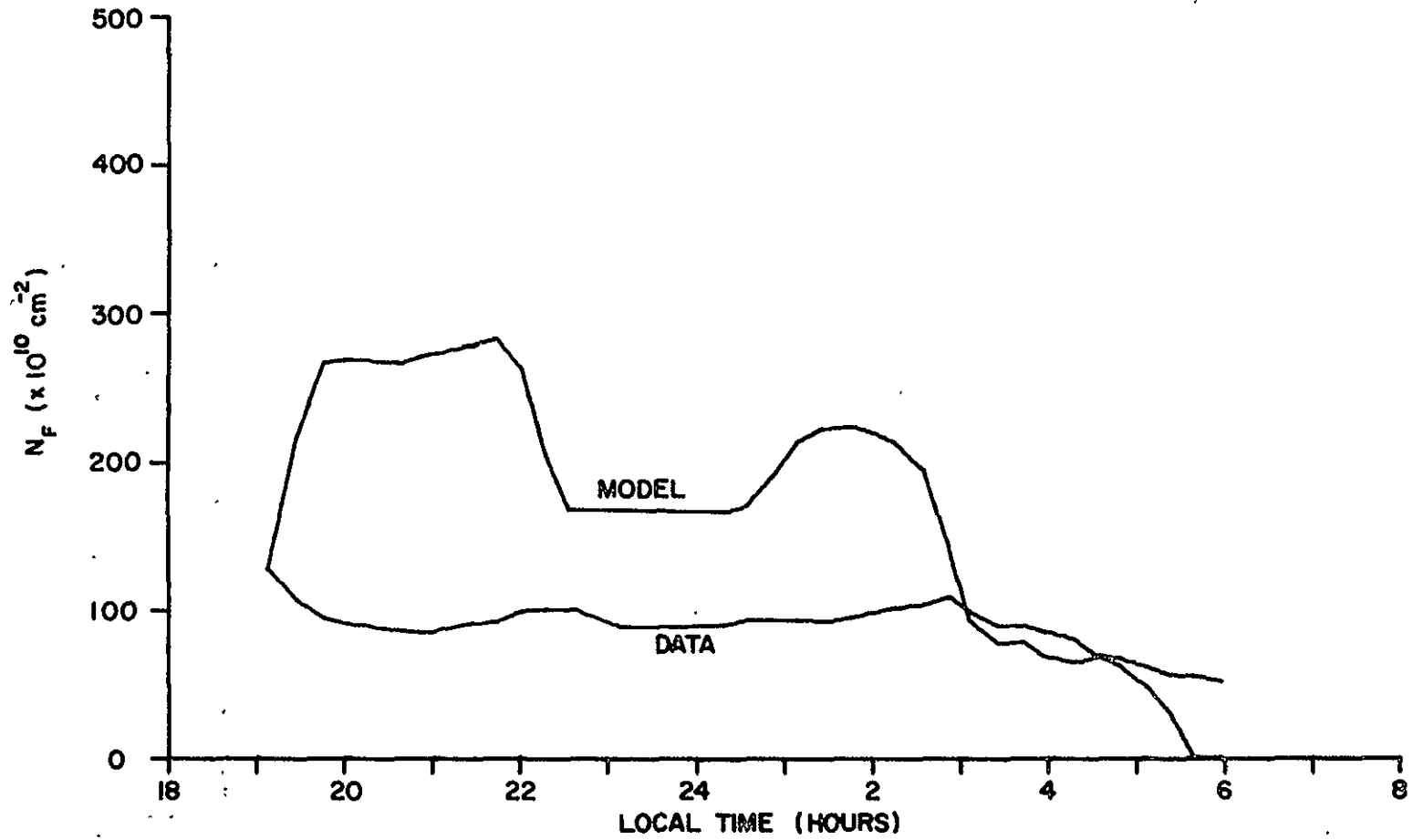


Figure 33: Time variation of N_F obtained from the data, and the solution of Equation 3.8 including recombination and the flux.

the electric field, neutral wind, and gravity terms, then adding recombination, then the diffusion term, and finally the flux terms. The results for September 17, 1974 are shown in Figures 34-37 and compared with the actual values of Σ_F calculated by the data. It is noted that the flat regions merely mean the solution is off the chosen scale for the plot. It is evident that recombination is important when the layer is low, and that the addition of the diffusion term helps the model slightly. The addition of the fluxes to the model again causes it to break down, except right at the beginning.

The other nights show similar behavior, as shown in Figures 38-43. The one exception is the May night, when the addition of the fluxes did not hurt the model greatly.

The issue of why the flux data, which have been assumed by most researchers to be accurate at Arecibo, do not agree with the rest of the data is a very important one. It will be examined in the next section.

The Perkins model of F_s assumes a quasi-equilibrium in which the time scale of the change in the equilibrium integrated Pedersen conductivity is much longer than the time scale of the development of F_s . As has been shown, the equilibrium value of the field integrated Pedersen conductivity changes rapidly through the night. To test the assumption that there is a quasi-equilibrium, the Perkins equilibrium condition (Equation 2.12) is used to obtain the equilibrium value of Σ_F . The results are shown in Figures 44-47 where the "model" solution includes only E_{RES} . This is consistent

SEPTEMBER 17, 1974
E_{RES} γ ONLY

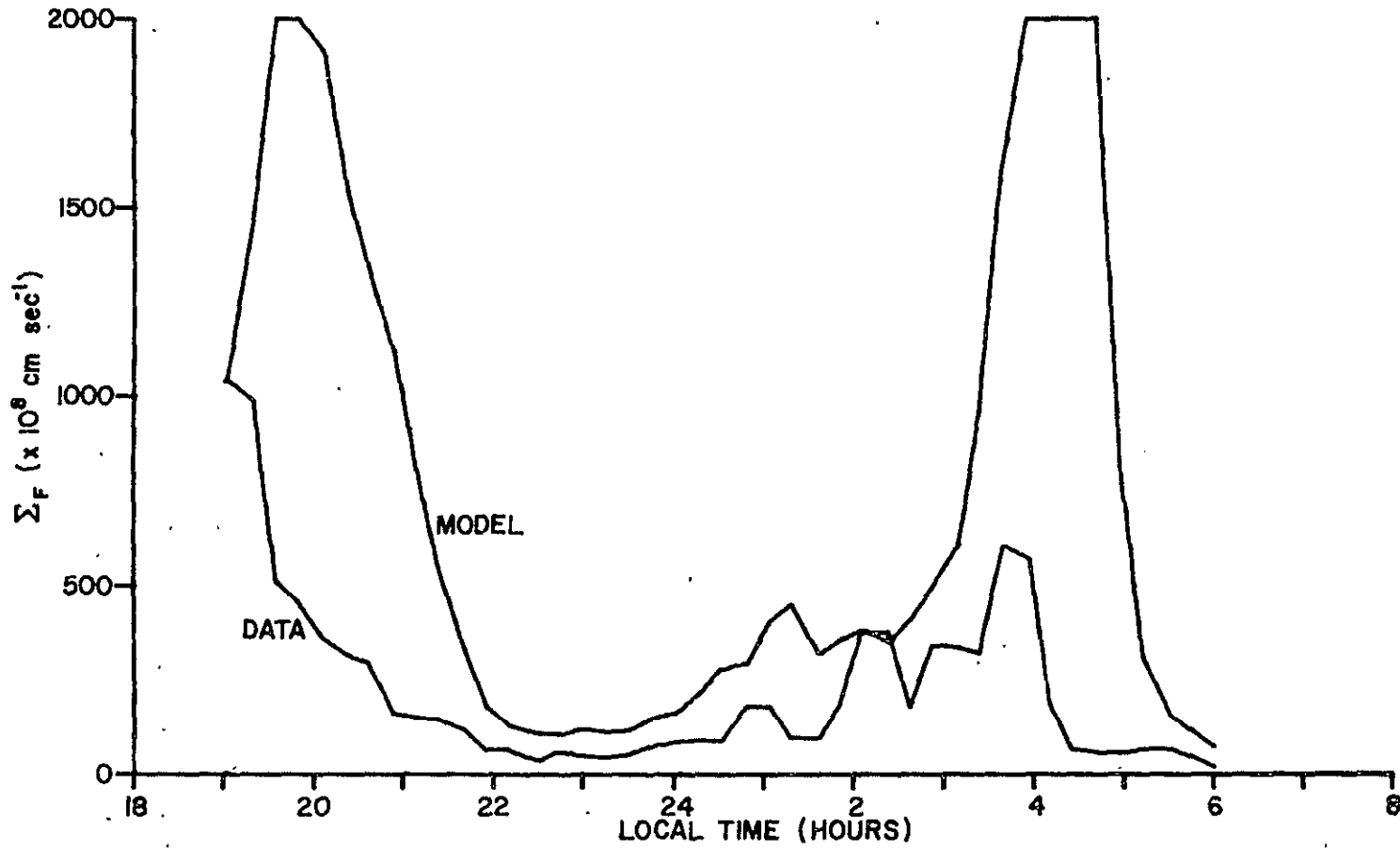


Figure 34: Time variation of Σ_F obtained from the data, and the solution of Equation 3.10 including E_{RESY} and gravity only.

SEPTEMBER 17, 1974
RECOMBINATION ADDED

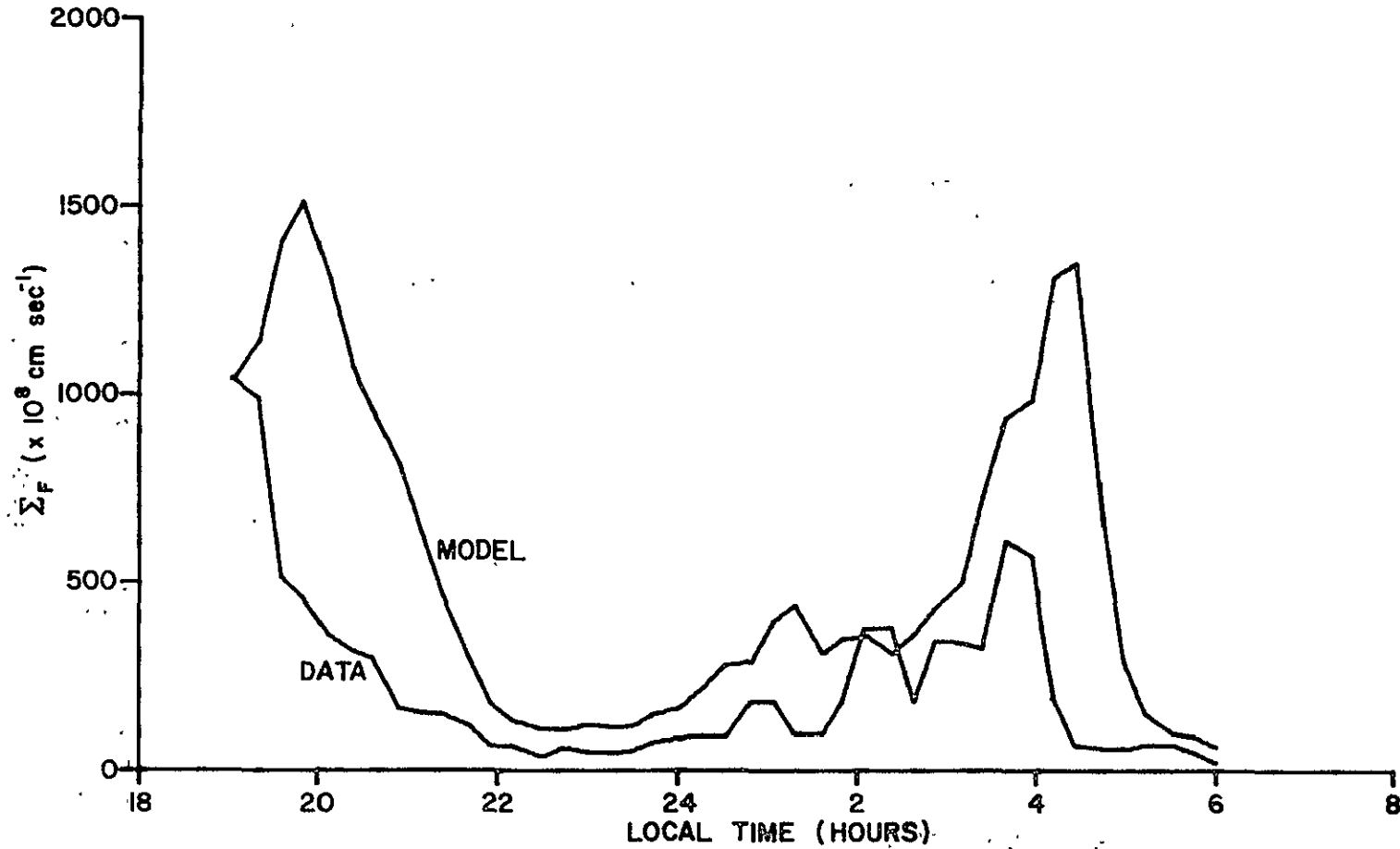


Figure 35: Time variation of Σ_F , obtained from the data, and the solution of Equation 3.10 including E_{RES} , gravity and recombination.

SEPTEMBER 17, 1974
DIFFUSION ADDED

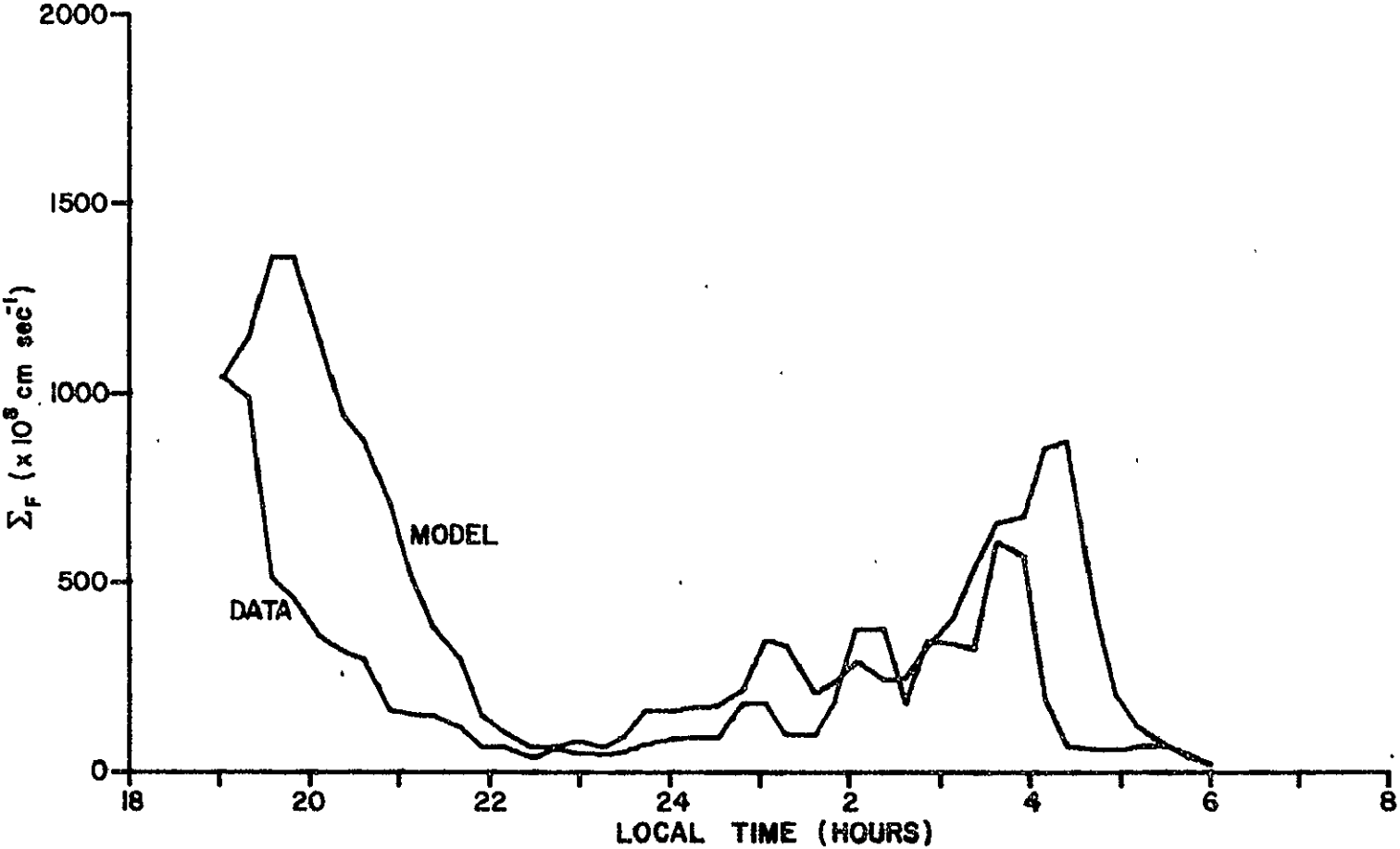


Figure 36: Time variation of Σ_F obtained from the data, and the solution of Equation 3.10 including E_{RES} , gravity, recombination and diffusion.

SEPTEMBER 17, 1974
FLUXES ADDED

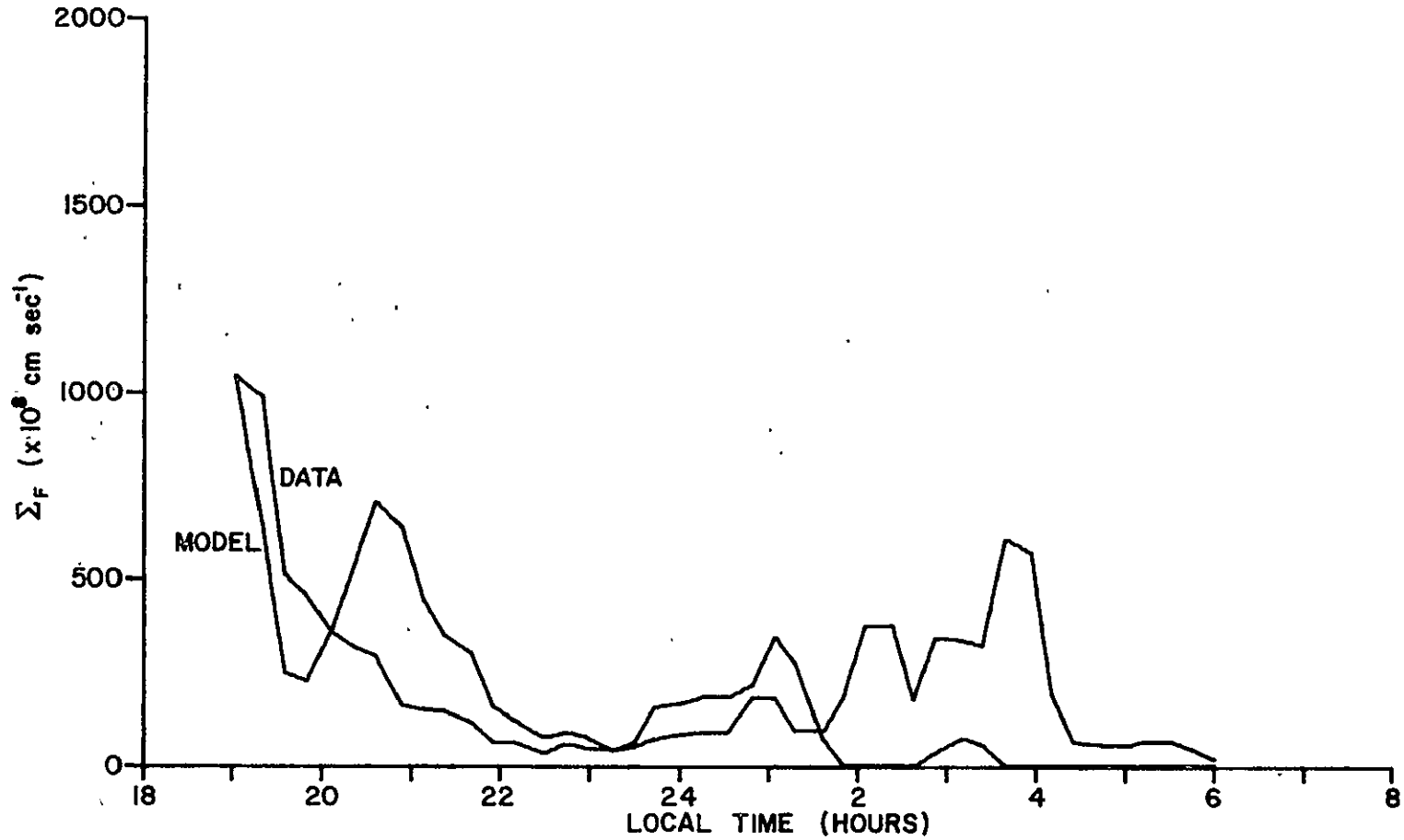


Figure 37: Time variation of Σ_F obtained from the data, and the solution of Equation 3.10 including E_{RES} , gravity recombination, diffusion and the flux.

NOVEMBER 9, 1974
DIFFUSION ADDED

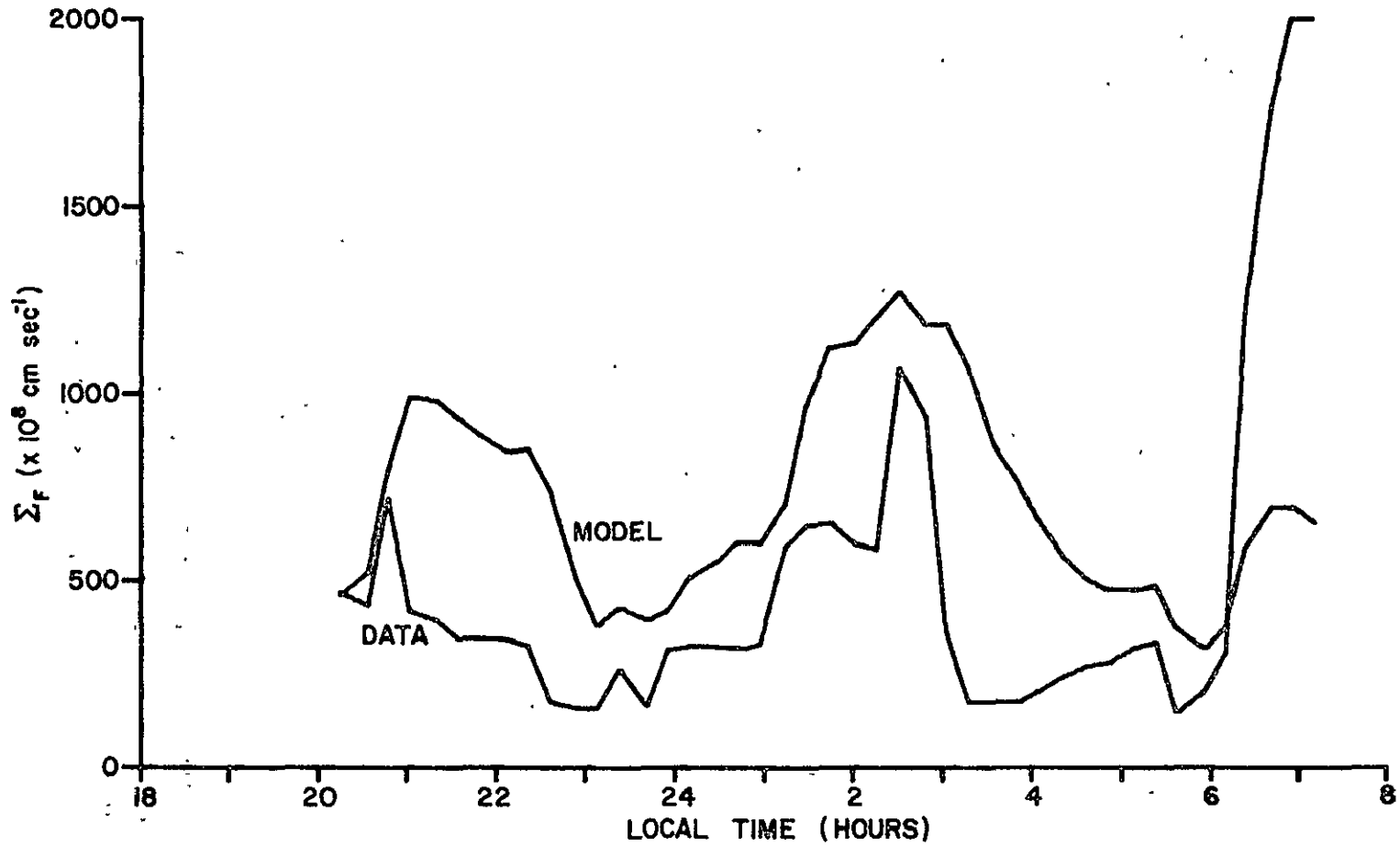


Figure 38: Time variation of Σ_F obtained from the data, and the solution of Equation 3.10 including E_{RES} , gravity, recombination and diffusion.

NOVEMBER 9, 1974
FLUXES ADDED

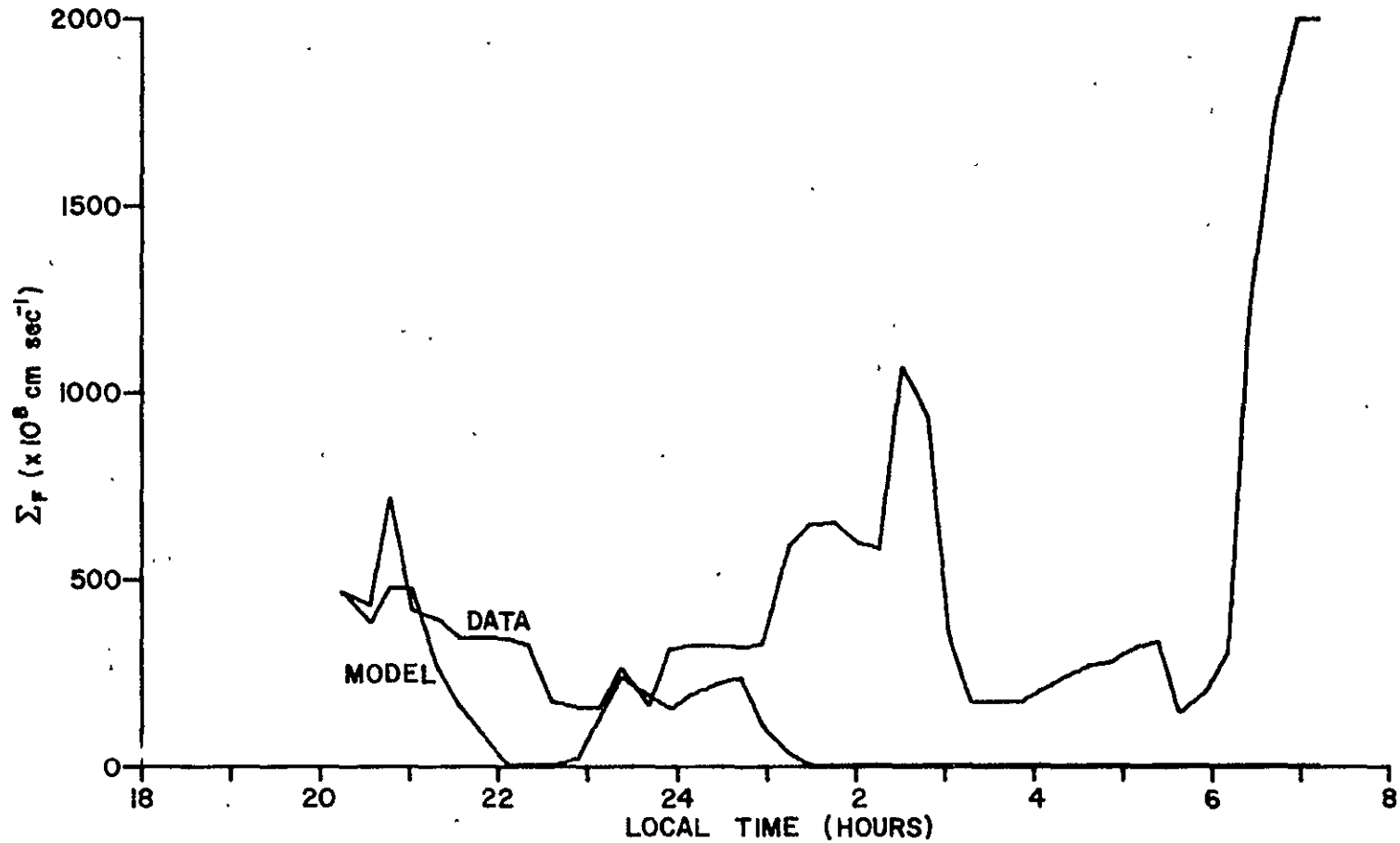
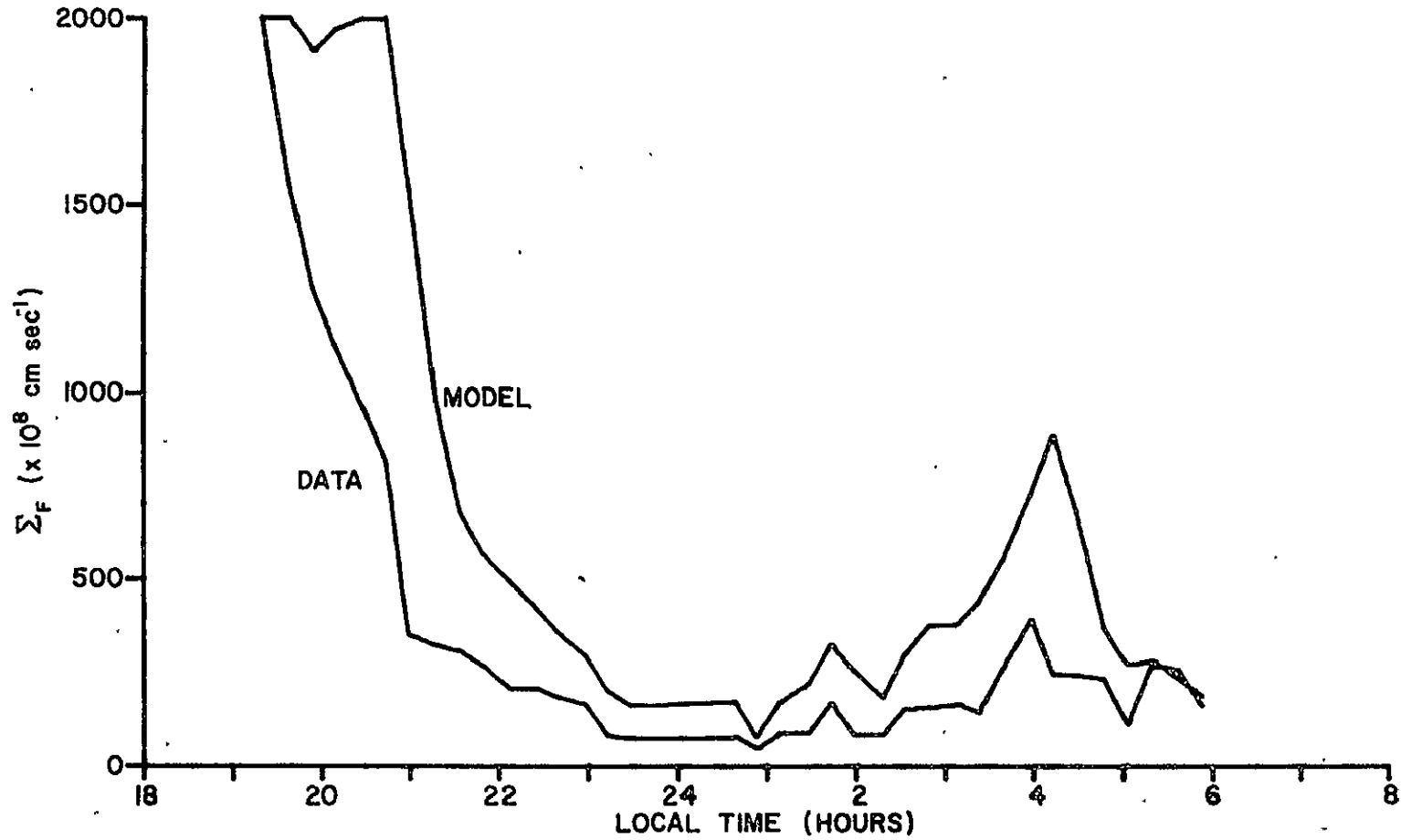


Figure 39: Time variation of Σ_F obtained from the data, and the solution of Equation 3.10 including E_{RES} , gravity, recombination, diffusion and the flux.

MAY 18, 1975
DIFFUSION ADDED



104

Figure 40: Time variation of Σ_F obtained from the data, and the solution of Equation 3.10 including E_{RES} , gravity, recombination and diffusion.

MAY 18, 1975
FLUXES ADDED

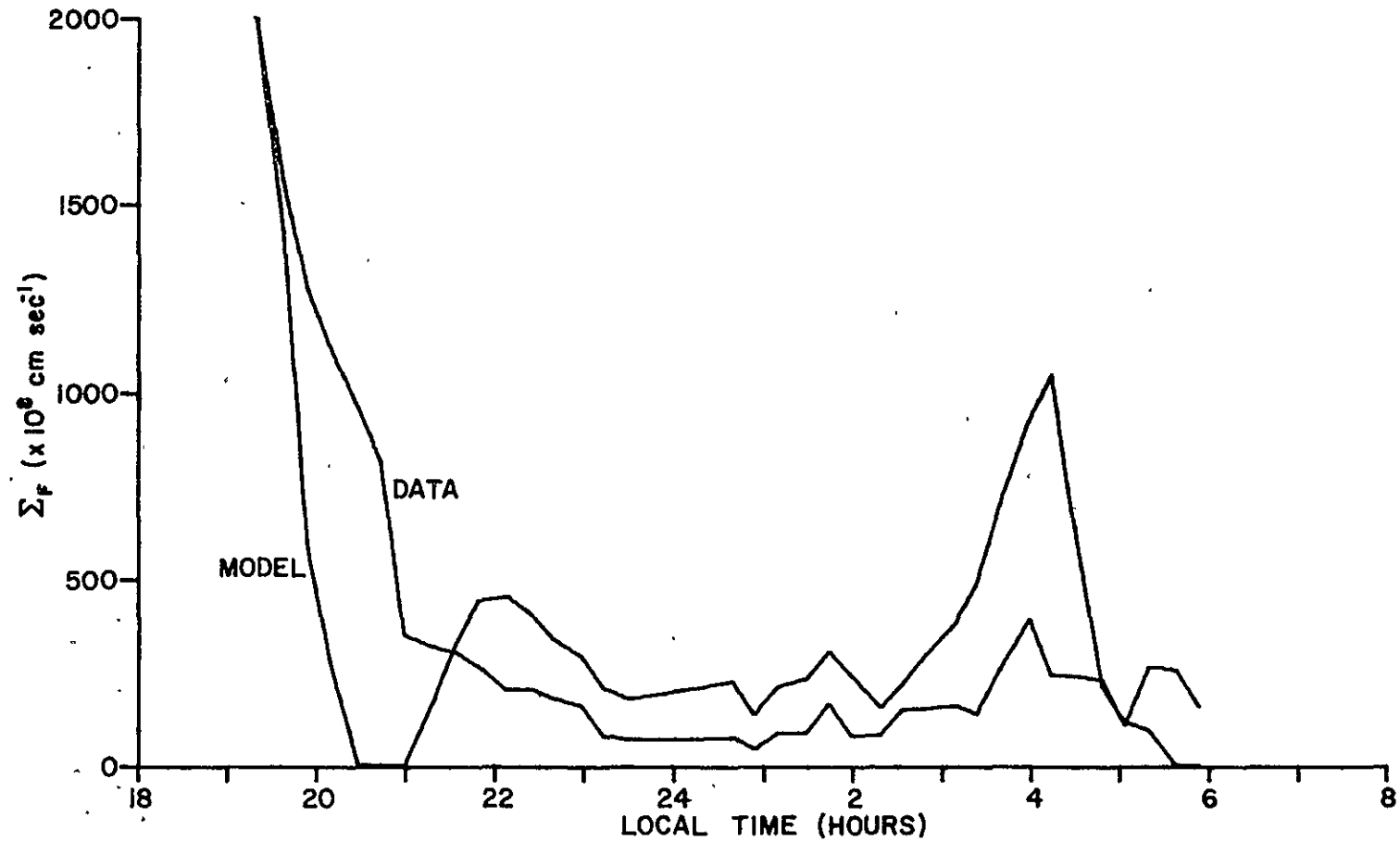


Figure 41: Time variation of Σ_F obtained from the data, and the solution of Equation 3.10 including E_{RES} , gravity, recombination, diffusion and the flux.

OCTOBER 14, 1975
DIFFUSION ADDED

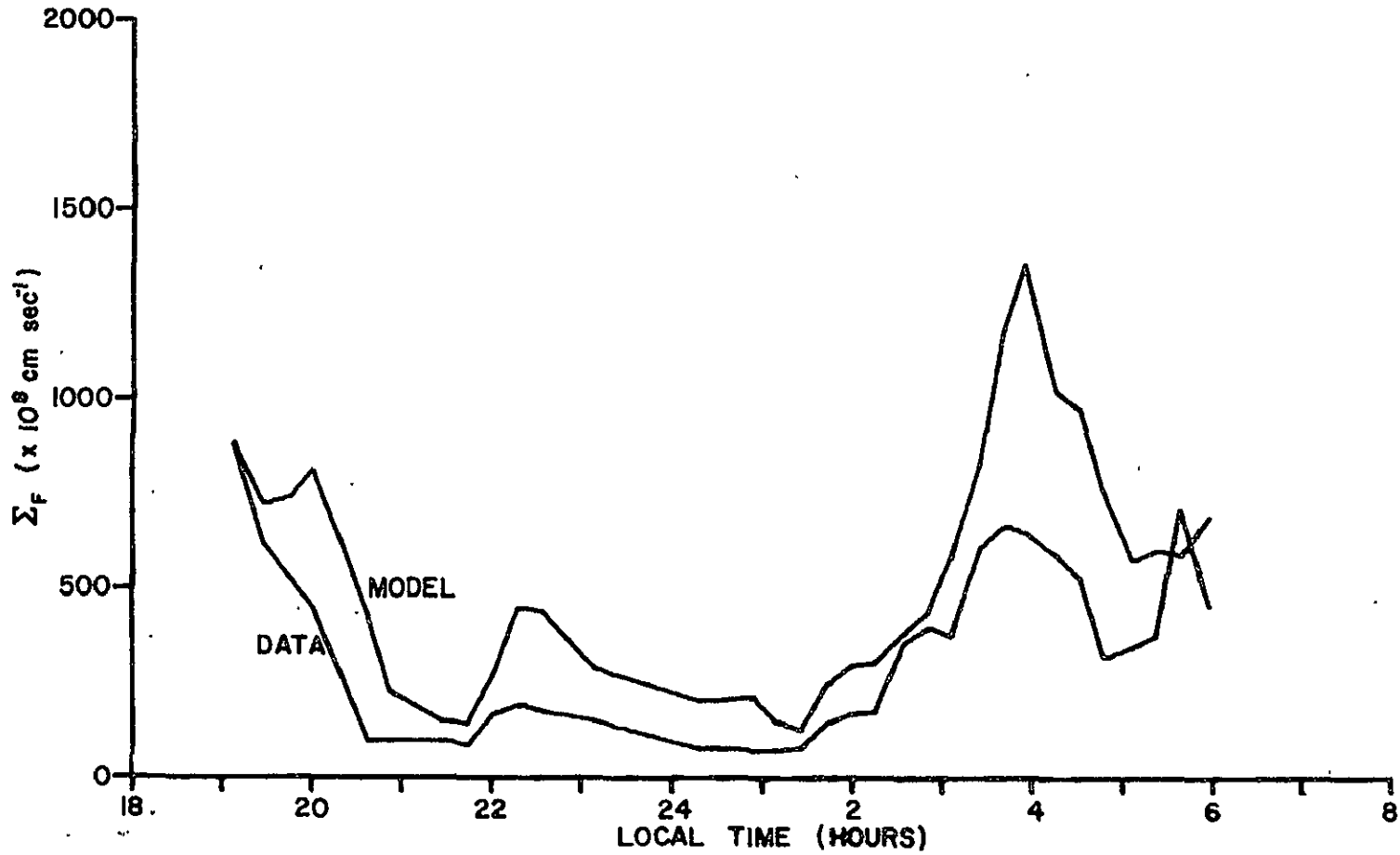


Figure 42. Time variation of Σ_F obtained from the data, and the solution of Equation 3.10 including E_{RES} , gravity, recombination and diffusion.

OCTOBER 14, 1975
FLUXES ADDED

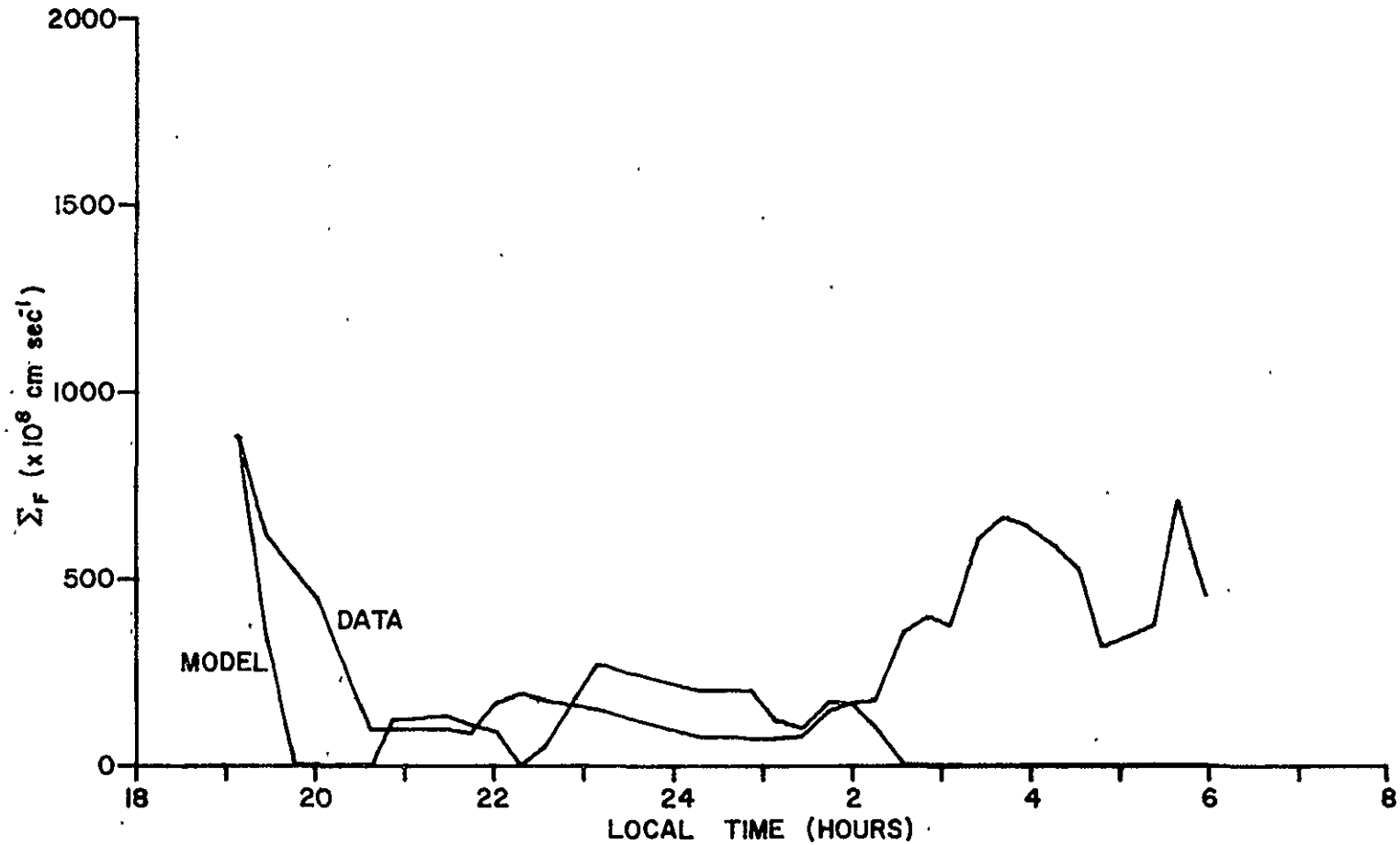


Figure 43: Time variation of Σ_F obtained from the data, and the solution of Equation 3.10 including E_{RES} , gravity, recombination, diffusion and the flux.

SEPTEMBER 17, 1974

E_{RES} ONLY

XXX QUASIEQUILIBRIUM

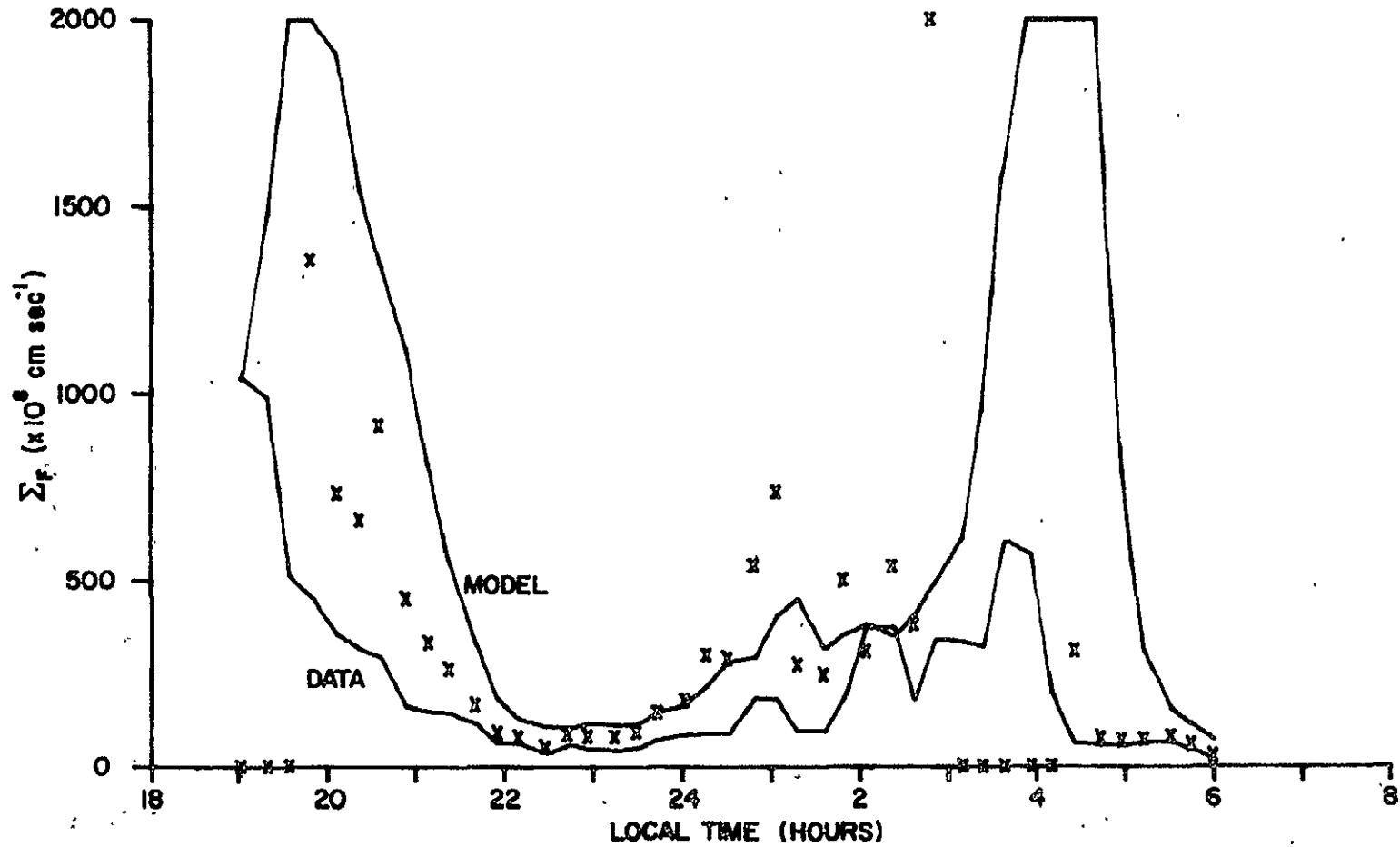


Figure 44: Time variation of Σ_F obtained from the data, the solution of Equation 3.10 including E_{RES} and gravity, and the quasi-equilibrium solution of the Perkins model (Equation 2.12).

NOVEMBER 9, 1974
E_{RES} ONLY
X X X QUASIEQUILIBRIUM

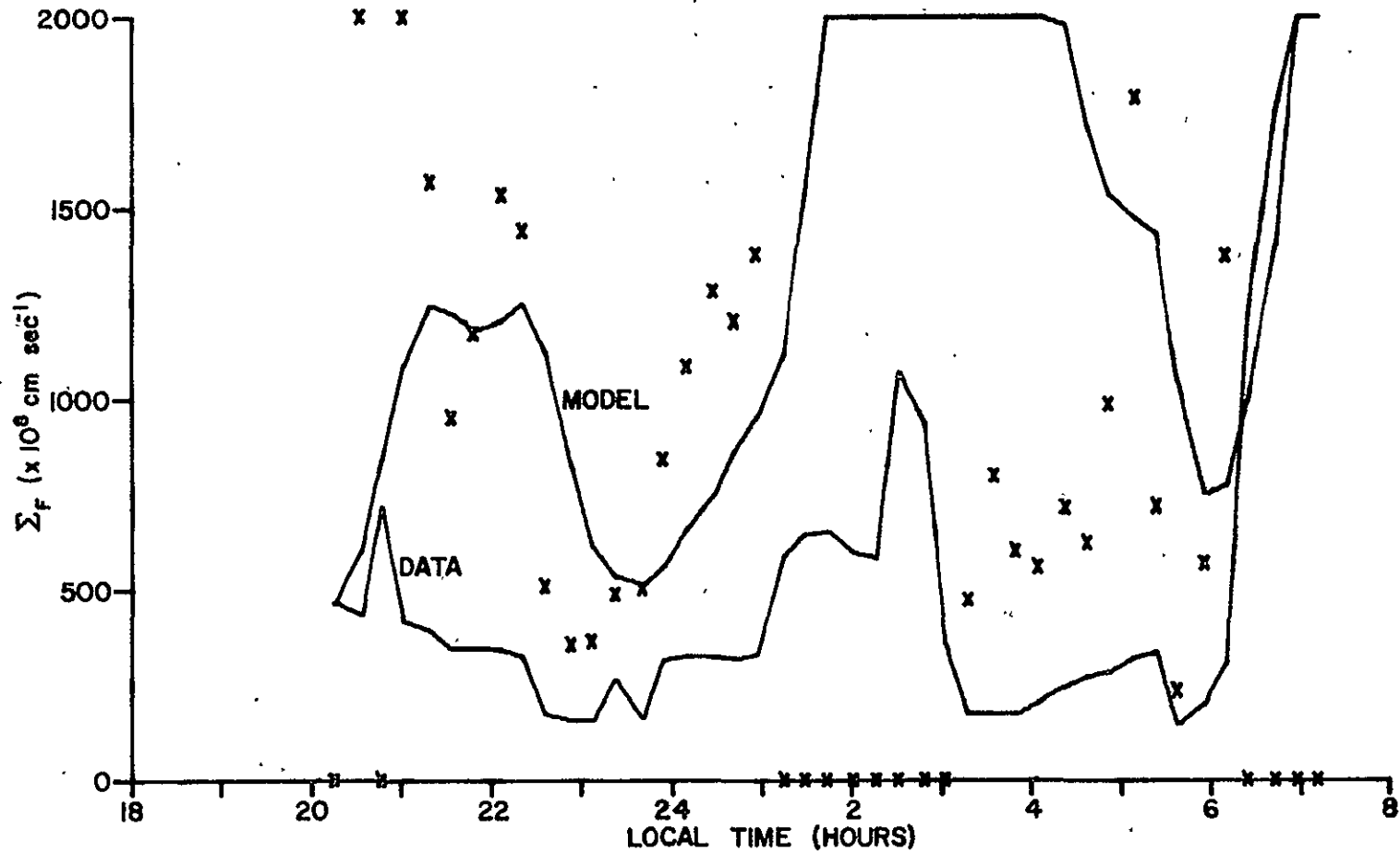


Figure 45: Time variation of Σ_F obtained from the data, the solution of Equation 3.10 including E_{RES} and gravity, and the quasi-equilibrium solution of the Perkins model (Equation 2.12).

MAY 18, 1975
E_{RES} ONLY
XXX QUASIEQUILIBRIUM

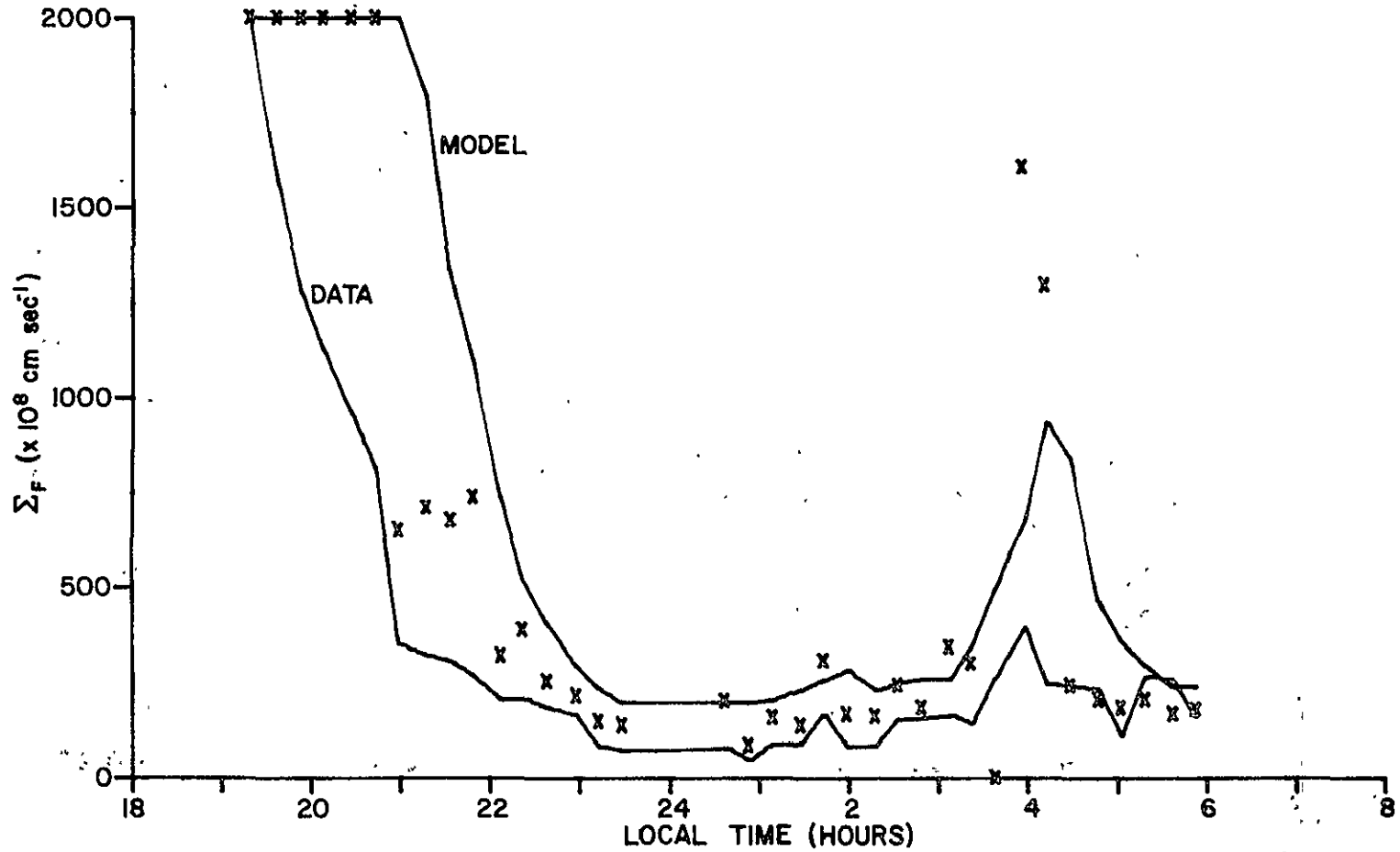


Figure 46: Time variation of Σ_F obtained from the data, the solution of Equation 3.10 including E_{RES} and gravity, and the quasi-equilibrium solution of the Perkins model (Equation 2.12):

OCTOBER 14, 1975
 E_{RES} ONLY
 X X X QUASIEQUILIBRIUM

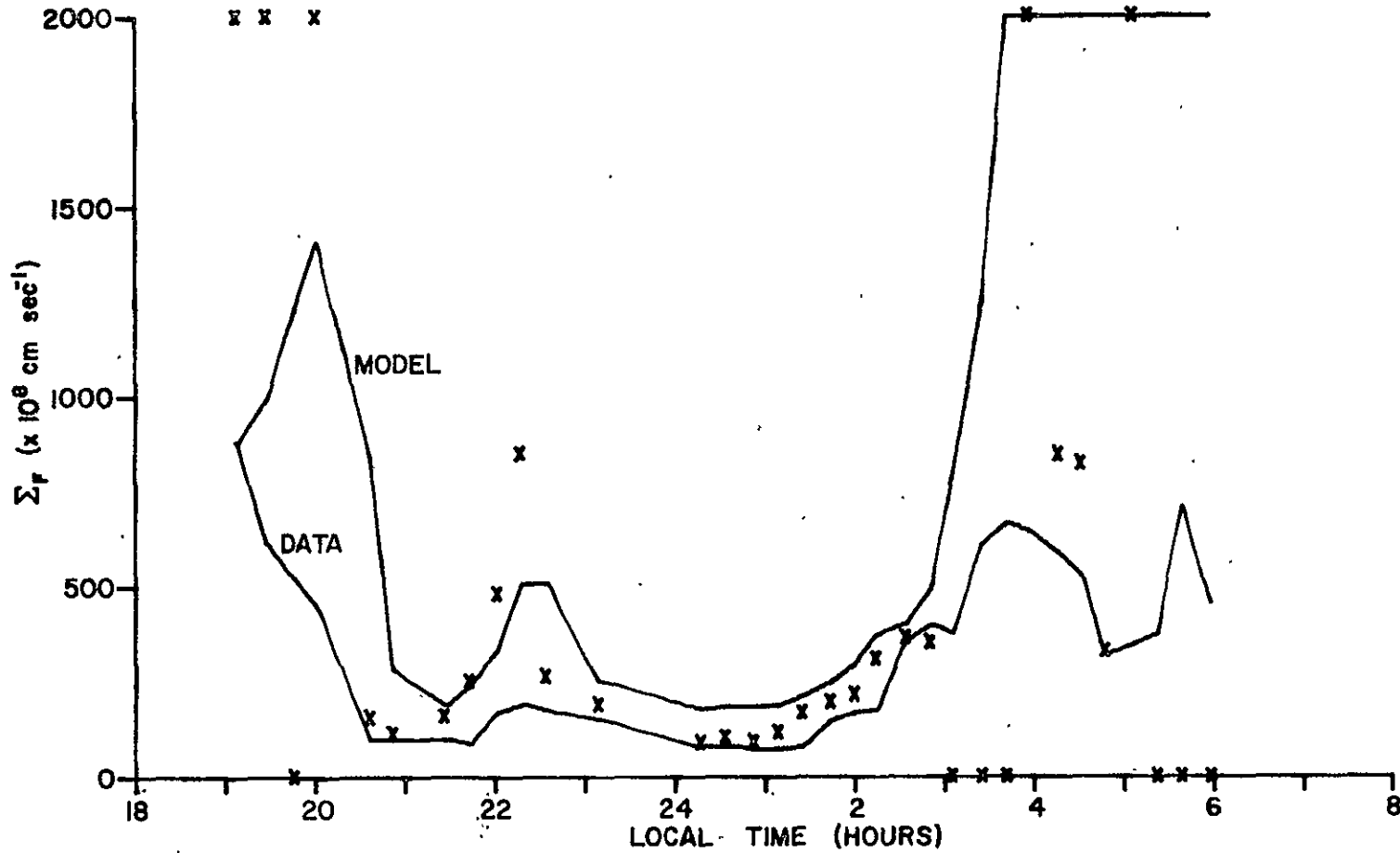


Figure 47: Time variation of Σ_F obtained from the data, the solution of Equation 3.10 including E_{RES} and gravity, and the quasi-equilibrium solution of the Perkins model (Equation 2.12).

with Perkins. It is seen that the agreement is reasonably good for the September, May and October nights, especially when the layer is high. The quasi-equilibrium predicted by the Perkins model is not good at all for the November night. Curiously, this is a night without F_s and with rather smooth behavior of the equilibrium parameters.

The assumption of a quasi-equilibrium is really a comparison of time scales:

$$\frac{1}{\Sigma_o} \frac{\partial \Sigma_o}{\partial t} \ll \gamma$$

where γ is the growth rate of F_s . Around the onset time for the September night (2150),

$$\frac{1}{\Sigma_o} \frac{\partial \Sigma_o}{\partial t} \approx \frac{1}{3600} \text{ sec}^{-1}.$$

The time scale for the development of F_s is assumed to be from 10 minutes to 30 minutes, so the assumption of a quasi-equilibrium is indeed a good one. For the May night, Σ_F is decreasing quite rapidly around onset. The quasi-equilibrium predicted by the Perkins model is not close to the actual value.

It is the conclusion of this analysis that great care must be taken when a quasi-equilibrium of the form in the Perkins model is chosen. It is a fairly good assumption on some nights, but on others it is not.

3.5 Fluxes and Gradients

A great deal has been written so far about the disagreement between the flux data and the rest of the data. The degree of disagreement will be demonstrated in this section, and some alternate explanations proposed.

One can solve for the flux required to give agreement with the rest of the data by solving Equations 3.8 and 3.10 simultaneously, in the following manner:

$$\Phi_T - \Phi_B = A \quad (3.12)$$

$$(v_{in})_T \Phi_T - (v_{in})_B \Phi_B = C \quad (3.13)$$

The quantities A and C are found from Equations 3.8 and 3.10:

$$A = \frac{\partial N_F}{\partial t} + \langle \beta \rangle N$$

$$C = \frac{\omega_{ci} B}{ec} \left[\frac{\partial \Sigma_F}{\partial t} + \frac{c}{B} \frac{\cos D}{H} E_{oy} \Sigma_F \right. \\ - \frac{ec}{\omega_{ci} B} \frac{g \sin^2 D}{H} N_F - \frac{\sin D}{H} V_{NZ} \Sigma_F \\ \left. - \frac{ec}{\omega_{ci} B} \frac{2T}{M} \frac{\sin D}{H} (n_T - n_B) + \bar{\beta} \Sigma_F \right]$$

The simultaneous solution of Equations (3.12) and (3.13) yields the required values of Φ_T and Φ_B :

$$\Phi_T = \frac{A v_B - C}{v_B - v_T}$$

$$\Phi_B = \frac{A v_T - C}{v_B - v_T}$$

The results of this calculation compared to the flux given by the data are shown in Figures 48-51 for two of the nights. It is immediately seen that the flux required is not even close to the flux given by the data. This result is hardly surprising based on previous attempts to use the flux data.

Much more informative are the results of the calculations of the net flux required to satisfy Equations 3.8 and 3.10 compared to the flux given by the data. This is shown in Figures 52-55. It is seen that the flux required to satisfy the N_F and Σ_F data are generally much lower than those given by the data. In addition, the required net flux does not exhibit the large amount of time variation that is seen in the flux calculated by the data.

An error analysis was performed on the flux data. It is seen from Figure 52 that the flux required and the flux from the data differ by a factor of 10 or greater for a large portion of the night. Assuming that the net flux required is on the order of 5×10^7 , while the net flux from the data is on the order of 5×10^8 , one would have to subtract an error of 4.5×10^8 to obtain agreement. The error analysis proceeds in the following way:

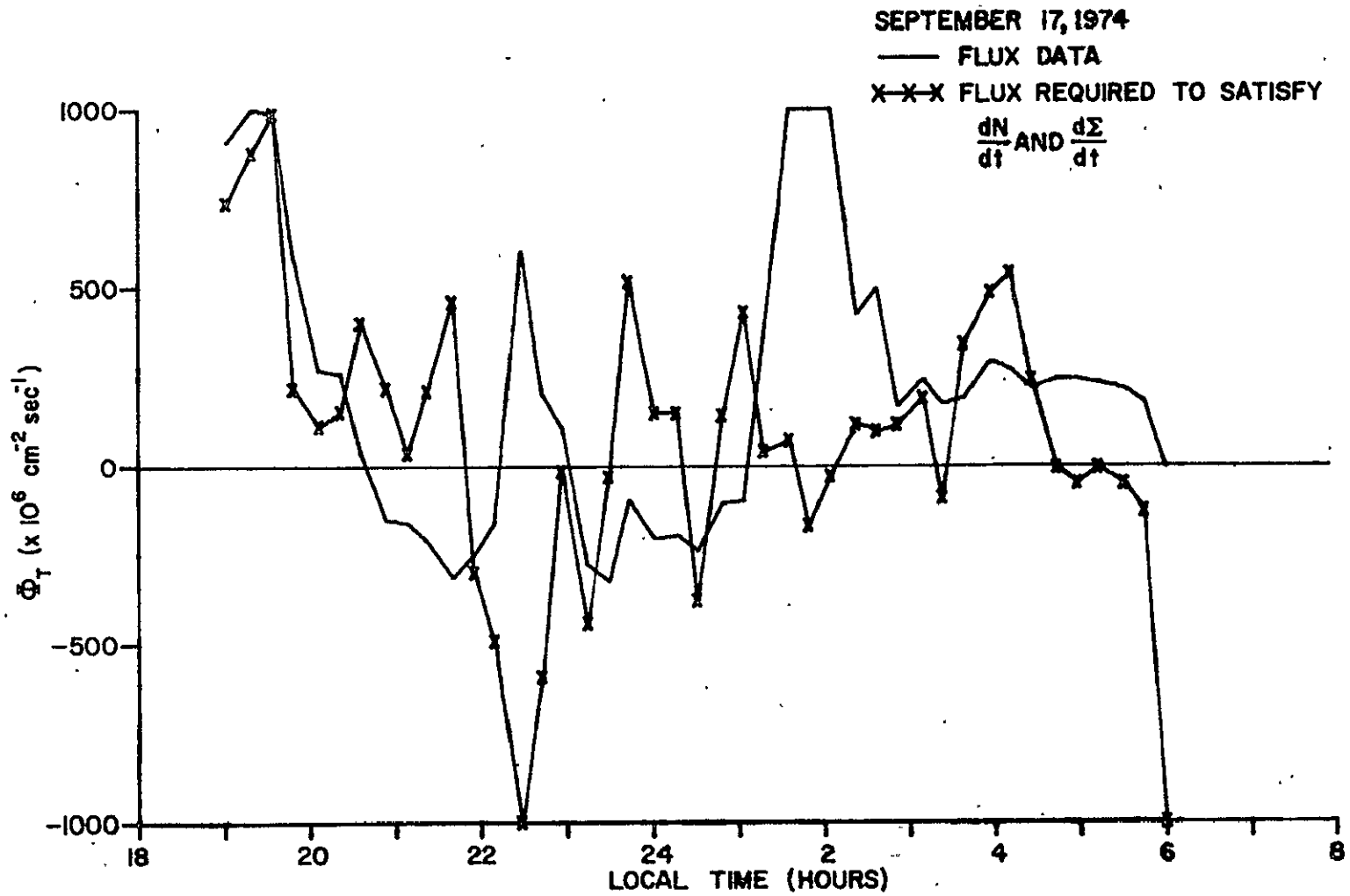


Figure 48: Time variation of top flux, and flux required to satisfy Equations 3.8 and 3.10.

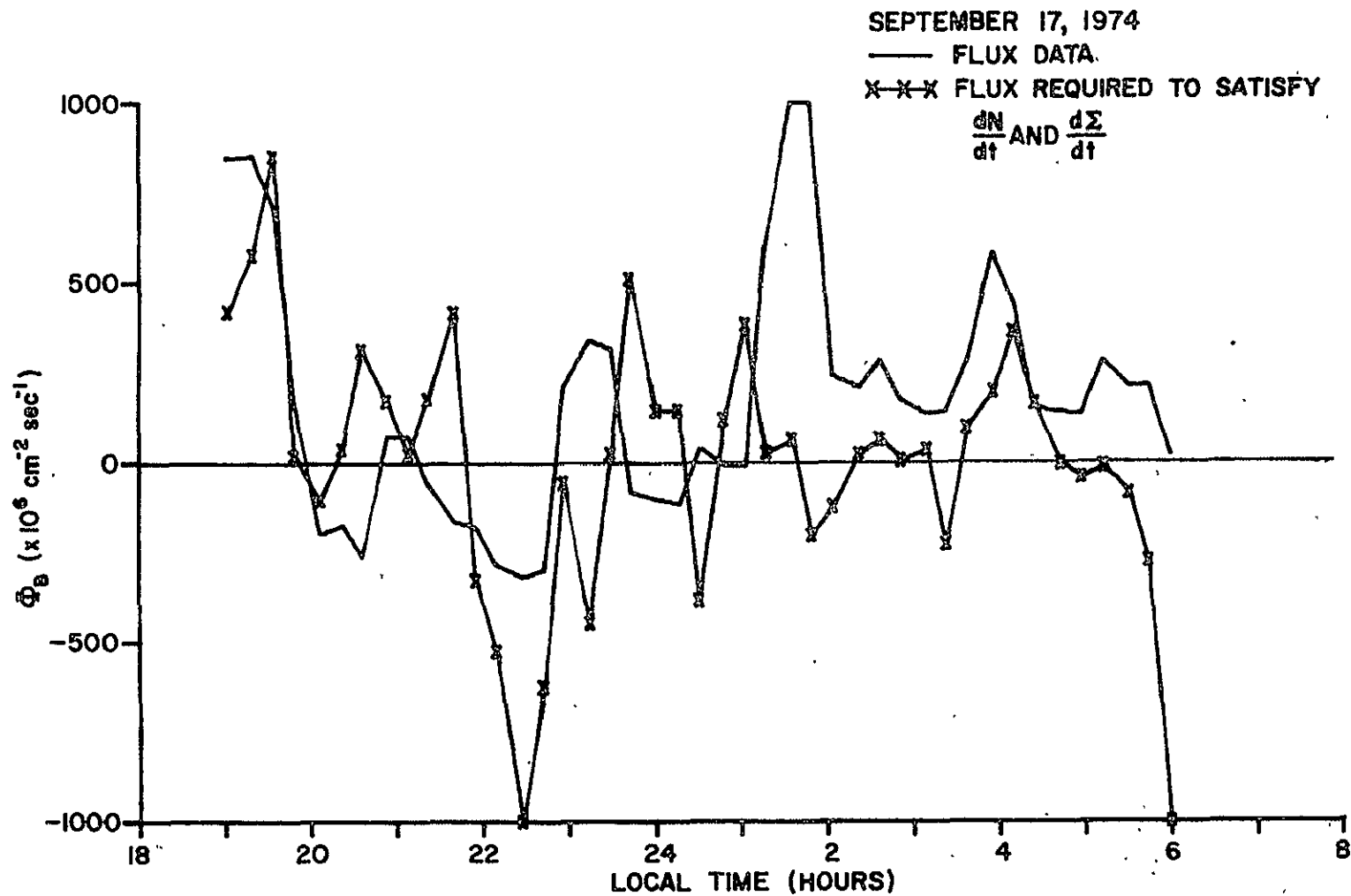


Figure 49: Time variation of bottom flux, and flux required to satisfy Equations 3.8 and 3.10.

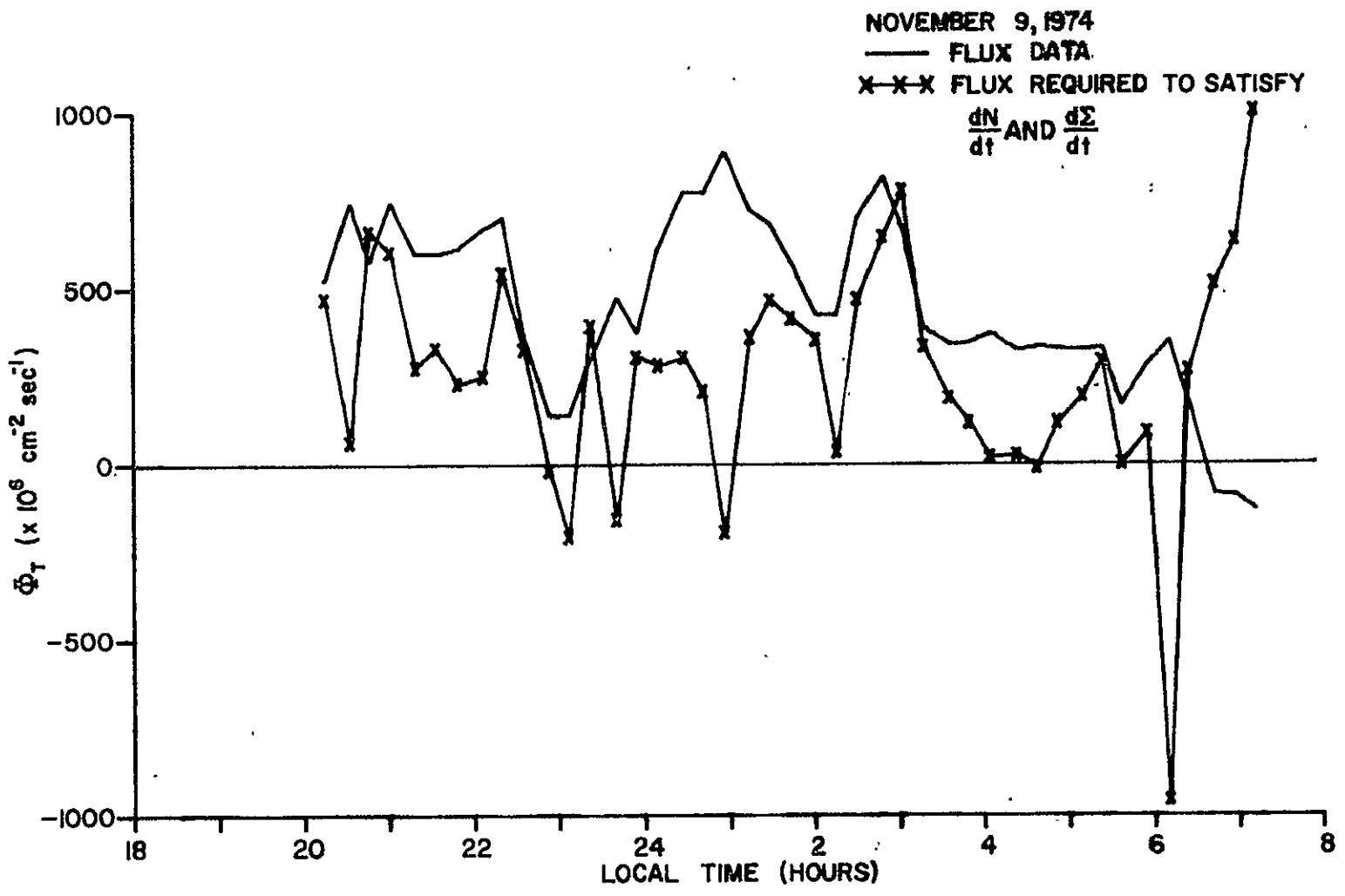


Figure 50: Time variation of top flux, and flux required to satisfy Equations 3.8 and 3.10.

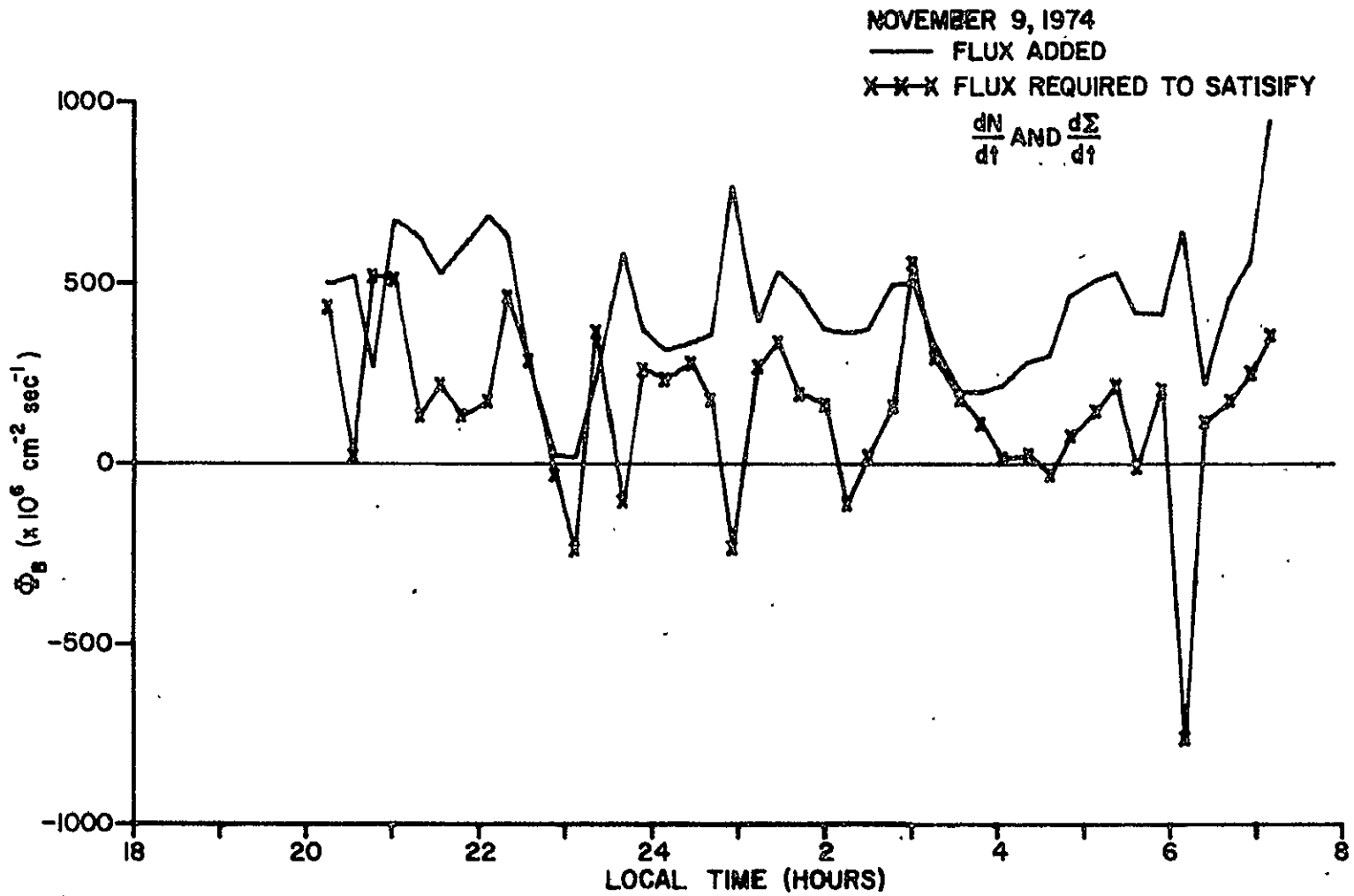


Figure 51: Time variation of bottom flux, and flux required to satisfy Equations 3.8 and 3.10.

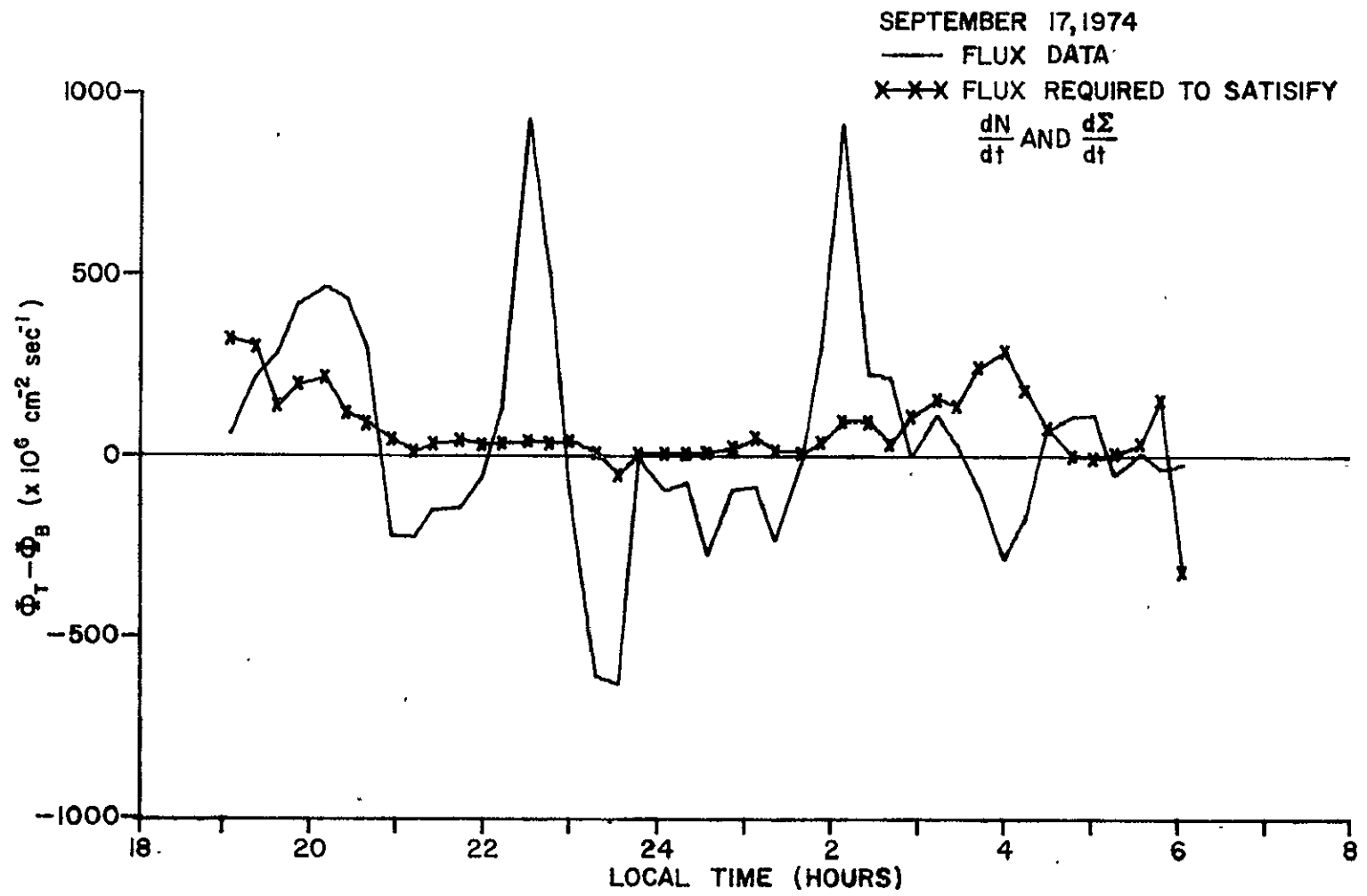


Figure 52: Time variation of net flux, and flux required to satisfy Equations 3.8 and 3.10.

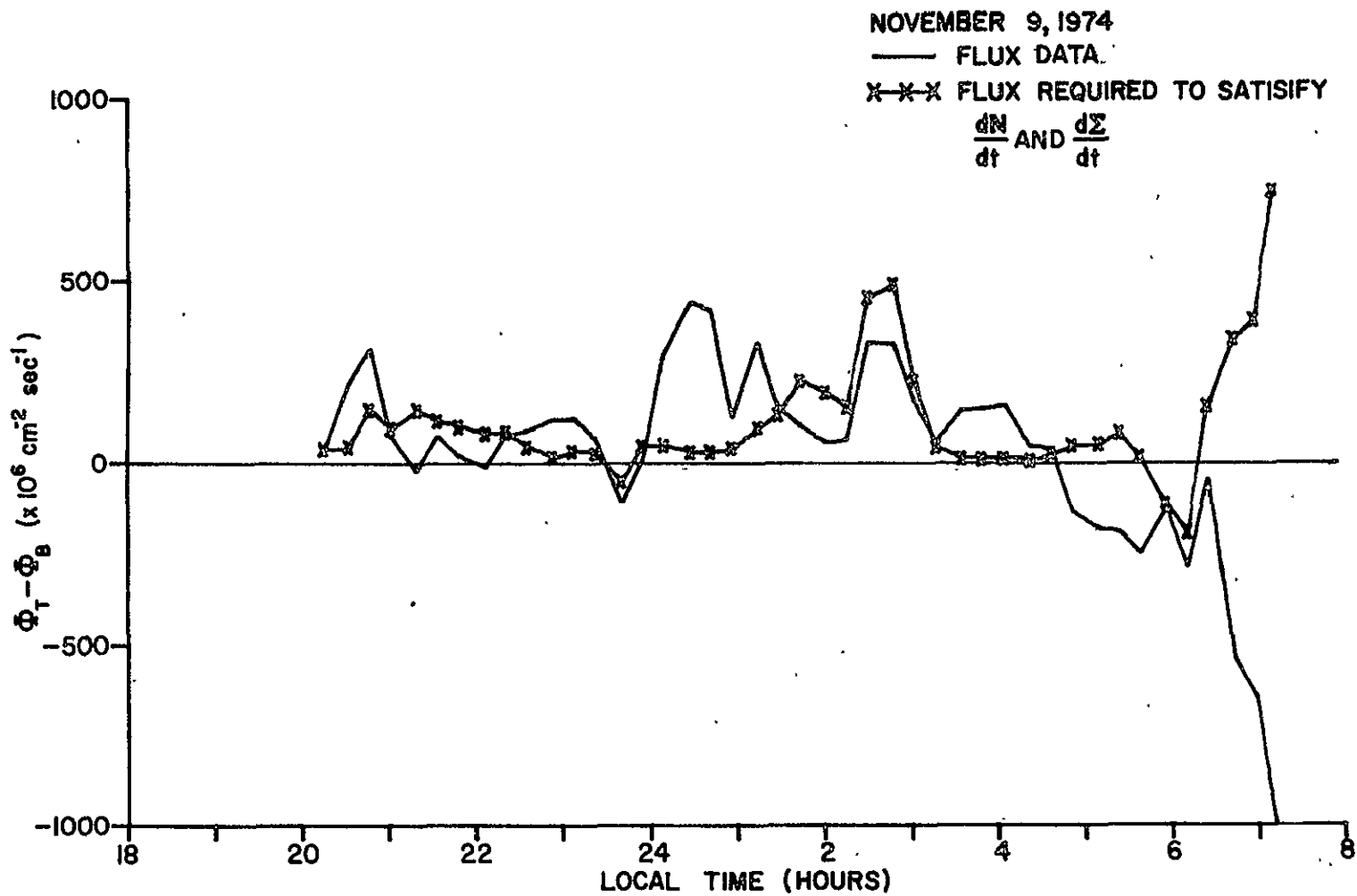


Figure 53: Time variation of net flux, and flux required to satisfy Equations 3.8 and 3.10.

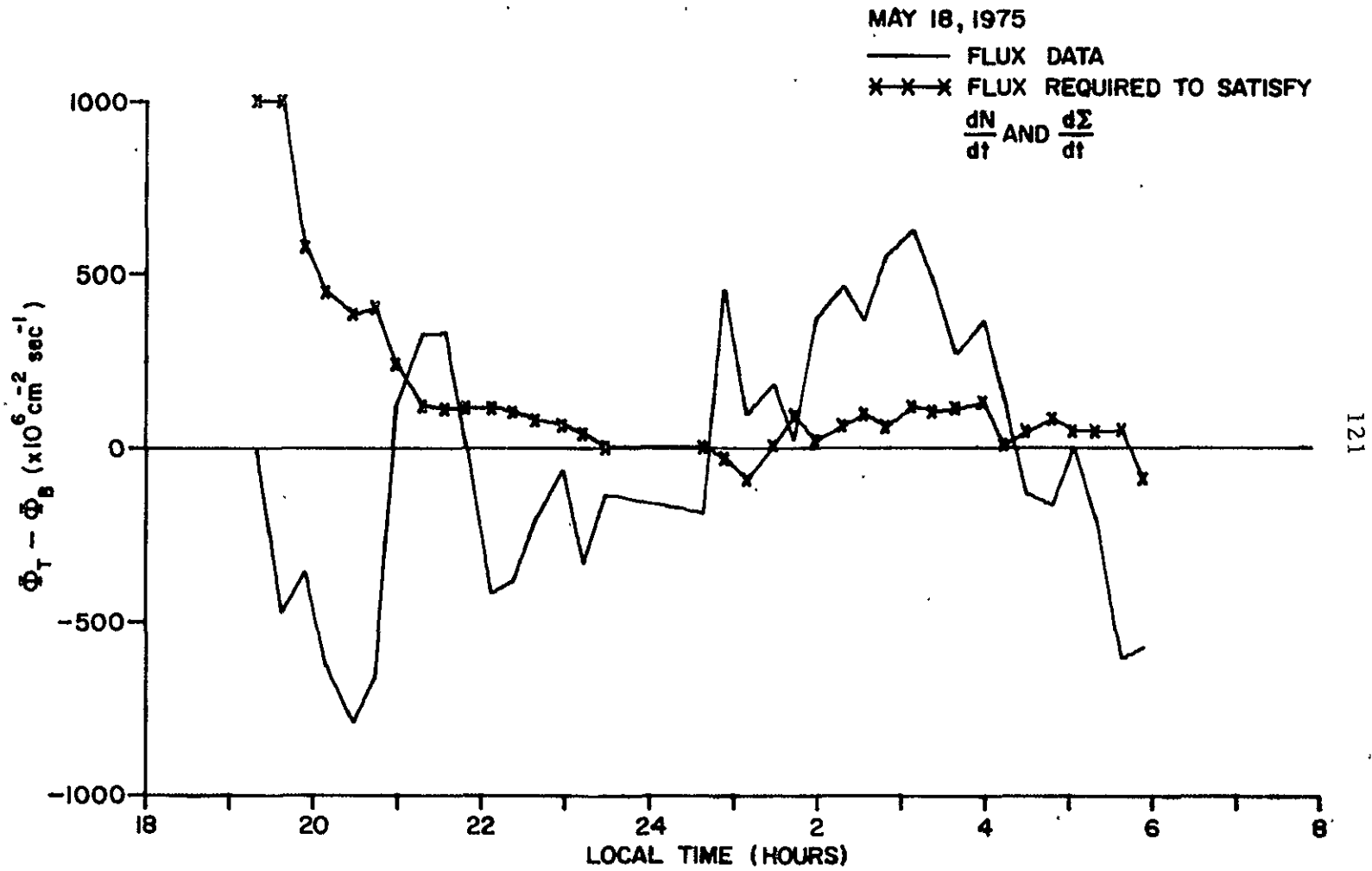


Figure 54: Time variation of net flux, and flux required to satisfy Equations 3.8 and 3.10.

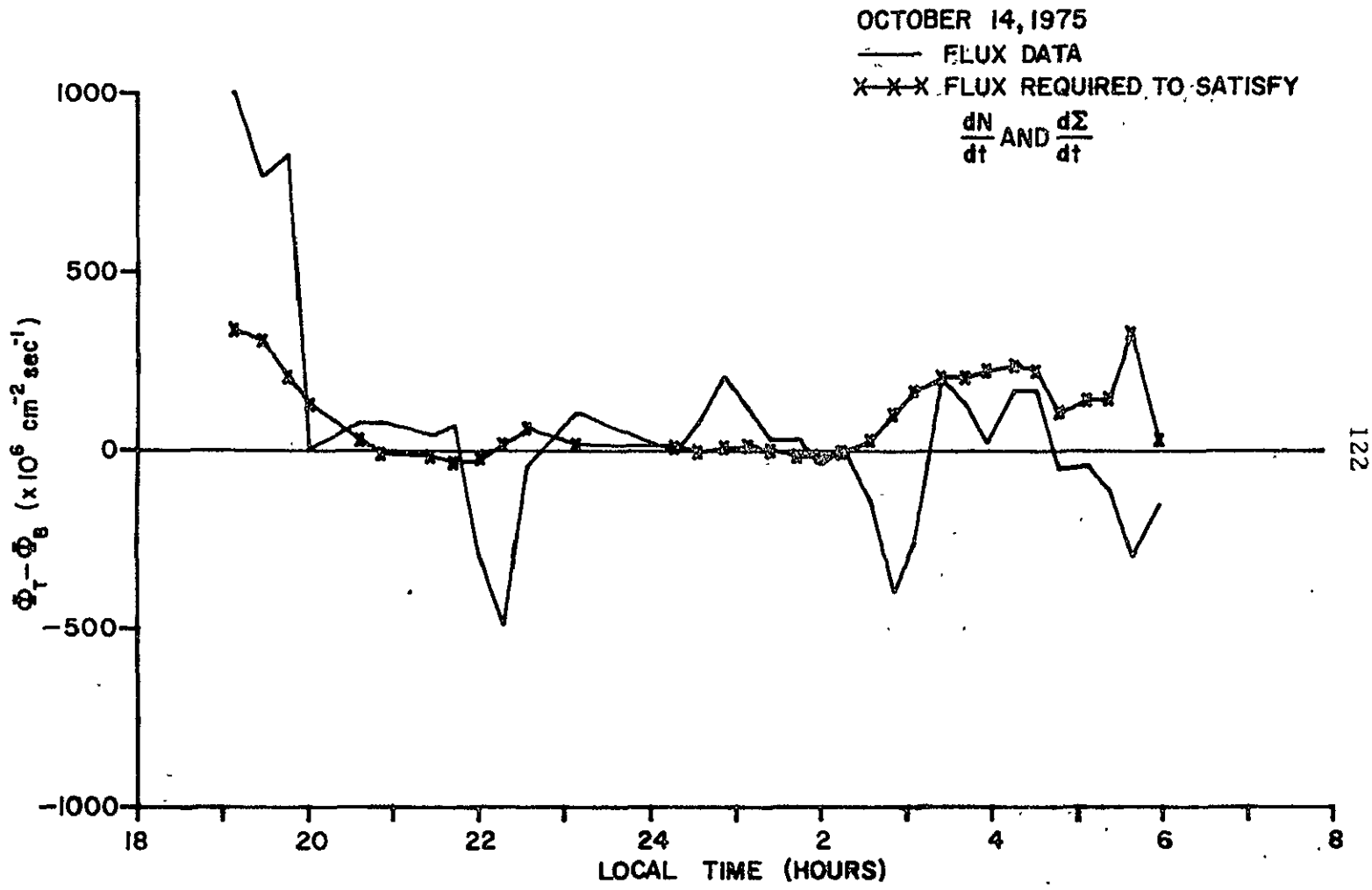


Figure 55: Time variation of net flux, and flux required to satisfy Equations 3.8 and 3.10.

$$\Delta (\text{NET FLUX}) = \sqrt{2} \Delta (nv)$$

$$\Delta (nv) = n \Delta v$$

$$\Delta (\text{NET FLUX}) = \sqrt{2} n \Delta v$$

$$n \approx 1 \times 10^5$$

$$\Delta v = \frac{\Delta (\text{NET FLUX})}{\sqrt{2} n} = \frac{4.5 \times 10^8}{\sqrt{2} 1 \times 10^5} = 32 \text{ m/sec}$$

It has been assumed that the error is identical for both north-south and vertical components of the velocity, and that errors in the density are significant compared to those in the velocities. If the uncertainty in the vertical component is reduced to 5 m/sec, the uncertainty in v_{NS} would increase to 50 m/sec.

It is difficult to come to the conclusion that the fluxes measured by such a high resolution instrument as the Arecibo radar are so erroneous. Before coming to this conclusion, the possibility of having a density gradient produce an effect that would explain the behavior of Σ_F and N_F will be examined. The largest flux that would be required to satisfy Equations 3.8 and 3.10 is about 2.5×10^8 . Assuming an electric field drift velocity of the order of 25 m/sec, one can solve for the density gradient required to yield a value of $2.5 \times 10^8 \text{ cm}^{-2} \text{ sec}^{-1}$ (cf. Equations 3.8).

$$2.5 \times 10^3 \text{ cm} \cdot \text{sec}^{-1} \times \frac{\Delta N}{\Delta x} = 2.5 \times 10^8 \text{ cm}^{-2} \cdot \text{sec}^{-1}$$

$$\frac{\Delta N}{\Delta x} \approx 1 \times 10^5 \text{ cm}^{-3}$$

This has more meaning if written in terms of the characteristic length of the gradient:

$$\frac{N}{\Delta N / \Delta x} \approx \frac{1 \times 10^{12} \text{ cm}^{-2}}{1 \times 10^5 \text{ cm}^{-3}} = 100 \text{ km}$$

Thus, if there were a density gradient of this magnitude (which is on the order of magnitude of the vertical density gradient) drifting horizontally at a speed of 25 m/sec, it could explain the behavior of N_F . In the data examined, there was no evidence of a horizontal gradient of this magnitude. However, other investigators have found evidence of substantial gradients (Matthews and Harper, 1972).

The above analysis merely states that a density gradient could explain the behavior of N_F and Σ_F , assuming there was no flux. If one assumes that the flux data is correct, then the effect of the density gradient would have to counteract the effect of the flux and produce the required curves shown in Figures 52-55. This is highly unlikely because some of the spikes seen in Figure 52 reach almost $1 \times 10^9 \text{ cm}^{-2} \cdot \text{sec}^{-1}$. To counteract these, and produce a resultant flow of particles of around 1×10^7 would require a much larger density gradient, as is shown below:

$$\Phi_{\text{NET}} + V_D \frac{\Delta N}{\Delta x} = 1 \times 10^7$$

$$\frac{\Delta N}{\Delta x} \approx \frac{10^9}{2.5 \times 10^3} \frac{\text{cm}^{-2} \cdot \text{sec}^{-1}}{\text{cm} \cdot \text{sec}^{-1}}$$

$$\frac{\Delta N}{\Delta x} \approx \frac{1 \times 10^{12}}{4 \times 10^5} \frac{\text{cm}^{-2}}{\text{cm}^{-3}} = 25 \text{ km}$$

This is a very large density gradient. It is highly unlikely that horizontal density gradients of sufficient magnitude would drift horizontally in exactly the right direction to counteract the enormous fluctuations that are seen in the flux to produce the source terms required as shown in Figures 52-55. It is also highly unlikely that particles would be building up in the flux-tube, causing the horizontal gradient, and then drift across the field lines. It is much easier for them to go straight on through the flux tubes along the field lines, thus causing no buildup.

It is unfortunate that nothing more can be said about the density gradients or the flux data. There is no direct data presently available for the horizontal density gradients, and it will probably be difficult to acquire such data. At the present time, the issue of the flux behavior remains unresolved.

The tentative conclusion is reached that the flux data given by the Arecibo data have much larger uncertainties in them than has previously been assumed.

A possible explanation of the large errors associated with the flux is found in the recent work of Vickrey et al., (1976). The reduction of the raw Arecibo data involves the assumption that atomic oxygen is the single species of ions in the upper F region. Vickrey et al., (1976) have shown that there is a large amount of hydrogen ions in the F region. The large mass difference between hydrogen and oxygen could produce errors in the drift velocities calculated from the Arecibo data on the order of 80 m/s.

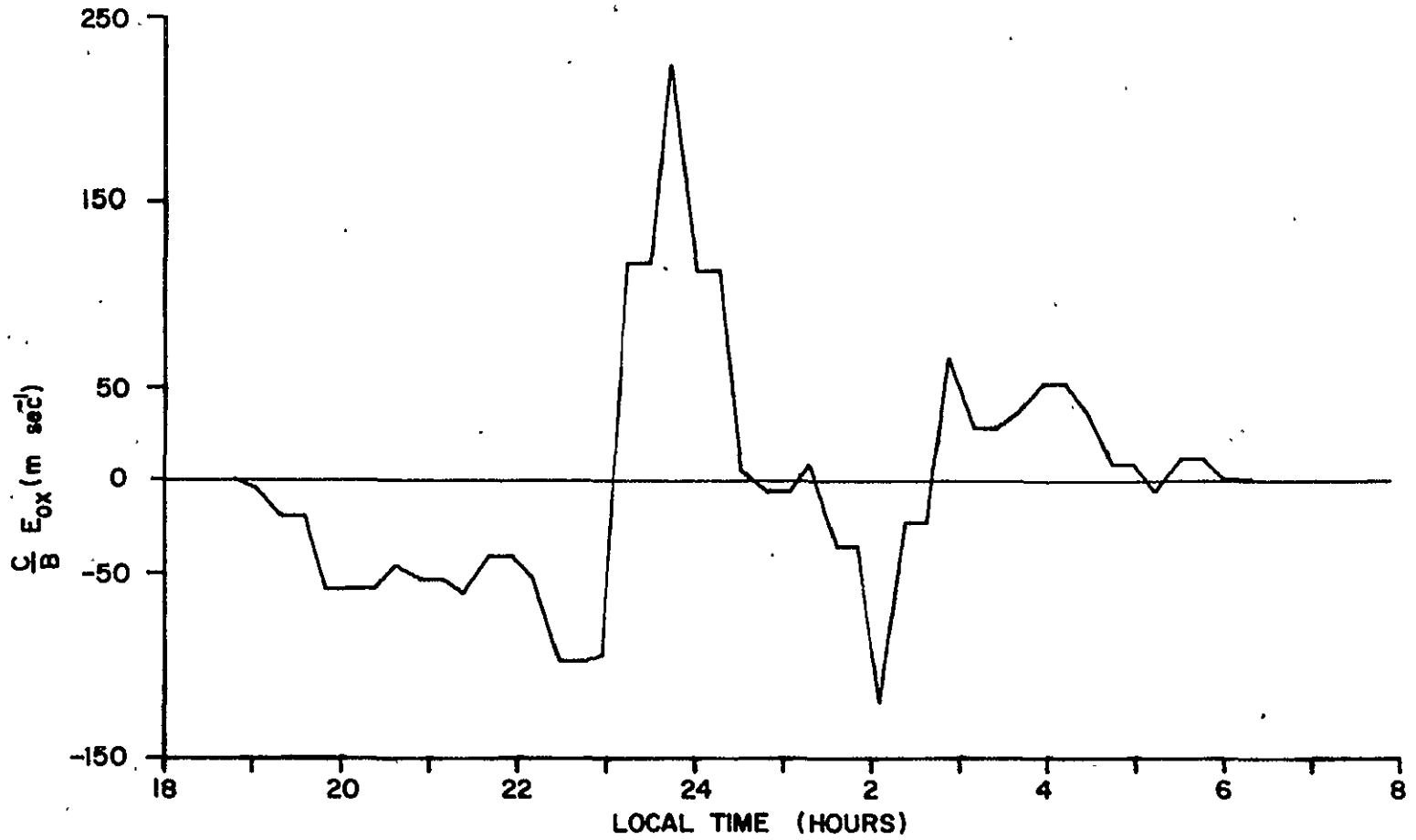
3.6 Equilibrium Behavior of F_s Nights vs. Non F_s Nights

The flux is somewhat more turbulent on F_s nights (September 17, 1974 and May 18, 1975) than on nights without F_s (November 9, 1974 and October 14, 1975) as is shown in Figures 22, 25, 28 and 31. It is also seen that the electric fields are more turbulent (Figures 9, 56-62) on F_s nights, in agreement with Kelley (1972).

There is no difference in the other equilibrium parameters such as the motion of the peak, Σ_F or N_F during non- F_s nights.

The next chapter will examine the growth rate predicted by the Perkins model of F_s , and compare it to the data.

SEPTEMBER 17, 1974



127

Figure 56: Time variation of northward electric field.

NOVEMBER 9, 1974

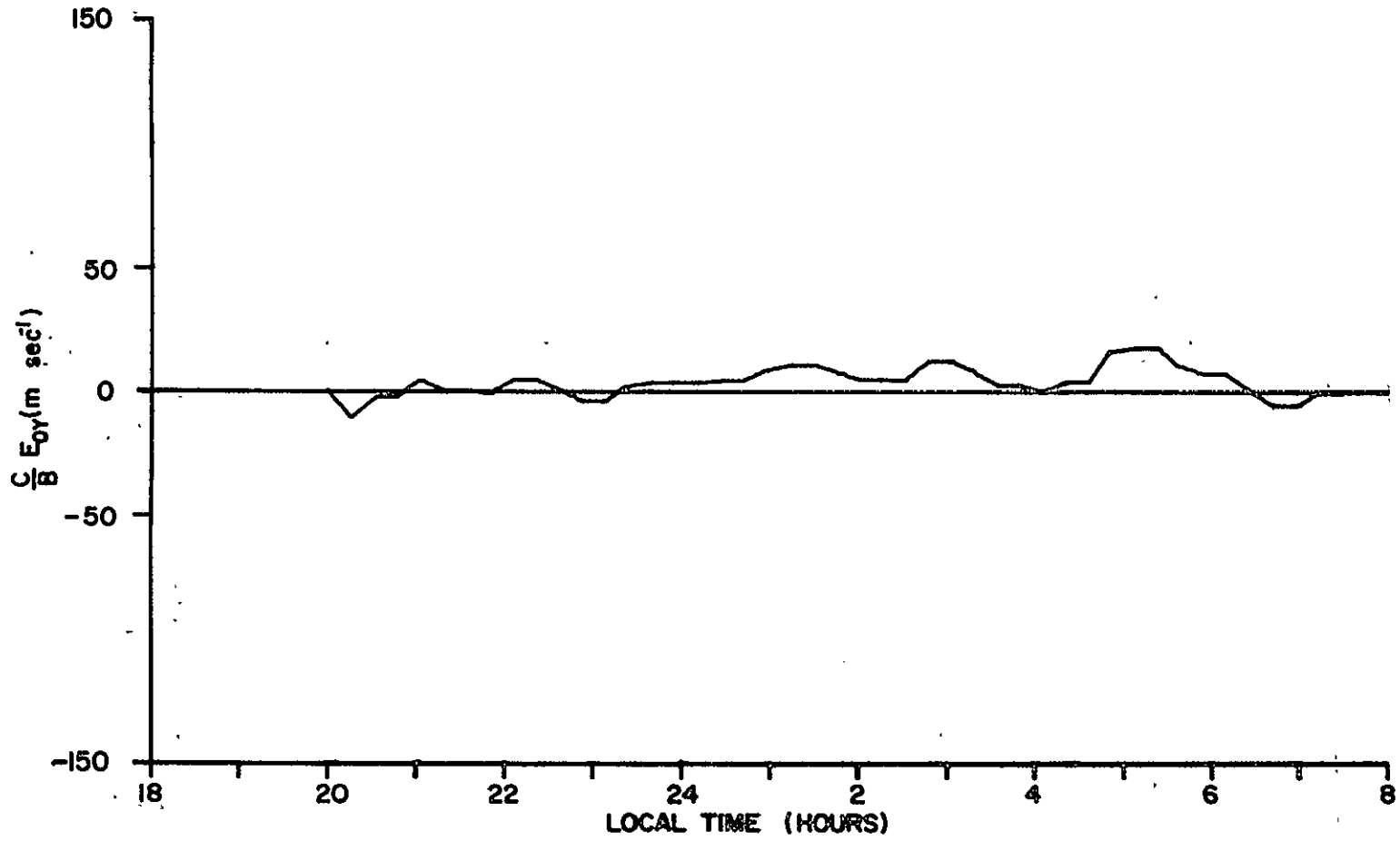
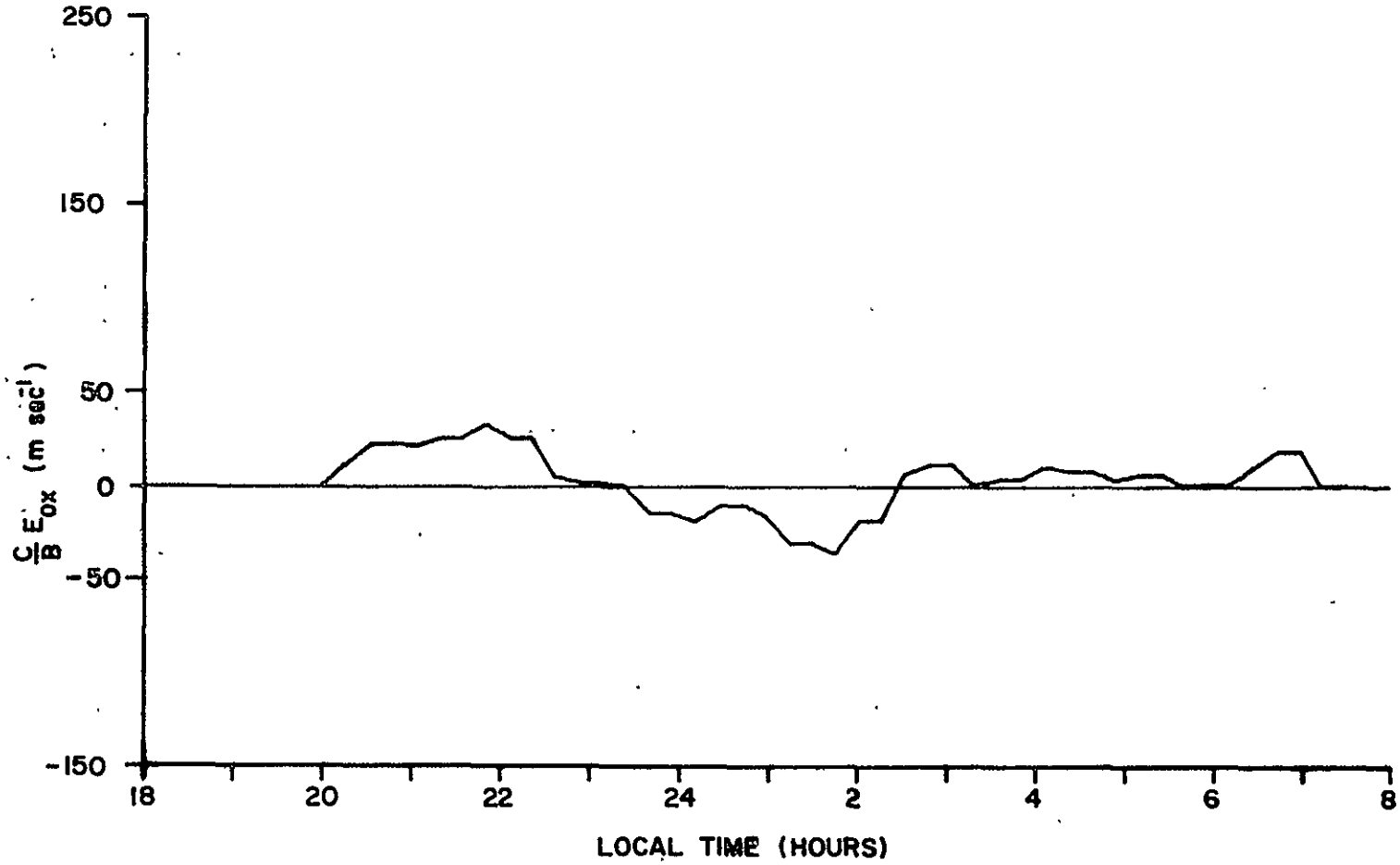


Figure 57: Time variation of eastward electric field.

NOVEMBER 9, 1974



129

Figure 58: Time variation of northward electric field.

MAY 18, 1975

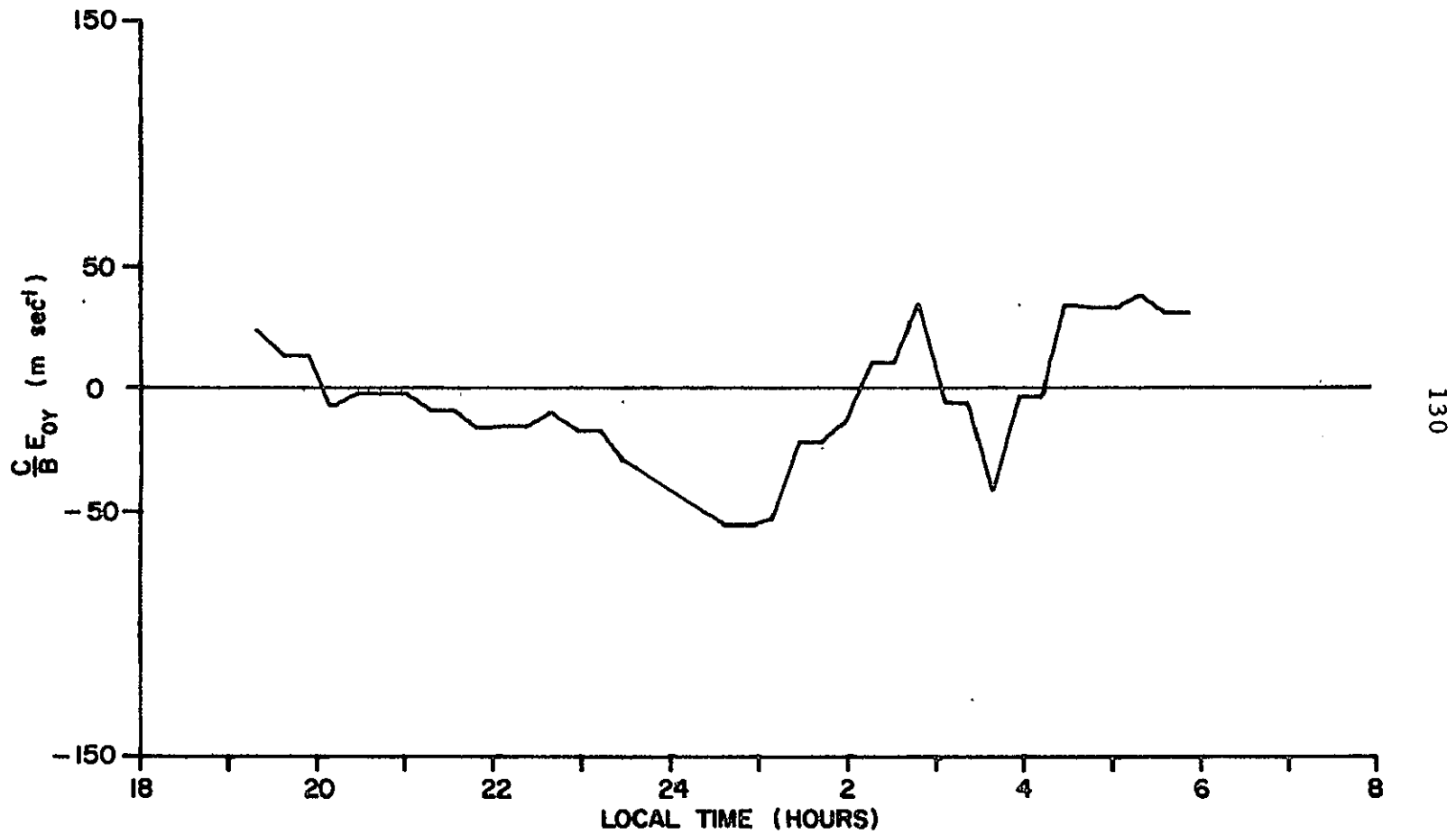
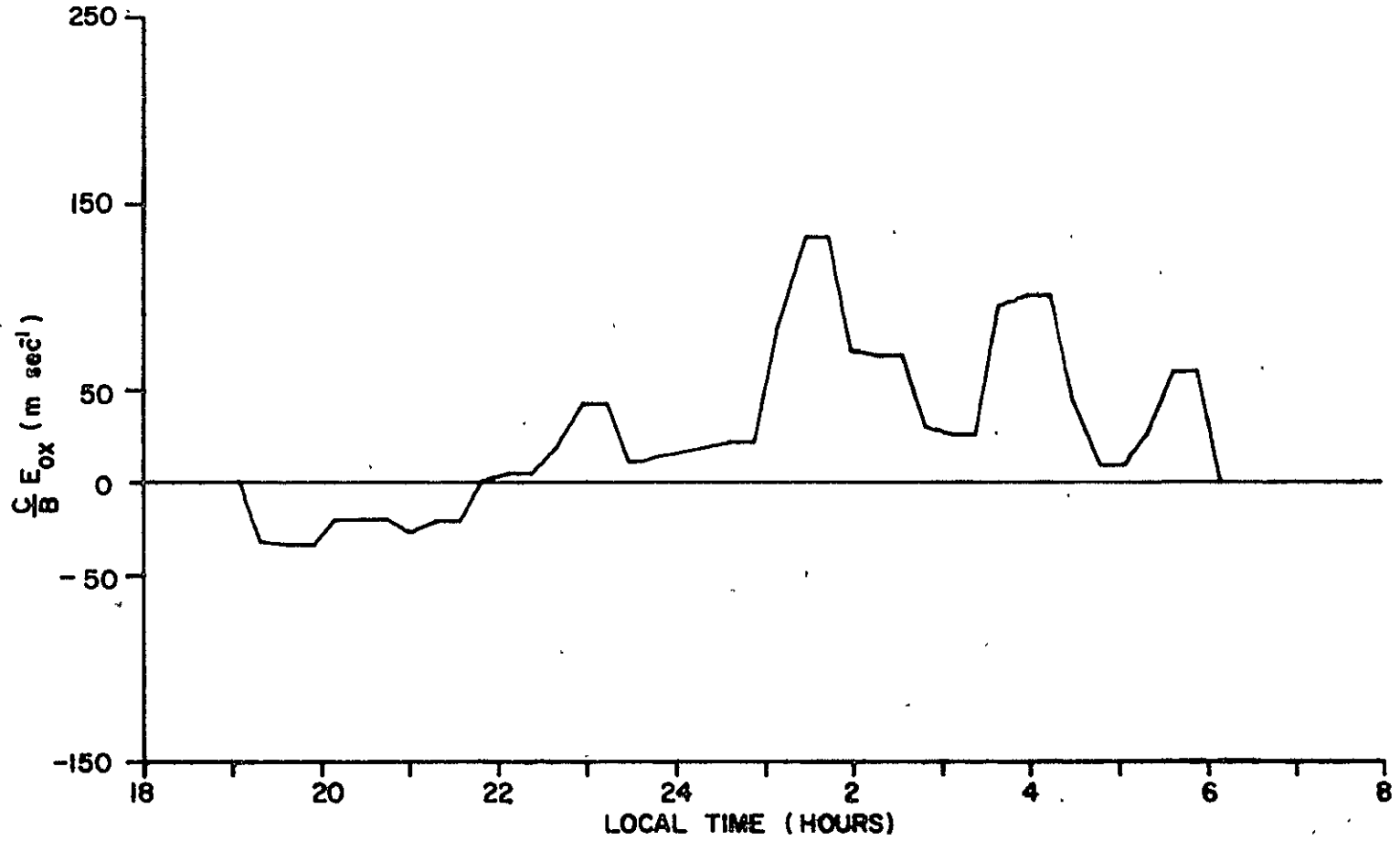


Figure 59: Time variation of eastward electric field.

MAY 18, 1975



131

Figure 60: Time variation of northward electric field.

OCTOBER 14, 1975

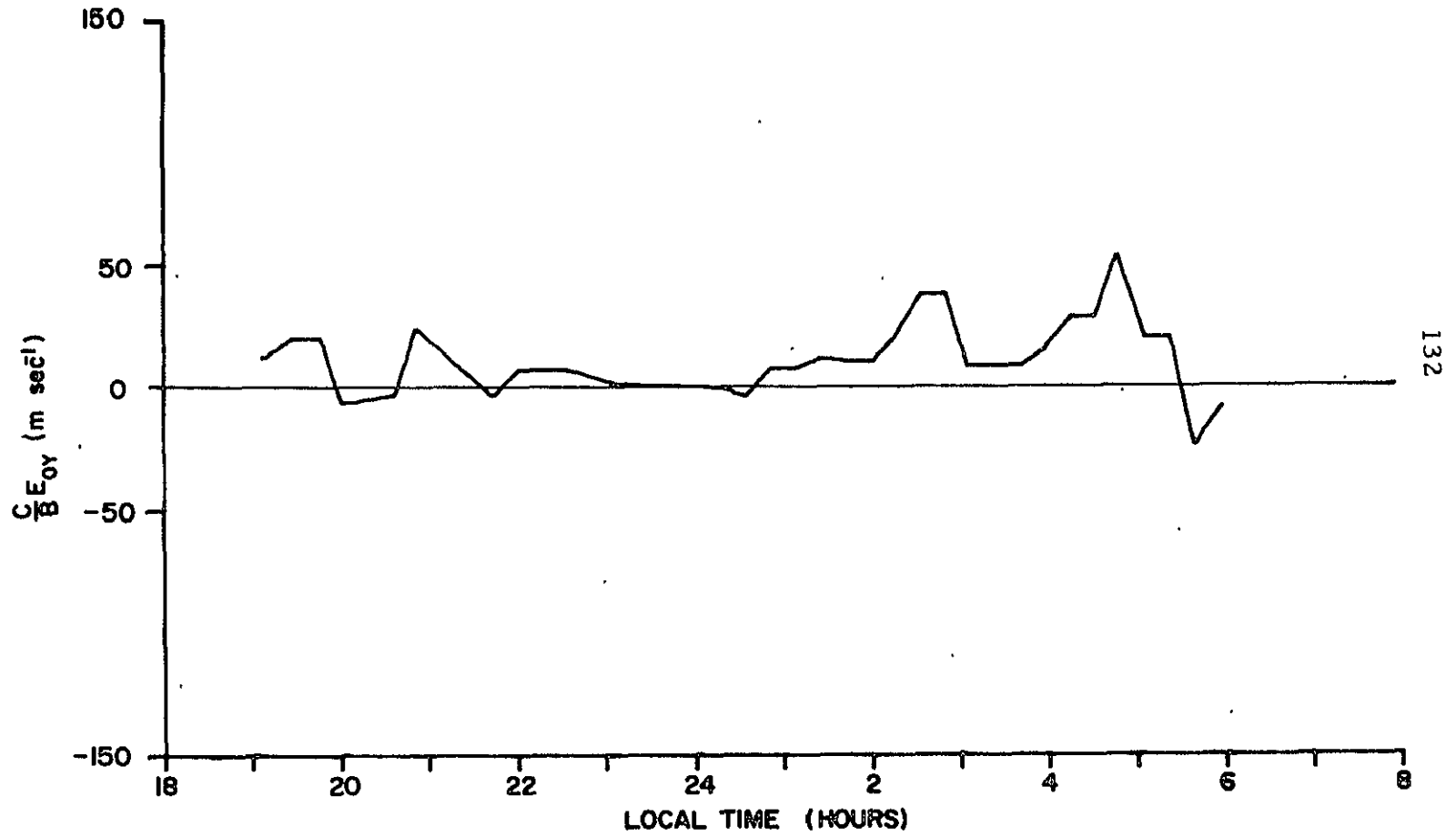


Figure 61: Time variation of eastward electric field.

OCTOBER 14, 1975

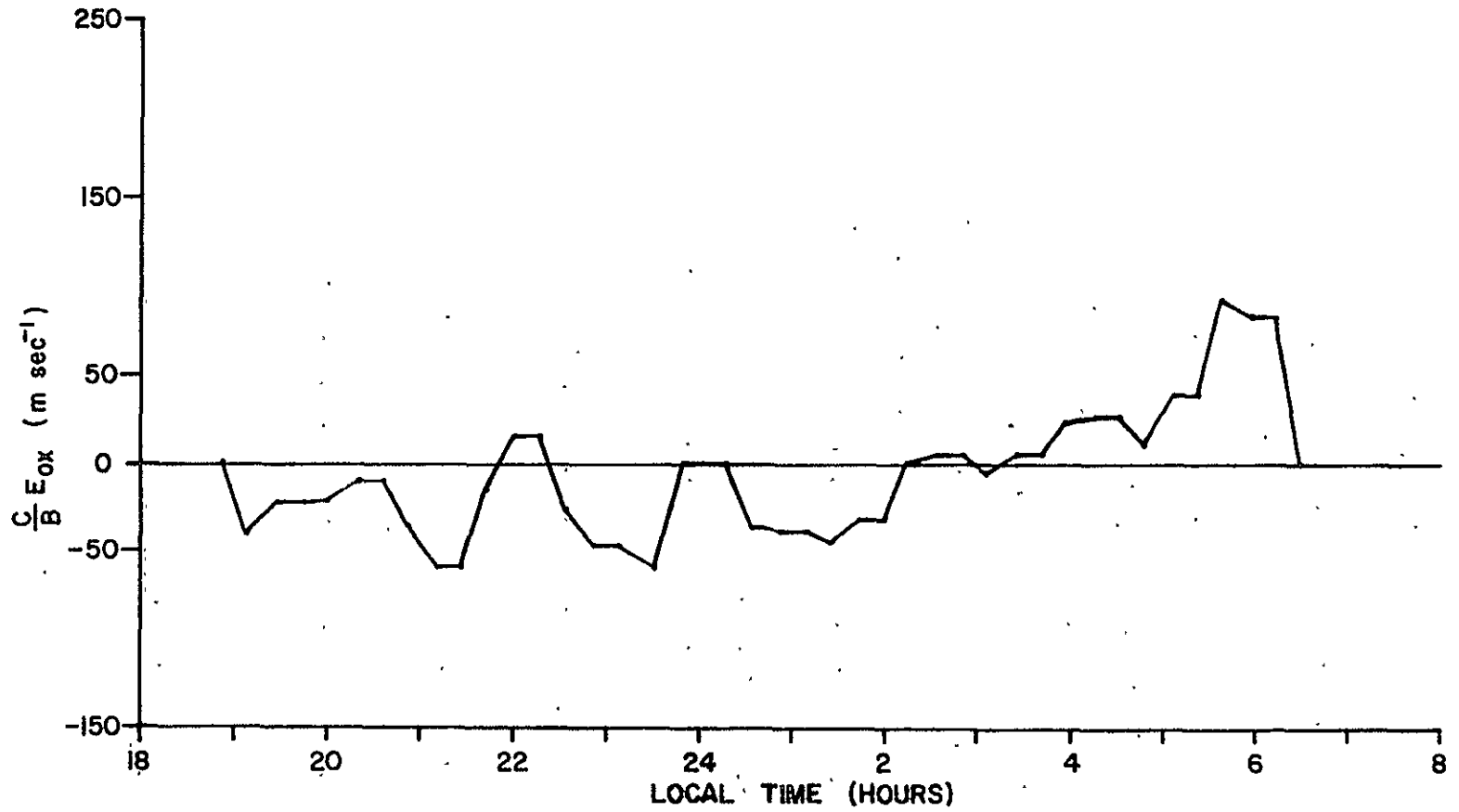


Figure 62: Time variation of northward electric field.

CHAPTER IV

GROWTH RATE ANALYSIS

In the last chapter, it was shown in Figures 44 and 46 that the equilibrium at the onset of F_s predicted by the Perkins model was in agreement with the data for one of the days with F_s (September 17, 1974) but not the other day (May 18, 1975). In this chapter, linear growth rates predicted by the Perkins model and the Scannapieco model will be examined. Using the Arecibo data, the conditions required to yield reasonable growth times will be obtained. In addition, the Perkins model will be extended to include the effects of short wavelength damping, recombination and E region coupling.

4.1 Comparison With the Data

The linear growth rate predicted by the Perkins model is

$$\gamma_P = \frac{c}{B} \frac{E_{RES} \cos D}{H} \sin^2 \theta/2$$

where the direction of the propagation of the irregularities has been assumed to be that which gives maximum growth, i.e., $\alpha = \theta/2$.

The linear growth rate of the Scannapieco model is

$$\gamma_S = \frac{c}{B} \left(\frac{Bg \cos D}{c \omega_{ci}} - E_{ox} \right) \frac{1}{\Sigma_o} \frac{\partial \Sigma_o}{\partial y} - \frac{c}{BH} \frac{eg \sin^2 D}{\omega_{ci}} \frac{N_o}{\Sigma_o}$$

where $\underline{k} = k_x \hat{x}$ is assumed in this model.

Ideally, one would like to use the data to calculate growth rates predicted by the two models and compare the predicted rates during the onset of F_s with the predicted rates when no F_s occurred. If either or both of the models could predict the occurrence of F_s , long growth times or damping should be seen before onset, and short growth times at onset.

This is not possible to do because of the lack of data on several critical parameters. One of these is the direction of propagation of the field aligned irregularities that cause F_s . This is important because the Perkins model predicts damping if the direction of propagation is more northward than the direction of the equilibrium resultant electric field. This issue can be bypassed if one assumes that the propagation direction will be that which yields maximum growth, i.e. $\alpha = \theta/2$ for the Perkins model and $\alpha = \pi/2$ for the Scannapieco model.

A much more serious problem is the lack of data on the east-west component of the neutral wind (V_{NY}) at Arecibo. This is required to calculate the resultant electric field in the x direction, which is the very parameter that is required for positive growth in both models. It should also be noted that there are no models that accurately predict V_{NY} at Arecibo (Behnke and Kohl, 1974). Finally, the lack of information on $\partial \Sigma / \partial y$ means that there are two critical parameters in the Scannapieco model which are unknown. Since there is only one unknown in the expression for the Perkins growth rate (γ_p) it is possible to pick reasonable growth rates and solve this

expression for V_{NY} , using the Arecibo data. This has been done for times around onset, and the results are shown in Tables 1-4.

It is immediately seen by looking at Tables 1-4 that the neutral wind required for growth times of 10 minutes is on the order of 200-500 m/s, and for growth times of 30 minutes, up to 200 m/s. These are not unphysical results, as can be seen in Figures 10, 63, 64 and 65 which show the neutral wind along the field line.

The next point that is noticed in the October data is that there is no difference in the neutral winds required for F_s onset between days with F_s and those without F_s . However, the actual magnitude of the east-west neutral wind does seem to be different for nights with and without F_s as seen in Figures 10, 63, 64 and 65. The winds reach much higher velocities, at least along the field lines, on the days with F_s . However, on the May night, the wind reaches its peak velocity at a time well beyond the onset time.

The last point is that there is no great change in the neutral wind required between onset and the times before onset. This suggests that the other equilibrium parameters do not trigger F_s , and the quantity V_{NY} must change before onset if the Perkins model is to predict the occurrence of F_s .

The conclusion can not be emphasized too strongly. Without an independent measurement of V_{NY} , it is impossible to calculate growth rates predicted by the Perkins model, or the Reid or Scannapieco models, for that matter. It is not possible to infer that because the values of V_{NZ} are higher on F_s nights that the values of

Table 1 September 17, 1974

Time	t = 10 Minutes		t = 30 Minutes	
	V_{NY} (m/s)	$\left(\frac{1}{\Sigma_o} \frac{\partial \Sigma_o}{\partial y} \right)^{-1}$ (km)	V_{NY} (m/s)	$\left(\frac{1}{\Sigma_o} \frac{\partial \Sigma_o}{\partial y} \right)^{-1}$ (km)
20.90	300	-83	150	-50
21.15	310	-83	160	-53
21.38	330	-83	170	-56
21.68	320	-77	170	-50
ONSET AT 21.83				
21.93	380	-63	210	-40
22.17	400	-62	230	-43
22.47	490	-53	300	-31
22.72	430	-72	260	-43
22.95	420	-53	260	-32
23.25	210	-53	48	-31
23.50	210	-63	42	-38
23.73	67	-59	-79	-37
.03	150	-63	9.2	-37

Table 2 November 9, 1974

20.00	240	- 91	79	-77
20.25	240	-111	74	-77
20.55	210	-103	58	-62
20.78	210	-114	54	-83
21.03	210	-100	56	-63
21.33	210	-100	58	-62
21.57	220	-100	65	-62
21.82	210	-100	55	-62
22.12	210	-100	53	-62
22.35	200	-100	53	-63
22.60	250	- 83	93	-50
22.90	260	- 83	110	-53

Table 3

May 18, 1975

Time	t = 10 Minutes		t = 30 Minutes	
	V_{NY} (m/s)	$\left(\frac{1}{\Sigma_o} \frac{\partial \Sigma_o}{\partial y} \right)^{-1}$ (km)	V_{NY} (m/s)	$\left(\frac{1}{\Sigma_o} \frac{\partial \Sigma_o}{\partial y} \right)^{-1}$ (km)
19.07	260	-143	92	-132
19.32	280	-123	120	-100
ONSET	19.50			
19.63	250	-108	110	- 83
19.90	250	-103	110	- 77
20.15	240	-100	99	- 71
20.47	240	-100	98	- 62
20.73	240	- 91	100	- 62
20.98	270	- 83	130	- 59
21.30	250	- 77	120	- 53
21.57	250	- 77	120	- 53
21.82	220	- 72	84	- 48
22.13	230	- 72	96	- 48
22.38	220	- 72	85	- 46

Table 4

October 14, 1975

18.88	230	-100	77	- 62
19.13	300	-133	130	-106
19.47	260	-118	100	- 91
19.77	250	-115	99	- 83
20.02	240	-108	96	- 77
20.35	250	-122	100	-111
20.62	290	- 77	140	- 50
20.87	330	- 83	170	- 50
21.20	340	-132	190	-127
21.45	330	- 72	180	- 46
21.72	260	- 56	120	- 33
22.03	210	- 72	79	- 48

NOVEMBER 9, 1974

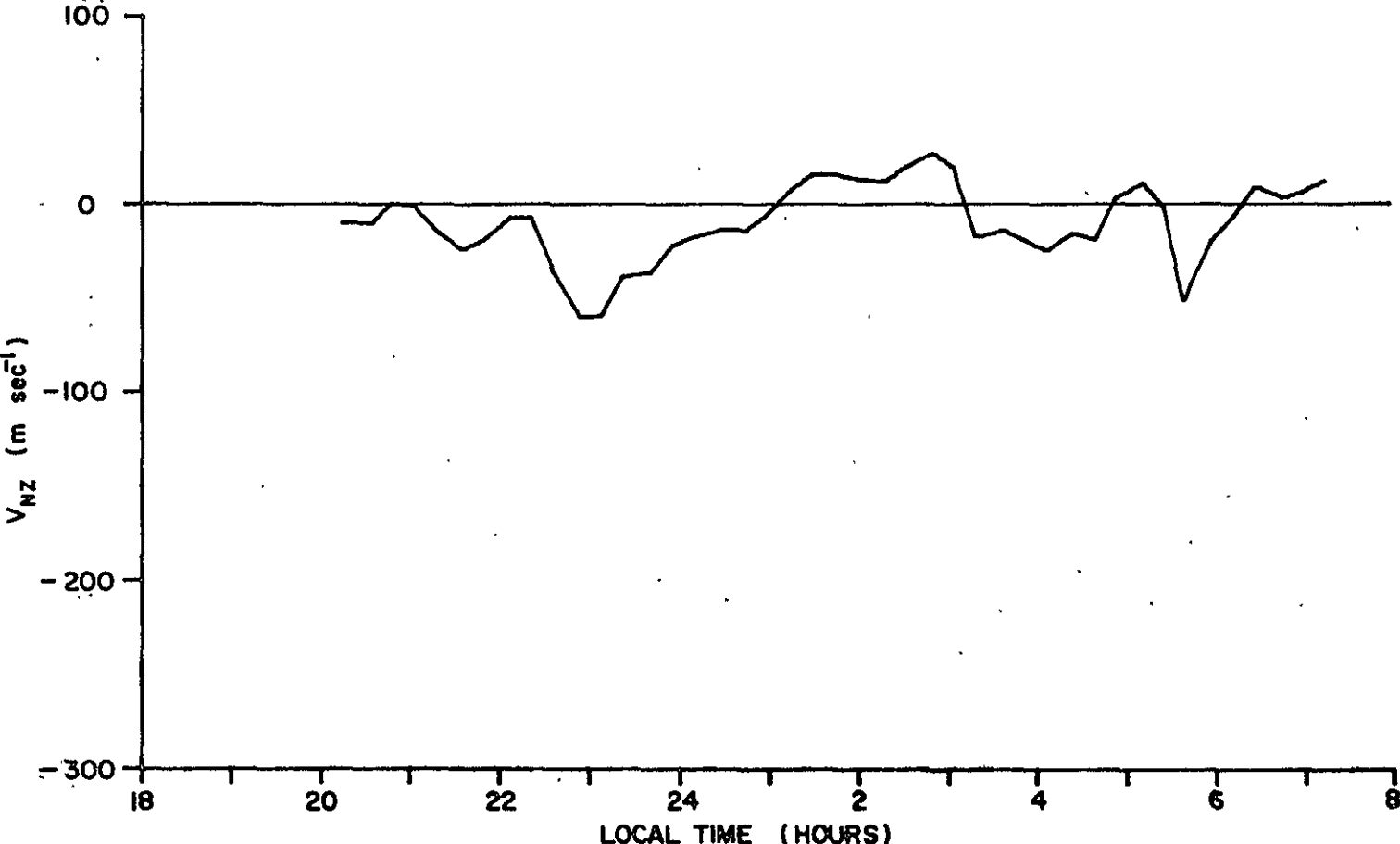
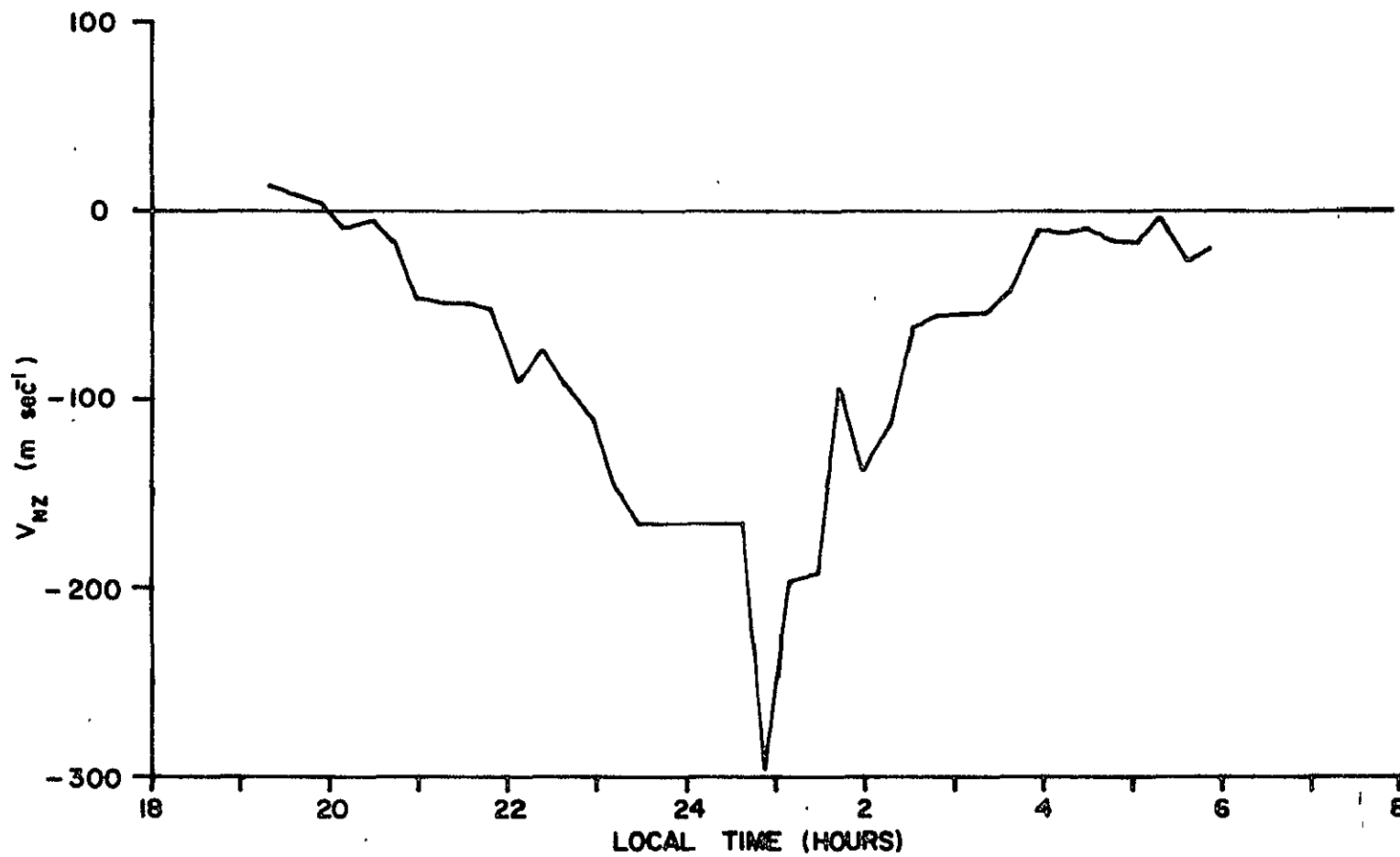


Figure 63: Time variation of neutral wind.

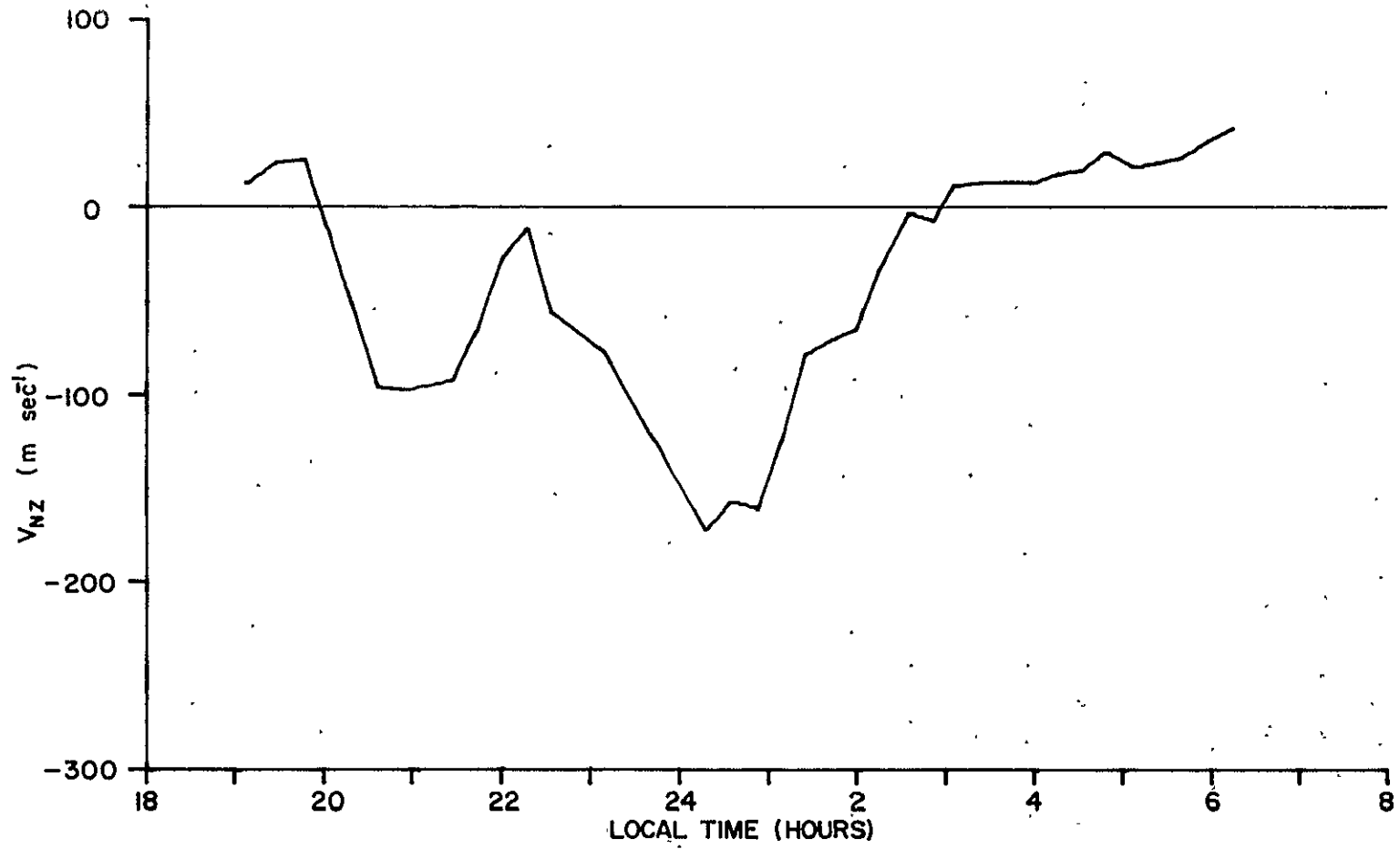
MAY 18, 1975



140

Figure 64: Time variation of neutral wind.

OCTOBER 14, 1975



141

Figure 65: Time variation of neutral wind.

V_{NY} will also be higher and hence reasonable growth times will be obtained. It is only possible to state that given the right values of V_{NY} before onset and at onset, the Perkins model can predict the development of F_s with reasonable growth times, and that the values required for V_{NY} are not too large to be unphysical.

The other two columns in Tables 1-4 show the characteristic size of the east-west equilibrium gradient $(1/\Sigma_o / \partial \Sigma_o / \partial y)^{-1}$ that would be required to yield reasonable growth times in the Scannapieco model, assuming the values of V_{NY} obtained in the previous calculation. This approach was used because the Scannapieco model has two unknown quantities, $\partial \Sigma_o / \partial y$ and V_{NY} . It was felt that the above procedure would yield an order of magnitude estimate of the gradient scale length required for instability and that a two-parameter study was not justified at this time.

The characteristic lengths of the gradients required are on the order of 50-100 km, which means that the horizontal gradient of either n or v_{in} must be of the same order of magnitude as the vertical gradient of these two quantities. This is not an unphysical requirement, but is much larger than is normally seen at Arecibo.

It should be noted that the gradients required to give growth times of 30 minutes are larger than those required to give growth times of 10 minutes because V_{NY} , which was calculated from the Perkins model, is smaller.

The only information that can be obtained from Tables 1-4 is that the Perkins model and the Scannapieco model are capable of predicting reasonable growth times under the proper set of conditions.

Unfortunately, there are not enough data to describe the full set of conditions that exist during the night. A judgement about whether the models actually can predict F_s will have to wait until simultaneous measurements are made of the east-west neutral winds, the horizontal gradients, and the drift velocities. The direction of propagation of the irregularities, although ignored in this thesis by assuming \underline{k} is in a direction which yields maximum growth, is also critical to both the Perkins and Scannapieco models.

4.2 Extension of the Perkins Model

The expressions for the growth rates predicted by the Perkins model and the Scannapieco model do not include short wavelength damping expected from diffusion, nor do they include contributions from recombination or E region coupling. The effect of recombination, while important in the description of the equilibrium, is a trivial extension to the models and merely adds the term $-\bar{\beta}$ to the growth rate. Its importance will be discussed later. The E region coupling issue is associated with the assumption that the integrated E region Pedersen conductivity is small compared to the integrated F region Pedersen conductivity. As will be shown, this is frequently not the case. Consequently, it becomes necessary to examine when E region coupling may be important, and its effect on growth. Focus is on the Perkins model, although much of the analysis is also common to the Scannapieco model.

4.2.1 Short Wavelength Diffusion

Intuitively, one would expect that the instability would be damped at short wavelengths by a diffusion process. It will be demonstrated that the short wavelength damping is contained in the Hall conductivity terms, which are the terms of order v_{in}^2/ω_{ci}^2 , neglected in the Perkins model. The Hall conductivity is:

$$\sigma_H = \frac{nec}{B} \frac{\omega_{ce}^2}{\omega_{ce}^2 + \nu_{eu}^2} - \frac{nec}{B} \frac{\omega_{ci}^2}{\omega_{ci}^2 + \nu_{in}^2} \quad (4.1)$$

Above 150 km, $\nu_{en} \ll \omega_{ce}$, so Equation 4.1 can be simplified:

$$\sigma_H \approx \frac{nec}{B} \left(1 - \frac{\omega_{ci}^2}{\omega_{ci}^2 + \nu_{in}^2} \right) \quad (4.2)$$

In the F region, $\nu_{in} \ll \omega_{ci}$, so the expression can be further simplified:

$$\sigma_H^F \approx \frac{nec}{B} \frac{\nu_{in}^2}{\omega_{ci}^2} \quad (4.3)$$

To extend the Perkins model to include the Hall conductivity terms, a new moment must be defined:

$$\psi = \frac{ec}{B} \int n \frac{\nu_{in}^2}{\omega_{ci}^2} dz$$

It is seen by comparison with Equation 4.3 that the quantity ψ is the F region integrated Hall conductivity.

The moment equations of the Perkins model including the terms of order (v_{in}^2/ω_{ci}^2) in Equation 2.4 are:

$$\frac{\partial N}{\partial t} - \frac{c}{B} \nabla \cdot N \nabla \phi \times \hat{z} = 0 \quad (4.4)$$

$$\begin{aligned} & \nabla \cdot \Sigma \nabla_{\perp} \phi - \nabla_{\perp} \cdot \psi \nabla \phi \times \hat{z} + \frac{2T}{e} \nabla_{\perp}^2 \Sigma \\ & + \frac{Mg}{e} \cos D \left(\frac{\partial \Sigma}{\partial x} + \frac{\partial \psi}{\partial y} \right) + \frac{2T}{e} \frac{\cos D}{H} \\ (x) & \left(\frac{\partial \Sigma}{\partial x} + 2 \frac{\partial \psi}{\partial y} \right) - \frac{g \cos D}{\omega_{ci}} \frac{\partial N}{\partial y} \\ & + \text{order } (v_{in}^3/\omega_{ci}^3) = 0 \quad (4.5) \end{aligned}$$

$$\begin{aligned} & \frac{\partial \Sigma}{\partial t} + \nabla_{\perp} \Sigma \cdot \left(\frac{g \times \hat{z}}{\omega_{ci}} - \frac{c}{B} \nabla \phi \times \hat{z} \right) + \nabla_{\perp} \cdot \psi \\ (x) & \left(\frac{g_{\perp}}{\omega_{ci}} - \frac{c}{B} \nabla \phi \right) = \frac{2T}{M \omega_{ci}} \nabla_{\perp}^2 \psi \\ & + \frac{6T}{MH \omega_{ci}} \cos D \cdot \frac{\partial \psi}{\partial x} + \frac{c}{B} \frac{\cos D}{H} \left(\frac{\partial \phi}{\partial y} \Sigma + \frac{\partial \phi}{\partial x} \psi \right) \\ & + \frac{ecg \sin^2 D N}{B H \omega_{ci}^2} + \frac{\cos^2 D}{H \omega_{ci}} \psi \left(\frac{4T}{MH} + g \right) + \text{order } (v_{in}^3/\omega_{ci}^3) \quad (4.6) \end{aligned}$$

Since ψ/Σ is of the order (v_{in}/ω_{ci}) , terms containing ψ are negligible when compared with Σ terms of similar structure. This means, for example, that $\left| \frac{\partial \psi}{\partial y} \right| \ll \left| \frac{\partial \Sigma}{\partial x} \right|$, suggesting that the gradients involved, whether equilibrium gradients or gradients from the perturbation, tend to have similar scale lengths. Equations 4.5 and 4.6 can now be reduced:

$$\begin{aligned} \nabla_{\perp} \cdot \Sigma \nabla_{\perp} \phi + \frac{2T}{e} \nabla_{\perp}^2 \Sigma + \frac{Mg}{e} \cos D \frac{\partial \Sigma}{\partial x} \\ + \frac{2T}{e} \frac{\cos D}{H} \frac{\partial \Sigma}{\partial x} - \frac{g \cos D}{\omega_{ci}} \frac{\partial N}{\partial y} = 0 \quad (4.7) \end{aligned}$$

$$\begin{aligned} \frac{\partial \Sigma}{\partial t} + \nabla_{\perp} \Sigma \cdot \left(\frac{g x \hat{z}}{\omega_{ci}} - \frac{c}{B} \nabla \phi \times \hat{z} \right) \\ = \frac{2T}{M \omega_{ci}} \nabla_{\perp}^2 \psi + \frac{6T}{M \omega_{ci} H} \cos D \frac{\partial \psi}{\partial x} \\ + \frac{c}{B} \frac{\cos D}{H} \frac{\partial \phi}{\partial y} \Sigma + \frac{ec g \sin^2 D N}{B H \omega_{ci}} \quad (4.8) \end{aligned}$$

The only significant addition for the instability analysis is the $\nabla_{\perp}^2 \psi$ term, which is a diffusion term. Since the perturbations are of the form $e^{i\mathbf{k} \cdot \mathbf{x}_{\perp} + \gamma t}$, it is seen that the $\partial \psi / \partial x$ term will not contribute to the real part of the growth rate. The $\nabla_{\perp}^2 \psi$ term is expected to be important when:

$$\frac{2T}{M \omega_{ci}^2} \psi k^2 \sim \frac{c}{B} E_{RESY} \frac{\cos D}{H} \Sigma$$

Using $\psi/\Sigma \sim v_{in}/\omega_{ci}$, one can obtain an estimate of the wavelength of the perturbation required for this term to be important:

$$\lambda \sim \sqrt{\frac{8 \pi^2 T v_{in}/\omega_{ci} H}{M \omega_{ci}^2 \cos D \cdot \frac{c}{B} E_{RESY}}} \approx 65 \text{ meters}$$

where the following parameters were used: $v_{in}/\omega_{ci} = 10^{-3}$, $H = 50 \text{ km}$, $kT = 10^{-13} \text{ erg}$, $\omega_{ci} = 200 \text{ sec}$ and $\frac{c}{B} E_{RESY} = 20 \text{ m/s}$.

To find the contribution of the growth rate from the $\nabla^2 \psi$ term, an expression for ψ must be obtained. It is possible to derive a fourth moment equation describing the time evolution of the Hall conductivity by multiplying the ion continuity equation by $\frac{ec}{B} (v_{in}/\omega_{ci})^2$ and integrating along a field line.

$$\begin{aligned} \frac{\partial \psi}{\partial t} + \nabla_{\perp} \psi \cdot \left(\frac{\mathbf{g} \times \hat{\mathbf{z}}}{\omega_{ci}} - \frac{c}{B} \nabla \phi \times \hat{\mathbf{z}} \right) \\ = \frac{2 \cos D}{H} \frac{c}{B} \psi \frac{\partial \phi}{\partial y} + \frac{2 \sin^2 D}{H \omega_{ci}} \Sigma \left(\frac{2T}{MH} + g \right) \\ + \text{order } (v_{in}^3/\omega_{ci}^3) \end{aligned} \quad (4.9)$$

One approach for obtaining ψ would be to use Equation 4.9. This appears to be straightforward if one neglects terms of order v_{in}^3/ω_{ci}^3 . Unfortunately, in the short wavelength limit, terms of order v_{in}^3/ω_{ci}^3 can become important. One is then not able to close the set of moment equations, since terms of order v_{in}^3/ω_{ci}^3 involve higher order moments.

The effect of this truncation problem is only evident at short wavelengths. If one carried the moment equations to any order, and truncated them to that order, the growth rate would be the Perkins growth rate (Equation 2.14) for all but the short wavelengths, where the expansion method would break down.

It is clear that a method to close the moment equations must be adopted that does not involve arbitrary truncation if the short wavelength dependence is desired. Two ways will now be presented that give essentially the same results.

The first method is to express ψ in terms of Σ , in an ad-hoc manner. Based on the definition of ψ , the following seems a good choice:

$$\psi = \left\langle \frac{v_{in}}{\omega_{ci}} \right\rangle \frac{ec}{B} \int n \frac{v_{in}}{\omega_{ci}} dz$$

where

$$\left\langle v_{in} \right\rangle = \frac{\int \frac{v_{in}}{\omega_{ci}} n dz}{\int n dz}$$

Using the definition of Σ and N , one obtains:

$$\psi = \frac{B}{ec} \frac{\Sigma^2}{N} \quad (4.10)$$

If it is assumed that N is constant during growth, equations 4.7 and 4.8 can be linearized using:

$$\psi = \frac{B}{ec} \left(\frac{\Sigma_0^2}{N_0} + 2 \frac{\Sigma_0}{N_0} \Sigma_1 \right) \quad (4.11)$$

It is easily shown that for perturbations of the form $e^{i\mathbf{k} \cdot \mathbf{x} + \gamma t}$, the term $\nabla^2 \psi$ adds a damping term to the growth rate:

$$\gamma = \gamma_{\text{PERKINS}} - \frac{4T}{e^2} \frac{\Sigma_0}{N_0} k_{\perp}^2 \quad (4.12)$$

The additional term will dominate as the wavelength approaches values on the order 20-40 meters.

The equilibrium solution is the same as was found for the Perkins model. There is no reason to suspect gradients in the Hall conductivity in the absence of gradients in the Pedersen conductivity. Thus, Equation 2.12 still describes the equilibrium condition.

A somewhat "ad-hoc" method was adopted to close the moment equations, so an alternative method, based on the use of Equation 4.9 is now presented. Assuming that the changes in ψ in time and space are small in the equilibrium, one obtains:

$$\frac{2 \cos D}{H} \frac{c}{B} \psi_0 E_{oy} = \frac{2 \sin^2 D}{H \omega_{ci}} \Sigma_0 \left(\frac{2T}{MH} + g \right)$$

Since $H = \frac{T}{Mg}$, and the mass of the neutrals is assumed to be the same as the mass the ions in the F region, one can write:

$$\psi_0 = \frac{3 B g \sin^2 D \cdot \Sigma_0}{\cos D c E_{oy} \omega_{ci}} = \frac{3B}{ec} \frac{\Sigma_0^2}{N_0} \quad (4.13)$$

Assuming that the perturbed state does not deviate greatly from the equilibrium, ψ_0 , Σ_0 and N_0 are replaced by ψ , Σ , and N .

The result:

$$\psi \approx 3 \frac{B}{ec} \frac{\Sigma^2}{N}$$

differs from Equation 4.10 by a factor of 3, so the damping contribution to the growth rate will only differ by a factor of $\sqrt{3}$. This would enable the perturbations of wavelengths shorter than 35 to 70 meters to be damped.

It has been shown in this section that there are problems associated with the closure of the Perkins moment equations when the wavelengths of the perturbed plasma layer becomes short. It is necessary to adopt a closure scheme based on intuition, and extreme care must be taken when the equations are truncated to any order.

It has been demonstrated that the short wavelength damping term is contained in the Hall conductivity terms that were neglected by Perkins (1973). Two methods of closure were presented that gave essentially the same results, except for a numerical coefficient. Neither of these approaches is fully satisfactory, so the question of the correct numerical coefficient for the short wavelength damping term can not be considered resolved at this time.

4.2.2 E Region Coupling

The Perkins model assumes that the E region contribution to the field integrated Pedersen conductivity is negligible. However, Zinchenko (1976) found that at the Arecibo Observatory the E and F

region Pedersen conductivities can be of the same order magnitude. (Figures 66 and 67). He also found that the E region Hall conductivity can be a factor of 10 greater than the F region Pedersen conductivity, but this does not turn out to be of significance in the present work. This point will be discussed later.

In this section, the effect of the large E region conductivities will be discussed in the framework of the flux tube model of Perkins (1973).

It is first noted from Figure 7 that the E and F regions can be treated as two separate regions. For the Arécibo data, on which the Zinchenko (1976) calculations are based, the E region extends from 82 km to 180 km, and the F region is considered to be heights greater than 180 km. One can not, for the Perkins model, extend the limit of integration into the E region because in the E region v_{in}/ω_{ci} is of order unity (or larger). An expansion of σ_P and σ_H in powers of v_{in}/ω_{ci} is not valid.

Because of this, it is not possible to develop a closed set of moment equations for the E region by the same method as that used by Perkins (1973). However, it is still possible to develop a model based on physical intuition which includes the effects of the high E region conductivities. This model can be explained with the help of Figure 68.

As shown, the E and F regions are two separate regions of the ionosphere connected by the magnetic field lines. The resistance to electron flow along the field lines is almost zero, so electrons can easily flow between the two regions. The Perkins model of F_s states

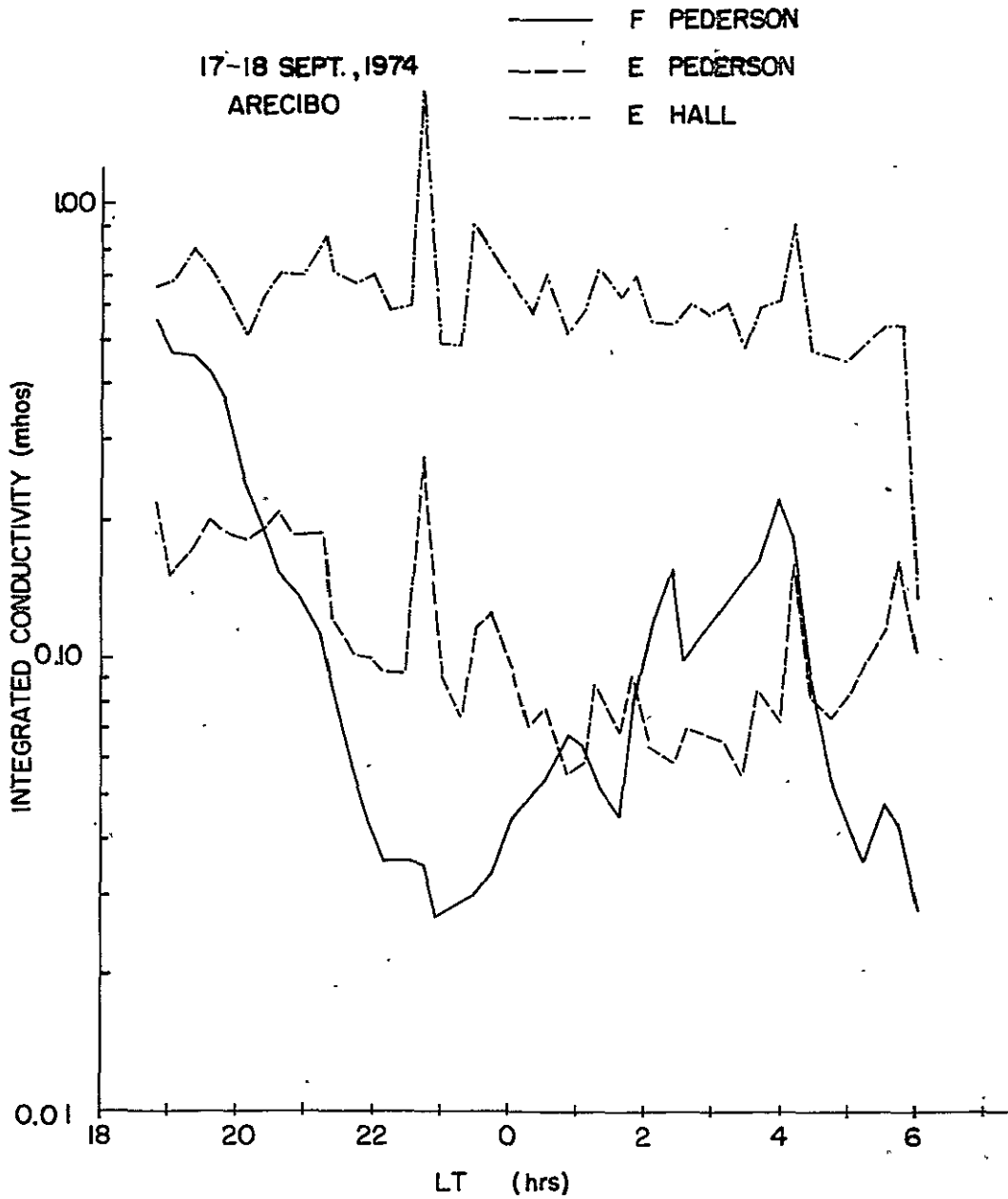


Figure 66: Time variation of integrated F region Pedersen conductivity, and E region Pedersen and Hall conductivities (from Zinchenko, 1976).

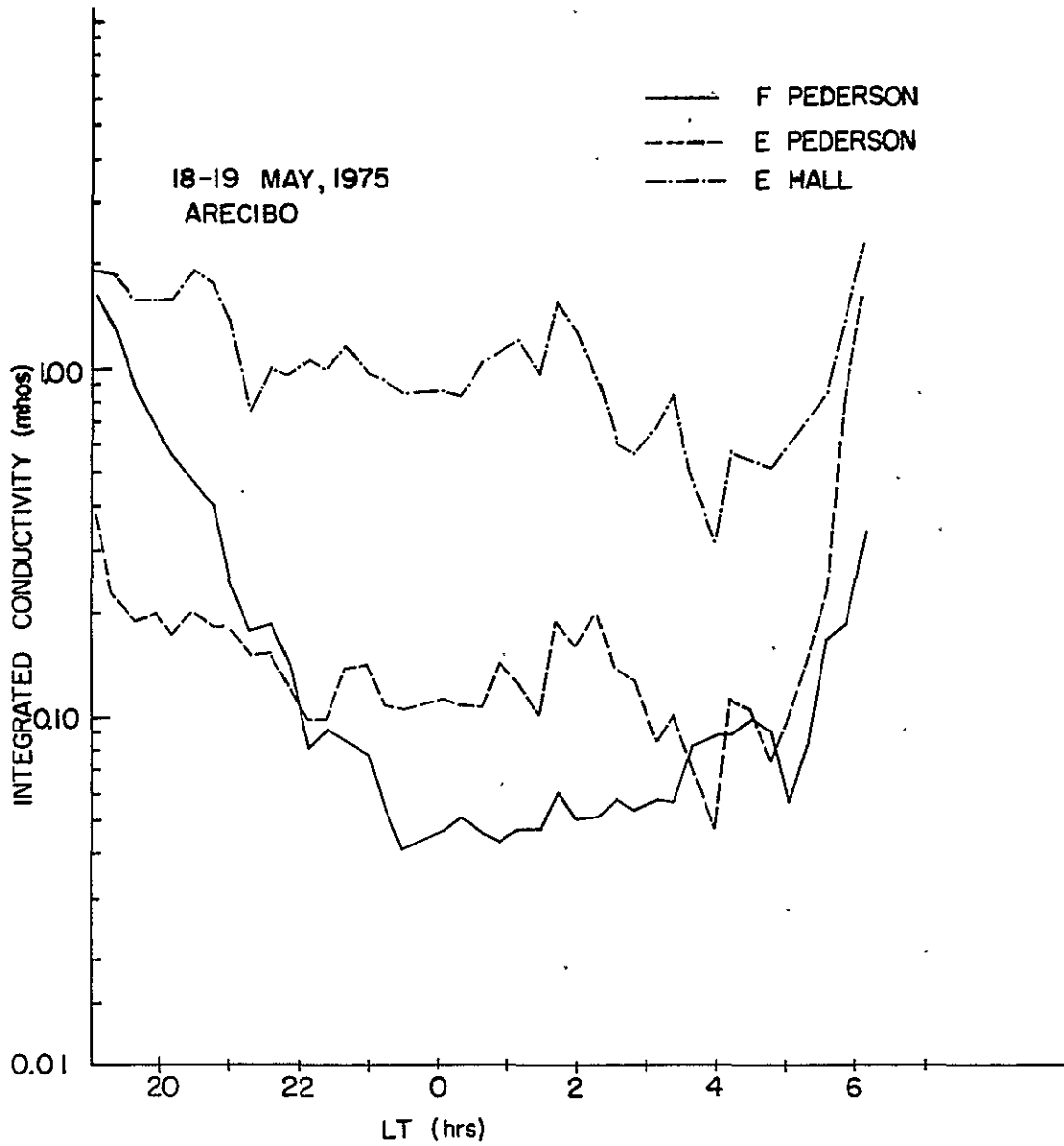


Figure 67: Time variation of integrated F region Pedersen conductivity, and E region Pedersen and Hall conductivities (from Zinchenko, 1976).

that a discontinuous electric field will be produced when the F region is perturbed in the manner shown in Figure 4.

Because of the high conductivity along \underline{B} , the field lines are assumed to be equipotentials. This will cause the same discontinuous field to appear in the E region. If the E region has a higher transverse conductivity than the F region, the particles can flow across field lines easily in the E region, (Path II) and equalize the electric fields in the E region. Because the field lines are equipotentials, electrons will then flow up the field lines to the F region and equalize the electric fields there. Thus, the E region acts as a short circuit. The short circuiting currents are Pedersen currents; the Hall current of the E region does not enter into the model because it is perpendicular to the electric field.

In reality, there is resistance between the E and F regions. Zinchenko and Nisbet (1976) included the resistance between the two regions and found that the E and F regions can be considered decoupled when perturbations with wavelengths less than a few kilometers are considered. For longer wavelength perturbations, the two regions are coupled. Dyson et al., (1974) have observed that the irregularities associated with F_g do not usually have wavelengths longer than 10 km. It is suggested that the E region short circuiting mechanism might be the cause.

The two region model shown in Figure 68 is developed mathematically by first assuming that the E region conductivities are not perturbed by the instability developing in the F region.

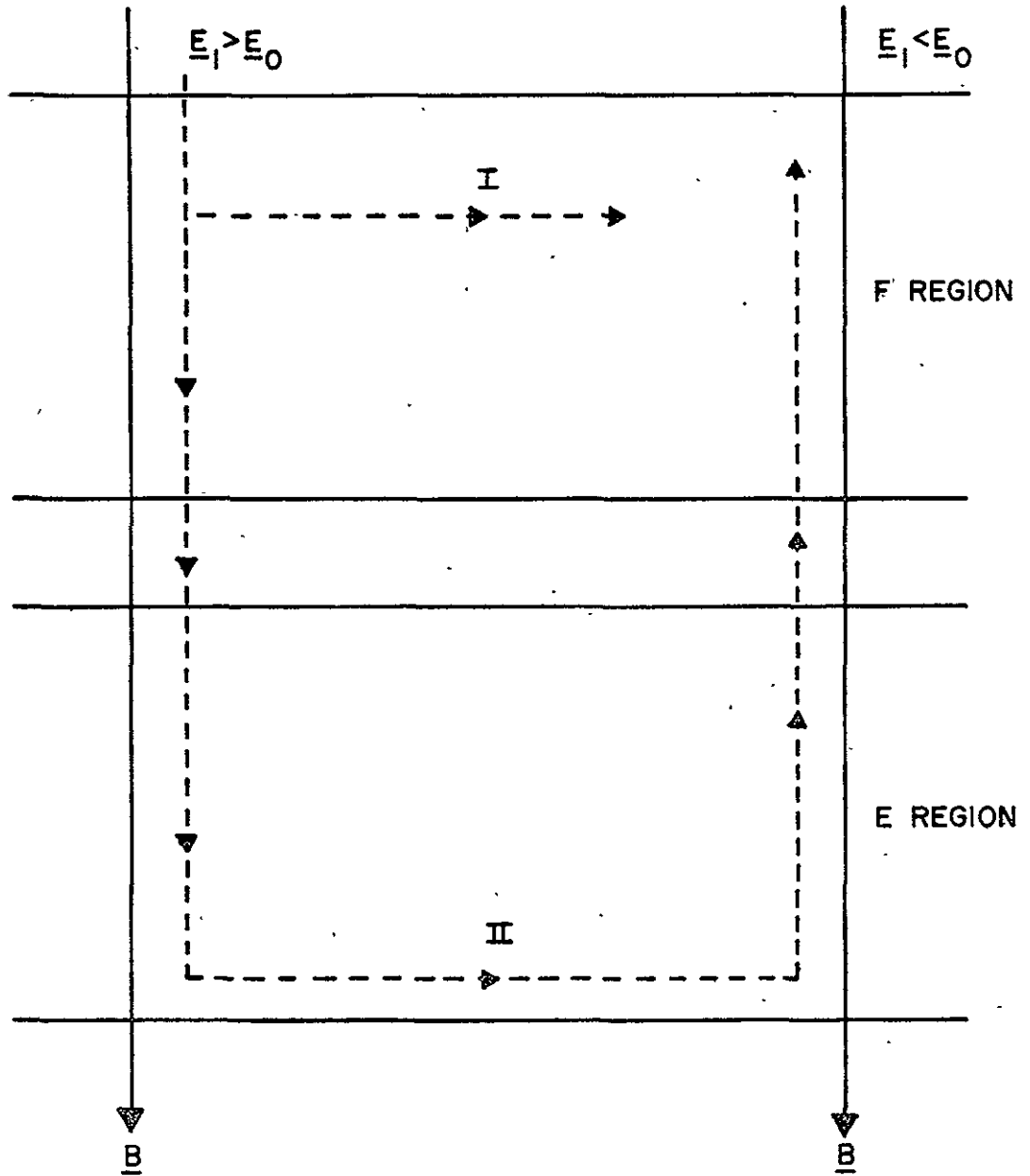


Figure 68: E region coupling model.

The assumption of plasma quasi-neutrality including the E region now states that:

$$\underline{\nabla}_{\perp} \cdot (\underline{J}_{\perp}^E + \underline{J}_{\perp}^F) = 0 \quad (4.14)$$

The major currents are assumed to be the E region Hall and Pedersen currents, and the F region Pedersen current.

$$\underline{J}_{\perp}^E = -\Sigma_P \underline{\nabla} \phi + \Sigma_H^E \underline{\nabla} \phi \times \hat{z} \quad (4.15)$$

$$\underline{J}_{\perp}^F = -\Sigma_F \underline{\nabla} \phi \quad (4.16)$$

where

$$\Sigma_P^E = \int_{\text{E REGION}} \frac{nec}{B} \frac{v_{in} \omega_{ci}}{v_{in}^2 + \omega_{ci}^2} dz$$

$$\Sigma_H^E = \int_{\text{E REGION}} \frac{nec}{B} \frac{\omega_{ci}^2}{v_{in}^2 + \omega_{ci}^2} dz$$

$$\Sigma_F = \int_{\text{F REGION}} \frac{nec}{B} \frac{v_{in}}{\omega_{ci}} dz$$

Assuming no gradients in the conductivities in the E region, Equations 4.14, 4.15 and 4.16 can be combined to yield the equation:

$$-\Sigma_P^E \nabla^2 \phi - \Sigma_F \nabla^2 \phi - \underline{\nabla}_{\perp} \Sigma_F \cdot \underline{\nabla}_{\perp} \phi = 0 \quad (4.17)$$

As was expected, the Hall current does not enter the analysis.

The analysis in Chapter III demonstrated that for the Perkins instability (horizontal uniformity in Σ_0), the effects of recombination and the resultant electric field adequately model the time evolution of the F region Pedersen conductivity.

$$\frac{\partial \Sigma_F}{\partial t} = \Sigma_F \frac{\partial \phi}{\partial y} \frac{c \cos D}{BH} - \bar{\beta} \Sigma_F \quad (4.18)$$

By linearizing Equation 4.18, and assuming a solution of the form $e^{i\mathbf{k} \cdot \mathbf{x} + \gamma t}$, the growth rate is found to be:

$$\gamma = (-E_{oy} + ik_y \Sigma_{F0} \frac{\phi_1}{\Sigma_{F1}}) \frac{c \cos D}{BH} - \bar{\beta} \quad (4.19)$$

The next step is to linearize Equation 4.17, solve for $\frac{\phi_1}{\Sigma_{F1}}$, and substitute the result in Equation 4.19. This yields:

$$\gamma = (-E_{oy} + \frac{k_y \mathbf{k} \cdot \mathbf{E}_0}{k^2} \frac{\Sigma_{F0}}{\Sigma_{F0} + \Sigma_P^E}) \frac{c \cos D}{BH} - \bar{\beta}$$

By using several trigonometric identities, one can rewrite the above expression as:

$$\gamma = \frac{c}{B} \frac{\cos D}{H} E_0 \left[\sin \alpha \sin (\theta - \alpha) \right. \\ \left. \frac{\Sigma_P^E}{\Sigma_P^E + \Sigma_{F0}} \cos \alpha \cos (\alpha - \theta) \right] - \bar{\beta}$$

The angles α and θ are defined in Figure 3.

Maximum growth occurs at $\alpha = \theta/2$.

$$\gamma_{\text{MAX}} = \frac{c}{B} \frac{\cos D}{H} E_0 \left[\sin^2 \theta/2 - \frac{\Sigma_P^E}{\Sigma_P^E + \Sigma_{F0}^E} \cos^2 \theta/2 \right]$$

$$- \bar{\beta} - \frac{4T}{e^2} \frac{\Sigma_{F0}^E}{N_{F0}} k_{\perp}^2 \quad (4.20)$$

The short wavelength dependence has been added for completeness.

Equation 4.20 is the final form of the growth rate for a model that includes recombination, E region coupling, and short wavelength diffusion. The first term is readily identified as the growth rate of the Perkins model. The additional terms all contribute to damping of the instability and will be important under different conditions. The term describing the wavelength dependence of the growth rate is only significant at short wavelengths. Assuming that $T = 1000^\circ\text{K}$ and $\Sigma_{F0}^E/N_{F0} = 0.1$, which are overestimations so that the maximum damping effect can be realized, the wavelength term can be written as:

$$\gamma_{\lambda} = \frac{-10^4}{\lambda^2} \text{ sec}^{-1}$$

This term would have to be on the order of $1/600 \text{ sec}^{-1}$ to $1/1800 \text{ sec}^{-1}$ to damp the positive term from the Perkins growth rate calculated in Tables 1-4. To yield this result, the wavelength would have to be on the order of 25 to 40 meters. This is normally much less than the

wavelength of the irregularities associated with F_s , (Dyson et al., 1974), suggesting that a damping mechanism may well exist.

The recombination term is only important when the layer is low. Observations indicate that F_s usually does not occur when the layer is low; damping by recombination may be a contributory factor under those conditions.

For the September night, $\bar{\beta} = 1.47 \times 10^{-6} \text{ sec}^{-1}$ at 22.47 when the layer was high, $1.69 \times 10^{-5} \text{ sec}^{-1}$ when onset occurred around 21.83, and $5.4 \times 10^{-4} \text{ sec}^{-1}$ at 0400 when the layer was low. The only significant addition to the growth rate for these three cases is at 0400. Assuming that the positive piece, which is the Perkins growth rate, is in the range of $1/600 \text{ sec}^{-1}$ to $1/1800 \text{ sec}^{-1}$, recombination will subtract values of the order of $5.4 \times 10^{-4} \text{ sec}^{-1}$ from this at 0400. Because $5.4 \times 10^{-4} \text{ sec}^{-1}$ is around $1/1800 \text{ sec}$, recombination would obviously have an effect, especially for the slower growth rate. In general, however, for onset conditions the layer is high enough that recombination will be a negligible effect.

The E region coupling term is hard to analyze because of the degree of uncertainty in E region conductivities. The source of the uncertainty becomes clear if one looks at the amount of fluctuations in the density profiles in the E region shown in Figure 7. However, if one looks at integrated conductivities only, as Zinchenko (1976) did, the integration process smooths some of the fluctuations.

Values of Σ_P^E and Σ_F are taken from Figures 64 and 65 at the onset times. These are:

September 17:

$$\Sigma_P^E = .1 \text{ mhos}$$

$$\Sigma_F = .05 \text{ mhos}$$

$$\frac{\Sigma_P^E}{\Sigma_P^E + \Sigma_{F0}} \approx .67$$

May 18:

$$\Sigma_P^E = .2 \text{ mhos}$$

$$\Sigma_F = 1 \text{ mho}$$

$$\frac{\Sigma_P^E}{\Sigma_P^E + \Sigma_{F0}} \approx .17$$

Equation 4.20 is rewritten assuming that the layer is high so recombination can be neglected and the wavelength of the perturbation is long so the diffusion term can be neglected:

$$\gamma = \frac{c}{B} \frac{\cos D}{H} E_0 \left[\sin^2 \theta/2 - \frac{\Sigma_P^E}{\Sigma_P^E + \Sigma_{F0}} \cos^2 \frac{\theta}{2} \right]$$

The values of V_{NY} calculated in Tables 1-4 were such that growth rates of $1/600 \text{ sec}^{-1}$ and $1/1800 \text{ sec}^{-1}$ were obtained from the first piece of this expression, which will be called γ_P .

$$\gamma = \gamma_P \left[1 - \frac{\Sigma_P^E}{\Sigma_P^E + \Sigma_{F0}} \frac{\cos^2 \theta/2}{\sin^2 \theta/2} \right]$$

where γ_P is in the range of $1/600 \text{ sec}^{-1}$ to $1/1800 \text{ sec}^{-1}$. To produce the smallest E region effect, set θ equal to $\pi/2 - \epsilon$, where ϵ is just large enough to yield an equilibrium eastward field. Assuming that ϵ is small, one can write:

$$\gamma = \gamma_P \left[1 - \frac{\Sigma_P^E}{\Sigma_P^E + \Sigma_{F0}} \right]$$

Thus, for the September night at onset, the E region coupling will reduce the growth rate by at least 67 per cent, while for the May night, it is reduced by only 17 per cent. Clearly, the E region coupling can have a significant effect on the growth rate.

CHAPTER V

SUMMARY AND CONCLUSIONS

In this thesis the current models of mid-latitude F_s were studied in detail. The Perkins flux tube model, which has led to two different mechanisms for F region instability, depending on the equilibrium state, seems especially promising for describing the nighttime F region at midlatitudes. Because particles are tied tightly to the field lines in the F region, the concept of a flux tube is a physical one. Also, the premise of the model that the nighttime ionosphere is supported by Pedersen currents and neutral winds agrees with the findings of Behnke and Kohl (1974).

To compare the predictions of equilibrium theory with data from the Arecibo Observatory, the Perkins model was then extended to include recombination and boundary terms. Also, the neutral wind was added explicitly to the model by deriving the equations in a stationary reference frame.

Data from four nights of observations at the Arecibo Observatory were analyzed. It was found that the resultant eastward electric field, defined as

$$\frac{c}{B} E_{RESY} = + \frac{c}{B} E_{oy} - V_{NX}$$

is extremely well correlated with the motion of the F layer. This indicates that Perkins (1973) was correct in assuming that the layer is supported by the eastward electric field and southward neutral

wind (cf. Equation 2.12). Good correlation was also found between the field integrated conductivity and the motion of the layer, also supporting the Perkins model..

The flux data were immediately seen to be in poor agreement with the rest of the data. Above 300 km there should be no significant change in the flux with altitude, because there are no sources or losses. The data showed large differences. It was found that the flux data did not agree at all with the data on the integrated plasma content. It was first thought that perhaps the interval of integration was too large, thus accentuating the difference between the top flux and the bottom flux. Also, there were times that the S/N ratio was poor at the boundaries because the layer moved toward the edge of the integration interval.

A method of analysis was proposed in which the interval of integration was narrowed and followed the vertical motion of the peak. This guarantees a good S/N ratio at the boundaries. Nonetheless, this method of analysis did not resolve the difficulties associated with the flux data because the flux difference for even adjacent heights was too large. The net flux into or out of a flux tube is much too large and turbulent, while the total content of the flux tube does not change much. There are only two ways to explain this flux behavior: either there is a large density gradient moving into the region of observation, or the flux data contains much greater errors than has previously been assumed. It was concluded that the latter is the more likely possibility.

The Perkins model was found to predict the general time behavior of the plasma content and Pedersen conductivity of a flux tube when recombination is added. Recombination was found to be a necessary addition to the model when the layer is low.

The quasi-equilibrium of the Perkins model was compared with the data. It was found that the model agreed with the data for a large percentage of the time for three of the four days studied. In comparing the days with F_g , it was found that the quasi-equilibrium assumption around the time of onset was a good one for only one of the days. For the other day, the time scale for changes in Σ and \underline{E}_0 were much too rapid to assume a quasi-equilibrium.

An attempt was made to analyze the growth rates predicted by the Perkins model and the Scannapieco model using the Arecibo data. However, it was immediately found that there are not sufficient data to calculate even linear growth rates. The quantities that are missing are the direction of propagation of the irregularities, the east-west component of the neutral wind, and the horizontal gradient of the field integrated Pedersen conductivity. To properly analyze the models of F_g , an experiment must be designed expressly for that purpose. The following quantities must be obtained simultaneously:

- (1) drift velocities;
- (2) east-west neutral winds;
- (3) density profiles;
- (4) propagation direction of the irregularities and wavelength, if possible;
- (5) horizontal gradients of the field integrated Pedersen conductivities.

Only when all of these quantities are obtained simultaneously will complete judgement of all the models be possible. It was found, however, that the magnitude of the neutral wind velocity

required to give reasonable growth times in the Perkins model is plausible. Also, the Scannapieco model will predict reasonable growth times if the characteristic length of the east-west gradient in the Pedersen conductivity is on the order of 100 km.

The growth rate formula of the Perkins model was extended also. It was demonstrated that a short wavelength damping term is contained in the Hall conductivity terms that were neglected by Perkins (1973). Recombination was added as a damping term that is only important when the layer is low. A model was also developed to include the effects of the high E region conductivity. It was shown that the E region can short-circuit the Perkins instability for long wavelengths (at least a few kilometers) if the E region conductivities are large enough.

Further study of mid-latitude F_s is clearly required. An experiment should be designed solely for this purpose. In the meantime, there is much work to be done on the data that is presently available. A detailed study of more nights should be done to determine the qualitative behavior of ionospheric parameters both during F_s conditions and quiet conditions. In addition, data from other mid-latitude stations should be analyzed. Density contour maps, which can be obtained from the available Arecibo data, would help resolve the question of the magnitude of horizontal density gradients. Clearer ionograms should be obtained; with higher resolution ionograms the intensity of F_s vs. the equilibrium ionospheric parameters can be studied. It is also possible to obtain information about the wavelength of the irregularities from good ionograms.

The model of E and F region coupling proposed in this thesis is clearly an oversimplification. A better model would include the resistivity between the E and F regions. Also, the response of the E region to F region instabilities should be included, rather than treating the E region as a constant sink, as was done in the proposed model.

This thesis has concentrated on equilibrium parameters and linear instabilities. The turbulent structure is also important. To study this, a non-linear computer simulation of the Perkins instability is required, similar to that performed by Scannapieco et al., (1975). Short pulse radar techniques (Rino and Livingston, 1974) could possibly supply information on the turbulent structure to compare with the simulations.

Finally, the question of flux behavior requires further investigation. Contour plots of the plasma velocities and of the flux may help to illuminate the flux behavior. A careful evaluation of the method of data reduction of plasma velocities should be undertaken with the view of obtaining better error estimates.

APPENDIX

DESCRIPTION OF ARECIBO MODEL USED FOR CALCULATION OF COLLISION FREQUENCY

A base collision frequency at 102 km, and a temperature profile for the heights 100 km to 137 km must be supplied. The base collision frequency was chosen as 3000 sec^{-1} , and the temperature profile is

<u>H (km)</u>	<u>T (°K)</u>
99.1	197.0
102.5	200.0
106.0	212.0
109.5	241.0
113.0	286.0
116.4	335.0
119.9	376.0
123.4	423.0
126.9	464.0
130.4	497.0
137.3	520.0

The neutral atmosphere densities at the base are then calculated,

$$n_b = 2.68 \times 10^9 * (v_{in})_b$$

$$n_b(N_2) = .759 * n_b$$

$$n_b(O_2) = .1758 * n_b$$

$$n_b(O) = .0558 * n_b$$

The exospheric temperature (T_{ex}) is defined as the average of the temperatures measured at 317.6 km and 346.5 km. The temperature profile above 137 km is calculated using the following model:

$$T(h) = T_{ex} - (T_{ex} - T_{137.0}) e^{-.028 (h-137.0)}$$

The neutral atmosphere density above the base (102 km) is calculated using the expression:

$$N = \frac{N_{base} \times T_{base}}{T} e^{-h/H}$$

where $H = \frac{KT}{Mg}$, and M is the mass of the neutral species whose density is being calculated.

The collision frequencies are calculated for various height ranges using the expressions:

102-215 km:

$$\begin{aligned} v_{in} &= 3.6 \times 10^{-10} * n(N_2) + 4.368 \times 10^{-10} * n(O_2) \\ &+ 2.02 \times 10^{-10} * n(O) \end{aligned}$$

215-463 km:

$$\begin{aligned} v_{in} &= 5.855 \times 10^{-10} * n(N_2) + 6.8 \times 10^{-10} * n(O_2) \\ &+ 7.3 \times 10^{-10} * n(O) \end{aligned}$$

The collision frequencies below the base are calculated using:

$$\nu_{in} = (\nu_{in})_b e^{h/H}$$

A mass of 28.0 is used for this expression.

The neutral atmosphere densities are extended below the base using the expressions:

$$N_{DENS} = N_{base} e^{h/H}$$

$$n(N_2) = .759 \times N_{DENS}$$

$$n(O_2) = (.1758 + \frac{.0279 \times h}{102-82}) \times N_{DENS}$$

$$n(O) = .0558 (1.0 - \frac{h}{102-82}) \times N_{DENS}$$

REFERENCES

- Balsley, B. B., G. Haerendal and R. A. Greenwald, Equatorial spread F: recent observations and a new interpretation, J. Geophys. Res., 77, 5025, 1972.
- Behnke, R. and R. Harper, Vector measurements of F region ion transport at Arecibo, J. Geophys. Res., 78, 8222, 1973.
- Behnke, R. and H. Kohl, The effects of neutral winds and electric fields on the ionospheric F₂ layer over Arecibo, J. Atmos. and Terr. Phys., 36, 325, 1974.
- Cunnold, D. M., Drift-dissipative plasma instability and equatorial spread F, J. Geophys. Res., 74, 5709, 1969.
- Dyson, P. L., J. P. McClure and W. B. Hanson, In situ measurements of the spectral characteristics of F region ionospheric irregularities, J. Geophys. Res., 79, 1497, 1974.
- Evans, J. V., Theory and practice of ionosphere study by Thomson scatter radar, Proc. of the IEEE, 57, 496, 1969.
- Farley, D. T., Irregularities in the equatorial ionosphere: The Berkner Symposium, Rev. Geophys. and Space Physics, 12, 285, 1974.
- Farley, D. T., B. B. Balsley, R. F. Woodman and J. D. McClure, Equatorial spread F: Implications of VHF radar observations, J. Geophys. Res., 75, 7199, 1970.
- Harper, R. M., Nighttime meridional neutral winds near 350 km at low to mid-latitudes, J. Atmos. and Terr. Physics, 35, 2023, 1973.
- Herman, J. R., Spread F and ionospheric F-region irregularities, Rev. Geophys., 4, 255, 1966.
- Hudson, M. K. and C. F. Kennel, Linear theory of equatorial spread F, J. Geophys. Res., 80, 4581, 1975.
- Kelley, M. C., Relationship between electrostatic turbulence and spread F, J. Geophys. Res., 77, 1327, 1972.
- Matthews, J. D. and R. M. Harper, Incoherent scatter radar observations of spread-F producing ionospheric structures at Arecibo, J. Atmos. and Terr. Phys., 34, 1119, 1972.
- McClure, J. P. and R. F. Woodman, Radar observations of equatorial spread F in a region of electrostatic turbulence, J. Geophys. Res., 77, 5617, 1972.

- McDonald, B. E., S. L. Ossakow, T. P. Coffey, R. N. Sudan, A. J. Scannapieco and S. R. Goldman, Recent results from theoretical and numerical modeling of E and F region irregularities, IES Symposium, Arlington, Virginia, 1975.
- Rino, C. L. and R. C. Livingston, Incoherent scatter measurements of ionospheric irregularity spectra, Trans. Am. Geophys. Un., 56, 1155, 1974.
- Perkins, F., Spread F and ionospheric currents, J. Geophys. Res., 78, 218, 1973.
- Reid, G. C., The formation of small-scale irregularities in the ionosphere, J. Geophys. Res., 73, 1627, 1968.
- Scannapieco, A. J., S. R. Goldman, S. L. Ossakow, D. L. Book and B. E. McDonald, Theoretical and numerical simulation studies of midlatitude F region irregularities, Naval Research Laboratory Report 3014, 1975.
- Vickrey, J. F., W. E. Swartz and D. T. Farley, Incoherent scatter measurements of ion counterstreaming, Geophys. Res. Letters, 217, 1976.
- Williams, R. H. and J. Weinstock, Strong turbulence theory of ionospheric cross-field instability, J. Geophys. Res., 75, 7217, 1970.
- Zinchenko, G. N., A study of the conditions necessary for the onset of mid-latitude spread F, The Pennsylvania State University, PSU-IRL-SCI-445, 1976.
- Zinchenko, G. N. and J. S. Nisbet, Coupling of mid-latitude spread F between conjugate stations, submitted to J. Atmos. and Terr. Physics, 1976.

Imel, George, A Comparison Between the Current Models of Mid-Latitude Spread F and Data from the Arecibo Observatory, The Ionosphere Research Laboratory, Electrical Engineering East, University Park, Pennsylvania, 16802, 1977.

PSU-IRL-SCI-451

Classification Numbers:

1.5.3 F-Region

The current models of mid-latitude F_2 are studied. The assumptions and derivations of the Reid model, the Scannapieco model, and the Perkins model are presented in detail.

Incoherent-scatter data of the density profiles and velocity profiles were obtained from the Arecibo Observatory in order that the models could be evaluated on the basis of experimental data. Initial studies indicated that the Perkins model was most representative of the data from Arecibo, so a detailed comparison of the predictions of the Perkins model and the data was made. Two of four nights studied are nights with F_2 .

The Perkins model is derived in a frame of reference moving with the velocity of the neutral wind; the model is transformed to the rest frame to facilitate comparison with data. Several data handling techniques are introduced. In particular, an integration interval that remains constant in length, but follows the vertical motion of the peak of the F layer is used to obtain the field integrated quantities of the Perkins model.

It was found that the Perkins model describes the general time behavior of the field integrated Pedersen conductivity if recombination is included, and the boundary flux is neglected. The numerical agreement is usually within a factor of two. It was found that the flux data is inconsistent with the rest of the data. Errors on the order of 30 m/s in the individual velocity measurements are believed to be present to account for the differences.

The Perkins model is able to predict reasonable growth rates of the development of F_2 ; however, a direct comparison between the growth rates predicted by the model and actual onset times is not possible because of the lack of data on the eastward neutral wind.

The linear growth rate of the Perkins model is extended by including recombination, and a short wavelength damping term and coupling to the E region. It is found that, for wavelength perturbations several kilometers or longer, the E region can short circuit instabilities in the F region and reduce the growth rate.

Imel, George, A Comparison Between the Current Models of Mid-Latitude Spread F and Data from the Arecibo Observatory, The Ionosphere Research Laboratory, Electrical Engineering East, University Park, Pennsylvania, 16802, 1977.

PSU-IRL-SCI-451

Classification Numbers:

1.5.3 F-Region

The current models of mid-latitude F_2 are studied. The assumptions and derivations of the Reid model, the Scannapieco model, and the Perkins model are presented in detail.

Incoherent-scatter data of the density profiles and velocity profiles were obtained from the Arecibo Observatory in order that the models could be evaluated on the basis of experimental data. Initial studies indicated that the Perkins model was most representative of the data from Arecibo, so a detailed comparison of the predictions of the Perkins model and the data was made. Two of four nights studied are nights with F_2 .

The Perkins model is derived in a frame of reference moving with the velocity of the neutral wind; the model is transformed to the rest frame to facilitate comparison with data. Several data handling techniques are introduced. In particular, an integration interval that remains constant in length, but follows the vertical motion of the peak of the F layer is used to obtain the field integrated quantities of the Perkins model.

It was found that the Perkins model describes the general time behavior of the field integrated Pedersen conductivity if recombination is included, and the boundary flux is neglected. The numerical agreement is usually within a factor of two. It was found that the flux data is inconsistent with the rest of the data. Errors on the order of 30 m/s in the individual velocity measurements are believed to be present to account for the differences.

The Perkins model is able to predict reasonable growth rates of the development of F_2 ; however, a direct comparison between the growth rates predicted by the model and actual onset times is not possible because of the lack of data on the eastward neutral wind.

The linear growth rate of the Perkins model is extended by including recombination, and a short wavelength damping term and coupling to the E region. It is found that, for wavelength perturbations several kilometers or longer, the E region can short circuit instabilities in the F region and reduce the growth rate.

Imel, George, A Comparison Between the Current Models of Mid-Latitude Spread F and Data from the Arecibo Observatory, The Ionosphere Research Laboratory, Electrical Engineering East, University Park, Pennsylvania, 16802, 1977.

PSU-IRL-SCI-451

Classification Numbers:

1.5.3 F-Region

The current models of mid-latitude F_2 are studied. The assumptions and derivations of the Reid model, the Scannapieco model, and the Perkins model are presented in detail.

Incoherent-scatter data of the density profiles and velocity profiles were obtained from the Arecibo Observatory in order that the models could be evaluated on the basis of experimental data. Initial studies indicated that the Perkins model was most representative of the data from Arecibo, so a detailed comparison of the predictions of the Perkins model and the data was made. Two of four nights studied are nights with F_2 .

The Perkins model is derived in a frame of reference moving with the velocity of the neutral wind; the model is transformed to the rest frame to facilitate comparison with data. Several data handling techniques are introduced. In particular, an integration interval that remains constant in length, but follows the vertical motion of the peak of the F layer is used to obtain the field integrated quantities of the Perkins model.

It was found that the Perkins model describes the general time behavior of the field integrated Pedersen conductivity if recombination is included, and the boundary flux is neglected. The numerical agreement is usually within a factor of two. It was found that the flux data is inconsistent with the rest of the data. Errors on the order of 30 m/s in the individual velocity measurements are believed to be present to account for the differences.

The Perkins model is able to predict reasonable growth rates of the development of F_2 ; however, a direct comparison between the growth rates predicted by the model and actual onset times is not possible because of the lack of data on the eastward neutral wind.

The linear growth rate of the Perkins model is extended by including recombination, and a short wavelength damping term and coupling to the E region. It is found that, for wavelength perturbations several kilometers or longer, the E region can short circuit instabilities in the F region and reduce the growth rate.

Imel, George, A Comparison Between the Current Models of Mid-Latitude Spread F and Data from the Arecibo Observatory, The Ionosphere Research Laboratory, Electrical Engineering East, University Park, Pennsylvania, 16802, 1977.

PSU-IRL-SCI-451

Classification Numbers:

1.5.3 F-Region

The current models of mid-latitude F_2 are studied. The assumptions and derivations of the Reid model, the Scannapieco model, and the Perkins model are presented in detail.

Incoherent-scatter data of the density profiles and velocity profiles were obtained from the Arecibo Observatory in order that the models could be evaluated on the basis of experimental data. Initial studies indicated that the Perkins model was most representative of the data from Arecibo, so a detailed comparison of the predictions of the Perkins model and the data was made. Two of four nights studied are nights with F_2 .

The Perkins model is derived in a frame of reference moving with the velocity of the neutral wind; the model is transformed to the rest frame to facilitate comparison with data. Several data handling techniques are introduced. In particular, an integration interval that remains constant in length, but follows the vertical motion of the peak of the F layer is used to obtain the field integrated quantities of the Perkins model.

It was found that the Perkins model describes the general time behavior of the field integrated Pedersen conductivity if recombination is included, and the boundary flux is neglected. The numerical agreement is usually within a factor of two. It was found that the flux data is inconsistent with the rest of the data. Errors on the order of 30 m/s in the individual velocity measurements are believed to be present to account for the differences.

The Perkins model is able to predict reasonable growth rates of the development of F_2 ; however, a direct comparison between the growth rates predicted by the model and actual onset times is not possible because of the lack of data on the eastward neutral wind.

The linear growth rate of the Perkins model is extended by including recombination, and a short wavelength damping term and coupling to the E region. It is found that, for wavelength perturbations several kilometers or longer, the E region can short circuit instabilities in the F region and reduce the growth rate.

Imel, George, A Comparison Between the Current Models of Mid-Latitude Spread F and Data from the Arecibo Observatory, The Ionosphere Research Laboratory, Electrical Engineering East, University Park, Pennsylvania, 16802, 1977.

The current models of mid-latitude F_2 are studied. The assumptions and derivations of the Reid model, the Scannapieco model, and the Perkins model are presented in detail.

Incoherent-scatter data of the density profiles and velocity profiles were obtained from the Arecibo Observatory in order that the models could be evaluated on the basis of experimental data. Initial studies indicated that the Perkins model was most representative of the data from Arecibo, so a detailed comparison of the predictions of the Perkins model and the data was made. Two of four nights studied are nights with F_2 .

The Perkins model is derived in a frame of reference moving with the velocity of the neutral wind, the model is transformed to the rest frame to facilitate comparison with data. Several data handling techniques are introduced. In particular, an integration interval that remains constant in length, but follows the vertical motion of the peak of the F layer is used to obtain the field integrated quantities of the Perkins model.

It was found that the Perkins model describes the general time behavior of the field integrated Pedersen conductivity if recombination is included, and the boundary flux is neglected. The numerical agreement is usually within a factor of two. It was found that the flux data is inconsistent with the rest of the data. Errors on the order of 30 m/s in the individual velocity measurements are believed to be present to account for the differences.

The Perkins model is able to predict reasonable growth rates of the development of F_2 ; however, a direct comparison between the growth rates predicted by the model and actual onset times is not possible because of the lack of data on the eastward neutral wind.

The linear growth rate of the Perkins model is extended by including recombination, and a short wavelength damping term and coupling to the E region. It is found that, for wavelength perturbations several kilometers or longer, the E region can short circuit instabilities in the F region and reduce the growth rate.

FSU-IRL-SCI-451

Classification Numbers:

1.5.3 F-Region

Imel, George, A Comparison Between the Current Models of Mid-Latitude Spread F and Data from the Arecibo Observatory, The Ionosphere Research Laboratory, Electrical Engineering East, University Park, Pennsylvania, 16802, 1977.

The current models of mid-latitude F_2 are studied. The assumptions and derivations of the Reid model, the Scannapieco model, and the Perkins model are presented in detail.

Incoherent-scatter data of the density profiles and velocity profiles were obtained from the Arecibo Observatory in order that the models could be evaluated on the basis of experimental data. Initial studies indicated that the Perkins model was most representative of the data from Arecibo, so a detailed comparison of the predictions of the Perkins model and the data was made. Two of four nights studied are nights with F_2 .

The Perkins model is derived in a frame of reference moving with the velocity of the neutral wind, the model is transformed to the rest frame to facilitate comparison with data. Several data handling techniques are introduced. In particular, an integration interval that remains constant in length, but follows the vertical motion of the peak of the F layer is used to obtain the field integrated quantities of the Perkins model.

It was found that the Perkins model describes the general time behavior of the field integrated Pedersen conductivity if recombination is included, and the boundary flux is neglected. The numerical agreement is usually within a factor of two. It was found that the flux data is inconsistent with the rest of the data. Errors on the order of 30 m/s in the individual velocity measurements are believed to be present to account for the differences.

The Perkins model is able to predict reasonable growth rates of the development of F_2 ; however, a direct comparison between the growth rates predicted by the model and actual onset times is not possible because of the lack of data on the eastward neutral wind.

The linear growth rate of the Perkins model is extended by including recombination, and a short wavelength damping term and coupling to the E region. It is found that, for wavelength perturbations several kilometers or longer, the E region can short circuit instabilities in the F region and reduce the growth rate.

FSU-IRL-SCI-451

Classification Numbers:

1.5.3 F-Region

Imel, George, A Comparison Between the Current Models of Mid-Latitude Spread F and Data from the Arecibo Observatory, The Ionosphere Research Laboratory, Electrical Engineering East, University Park, Pennsylvania, 16802, 1977.

The current models of mid-latitude F_2 are studied. The assumptions and derivations of the Reid model, the Scannapieco model, and the Perkins model are presented in detail.

Incoherent-scatter data of the density profiles and velocity profiles were obtained from the Arecibo Observatory in order that the models could be evaluated on the basis of experimental data. Initial studies indicated that the Perkins model was most representative of the data from Arecibo, so a detailed comparison of the predictions of the Perkins model and the data was made. Two of four nights studied are nights with F_2 .

The Perkins model is derived in a frame of reference moving with the velocity of the neutral wind, the model is transformed to the rest frame to facilitate comparison with data. Several data handling techniques are introduced. In particular, an integration interval that remains constant in length, but follows the vertical motion of the peak of the F layer is used to obtain the field integrated quantities of the Perkins model.

It was found that the Perkins model describes the general time behavior of the field integrated Pedersen conductivity if recombination is included, and the boundary flux is neglected. The numerical agreement is usually within a factor of two. It was found that the flux data is inconsistent with the rest of the data. Errors on the order of 30 m/s in the individual velocity measurements are believed to be present to account for the differences.

The Perkins model is able to predict reasonable growth rates of the development of F_2 ; however, a direct comparison between the growth rates predicted by the model and actual onset times is not possible because of the lack of data on the eastward neutral wind.

The linear growth rate of the Perkins model is extended by including recombination, and a short wavelength damping term and coupling to the E region. It is found that, for wavelength perturbations several kilometers or longer, the E region can short circuit instabilities in the F region and reduce the growth rate.

FSU-IRL-SCI-451

Classification Numbers:

1.5.3 F-Region

Imel, George, A Comparison Between the Current Models of Mid-Latitude Spread F and Data from the Arecibo Observatory, The Ionosphere Research Laboratory, Electrical Engineering East, University Park, Pennsylvania, 16802, 1977.

The current models of mid-latitude F_2 are studied. The assumptions and derivations of the Reid model, the Scannapieco model, and the Perkins model are presented in detail.

Incoherent-scatter data of the density profiles and velocity profiles were obtained from the Arecibo Observatory in order that the models could be evaluated on the basis of experimental data. Initial studies indicated that the Perkins model was most representative of the data from Arecibo, so a detailed comparison of the predictions of the Perkins model and the data was made. Two of four nights studied are nights with F_2 .

The Perkins model is derived in a frame of reference moving with the velocity of the neutral wind; the model is transformed to the rest frame to facilitate comparison with data. Several data handling techniques are introduced. In particular, an integration interval that remains constant in length, but follows the vertical motion of the peak of the F layer is used to obtain the field integrated quantities of the Perkins model.

It was found that the Perkins model describes the general time behavior of the field integrated Pedersen conductivity if recombination is included, and the boundary flux is neglected. The numerical agreement is usually within a factor of two. It was found that the flux data is inconsistent with the rest of the data. Errors on the order of 30 m/s in the individual velocity measurements are believed to be present to account for the differences.

The Perkins model is able to predict reasonable growth rates of the development of F_2 ; however, a direct comparison between the growth rates predicted by the model and actual onset times is not possible because of the lack of data on the eastward neutral wind.

The linear growth rate of the Perkins model is extended by including recombination, and a short wavelength damping term and coupling to the E region. It is found that, for wavelength perturbations several kilometers or longer, the E region can short circuit instabilities in the F region and reduce the growth rate.

FSU-IRL-SCI-451

Classification Numbers:

1.5.3 F-Region